Indian Journal of Contemporary Science

ISSN 2229-5321

Volume 13 No. 3

July-September, 2022

PUBLISHER

NEW GENERATION PRESS
F-3/139, Sector 16, Rohini, Delhi-85

Volume 13 No. 3
July-September, 2022

Indian Journal of Contemporary Science

Editorial Address:
448, Pocket V, Mayur Vihar, Phase - I
Delhi - 110091
Phone: 011-22753916, 40564514
e-mail: editorialindia@gmail.com

Editorial

The future of scientific research in India is very promising. India is the Promised Land of scientific and technology research. Advances in these two areas are having a significant impact in India's present and therefore, future. India is the primary source for many outsourcing companies for that reason. In addition, India has a large pool of professionals who are high skilled and a valuable asset to the country. India's government is a democracy that favours advances and research in the technological and scientific areas. The future of India seems bright. India's research and development in many areas such as genetic modification, bio-energy sources, biochemistry, atomic energy, organ donation, biomedical science, and many other issues will determine much of the way these issues are viewed by the world in the near future. How India handles many of the ethical dilemmas that scientific research presents will be an education for many other countries, including developed countries.

India is leading in many areas and evolving in others. However, most funding comes from public sources, and many times, it is limited. This area has to evolve, and more private funding is to be encouraged so India can compete with other countries like China. Industrial research and development competitiveness must be encouraged more, as most of the effort goes into the field of space, defence, oceanography, and atomic energy. However, India is strong in Software technology and computer science. The lack of attractive salaries compared to the private sector has created a void in the education and research sectors. However, it is a matter of money and not quality of talent. Indian minds are among the brightest and skilled, and many students from the ITT's are highly sought by European and American universities. India has to its advantage the willingness to work with other countries in research and science development and lend its talents to the project. Controversy about India not producing enough PhD's in the science arena is one that have been going on recently. If India wants to continue to prosper in this area, something must be done in respect. It is the opinion of Professor CNR Rao - a leading Indian scientist - that if India wants to keep and surpass its place in the scientific world, it must contribute more in that area, as right now it is not producing enough professionals to compete. This is viewed as one of the biggest obstacles for India. India is not producing the required number to meet the demand of the students in universities and colleges. The debate continues about the need to focus more in the basic sciences, open-ended research, and less in targeted research. Politics is said to be blamed, wrong allocating of efforts and funding, and lack of private funding as well.

—Editors

Contents

Description of a New Species of Genus Rhagovelia Mayr, 1865 from India (Hemiptera: Heteroptera)

V.K. Khandelwal

Dept. Of Zoology, K.R. (P.G.) College, Mathura

Abstract: Rhagovelia Mayr,1865 is an important genus of family Veliidae,1843 This genus is represent by Mayr ,1865 with the type species Rhagovelia nigricans Burm. One new species of the genus Rhagovelia miniscula sp.nov. reported from Mathura India.

The Veliidae are perhaps the best known of all aquatic Hemiptera of the world and are extremely common in Indian water. The members of the family Veliidae are well recognized from the related family Gerridae on the basis of hind leg not surpassing beyond the tip of abdomen and the presence of median longitudinal groove on vertex. Rhagovelia Mayr,1865 belongs to the sub family Rhagovellinae China & Usinger,1949 This sub family includes the important genera Rhagovelia Mayr,1865.The species are easily recognized due to large compound eyes:labrum small located anterior to the anteclypeus,paraclypeus lies lateral to the anteclypeus, four segmented rostrum and ocellus absent.Pronotum well developed posteriorly. Pleurum and the sternum fused. Forewing in macropterous form not well differentiated. Abdomen with well-developed carina.

Genus – Rhagovelia Mayr,1865

Type species: Rhagovelia nigricans Burm.

Type: British Museum , London

Rhagovelia Mayr,1865. Verh. Zool-Bot. Ges.,Wien, P.445

Rhagovelia Champion, 1898. Biol. Centr.-Am. Rhync. Vol.ii, P.131

Buccla Stal, 1866.Hem.Afr.Vol.III, P.167

NeoveliaBuch. White, 1879. Journ. Linn.Soc. Zool. Vol. XIV. P.487

The genus is well characterized by three jointed tarsi,and a long ,deeply fissured, terminal joint of intermediate tarsi . Eyes large usually as wide as the vertex at the posterior margin. Rostrum four segmented with the second segment the longest. Antennae four segmented with the conspicuous protuberance at the base. Ocellus absent. Pronotum well developed. Anterior trochanter unarmed.First genital segment longer than seventh sternite. Second genital segment not modified. Female with eighth

abdominal segment with usually lateral tuft of latero-caudally directed long hairs: ninth abdominal segment bent.

Rhagovelia miniscula sp.nov.

Description: Size: Male, Apterous 2.43 mm in length; width of head across mesoacetabula 0.66mm -1.05 mm ; Female , Apterous , 2.54mm in length,width of head across mesoacetabula 0.56mm- 1.23mm.

Colour: Dorsal surface of body dark, black colour rectangular spot on pronotum, lateral part of pronotum and lateral abdominal region covered with blackish pubescence.Venter and pleura grayish. Antennae and legs brownish. Abdomen covered with golden white hairs.

Structural Characteristics:

Head: Head including eyes about two times as wide as long. Eyes of male covered outward while eyes of female depressed slightly. Relative length of antennal segment of male Ist:IInd:IIIrd:IVth :: 28:12:12:15 and of Apterous female Ist:IInd:IIIrd:IVth ::27:14:16:18.Antenniferous tubercles inconspicuous. Basal margin of clypeus indistinct.Mandibular and maxilliary plates separated. Rostrum surpassing posterior margin of post sternum: third segment three times longer than last segment.

Thorax: Pronotum much longer,rounded on caudal margin. Intersegmental suture between meso and metanotum distinct. Femur with a comb of teeth apically. Middle femur with thickened bristles.Hind femur moderately incrassate. In Apterous female front femur more slender than in male. Hind femur not incessate.

Relative Length of Leg Segments:

Apterous Male: 2.43mm

Femur	*Tibia*	*tarsus*	*First tarsal segment*	*Second tarsal segment*	
Fore leg	28	29	07	-	-
Mid leg	56	41	47	22	26
Hind leg	48	51	14	4	10

Apterous Female: 2.54mm

Femur	*Tibia*	*tarsus*	*First tarsal segment*	*Second tarsal segment*	
Fore leg	32	31	08	-	-
Mid leg	60	42	48	21	28
Hind leg	45	56	16	5	11

Abdomen: All connexival segments strongly constricted to overlap the abdominal tergites. Last abdominal tergite a little longer then the preceding two segments. Abdominal venter with a dense layer of long hairs.

Male genitalia: First genital segment longer than seventh sternite with a median longitudinal ridge and lateral depressions. Second genital segment with parallel sides, without modifications. Parameres slender,pointed broad at base with apical third strongly bent. Pygophore subovate ventrally.Proctiger elongate. Endosoma with dorsal plate long and recurved proximally: apical accessory plates small, lateral plates small but distinctly hooked basally. Ventral plate very long.

Female genitalia:Eighth abdominal segment with lateral tuft of latero-caudally directed hairs, abdominal segment strongl bent downwards. First valvulae with very short inner lobe, attached with vulva. Outer lobe relatively very long, narrow, membranous, pointed apically. Second valvulae bifid. Vulva membranous.

Material examined: Holotype one Apterous male, allotype one Apterous female, Paratypes 11 males,5 females in spirit.

Distribution: INDIA: Mathura

Remark: This species belong to minuta group of Rhagovelia. The species Rhagovelia miniscula sp. nov. is closely related to Rhagovelia mindanaoensis Hungerford & Matsuda which , however, are larger species with somewhat different parameres and without long hairs on abdominal sternite in male.

The species named because of its minute size.

Acknowledgement: The Author is greatful to Dr. Y.C.Gupta former Head & Director, B.S.A. College, Mathura for providing material on loan.

References:

1. Amyot, E. and Serville, A., (1843). Hemipteres Paris pp. 675.
2. Burm, (1935). Handb. Ent. Ii, p.213.
3. China, W.E. & Usinger, R. L., (1949). Ann. Nat. Hist., (12) 2: 343-354.
4. Drake, C.J., (1948). Proc. Ent. Soc. Washington, 50(3): p. 61-62.
5. Hungerford, H.B. & Matsuda, R.,(1961). Lbid;42(2): pp. 257-259, 5 figs.
6. Kirkaldy, G.W., (1902). Entomologist 3:pp. 136-138.
7. Lundblad, O., (1937). Rhagovelia, Arten. Ent. Tidskr. 1-9, 4 figs. 2pls.
8. Mayr, (1865). Verh. Zool. Bot.Ges. Wien.p.445.

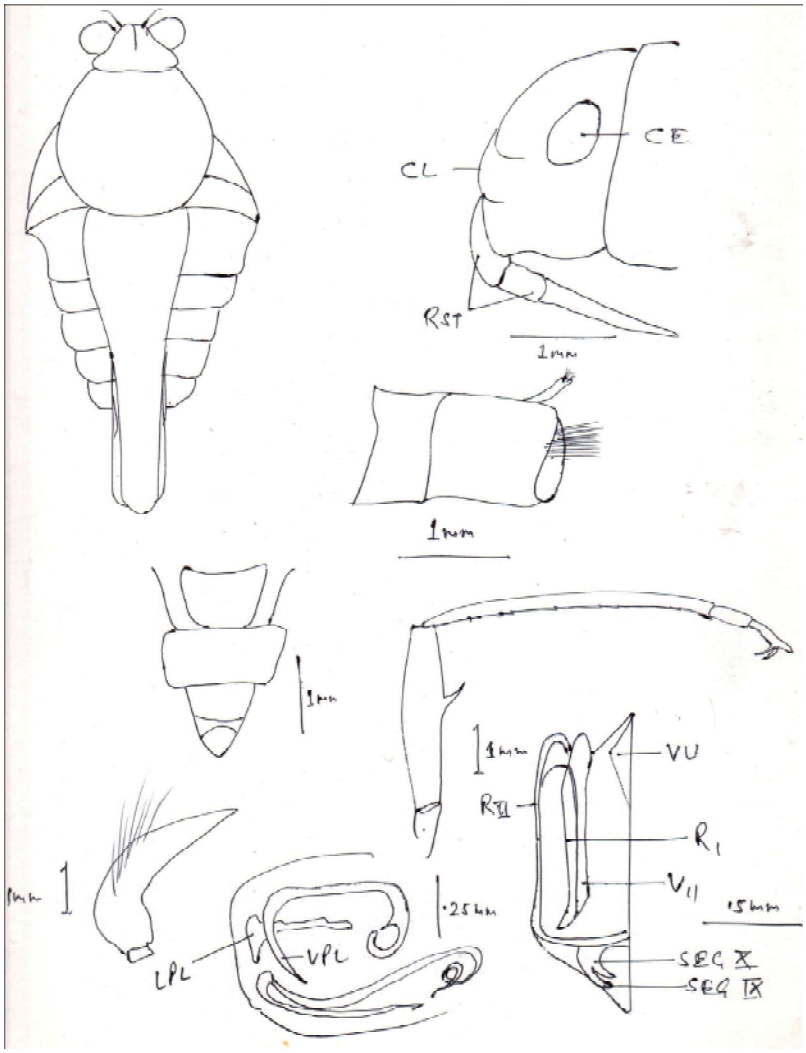
CE
CL
RST
1mm
1mm
1mm
1mm
VU
RII
R1
VII
.15mm
SEG X
SEG IX
LPL
VPL
.25mm

Dissolved Organic Carbon in The River Ganga and Brahmaputra With Special Reference To Heteroatoms

Poonam Kumari
Research Scholar, Department of Chemistry, V.K.S.U., Ara (Bihar)

Abstract:

This paper reveals that the Ganges and the Brahmaputra, two major rivers in India and Bangladesh, contribute major loads of dissolved organic matter (DOM) into the Bay of Bengal. The composition, sources, availability, and seasonal heterogeneity of DOM in these two rivers are thus very important to know about the biogeochemical cycles, fate, and ecological and environmental aspects before discharge into the Bay of Bengal. In this study, DOM was characterized in the downstream reaches of the Ganges and Brahmaputra rivers before their confluence with each other. The concentration of dissolved oxygen decreased in the pre-monsoon and monsoon in both rivers due to the increased decomposition and oxidation of rainfall-washed substances and thus made the water unsuitable for drinking. The amount of total coliform also made the water of both rivers unsuitable for drinking, recreational, and irrigation purposes. In total, four DOM components (one humic, one detergent-, and two protein-like) in the Ganges River and five DOM components (three humic- and two protein-like) in the Brahmaputra River were identified at their downstream reaches using fluorescence spectroscopy, three-dimensional excitation emission matrix (EEM) measurement, and parallel factor analysis (PARAFAC). The abundances of DOM components were higher in the pre-monsoon and monsoon seasons than in the post-monsoon season. Protein-like components contributed the most in two rivers. DOM was obtained mostly from terrestrial sources and was matured and less aromatic. This study also identifies that sewage water is the largest contributor to DOM in surface water, next to natural sources, and indicates the excessive anthropogenic activities in the river basins .

Keywords: Dissolved organic matter, fluorescence spectroscopy, excitation-emission matrix, parallel factor analysis, anthropogenic activities

Introduction:

Dissolved organic matter (DOM) is a complex pool of compounds critical in the global carbon cycle (Wünsch and Murphy, 2021) and plays a

vital role in aquatic ecosystems (Chaves et al., 2020; He et al., 2021). Identifying the molecular composition of riverine DOM is essential for knowing the source, mobility, and fate across landscapes. Geomorphological characteristics of the watershed, land use, and sediment load can change DOM's quality, quantity, and reactivity over time (Wagner et al., 2015). Globally, large rivers are significant sources of DOM to the oceans and connect the terrestrial and marine biogeochemical cycle (Wagner et al., 2015; Riedel et al., 2016; Pang et al., 2020). The Ganges–Brahmaputra–Meghna (GBM) river basin is the third-largest hydrological system globally in terms of freshwater flow to the ocean. It is also one of the most populated deltas (Sharma et al., 2021). These transboundary river basins confront intensified stress on water resources (Munia et al., 2020). Moreover, the structure and composition of DOM remain poorly understood in rivers flowing through different climates and landforms (Liu et al., 2021). Therefore, a more detailed study is needed on DOM quality, quantity, and reactivity on their global drivers, such as changes in local natural runoff and inflows from upstream parts of a basin and local and upstream water consumption.

Himalayan rivers play a pivotal role in regional water and food supply, global sediments, and carbon budgets (Chen et al., 2020). Land use and anthropogenic activities directly affect downstream DOM quality and carbon (C) fluxes in the Asian rivers (Wagner et al., 2015; Park et al., 2018). Considering the physicochemical parameters, the water quality was found to be in the maximum deteriorated state during the monsoon and in the minimum state in the pre-monsoon in the Ganges and Brahmaputra rivers in Bangladesh (Tareq et al., 2013). Heavy metals were found exceeding the standard limits during the monsoon in the Brahmaputra River in Bangladesh (Rahman et al., 2017; Bhuyan et al., 2019). The water quality in the upstream Ganges River in Bangladesh was found to be unsuitable for drinking purpose and household consumption (Haque et al., 2020). The fluorescent DOM properties in the upstream Ganges of fulvic acid (M-type), fulvic acid (C-type), and protein-like were higher in the pre-monsoon (March–June) and monsoon (July–October) periods than in the post-monsoon (November–February). The components were fresh, autochthonous, and had less aromatic characteristics from natural and anthropogenic sources. The DOM components were abundant from the late pre-monsoon to the ^{monsoon} period in the upstream Ganges River in Bangladesh (Niloy et al., 2021a; Niloy et al., 2021c). However, there is no insight into the downstream evolution of DOM composition in the Ganges and Brahmaputra rivers in Bangladesh.

Fluorescence spectroscopy is a powerful, sensitive, and broadly used method to characterize DOM in fresh and marine water (Hudson et al., 2007; Mostofa et al., 2010; Nelson and Gauglitz, 2016). Fluorescence measurements require no pre-concentration of samples to generate three-dimensional excitation emission matrix (EEM) landscapes of conjugated DOM components.

The particular wavelength position in an EEM landscape can reveal the DOM components, sources, and compositional states. Further analyzing EEM landscapes using a parallel factor multivariate analysis (PARAFAC) can separate the conjugated DOM components from the EEM (Stedmon and Markager, 2005a; Stedmon and Markager, 2005b; Stedmon and Bro, 2008). PARAFAC could separate the conjugated DOM components from the EEM. The simple sample preparation technique and facile duo function of EEM-PARAFAC in fluorescence spectroscopy were worth using in this study.

The degradation potential index (DPI) is used to observe differences in the degradability of DOM among sources. It is defined as the ratio of availability of the labile to recalcitrant organic components (Liao et al., 2021). The DPI is nowadays tagged with an end-member mixing (EMM) model to identify the contribution of various DOM sources to surface water (Yang et al., 2015; Liao et al., 2021). The Ganges and Brahmaputra rivers carry huge loads of natural and anthropogenic organic matters from their origin to downstream before the confluence (Steckler et al., 2022). The fluorescence intensity of DOM and microbial contamination was higher in the Brahmaputra River than that in the Ganges at the upstream position of these two rivers (Niloy et al., 2021a; Niloy et al., 2022).

On the contrary, the Ganges River contained more aromatic, high molecular size and weight DOM, and anthropogenically derived pollutants than the Brahmaputra River at the upstream location of these rivers in Bangladesh. Both terrestrial and aquatic-originated DOM were present, fluctuations in DOM intensity were related to rainfall, and other climatic effects, photodegradation, and microbial activity affected the DOM composition in both rivers (Niloy et al., 2021a; Niloy et al., 2022). The selection of the downstream position was thus very significant to know about the types and concentration of DOM, their originations, and factors influencing their availability in both rivers. Considering these needs, this study aimed to characterize DOM components and identify their sources and fate downstream of the Ganges and Brahmaputra rivers of Bangladesh. This study also targeted determining the degradation level of DOM of various origins and their contribution to the river water.

Materials and Methods

Study Area

The Ganges and Brahmaputra rivers are major transboundary rivers and originate from the Gangotri and Chemayungdung glaciers of the Himalayas. After flowing through the Indian regions, the Ganges and Brahmaputra River enter Bangladesh through northwestern and northern districts named Chapainawabganj and Nilphamary. The Ganges–Brahmaputra system discharges around 30,770 m^3/s of water monthly. It carries about 1.84 billion tons of sediment/year, securing the third greatest water discharge and maximum sediment loads among world rivers (Papa et al., 2012; Steckler et al., 2022). Both river basins are greatly affected by the tropical climate. The average monthly rainfall data in the corresponding sampling location were collected using a rain gage during the study period to identify its roles in DOM intensity fluctuations (Supplementary Table S1). About 400 million and 83 million people live in the Ganges and Brahmaputra river basins, and in Bangladesh, the population density is around 390 person/km^2 and 828 person/km^2 (Mahanta et al., 2014; The Himalayan Climate and Water Atlas, 2015). The Ganges–Brahmaputra basin is used for agricultural production, fisheries, recreation, irrigation, and navigation, making it an economic hub. However, the basins of the two rivers are affected by biophysical, socioeconomic challenges, climatic stress, and substantial anthropogenically derived pollutants (Anwar, 2006; Rahman et al., 2020).

DOC and DOM Measurement

DOC was determined using a catalytic oxidation method (Shimadzu TOC analyzer LCPH/CPN) at high temperature through a non-dispersive infrared (NDIR) detector. The samples were tested for fluorescence characterization in Hitachi F-4600. The samples were measured keeping excitation (Ex) wavelength 225–400 nm and emission (Em) wavelength 250–550 nm with 5- and 1-nm intervals, respectively. The excitation and emission slits were set to 5 nm of band-pass at 1200 nm min^{-1} scan speed. Before analysis, all the quartz cuvettes were rinsed with a 5% (w/w) nitric acid solution. The Milli-Q water blank EEM spectra were taken before the sample spectra. EEM data were further rectified for inner filter effects (Panigrahi and Mishra, 2019). The ultrapure Milli-Q water was used as a blank reference sample and was also used to convert arbitrary units of data into Raman units. The filtered samples were also measured using an UV spectrophotometer (SPECORD 210 Plus, Analytikjena) concurrently in the wavelength ranges between 190–1100 nm, keeping scanning speed at 60 nm/min.

Organic Matter Components

The parallel factor analysis (PARAFAC) model was used to separate individual DOM components from the EEM using the DOMFluor toolbox (v1.7) in MATLAB software (v.2016a) (Stedmon and Bro, 2008). Blank Milli-Q water data were subtracted from the original sample data to remove Raman and Rayleigh scattering (Goletz et al., 2011; Stedmon and Bro, 2008). Sample data were validated properly using the split-half technique to identify the exact number of DOM components. The identified intensity (i.e., F_{max}) values were read at Raman Unit (RU).

Degradation Potential Index Calculation and its Coupling with the End-Member Mixing Model

The degradation potential index (DPI) was calculated from the labile/recalcitrant ratio of the DOM components (Liao et al., 2021). The humic (C)-like DOM component shows fluorophores at a longer wavelength (UV–Visible), while the humic (M)-like component shows fluorophores at the midrange wavelengths (UV-A). Tryptophan-, tyrosine-, and detergent-like components show fluorophores at shorter wavelengths (UV-B and UV-C). The fluorophores in longer wavelengths might be significantly affected by photodegradation and lose their availability significantly, while fluorophores of shorter wavelengths are more susceptible to microbial degradation (Mostofa et al., 2010; Mann et al., 2012; Zhou et al., 2019; Yang et al., 2020). The tyrosine-like component could be removed entirely by biodegradation (Cory and Kaplan, 2012). However, tryptophan-like components exist as a persistent DOM in water as microbes cannot ingest and metabolize them properly (Cory and Kaplan, 2012). The differentiation of lability and recalcitrant nature of DOM was defined considering both photo- and microbial degradation in this study. The synergistic effects of photo- and microbial degradation widely reduce humic (C)-, tyrosine-, and detergent-like components. However, due to mid-wavelength position and microbial inability in mineralization, the photo- and microbial degradation effects could remove humic (M)- and tryptophan-like components in small amounts from river water (Mostofa et al., 2010; Cory and Kaplan, 2012; Mann et al., 2012; Zhou et al., 2019; Yang et al., 2020). Considering the degradation effects on the DOM, humic

Results and Discussion

Comparative Analysis of Water Quality Parameters

The temperatures in both river basins had higher values in the pre-monsoon and monsoon than in post-monsoon and showed a similar pattern of seasonal variation ($r = 0.992$, $p < 0.01$) (Table 1). Turbidity was

higher in the monsoon than in pre-monsoon and post-monsoon, and this might be due to the significant organic matter inputs by rain in both the Ganges and Brahmaputra rivers. The water was alkaline in both rivers (Table 1). It exceeded the permissible limits set by the Department of Environment (DoE) in Bangladesh (BECR, 1997) for drinking, irrigation, and fishery purposes most of the time of the year in the two rivers. DO was comparatively low in the monsoon in both rivers, indicating the additional oxygen consumption to decompose and oxidize increased organic matters (Table 1). However, DO was within the accessible limit according to the standards set by the DoE (BECR, 1997) to use water for drinking, fisheries, and irrigation. EC was comparatively lower in the monsoon (Table 1). According to the World Health Organization WHO, (2004), EC was within the permissible limit. TDS was relatively lower in the pre-monsoon and monsoon than in post-monsoon (Table 1). TDS was within the acceptable limits according to WHO, (2004). BOD was comparatively high and

TABLE 1 | Physicochemical parameters in the downstream of Ganges (G) and Brahmaputra (B) rivers.

Parameters	River	Mar 2019	Apr 2018	May 2018	June 2018	July 2018	Aug 2018	Sep 2018	Oct 2018	Nov 2018	Dec 2018	Jan 2019	Feb 2019
Temperature (°C)	G	28.5	33.9	31.8	32.2	30.9	32	30.8	32.5	25.7	20.7	21	22.9
	B	26.7	33.3	30.7	30.9	29.7	31.1	30.5	29.7	24.3	18.7	18.2	21.2
pH	G	8.8	9	9.4	8.4	8.9	8.3	8.8	8.4	8.5	8.4	8.3	8.7
	B	8.4	9.2	8.7	8.4	9.2	8.2	8.8	8.3	7.5	8.4	8.2	8.6
DO (mg/L)	G	8.7	7.2	7.3	7.9	7.7	8.1	7.6	7.4	7.8	9.2	11.3	10.3
	B	8.2	7.4	7.4	7.7	7.5	7.4	7.6	7.6	7.8	9.5	10.8	9.6
EC (µS/cm)	G	244.2	189.2	204.6	154	157.3	195.8	134.2	146.3	158.4	182.6	232.1	237.6
	B	245.3	200.2	184.8	160.6	156.2	161.7	132	149.6	169.4	172.7	260.7	243.1
TDS (mg/L)	G	116.6	83.6	181.5	143	67.1	112.2	148.5	156.2	225.5	231	240.9	254.1
	B	117.7	90.2	162.8	152.9	68.2	84.7	147.4	158.4	215.6	239.8	269.5	256.3
Turbidity (FTU)	G	9.2	19.5	43.5	141.2	167.6	133.9	149.4	145.2	75.1	21.5	20.8	16.7
	B	11.9	15.9	37.2	108.2	149.2	95	123.3	185.8	22.7	11.4	15.7	18.8
BOD (mg/L)	G	2.6	3.9	7	4.7	4.3	2.8	2.2	2	2.6	2.7	3.9	4.5
	B	2.5	2.8	6.1	5.1	3.7	2.6	1.5	2	2.6	3.3	4.2	4.4
COD (mg/L)	G	27.5	45.1	82.5	61.6	53.9	51.7	44	42.9	42.9	37.4	29.7	25.3
	B	20.9	47.3	72.6	50.6	47.3	48.4	42.9	40.7	34.1	31.9	19.8	17.6
Total coliform (CFU)*10^3	G	1.53	1.78	2.02	2.07	0.23	0.44	1.16	0.85	0.94	1.05	1.19	0.83
	B	1.49	1.64	1.8	1.89	0.47	0.29	1.87	0.91	1.11	1.18	1.01	0.64

exceeded the permissible limit set by the DoE (BECR, 1997) at the end of the pre-monsoon (Table 1). COD was also higher from pre-monsoon to the entire monsoon in both the rivers (Table 1). COD values exceeded the permissible limit set by the DoE (BECR, 1997) for drinking purposes throughout the year. Total coliform was in a minimum amount in the early monsoon in both rivers (Table 1). This could be due to the large deposition of organic matter and resistance to the growth of coliform bacteria by intense chlorophyll a production in eutrophication (Seo et al., 2019). However, the total coliform exceeded the limits set by the DoE (BECR, 1997) and confirmed that the water was unsuitable for drinking, recreational, and irrigation purposes in both rivers.

Excitation Emission Matrix, Parallel Factor Analysis, and DOC Concentration

The EEM measurement identified five fluorophores in the Ganges River: Peak A (Ex/Em = 245/414 nm), Peak M (310/398 nm), Peak W (340/ 428 nm), Peak T (275/334 nm), and Peak Tuv (230/ 346 nm) and seven fluorophores in the Brahmaputra River: Peak A (Ex/Em = 245/418 nm), Peak C (365/442 nm), Peak M (295/ 404 nm), Peak T (275/312 nm), Peak Tuv (230/304 nm), Peak T (275/358 nm), and Peak Tuv (230/348 nm). Peaks A, C, and M represent humic-like component (Coble, 1996), while Peak W represents detergent-like anthropogenic substance (Mostofa et al., 2010; Niloy et al., 2021c). Peak T and Peak Tuv describe the tyrosine- and tryptophan-like component at the low and high emission wavelengths, respectively (Coble et al., 1990). The identified fluorophores thus indicated the natural and anthropogenically derived DOM components in the two rivers. PARAFAC analysis identified DOM components in the Ganges and Brahmaputra rivers, considering monthly water samples of each year. The PARAFAC analysis found four DOM components in the Ganges River: C1-G (Ex/Em = 230/406 nm, 310/406 nm), C2-G (265/462 nm, 340/462 nm), C3-G (225/334, 270/338), and C4-G (285/354) (Supplementary Figure S2). C1-G could be characterized as humic (M)-like, C2-G as detergent-like, and C3-G and C4-G as protein-like components. C1-G in such wavelength could be labile and originated from terrestrial sources (Goldman and Sullivan, 2017). FI, HIX, and $SUVA_{254}$ values also indicated the composition and source of C1-G as labile, less aromatic, and terrestrially derived. Anthropogenically derived component C2-G is widely used as a fluorescent whitening agent (FWA) in maximum commercial and household detergents in Bangladesh at a concentration higher than the usage standard (Niloy et al., 2021c). This component was also identified upstream of the Ganges River in Bangladesh (Niloy et al., 2021a), in the rainwater of Bangladesh (Niloy et al., 2021b), and even in the sewerage drainage water in China (Mostofa et al., 2010). C3-G and C4-G are two tryptophan-like components (Mostofa et al., 2010; Baghoth et al., 2011; Wu et al., 2011). Anthropogenically derived C3-G component is available in sewerage water and municipal leachate, while C4-G is autochthonous and could be found in water treatment plants. Tryptophan-like component is a dominant organic compound found in microbially derived precursor materials, and a small portion of this component is labile or semi-labile. The encapsulation of tryptophan-like component in the humic matrix helps it behave as a recalcitrant molecule in the environment (Cory and Kaplan, 2012). This persistent nature of the tryptophan-like component has well-resembled with the C3-G in this study in terms of similar wavelength

ranges (Table 2). C4-G had a bathochromic shift (red shift) in emission wavelength, and it could be due to its increased solvent polarity and bonding with metal ions (Kowalczuk et al., 2009).

Conclusion

This study provided a precise figure about the insights of the DOM components in the downstream of the Ganges and the Brahmaputra rivers. Both natural and anthropogenically derived DOM prevailed in both rivers. The fluorescent intensity of DOM components was higher in the pre-monsoon and monsoon than in post-monsoon seasons in both rivers. DOM components were mostly from terrestrial sources in both rivers. The significant presence of detergent- and tryptophan-like DOM in the Ganges River indicated intense anthropogenic activities nearby its basin. On the contrary, the Brahmaputra River basin was mainly covered by forest and vegetation due to the dominant presence of humic-like components. The DPI and EMM identified sewerage water as the maximum DOM contributing source, followed by terrestrial plants > algae > soil > groundwater > industrial effluents. DOM components were matured and less aromatic. DOM molecules contained lower energy from the late pre-monsoon to the entire monsoon than the rest of the year. The downstream Ganges and the Brahmaputra River had more DOM than the upstream portion. The deteriorated condition in the downstream warned about the severe health effects on living species and suggested taking prompt actions to control and treat anthropogenic sources of DOM before discharging into surface water.

References

1. Aktar, P., and Moonajilin, M. S. (2017). Assessment of Water Quality Status of Turag River Due to Industrial Effluent. Int. J. Eng. Inf. Syst. 1 (6), 105–118.
2. Anwar, J. (2006). Pollution in the Ganges Brahmaputra Delta Plain.
3. Baghoth, S. A., Sharma, S. K., and Amy, G. L. (2011). Tracking Natural Organic Matter (NOM) in a Drinking Water Treatment Plant Using Fluorescence Excitation-Emission Matrices and PARAFAC. Water Res. 45, 797–809. doi:10. 1016/j.watres.2010.09.005

4.BECR (1997). Industrial Effluents Quality Standard for Bangladesh. Bangladesh Gaz. Addit., 179–227.

5.Bhuyan, M. S., Bakar, M. A., Rashed-Un-Nabi, M., Senapathi, V., Chung, S. Y., and Islam, M. S. (2019). Monitoring and Assessment of Heavy Metal Contamination in Surface Water and Sediment of the Old Brahmaputra River, Bangladesh. Appl. Water Sci. 9, 1–13. doi:10.1007/s13201-019-1004-y

6.Chaves, R. C., Figueredo, C. C., Boëchat, I. G., de Oliveira, J. T. M., and Gücker, B. (2020). Fluorescence Indices of Dissolved Organic Matter as Early Warning Signals of Fish Farming Impacts in a Large Tropical Reservoir. Ecol. Indic. 115, 106389. doi:10.1016/j.ecolind.2020.106389

7.Chen, M., Zeng, C., Zhang, F., Kang, S., and Li, C. (2020). Characteristics of Dissolved Organic Matter from a Transboundary Himalayan Watershed: Relationships with Land Use, Elevation, and Hydrology. ACS Earth Space Chem. 4, 449–456. doi:10.1021/acsearthspacechem.9b00329

8.Coble, P. G. (1996). Characterization of Marine and Terrestrial DOM in Seawater Using Excitation-Emission Matrix Spectroscopy. Mar. Chem. 51, 325–346. doi:10.1016/0304-4203(95)00062-3

9.Coble, P. G., Green, S. A., Blough, N. V., and Gagosian, R. B. (1990). Characterization of Dissolved Organic Matter in the Black Sea by Fluorescence Spectroscopy. Nature 348, 432–435. doi:10.1038/348432a0

10. Cory, R. M., and Kaplan, L. A. (2012). Biological Lability of Streamwater Fluorescent Dissolved Organic Matter. Limnol. Oceanogr. 57, 1347–1360. doi:10.4319/lo.2012.57.5.1347

11. Gao, S.-J., Zhao, C., Shi, Z.-H., Zhong, J., Liu, J.-G., and Li, J.-Q. (2016). Spectroscopic Characteristics of Dissolved Organic Matter in Afforestation Forest Soil of Miyun District, Beijing. J. Anal. Methods Chem. 2016, 1–10. doi:10.1155/2016/1480857

12. Goldman, J. H., and Sullivan, A. B. (2017). Characteristics of Dissolved Organic Matter in the Upper Klamath River , Lost River , and Klamath Straits Drain , Oregon and California. U.S. Geol. Surv. Open File Rep. 21, 2017–1160. doi:10. 3133/ofr20171160

Reproductive Biology of Fresh Water Fish *Catla*

Dr. Akhil Abhishek

Assistant Professor of Zoology, C.M. Science College, Darbhanga

Abstract:

The present study was carried out to analyze the differences in the activity of hormone stanniocalcin (STC) between male and female fishes of Catla during their gonadal cycle. A large variation in nuclear diameter of cells of corpuscles of Stannius (CS) were recorded in relation to testicular cycle as well as ovarian cycle which indicates that the cellular activity varied with different phases of reproductive cycle in both male and female fish. Similar changes in nuclear diameter of CS cells were also observed after 17alpha-methyltestosterone administration in males and 17 b-estradiol administrations in females. A positive correlation was observed between plasma STC levels, gonadosomatic index (GSI) and the sex steroids in both sexes, suggesting that STC has a role in the processes involved in gonadal development. In addition females showed remarkable changes in plasma calcium level during gonadal cycle while no such change for males were observed. In females the plasma calcium level estimated during different phases of reproductive cycle indicates positive correlation between plasma level of calcium and gonad growth. Thus hyperactivity of CS cells was noted in both male and female fishes during gonadal cycle along with the differences in the activity of STC as well. In female it may act as hypocalcemic factor and bring the level of calcium to normal which increases during preparatory and pre spawning phases to fulfill the increased demand of calcium for vitellogenesis. However data of male fishes indicated that plasma STC concentration varied widely during gonadal cycle but showed no consistent relationship to plasma calcium level.

Keywords: plasma calcium level, gonadal cycle, gonadal development

Introduction

The corpuscles of Stannius (CS) are unique calcitropic endocrine gland found associated with kidney of teleostean and holostean fishes. It synthesizes and secretes hormone stanniocal-cin-1 (STC-1) and stanniocalcin-2 (STC-2). Stanniectomy in eels results in significant hypercalcemia [1], while on the other hand administration of CS extracts

in to stanniectomized eels restored the serum electrolyte level to normal [2]. It has been observed that auto transplantation of CS in eels brings the plasma calcium level to normal [3]. STC-1 maintain calcium homeostasis by inhibiting calcium transport through gills [4], reducing calcium uptake through intestine [5], and stimulating phosphate reabsorption by renal proximal tubules [6]. Synthesis and secretion of STC-1 by the CS have been shown to be sensitive to extracellular ionized calcium concentration [7]. It is now a well established fact that calcium homeostasis in fishes is mainly mediated through the secretions of CS [8–12]. A second stanniocalcin (STC-2) has been identified in fishes [13], however no report exists in evidence of its role in calcium regulation [14].

Plasma calcium rises during gonadal maturation in fishes [15]. There exists a difference in the increase of plasma calcium level with respect to sex of the fish. It is more pronounced in females as reported from time to time by various workers [16–18]. The increase in plasma calcium during ovarian maturation is due to increased secretion of estrogen from the ovary [19,20] as administration of estradiol was found to induce hypercalcemia [15,20]. Estradiol increases the level of plasma calcium by acting directly on gills [21] as well as on intestine [22]. It may act indirectly via some endocrine factor like PTHrP or a related factor responsive to E2 [23]. Most of the studies indicated that there exists no correlation between serum calcium level and testicular maturation in fishes. However Woodhead and Woodhead suggested a positive correlation between blood calcium level and testicular maturation in sea cod.

CS becomes activated during gonadal maturation and this response is more pronounced in case of females. Increase in the activity of CS in male is not common but has been reported earlier by Balbontin et al.. This hyperactivity of CS during gonadal maturation may due to elevated calcium level or it may stimulate gonadal development as reported by Hiroi.

As Catla is one among the economically important species in rural parts of India it becomes necessary to know every aspect of its reproductive physiology. The role of STC in females Catla has been established as calcium regulating factor by us in our earlier work, however no such report exists in this regard evaluating the gender specific differential activity of STC during gonadal maturation in Catla. Therefore the present study was undertaken to analyze the differential activity of STC in male and female fresh water teleost Catla (Lacepede) during gonadal maturation. We hypothe-sized that positive correlation between plasma calcium and STC level during gonadal maturation will indicate towards its definite role in calcium homeostasis while on the other hand variation in plasma STC

level during different phases of gonadal cycle without any significant change in the level of calcium will indicate towards its possible role in gonadal maturation.

Materials and Methods

Fish Collection and Maintenance

Ten healthy and adult specimens of fish Catla were collected every month throughout the year with the help of fishermen. The live fishes were brought to the laboratory and were acclimatized to laboratory conditions for 15 days in plastic pool tanks having size of 90 cm diameter and 60 cms height. During this period, fish were fed with live earthworms and boiled eggs. Water was replaced every 24 h to remove fecal matter, other waste materials and residue food particles as well as to maintain suitable environment for fishes with sufficient oxygen. The tank water was maintained with following composition: temperature = 28uC6 1.0uC, salinity = 0.660.02 ppt, total hardness = 2860.05 mg/l, pH = 6.560.2 units, dissolved oxygen = 6.660.01 mg/l. The photoperiod maintained through the entire experiment was 12:12 h. The average (6SD) body weight and length of male and female fishes were 30062.50 g, 2660.35 cm and 35062.86 g, 3160.35 cm respectively. After anesthetized with phenoxyethanol the tail was severed and the blood samples were collected from the caudal vessels using a heparinized syringe for estimation of plasma calcium, 17 b-estradiol, testosterone and STC level. The fishes were sacrificed, gonads were taken out after which they were weighed (gm) for the determination of gonadosomatic index and fixed in Bouin's solution for 12 to 16 hours (depending upon the size of the tissue) after which they were completely dehydrated. Kidney along with CS was also taken out and fixed in Bouin's solution for 24 hours. Paraffin blocks of both gonads and kidney were prepared and sections of 5–7 mm were made using a microtome. Maturity stages of gonads were determined by studying histological changes after staining sections in haematoxylin and counterstaining in eosin. The sections of kidney along with CS were also stained in haematoxylin and counterstained in eosin.

Nuclear diameter of cells of CS (mm) was measured by image analyzer microscope (Metavis image analyzing system with Meltmage Lx Software). 50 nuclei were randomly selected from every fifth section of the gland. Total number of the nuclei measured was always more than 300 for each individual.

Plasma Calcium Estimation

After centrifugation in cooling centrifuge (maintained at 4uC, 4000 rpm for 5 minutes) plasma was analyzed for total plasma calcium

concentrations using calcium kit (Sigma Diagnostics).

Enzyme Linked Immunosorbent Assay

A competitive ELISA technique which is based on competition between free STC in standard or plasma samples and STC immobilized on microtiter plates for the STC antibodies was used for determination of plasma STC level.

Radioimmunoassay

Plasma testosterone and 17 b-estradiol levels were determined by RIA method following Guerriero et al.. The sensitivity of testosterone was 7 pg (intraassay, 6%; interassay, 12%), and that of 17 b-estradiol was 5 pg (intra-assay, 8%; interassay, 12%). The antibody used for testosterone determina-tions cross-reacted with dihydrotestosterone, and therefore the data are reported as androgens.

Experiment

To determine the differential activity of CS cells during gonadal cycle, an experimental set up was designed. 24 live, (12 male and 12 female) adult and healthy specimens of Catla were collected from local fishermen, during the month of December which is the resting phase for gonads. Fish were acclimatized to laboratory conditions for 15 days in plastic pool tanks having size of 90 cm diameter and 60 cms height. During this period, fish were fed with live earthworms and boiled eggs. Water was replaced every 24 h to remove fecal matter, other waste materials and residue food pellets as well as to maintain suitable environment for fishes with sufficient oxygen. The aquarium water was maintained with following composition: temperature = 28uC61.0uC, salinity = 0.660.02 ppt, total hardness = 2860.05 mg/l, pH = 6.560.2 units, dissolved oxygen = 6.660.01 mg/l. The photoperiod maintained through the entire experiment was 12:12 h. After 15 days the fishes were divided in four groups, two groups consisting of 06 female each and other two groups with 06 males each and kept in four separate aquaria of 100 L capacity. Out of the two groups of females one group was injected with 0.1 ml of vehicle (peanut oil), the other group was administrated with 100 mg of 17 b-estradiol (sigma) in 0.1 ml of vehicle. One group of males was injected with 0.1 ml of vehicle (peanut oil), while other group of males was injected with 100 mg of 17alpha-methyltestosterone (sigma) in 0.1 ml of vehicle. The fishes were injected intraperitonially on alternate days and injections were given at the same time of the day to avoid diurnal variations. The blood samples were analyzed for plasma calcium, 17 b-estradiol, testosterone and STC level estimation after 15 days. At the same time the CS was also removed for histological analysis.

Statistical Analysis

Distribution parameters are presented as means and Standard Deviation (SD). Assignment of data correlation was done by Pearson tests, and the relationships between total plasma calcium and STC were evaluated by linear regression. The accepted statistical significance level was P,0.05.

Ethics Statement

The study plan was approved by the ethical committee of Ranchi University, Ranchi (Jharkhand). Experiments were con-ducted according to guidelines approved by the relevant author-ities in India (Indian National Science Academy and Indian Council of Medical Research).

Results

Gonadal Cycle

On the basis of morphological and histological changes occurring in gonads five different stages for gonadal cycle of Catla have been identified- Phase 1 or Resting phase (Decem-ber–February), Phase II or Preparatory Phase (March–May), Phase III or Pre spawning phase (June–early July), Phase IV or Spawning phase (Late July- September) and Phase V or Post spawning phase (October–November). Morphological and histo-logical characteristics of gonads during these phases are shown in table 1.

Plasma Calcium, Sex Steroid and Stanniocalcin Level

In males. The plasma calcium level estimated during different phases of testicular cycle in the fish Catla indicates that there exists no correlation between plasma calcium level and testes growth. Negligible variation in plasma calcium level was observed in male fishes as compared to female fishes during various phases of reproductive cycle (Fig. 1). However a considerable variation in plasma testosterone as well as STC level was noted during various reproductive phases in male fishes (Fig. 2). A weak correlation between plasma STC and calcium level ($R = 0.3257$, $y = 621.65x-1978.34$), whereas a moderate positive correlation ($R = 0.6496$, $y = 3.52+0.04x$) was found between plasma testosterone and calcium level during various phases of testicular cycle. The gonadosomatic index increases from preparatory phase to pre-spawning phase and further decreases after spawning in the post spawning phase which indicates that the gonads undergo increase is weight during prespawning phase and depletion after spawning in the post spawning phase. Testosterone ranged from 0.5–1.7 ng/ml.

In females. There exists a strong positive correlation between plasma calcium and STC level ($R = 0.8763$, $y = 24.18x-25.01$) as well as between

plasma calcium and 17 b-estradiol (R = 0.9161, y = 5.39+2.09x) in female Catla during different phases of reproductive cycle. Increase in the plasma calcium level was observed during preparatory phase reaching the peak during pre spawning and spawning phase. Afterwards gradually decreases with spawning and reduced to minimum at resting phase. 17 b-estradiol changes along with GSI during ovarian cycle and ranged from 2–4.5 ng/ml. A sudden increase in gonadosomatic index was observed after preparatory phase and reaches maximum during spawning phase after which it decreases.

Nuclear Diameter of CS Cells

Nuclear diameter of CS cells also showed a large variation. Maximum hypertrophy in nuclei of CS cells was observed during pre-spawning and spawning phase in both male and female fish.

Effects of Synthetic Steroid Administration

The result of synthetic steroid administration in both male and female is shown. Administration of 17alpha-Methyltestosterone in males resulted in negligible increase in the plasma calcium levels whereas considerable increase in plasma STC as well as nuclear diameter of CS cells was observed. However administration of 17 b-estradiol in females resulted in an increase in plasma calcium level, nuclear diameter of CS cells and plasma STC levels.

Discussion

In fishes, corpuscles of Stannius synthesizes and secretes stanniocalcin, a hormone involved in calcium homeostasis [4–6], but difference in its activity between the sexes during reproductive cycle has been reported in fishes like O. mossembicus, Mugil cephalus and Notopterus notopterus.

The annual sex cycle of the fish Catla has been divided into 5 phases on the basis of the variation in the gonadosomatic index and histological features displayed by the testes and ovaries. Variations in the plasma level of 17- b-estradiol in females and testosterone in males during various reproductive phases were observed which showed similar pattern in changes as that of GSI and thus helpful in accessing the seasonal activity of gonads. High values of 17- b-estradiol between late July to September clearly indicates that females would likely to spawn during these months as increased level of 17- b-estradiol initiates vitellogenesis. High levels of testosterone during preparatory phase and spawning phase signified that fishes undergo spermatogenesis and spermio-genesis while low value indicates spermatogonia proliferation. High level of testosterone from August to September in Catla indicates it produce milts during this period. December to February is the months having low levels of testosterone

indicating spermatogonia proliferation phase for Catla. It has been observed that the seasonal changes in the activity of CS, indicated by increase in the nuclear diameter of CS cells as well as plasma STC level was found to increases in parallel with the growth of ovaries and testis similar to the result obtained previously by Subhedar and Rao in Heteropreustes fossilis. There is an increase in the nuclear diameter of CS cells at the beginning of preparatory phase (March). Maximum hypertrophy in nuclei of CS cells was observed during pre-spawning (June-early July) and spawning phase (Late July– September) in both male and female fish. These concomitant changes occurring in the nuclear diameter of CS cells and the gonads definitely suggest a correlation between gonadal maturation and CS activity. A remarkable increase in STC levels were observed in both male and female Catla during the preparatory phase reaching the peak during pre spawning phase and spawning phase after which it decreases and considerably reduced during resting phase, suggesting that secretory activity of CS is related to gonadal maturation.

Thus a correlative changes between CS cells and gonadal development has been observed in the fish Catla in the present investigation.

A marked seasonal variation in plasma calcium level was observed in female Catla associated with ovarian maturation, similar to the result obtained by earlier workers in other fishes. Increase in its level was observed during the preparatory phase reaching the peak during pre spawning phase and spawning phase and considerably reduced during resting phase. This variation in plasma concentration of calcium showed similar pattern in changes as that of plasma STC level. Female fish develop hypercalcemia during sexual maturation due to increased estrogen secretion by ovary. Level of 17-b estradiol also changes with the ovarian cycle as that of calcium level, which is similar to the observations of earlier workers. Previously it was observed that ovariectomy leads to fall in plasma calcium level as well as activity of CS which can be restored by administration of estradiol. Increased level of estrogen during ovarian maturation initiates vitellogenesis by increasing the rate of transcription and translation of vitellogenin in liver as a result of which protein-bound fraction of plasma calcium level rises. Thus increase in total plasma calcium during advance phase of ovarian maturation is due to the appearance of the calcium containing yolk protein precursor vitellogenin in plasma. As the maturation of ovary advances, increase in plasma calcium level occurs because one atom of calcium is associated with every protein phosphate group in vitellogenin complex. Plasma calcium level was also found to be increased after 17- b-estradiol administration. The CS cells are stimulated when plasma calcium rises during the exposure of fish to increased calcium level (Wendelaar Bonga, et al., 1980). Thus CS hyperactivity during ovarian

maturation is due to an increase in serum calcium level which in turn is the effect of increased secretion of estradiol. Thus high state of CS activity during prespawning and spawning phase points to the probable hypercalcemia in female Catla. Administration of estradiol induced hypercalcemia in the present investigation which stimulates CS to secrete its anti hypercalcemic hormone, STC.

Conclusion:

Plenty of research papers concluded the existence of no correlation between plasma calcium level and testicular maturation. However Woodhead was of different opinion who reported a positive correlation between blood calcium level and testicular maturation in arctic cod and sea cod. Our study also indicates plasma calcium almost remains constant throughout and gonadal cycle in male Catla but plasma STC level changes with testicular cycle. No considerable variations in plasma calcium level along with testicular cycle were observed in male Catla which simply indicates that STC might be involved in some function other than calcium homeostasis. Administration of 17alpha-Methyltestosterone in males during resting phase resulted in no significant increase in plasma calcium level while plasma level of STC increases. This also supports the fact that STC is not involved in calcium homeostasis rather it may involved in gonadal maturation.

We came to conclusion that STC is involved in testicular maturation in male Catla and does not play any role in calcium homeostasis while in females it is involved in gonadal maturation as well as calcium homeostasis.

References

1. Fontane M (1964) Corpuscles de Stannius et regulation ionique (Ca, K, et Na) du milieu interieur de I''Anguille, (Anguilla anguilla). C.R. academic Science, Paris 259:875–878.
2. Jones C, Henderson IW, Chan DKO, Rankin JC, Mosley W (1996) Pressure activity of the extracts of the corpuscles of Stannius from the European eel, (Anguilla anguilla Lacepede). J Endocrinol 34: 393–408.
3. So YP, Fenwick JC (1979) In vivo and in vitro effects of Stannius corpuscles extracts on the branchial uptake of Ca in stanniectomized North American eels (Anguilla rostrata). Gen Comp Endocrinol 37:143–149.
4. Lafeber FP, Hanssen RG, Choy YM, Flik G, Herrmann-Erlee MP, et al. (1988) Identification of hypocalcin (teleocalcin) isolated from trout Stannius corpuscles. Gen Comp Endocrinol 69:19–30.
5. Sundell K, Bjornsson BT, Itoh H, Kawauchi H (1992) Chum salmon (Oncorhynchus keta) stanniocalcin inhibits in vitro intestinal calcium uptake in Atlantic cod (Gadus morhua). J Comp Physiol [B] 162:489–495.

6. Lu M, Wagner GF, Renfro JL (1994) Stanniocalcin stimulates phosphate reabsorption by flounder renal proximal tubule in primary culture. Am J Physiol 267(5 Pt 2):R1356–R1362
7. Wagner GF, Jaworski EM, Haddad M (1998) Stanniocalcin in the seawater salmon: structure, function, and regulation. Am J Physiol 274(4 Pt 2):R1177–R1185.
8. Srivastava AK, Srivastava SK, Sasayama Y, Suzuki N (1996) Corpuscles of Stannius- extract-induced rapid but transient hypocalcemia and hyperphospha-temia in string ray Dasyatis akajei. Gen Comp Endocrinol 104(1):37–40.
9. Wei-guo LI, Wang Kun-ying (1999) Advances in the Research of stanniocalcin produced by the corpuscles of Stannius in teleost. Zool Res 20 (2):147–152.
10. Clark MS, Bendell L, Power DM, Warner S, Elgar G, et al. (2002) Calcitonin: characterization and expression in a teleost fish, Fugu rubripes. J Mol Endocrinol 28: 11–123.
11. Hang X, Balment RJ (2005) Stanniocalcin in the euryhaline flounder (Platichthys flesus): Primary structure, tissue distribution, and response to altered salinity. Gen Comp Endocrinol 144:188–195.
12. Shin J, Sohn YC (2008) Molecular cloning of stanniocalcin 1 and its extra corpuscular regulation by salinity and $Ca2^{+}$ in the Japanese Flounder. Zool Sci 25(7): 728–738.
13. Luo CW, Pisarska MD, Hsueh AJ (2005) Identification of a stanniocalcin paralog, stanniocalcin-2, in fish and the paracrine actions of stanniocalcin-2 in the mammalian ovary. Endocrinol 146:469–476.
14. Wagner GF, Dimattia GE (2006) The stanniocalcin family of proteins. J Exp Zoolog A Comp Exp Biol 305:769–780.
15. Guerreiro PM, Fuentes J, Canario AV, Power DM (2002) Calcium balance in sea bream (Sparus aurata): the effect of oestradiol-17b. J Endocrinol 173(2): 377– 385.
16. Ahmad N, Swarup K (1990) Seasonal Changes in structure and changes in serum calcium level and the reproductive cycle of a freshwater female catfish, Mystus vittatus (Bloch). European Archives of Biology (Bruxelles) 101: 285–294.
17. Srivastava SJ, Srivastava SK (1994) Seasonal changes in liver and serum proteins, serum calcium, inorganic phosphate and magnesium levels in relation to vitellogenesis in a freshwater catfish, Heteropneustes fossilis (Bloch). Ann d'Endocrinol Paris 55:197–202.
18. Srivastava SK, Srivastava AK (1998) Annual changes in serum calcium and inorganic phosphate levels and correlation with gonadal status of a freshwater murrel, Channa punctatus (Bloch). Braz J Med Biol Res 31:1069–1073.
19. Guerreiro PM, Fuentes J, Power DM, Ingleton PM, Flik G, et al. (2001) Parathyroid hormone-related protein: a calcium regulatory factor in sea bream (Sparus aurata L.) larvae. Am J Physiol Regul Integr Comp Physiol 281: R855–R860.

20. Gillespie DK, de Peyster A (2004) Plasma calcium as a surrogate measure for vitellogenin in fathead minnows (Pimephales promelas). Ecotoxicol Environ Saf 58: 90–95.
21. Filby AL, Tyler CR (2005) Molecular characterization of estrogen receptors 1, 2a, and 2b and their tissue and ontogenic expression profiles in fathead minnow (Pimephales promelas). Biol Reprod 73: 648–662.
22. Wang DS, Senthilkumaran B, Sudhakumari CC, Sakai F, Matsuda M, et al. (2005) Molecular cloning, gene expression and characterization of the third estrogen receptor of the Nile tilapia, Oreochromis niloticus. Fish Physiol Biochem 31: 255–266.
23. Fuentes J, Guerreiro PM, Modesto T, Rotllant J, Canario AVM, et al. (2007) A PTH/PTHrP receptor antagonist blocks the hypercalcemic response to estradiol-17. Am J Physiol Regul Integr Comp Physiol 293: R956–R960.
24. Oguri M, Takada N (1967) Serum calcium and magnesium levels of goldfish with special reference to the gonadal maturation. Bull Jpn Soc Sci Fish 33: 161– 166.
25. Woodhead PMJ, Woodhead AD (1964) Seasonal Changes in the Physiology of the Sea Cod in Relation to its Environment. I. Seasonal Changes in the Physiological Reactions of Barentzsea Cod, Gadus morhua L. Particularly Affecting Migration and Maturation. IONAF Envir. Symp. Ser. No. 117–175. Academic Press, New York and London.

Study on Nephro Toxicity and Stress Response of *Clarias Batrachus*

Dr. Anshu Sinha

Assistant Professor of Zoology, C.M. Science College, Darbhanga, Bihar

Abstract

This paper reveals that traditional wisdom a propos the nutritional benefits of Indian catfish *Clarias batrachus* is the domino effect into its high consumer demand (global market value ≈800000 USD). Analytical studies also indicated towards easily digestible protein, mineral & adequate good cholesterol (HDL concentration >150 mg/dl, HDL > 60% of Total Cholesterol) content of the fish species. The species is well adapted in virtually all Indian aquatic ecosystems, though production remains low. This paper reviews recent developments in catfish physiology with respect to *Clarias batrachus* and its aquaculture significance.

Keywords: *Clarias batrachus,* Indian catfish, Fish physiology, Nutritional benefits, High Density Lipoprotein, Aquaculture.

Introduction

Candidates of the genus *Clarias* has been traveled to many continents, adapting itself successfully & found throughout Asia & Africa. *Clarias batrachus* in some parts of India, particularly in West Bengal & Tripura is considered as a medicinal fish & traditionally remained a strike among the pregnant & lactating mothers, the elderly & children.Many a times consumption of "Magur" (Local name of *C.batrachus*) is prescribed prophylactically to the anemic & malnourished individuals as well as for the convalescent of the patients due to the nutritional superiority. Intensive *C.batrachus* culture in several Indian states as in rural Bengal & Tripura have much potential towards livelihood development, employment generation & ensureing nutritional enrichment in the regular diet among of the people.

This rough & tough species has been studied extensively by many workers in terms of physiology, biochemistry, toxicology, host parasite interaction, pathology, culture characters as well as its population genetics. This paper illustrates the significant content of serum HDL (High Density Lipoprotein) and reviews the major studies carried out by the physiologists, biochemists & aquaculturists throughout the world that contributed immensely in our understanding the life & biology of *Clarias batrachus.*

Why Intensive Culture of *Clarias Batrachus*?

Successful aquaculture of this species may bring about socioeconomic sustainability of the rural people. Intensive *C.batrachus* culture will gain popularity mainly because the species require no special treatment with respect to the conditioning and the growth factors unlike many other aquaculture species. A comparatively simple culture characteristic with efficient food conversion (Ali & Jauncey 2005) & excellent nutritional profile (Rui et al 2007) makes *Clarias* very suitable for commercial intensive culture. A common perception of easily digestible high grade protein, high concentration of iron & beneficial lipid content may be instrumental towards its high acceptance as medicinal fish. A yearlong study on the blood plasma lipid of *C.batrachus* in a population (logW= - 0.8628+2.097 logL, Debnath 2008) revealed that the HDL content ranges from 150 mg/dl – 180 mg/dl which is more than 60% of total cholesterol (Fig 1).

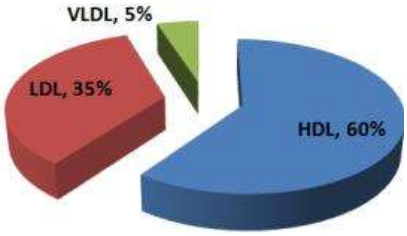

***Figure 1: Lipid Fraction in the blood plasma of* C batrachus.**

According to the data released by the Fisheries & Aquaculture department, Food & Agriculture Organization of the United Nations, *C.batrachus* has been propagated throughout the Asia from Thailand & Indonesia (Java). The species has been introduced to as far as Europe (United Kingdom), USA & Australia (Papua New Guinea) from various pockets of South Asia & South East Asia. FAO data also divulge the regular growth in the global production, processing & subsequent earning from different catfish varieties (global market value $\approx$800000 USD) (Fig 2).

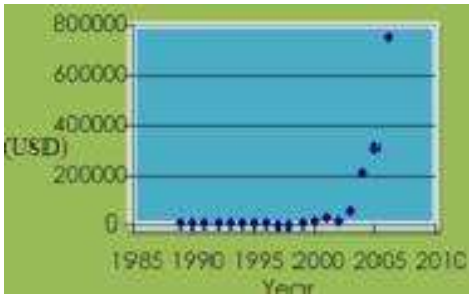

Figure 2: Global market value of Catfish produced worldwide (FAO, 2010).

Recent Advances *in Physiology & Aquaculture of Clarias Batrachus*

Reproductive and Developmental Physiology of Clarias Batrachus

Our knowledge & understanding of the reproductive physiology, breeding & culture of fishes has been constantly upgrading because the dynamics of nature sometimes bring about unique combinations of factors, that generates diversification of experimental conditions. Aquaculture is a very efficient system for conversion of low grade raw materials into high grade protein via poikilotherms, accordingly study of breeding biology & culture practices in fishes are of fundamental importance both for economics and ecology as well.

The mechanisms of endocrine regulatory pathways involving reproductive physiology (Mazumdar et al 2007) & culture of *C.batrachus* in wild or controlled environment (Ghosh 2004) are well studied. Induced breeding in order to develop cost-effective & protractable practices is imperative in aquaculture (Muir 2005). In search of an effective & economical inducer of spawning & related changes, arificial spermiation, ovulation and maturation of gamates in *C.batrachus* a number of modulators & methods (Raghuveer & Senthilkumaran 2009, Sahoo et al 2007) have been scanned.

Observations & studies of post spawning, post fertilization events & developments (Nath & Maitra 2001) are equally significant for successful outcome. *C.batrachus* is much popular in Asia as a model to study various aspects of its physiology,organ function as well as molecular biology since it has its origin in this continent.Recent studies on the developmental biology in the species describes nural and sense organ (Gaikwad et al 2009) generation. Majumdar et al (1999) studied the phosphorus containing metabolites of the developing embryos of *C batrachus* (L.) by NMR. FAO has published several reports of culture & production of *C.batrachus*.Traditional knowledge of culture practices integrated with our new findings on the intricacies of various physiological mechanisms will enable sustainable development in the yield and therefore can ensure good-food availability in the future.

Environmental Adaptation in Toxicity & Stress Response of *Clarias Batrachus*

C.batrachus has exceptionally well tolerance level in varied environment that suggests an advantageous evolutionary trait. Toxicity & stress studies can through light on the adaptation strategy of a species according to the vibrant changes of the environment and the changed character of the wild habitat,much of which is altered by now due to

increasing human intervention & exploitation.Observations by Manna et al (2008) worth mentioning in this regard where a negative confounding effect in the evaluation of toxicity has been reported in fishes.Among the other observations conducted ; Naqvi et al(1993) evaluated the severe hematotoxic effect of the commonly used farm fertilizer diammonium-phosphate compared to urea in *C.batrachus.* Effect of pollutants as pesticides, drugs, radionucleids (Joy & Sathyanesan 1981)& heavy metals(Panigrahi et al 1990) on factors like hematological indices, histopathological characters(Ray etal 1990)injuring the liver (Goel & Agrawal 1981) , brain (Kirubagaran&Joy1990), kidneys (Kirubagaran & Joy 1988) are well acknowledged in *C.batrachus*.Organ & system specific effects as on neural system (Jyothi & Narayan 2004),immune system(Datta etal 2009),endocrine level(Kirubagaran & Joy 1991),etc and general metabolism (Begum & Vijayaraghavan 1995) are also well documented in *C.batrachus*.

Latest studies on oxidative stress (Bhattacharya & Bhattacharya 2007), DNA damage & apoptosis (Datta et al 2007), gonadal development (Singh & Joy 2000), reproductive cycles, etc influenced by allogens are indicating towards the immediate need to preach & practice habitat protection and implement stringent regulation against tampering with the environment.

Immune Response & Host Parasite Interaction in *Clarias Batrachus*

Studies on the immune response of *C.batrachus* by experimental or wild infection as well as by microbial toxins enable our understanding of host parasite interaction,disease resistance mechanism and risk factors of culture practices.Effects on a host with a pathogen load may be useful to propose preventive protocols & vulnerability assessment.Dash et al (2003) studied immune system in the species.Observations relating to infection load with that of the environmental parameters can through light on the modification on cultural aspects to maintain yield.Immunological response to foreign substances & dietary supplements (Kumari & Sahoo 2005)will help to evaluate therapeutic possibilities.Observation of molecular (Joshi 1982)& organ specific responses (Ruhela et al 2008) to pathogens (Majumdar et al 2007) & parasites (Sharma & Saxena 2001)will help to standardize symptomatic diagnosis.Swain et al(2004)reported the purification & characterization of immunoglobulins from *C.batrachus*. Immunological response to microbial toxins (Majumdar et al 2007) may be extended for the appraisal of perspective immunization protocols.

Rythmicity & Behavior in *Clarias Batrachus*

Biological rhythms ensure the balance of numerous fundamental processes sustained in nature. Seasonal changes influence physiology of animals in terms of cellular (Tripathi et al 2005)& molecular (Sarkar &

Subhedar 2001)cascades in various ways. Selections of mate, breeding ground, endocrine secretion (Mazumdar et al 2007)etc follow an inherent natural instinct & rhythm.The timeliness of sexual maturation & gravidity ensures that environment is conducive for the newcomers & guarantees survival.Several workers(Singh & Lal 2008) observed seasonal influence on reproductive physiology of *C batrachus*. Responses to the environmental factors (Srivastava 2003)like photoperiod, temperature, water current etc & internal physiological parameters (Sahu&Shedpure 2006)are also studied in *C.batrachus*.These studies has enriched our knowledge on the factors influencing rhythmcity & related changes in *C.batrachus*. Modulator substances thus can be evaluated with their beneficial response actions. Behavioral responses as frequency and aggression for feeding (Siddiqui 1975) & mating also follow some rhythms & have precise adaptive advantages.

Recent Studies on Population Genetics & Diversity of *Clarias Batrachus*

In order to find ways for stock improvement & conservation for any fish species genetic makeup & its variations in terms of whole genome or a loci (Insulin Like Growth Factor–I, Debnath 2010;Growth hormone, Debnath 2009) can disclose crucial attributes.Khedkar et al (2009) studied genetic similarity & diversity of catfish *C.batrachus* populations of three Indian riverine system using randomly amplified polymorphic DNA-polymerase chain reaction (RAPD-PCR) & reported that the populations lack diversity.This may be due to rearing in the same environmental conditions,migration or by inbreeding during several generations.In nearer future, the lack in genetic diversity can lead to depression in growth & disease resistance.Islam et al(2007) described the genetic formation of different populations of *C.batrachus* in Bangladesh & mentioned the potentialities for improving the species through selective breeding.Their study revealed a recent bottleneck in some wild populations of this species that necessitates habitat protection to increase the population size & lower the vulnerability of *C.batrachus* in the future.To evaluate diversity Padhi et al(1998)characterized the MboI satellites in *C.batrachus*.Phylogenetic inference from the correlation of some microsatellite DNA segments for indirect assessment of genetic diversity in *C.batrachus* has also been described (Debnath & Gupta 2009).In a study Ahmad & Hasnain (2006) reported correlation between biochemical properties & adaptive diversity of skeletal muscle myofibrils & myosin of some air-breathing teleosts including *C.batrachus*.

Conclusion

Fisheries & aquaculture is gaining additional emphasis due to our concern in sustainability, greener solutions, conservation & food

security.Detail studies on physiology, genetics & general biology are therefore in a fish species very much relevant in order to put forward conservation protocols and to propose newer & improved culture practices.Establishment of *Clarias batrachus* in several continents & its popularity as a freshwater culturable fish species among consumers made the species suitable for meticulous reviews with respect to various parameters.According to FAO estimates the demand for catfishes throughout the world is increasing & *Clarias batrachus* with its several beneficial aspects remain as a hit among the Asians in particular. Besides in order to protect the genetic resources of this species from unwanted hybridization, which the species is very much vulnerable, the fish geneticists & the government bodies should work together. Habitat protection & sustainable consumption of this excellent fish species is the call of the day.

Intensive aquaculture of *C.batrachus* in the rural water bodies with very little infrastructure development may bring-about socioeconomic development in many parts of Bengal & Northeast India. Coordination between government bodies with respect to skill up gradation of the workers, market regulation etc together with the scientific community ensuring timely delivery of better quality seed stock will generate success stories in intensive *Clarias batrachus* culture. Since the species is a part of the natural fauna in this region therefore culture practices will be much easier to follow & therefore much more viable in economic point of view. Government bodies & organizations should come forward for training of the rural unemployed youth women for human resource development & dexterity enhancement related to technical know-how of culture & disease management. Regional rural banks & agro finance bodies may be approached for capital requirement & the local governance of Panchayats may forward financial help to the rural entrepreneurs.

References

[1] S, Debnath.A review on the physiology of IGF-I peptide in bony fishes & its phylogenetic correlation in 30 different taxa of 14 families of teleosts.*Adv in Environ Biol*, 2010.5(1): 31-52, *ISSN 1995-0756*. [PDF] from aensionline.net

[2] S, Datta. S, Mazumder. D, Ghosh. S, Dey. S, Bhattacharya. Low concentration of Arsenic could induce caspase-3 mediated head kidney macrophage apoptosis with JNK - p38 activation in *Clarias batrachus*.*Toxicol Appl Pharmacol*.2009, 15; 241(3):329-38.

[3] S, Debnath. R, Gupta. Phylogenetic Inference from the Correlation of Some Microsatellite DNA Segments for Indirect Assessment of Genetic Diversity in the Asian Catfish, C. batrachus" .*The ICFAI Journal of ComputationalMathemetics*. 2009. *ISSN 0974-6544*., Vol. II, No. 2.

[4] A, Gaikwad. KC, Biju. V, Barsagade. Y, Bhute. N, Subhedar. Neuronal nitric oxide synthase in the olfactory system, forebrain, pituitary & retina of the adult teleost *C batrachus*. *J Chem Neuroanat*.2009; 37(3):170-81.

[5] G.D, Khedkar. A.C, Reddy. P, Mann. K, Ravinder. K, Muzumdar. *C. batrachus* (Linn.1758) population is lacking genetic diversity in India. *Mol Biol Rep*.2009.10.

[6] K, Raghuveer. B, Senthilkumaran. Identification of multiple dmrt1s in catfish: localization, dimorphic expression pattern, changes during testicular cycle & after methyltestosterone treatment. *J Mol Endocrinol*. 2009; 42(5):437-48.

[7] S, Debnath. Phylogenetic Correlation Among Carpfishes & Catfishes Using a Nuclear Protein Coding Genetic Data (Gh) Retrieved from Genebank Using a Freeware Computational Evolutionary Biology Package MEGA, 4.*International Conference on Biotechnol Soln. For Environ Sustain. 2009, Vellore Institute Of Technology, Vellore, Tamil Nadu, Oct 21-23,*.http://papers.ssrn.com/sol3/papers.cfm?abstract_id=1403133

[8] S.K, Manna. R, Das.C, Manna.Microbiological quality of finfish & shellfish with special reference to shiga toxin-producing Escherichia coli O157. 2008. *J Food Sci*.; 73(6):M283-6.

[9] S, Ruhela. AK, P&ey. AK, Khare. Histopathological manifestations in kidney of *C batrachus* induced by experimental Procamallanus infection. *J Environ Biol*. 2008; 29(5):739-42.

[10] AK. Singh, B, Lal. Seasonal & circadian time-dependent dual action of GH on somatic growth & ovarian development in the Asian catfish, *C batrachus*: role of temperature. *Gen Comp Endocrinol*. 2008; 159(1):98-106.

[11] S, Debnath.Growth Economics & Biometric Comparison of Length Weight Relationship in Two Intra Generic Varieties of *C.batrachus* Isolated from DumburLake, in a Rural District of Tripura, India. *XIthScienceCongress*, *ManipurUniversity,* 2008.www.iutripura.edu.in/annualreport.pdf

[12] S, Datta. DR, Saha. D, Ghosh. T, Majumdar. S, Bhattacharya. S, Mazumder. Sub-lethal concentration of arsenic interferes with the proliferation of hepatocytes & induces in vivo apoptosis in *C batrachus* L.*Comp Biochem Physiol C Toxicol* Pharmacol.2007; 145(3):339-49.

[13] M.N, Islam. M.S, Islam. M.S, Alam. Genetic structure of different populations of walking catfish (*C batrachus* L.) in Bangladesh. *Biochem Genet*.2007; 45(9-10):647-62.

[14] A, Bhattacharya. S. Bhattacharya. Induction of oxidative stress by arsenic in *C batrachus*: involvement of peroxisomes. Ecotoxicol Environ Saf.2007; 66(2):178-87.

[15] T, Majumdar. D, Ghosh. S, Datta. C, Sahoo. J, Pal .S, Mazumder. An attenuated plasmid-cured strain of Aeromonas hydrophila elicits protective immunity in *C batrachus* L. *Fish Shellfish Immunol*. 2007; 23(1):222-30.

[16] M, Mazumdar. A.J, Sakharkar. P.S, Singru . N, Subhedar.Reproduction phase-related variations in neuropeptideY immunoreactivity in the olfactory system,

forebrain & pituitary of the female catfish, C.batrachus. J Comp Neurol. 2007.504(5):450-69.

[17] Rosa Rui, Narcisa Bandarra & Maria Leonor Nunes. Nutritional quality of African catfish *C.gariepinus* (Burchell 1822): a positive criterion for the future development of the European production of Siluroidei. *Int J of Food Sci & Tech.*2007.42.3, Pages 342 – 351.

[18] SK.Sahoo ,SS. Giri. S.Chandra,AK.Sahu. Effect of Ovim doses & latency periods on induced spawning of *C batrachus*: observation on larval deformity. *Indian J Exp Biol.* 2007; 45(10):920-2.

[19] Ahmad R, Hasnain AU. Correlation between biochemical properties & adaptive diversity of skeletal muscle myofibrils & myosin of some air-breathing teleosts. *Ind J Biochem Biophys*.2006;43(4):217-25.

[20] S, Sahu, M. Shedpure. Air-breathing rhythm in *C. batrachus*: modulatory role of eyes, pineal & exogenous melatonin. *Indian J Exp Biol.* 2006; 44(1):55-62.

[21] G. Tripathi, A. Gaur, BM. Sharma .Temperature related seasonal changes in Golgi complex of brain, heart & intestine of a teleost. *J Environ Biol*. 2005; 26(2):265-8.

[22] James Muir. Managing to harvest? Perspet. On the potential of aquaculture. *Phil. Trans. R. Soc.B.*2005.360, 191-218.

Hepatoprotective Efficacy Of Stem Bark Extract Of *Ficus Religiosa* On Lipid Profile And Histological Tissue Of *Rattus Norvegicus* (Wistar Rats)

Rashmi

Asstt. Professor, Department of Zoology, College of Commerce, Arts and Science, Patliputra University, Patna

Keywords : Liver, hepatoprotective, Acetaminophen, *R. norvegicus*

The liver diseases are mainly caused by toxic chemicals (certain antibiotics, chemotherapeutic, peroxidised oil, aflatoxin, carbontetracholoride, acetaminophen, chlorinated hydrocarbons etc.) Liver has a pivotal role in regulation of physiological processes. Thus there is a definite need to search alternate drug having maximum therapeutic value with no or least toxicity. *Ficus religiosa* (Moraceae) commonly known as "Peepal" tree is distributed throughout India. It is popular indigenous system of medicine like Ayurveda Siddha, Unani and Homeopathy and used traditionally as analgesic.

Introduction

Liver is the largest gland and play a vital role in the metabolism so called "engine room of the body". All most all the drugs, foods and water constitutes are metabolised and detoxified in the liver. Many chemicals, foods, drugs and infections (Parasitic, Bacterial, Viral or Fungal) can cause variety of liver diseases such as Hepatitis, Jaundice, Cirrhosis, liver cancer etc. Besides this modern (allopathic) drugs exhibit severe toxicity on liver. One such drug commonly used is paracetamol. Because of variation in liver dysfunctions and difficulties encountered in reaching to a proper diagnosis, physician is rarely able to provide specific treatment. The most supportive and symptomatic treatment are given but the multiplicity of deranged functions renders the treatment still more complicated. (Pandey et. al 1980 and 1990). Liver has a pivotal role in regulation of physiological processes. Thus there is a definite need to search alternate drug having maximum therapeutic value with no or least toxicity. The liver diseases are mainly caused by toxic chemicals (certain antibiotics, chemotherapeutic, peroxidised oil, aflatoxin, carbontetracholoride, acetaminophen, chlorinated hydrocarbons etc.)

Most of the hepatotoxic chemical damage liver cell mainly by inducing lipid per oxidation produced during the liver microtonal metabolism of ethanol may result in hepatitis and cirrhosis. (Graham et. al 2001)

Approximately 90 percent of the acute hepatitis is due to viruses. World health organization (WHO) has estimated about 170 million people (3% of the world's population) infected with hepatitis-C virus are at the risk of developing liver cirrhosis and or liver cancer. Hepatoprotective is a class of therapeutic agents that included many synthetic as well as natural products used for protection against hepatic damage induced by various toxins. (Shandalik et. al 1992). The available synthetic drugs to treat liver disorder in this condition also cause further damage to liver. Paracetamol is also known as "Acetaminophen", taken in overdose can cause the several hepatotoxicity and nephrotoxicity. Paracetamol is activated and converted by Cytochrome P450 enzymes to toxic metabolite NAPQI (N-acetyl - p - benzoquinoneimine) that causes oxidative stress and liver damage (Parmar et.ai, 2010) It is an antipyretic and analgesic substance of the non – steroidal anti - inflammatory drugs. The analgesic properties of paracetamol primarly due to centrally mediated cylcloxygenase inhibiton by revesible, non-competitive blinding and preventing the conversion of arachidonic acid to prostaglandin metabolites. *Ficus religiosa* (Moraceae) commonly known as "Peepal" tree is distributed throughout India. It is popular indigenous system of medicine like Ayurveda Siddha, Unani and Homeopathy and used traditionally as analgesic. (Verma, et. al 2010) Preliminary photochemical screening of *Ficus religiosa* barks, showed the presence of Tannins, Spooning, Flavonoids, Steroids, Terpenoids and Cardiac glycosides. The barks of *Ficus religiosa* also showed the presence of bergapten, Lnosterol, beta – sitosterol – d – glycoside (phytosterolin) vitamin K, beta – leucocyanidin – 3 – O – beta – d – glucopyrancoside, lupeol acetate, alpha – amyrin acetate. This plant is known for its hepatic protective effect (Joseph et. al 2010 ; Husain et. al 1992)

Materials and Methods

Animal model : Wistar Rats were used as an experimental model for the present research work. The selected test species were :-

Test Animal

Rattus norvegicus (Wistar rat) :- The animal used in the experiments were *Rattus norvegicus albus* (Wistar rats).

Thirty Wistar rats of same age groups and weight 100 gm were procured from the Animal market near Tripolia Hospital, situated at Alamganj, Patna-06. Wistar rats were divided into four groups. The Wistar rat were housed in poly propylene cages and maintained in controlled

temperature (27 degree centigrade), humidity (0.5 – 10%) and light cycle they were fed with gold mohar brand animal feed manufactured by Lipton India Limited Company Delhi and water ad *libitem*. Mice was selected to know the impact of *F.religiosa* on mammal as well as in human.

Nutritional Management

Rats – During period of acclimatization and during the treatment period, they were feed on bread made of following ingredients :

Oats, Wheat flour, Rice flour, Soyabean flour, Gram flour and Roasted peanut flour. The extra supplements that were given was carrot and gram sprouts.

Experimental Protocol

The rats were categorized into following groups:-

Group I – Normal, Group II – Paracetamol treated and Group III – Ethanolic extract of stem bark of *F. religiosa*

Table : Treatment given to Rat

Cage No.	Treatment	Average Weight	No. of mice in each cage	Selected Dose (mg/kg body wt.)
1	Normal / Control	120 gm	6	Saline water
2	Paracetamol	145 gm	6	1000mg/kg b. wt
3	*Ficus religiosa* (4 days treated)	145 gm	6	400 mg/kg b. wt
4	*Ficus religiosa* (8 days treated)	145 gm	6	400 mg/kg b. wt
5	*Ficus religiosa* (12 days treated)	145 gm	6	400 mg/kg b. wt

In the mice of all the four groups, blood sample were collected in heparinzed tube by cardiac puncture, blood were collected and refrigerated at -20^{O}C in sterilized vials for amino acid and biochemical analysis. Serum was analyzed for quantitative estimation of Total protein, Triglyceride, Total Cholesterol, HDL, respectively. After each schedule exposure, the mice were anesthetized and liver tissues were dissected out, ringed in NaCl (85%) to remove any adhering unwanted tissues. The tissues were cut into small pieces with sharp surgical blades and were fixed and processed for Light Microscopy.

Paracetamol Treatment

In experimental protocol, commercially available pure paracetamol aqueous solution (1000mg/kg.b.wt) was used to damage the liver of Rat.

Plant Extract Treatment

Fresh stem bark of *Ficus religiosa* plant was collected after identification. The stem bark of *Ficus religiosa* were dried under shady place, powdered with mechanical grinder machine. The solvent containing extract was

filterd with Whitman no. 1 filter paper to remove plant colour and other debris. The pure extract was obtained under reduced pressure by using vaccuma rotary. An extract was prepared freshly for every day. The extract was prepared, 400 mg extract dissolved in 10ml normal saline. The extract was given orally to rats daily by using cannula.

Phytochemical Screening

Alkaloids

Fraction of extract were treated with Meyer's reagent with 1.36 g of mercuric chloride, 5g of KI in 100 ml distilled water. The extract will react with Meyer's reagent to form Urea.

Phenolic Compounds

Fraction of extract were taken with 5% $FeCl_3$ in solution. (5g $Facl_3$ in 100 ml distilled water) results into deep blue colour that proved the presence of phenolic compounds.

Flavanoids

Fraction with conc. H_2SO_4 solution were taken and flavonoids compounds were confermed.

Calculation of LC_{50}

In this experimental protocol, the L50 of *Ficus religiosa* for *Rattus norvegicus* was taken as 400 mg/kg.b.wt. The one dose considered in the experimental protocol was 400 mg/kg.b.wt of *Ficus religiosa* for 4, 8 and 12 days exposure. Accordingly, stock solution was prepared by dissolving appropriate amount of *Ficus religiosa* to distilled water.

The following groups of mice were considered during experimental protocol and were designed by separated codes as noted below :

Sl. No.	Group	Code
1.	Control (treated with 0.75% Normal saline)	NS
2.	Paracetamol (treated with 1000 mg/kg.b.wt) for 4 days	PCT
3.	*F. religiosa* (400 mg/kg BW) treated for 4 days.	FRT1
4.	*F. religiosa* (400 mg/kg BW) treated for 8 days.	FRT2
5.	*F. religiosa* (400 mg/kg BW) treated for 12 days.	FRT3

Method for Light Microscopy for Histopathology

Small pieces of liver tissues were fixed in the following fixatives for subsequent histopathological studies. In a clean dry bottle following chemicals were mixed properly to prepare neutral formalin –

Formalin (40%) – 10 ml, Distilled water – 90 ml

The tissues were fixed for 5 days and washed overnight under running tap water and dehydrated in graded series of alcohal for 2 hours in each grade with changes in between, then Cleaned in absolute alcohal and xylene (1:1) and taken in pure xylene for 1 hour with a change in between, finally embedded in molten paraffin wax with cerasine (Melting point 58^{O}C to 68^{O}C) after passing through xylene and molted wax (1:1).

Blocks were prepared and sections were cut in semi-thin microtome at 4-6 micrometer and then stained for histological slide preparation.

4–5 micrometer thick section were fixed on clean glass slide using Meyer's solution and deparaffinized in xylene and hydrated through descending series of alcohol up to water. These hydrated sections were stained in Delafielts haemotoxylene for ten minutes then section was washed in running tap water and then rinsed in distilled water and were dehydrated in ascending series of alcohol up to 70% counter stained in Eosin and dehydrated further in 90% and absolute alcohol. The sections were cleared in xylene and mounted in DPX with clean glass cover slip (0 No.)

Biochemical Analysis

All biochemical analysis was done on BT-260 plus Semi-Automatic Chemistry Analyzer, manufactured by Nanchang Biotech A&C Biotechnical Industry Co. China. All the biotechnical assessments have been done for normal/control, Paracetamol and *Ficus religiosa* treated *Rattus norvegicus* independently. Six observations have been taken in each group. In Liver Functioning Test (LFT), following parameters have been estimated.

Total proteing (Biuret Method), Tissue lipid profile test.

Triglyceride (GPO-POD method), Total cholesterol & HDL cholesterol (CHOD/POD method) and LDL, VLDL were calculated by using "Friedwald method".

Six observations have been taken in each case, then Mean and Standard deviation is calculated by the formala. The 't' test have been applied thorugh standard biostatistical formula by considering mean of normal *Rattus norvegicus* and *Rattus norvegicus* as standard mean and comparing individual mean of different doses and duration of Pracetamol exposures to their respective control mean. After applying test, the calculated values were referred to Fisher's table upto level of significance at ($P<0.05$) and ($P<0.01$).

The Mean and Standard Deviation (SD) was calculated by using the formula –

MEAN

$$\bar{X} = \frac{\Sigma X}{N}$$

where $\bar{X}$ = Mean, Σ = Sum of ; X = Individual quantities; N = Total number of total quantities

Standard Deviation

$$\text{S.D. or } \sigma = \sqrt{\frac{\Sigma(X-\bar{X})^2}{N-1}}$$

where σ = Standard deviation, = Sum of $\sqrt{}$ = sign of square root;

$\bar{X}$ = Mean of the items; X = Individual items; N = Number of individual items

Statistical analysis were carried out using Student 't-test'.

Results And Discussion

Light Microscopic Observations

Paracetamol Treatment: Paracetamol treatment has been done to induce hepatotoxicity in rat for one concentration of 1000mg/kg body wt. for 4 days respectively.

4 days 1000 mg/kg paracetmol treated rat shows degenerated Hepatocytes, rupture and widening of Hepatic vein, widening of sinusoids and acellularity. Some deposition in central vein. (Plate - I, Fig. 1, 2).

Ficus religiosa Extract Treatment: *Ficus religiosa* treatment has been done for one concetration of 400 mg/kg for 4, 8 and 12 days respectively.

4 days 400 mg/kg bodywt. Ficus religiosa treated rat: 4 days 400 mg/kg body wt. *Ficus religiosa* treated liver of rat shows regeneration of Hepatocytes along with nucleus decrease in sinusoidal space and normal Central vein. (Plate - II, Fig. 1, 2).

8 days 400 mg/kg bodywt. Ficus religiosa treated rat: 8 days 400 mg/kg body wt. *Ficus religiosa* treated liver of rat shows regenerating hepatocytes and nucleus decreased in Sinusoidal.

12 days 400 mg/kg bodywt. Ficus religiosa treated rat: 12 days 400 mg/kg body wt. *Ficus religiosa* treated liver of rat regenerated hepatocytes and nucleus less widening of Sinusoid and hepatic vein (Plate - III, Fig. 1, 2).

Observation of Serum Biochemical

Total Protein

Table 1 : Showing variation of total protein in control, Paracetamol and **F. religiosa** *treated* **R. norvegicus.** *(n=6)*

S. No.	Sample	Mean value ± SD (g/dl)
1.	Control	7.97 ± **0.04**
2.	Paracetamol	1.75 ± **0.06**
3.	4 Days	2.18 ± **0.00**
4.	8 Days	1.80 ± **0.09**
5.	12 Days	2.84 ± **0.08**

Graph – 1

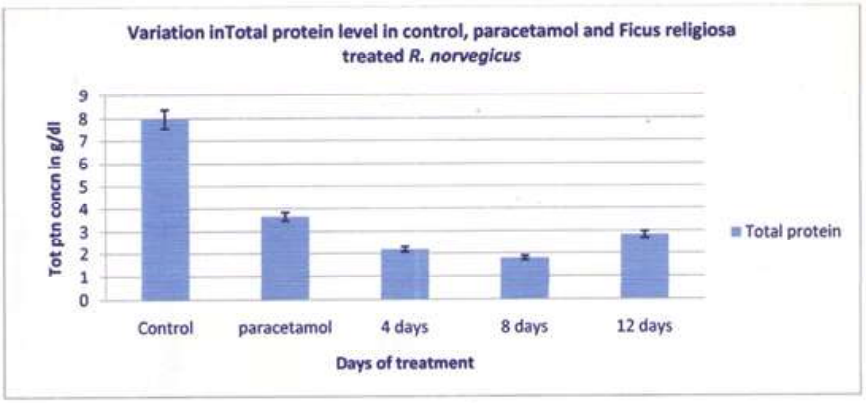

Paracetamol Treated

The total protein level in Paracetamol treated rat decreased up to 3.65 g/dl as comparison to control (Table No. 1)

Ficus religiosa treated for 4 Days: The total protein level in *Ficus religiosa* extract (400 mg/kg body wt.) treated rat decreased up to 2.18 g/dl as comparison to control (Table No. 1)

Ficus religiosa treated for 8 Days: The total protein level in *Ficus religiosa* extract (400 mg/kg body wt.) treated rat decreased up to 1.84 g/dl as comparison to control (Table No.1)

Ficus religiosa treated for 12 Days: The total protein level in *Ficus religiosa* extract (400 mg/kg body wt.) treated rat decreased up to 2.84 g/dl as comparison to control (Table No. 1)

Triglyceride

Table 2 : Showing variation of Triglyceride in blood of control, Paracetamol and **F. religiosa** *treated* **Rattus norvegicus.** *(n=6)*

S. No.	Sample	Mean value ± SD (mg/dl)
1.	Control	55.04 ± **0.33**
2.	Paracetamol	193.76 ± **2.63**
3.	4 Days	185.87 ± **2.06**
4.	8 Days	105.71 ± **2.77**
5.	12 Days	239.73 ± **2.79**

Graph – 2

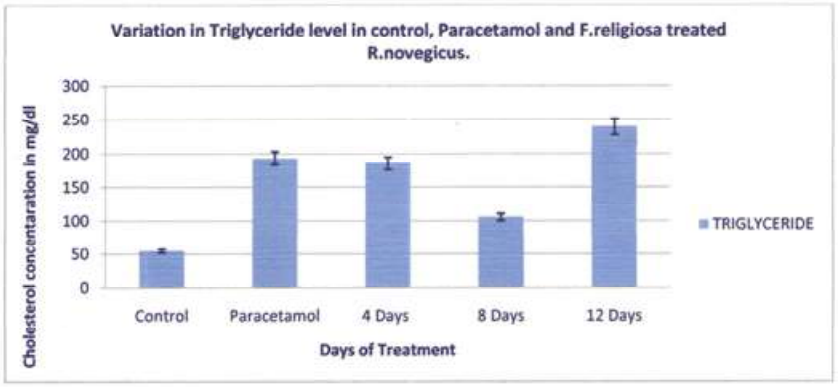

Paracetamol Treated

The total protein level in Paracetamol (1000 mg/kg Body) treated rat decreased up to 193.76 mg/dl as comparison to control (Table No. 2)

Ficus religiosa treated for 4 Days: The total protein level in *Ficus religiosa* extract (400 mg/kg body wt.) treated rat decreased up to 185.87 mg/dl as comparison to control (Table No. 2)

Ficus religiosa treated for 8 Days: The total protein level in *Ficus religiosa* extract (400 mg/kg body wt.) treated rat decreased up to 105.71 mg/dl as comparison to control (Table No.2)

Ficus religiosa treated for 12 Days: The total protein level in *Ficus religiosa* extract (400 mg/kg body wt.) treated rat decreased up to 239.73 mg/dl as comparison to control (Table No. 2)

Cholesterol

Table 3 : Showing variation of Cholesterol of control, Paracetamol and **F. religiosa** *treated* **Rattus norvegicus.** *(n=6)*

S. No.	Sample	Mean value ± SD (mg/dl)
1.	Control	155.55 ± **15.72**
2.	Paracetamol	21.52 ± **1.24**
3.	4 Days	80.04 ± **1.93**
4.	8 Days	63.82 ± **0.06**
5.	12 Days	42.95 ± **0.06**

Graph – 3

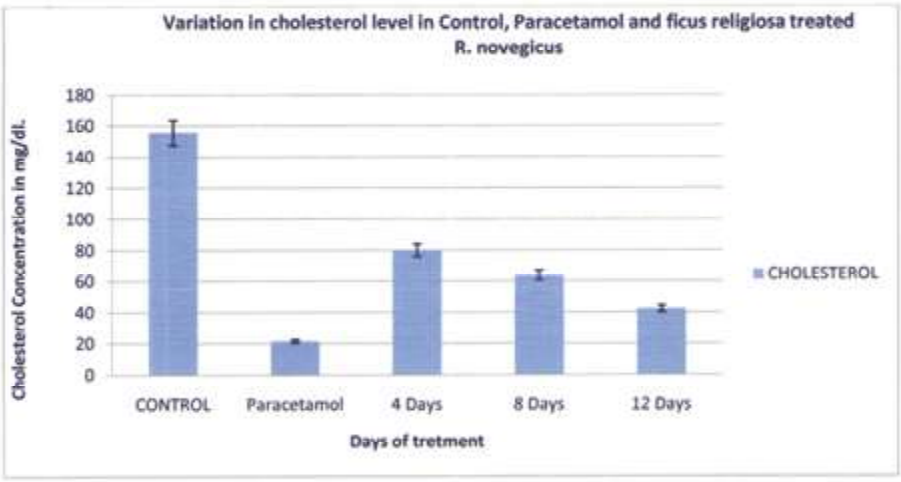

Paracetamol Treated

The total protein level in Paracetamol (1000 mg/kg Body) Treated rat decreased up to 21.52 mg/dl as comparison to control (Table No. 3)

Ficus religiosa treated for 4 Days: The total protein level in *Ficus religiosa* extract (400 mg/kg body wt.) treated rat decreased up to 80.04 mg/dl as comparison to control (Table No. 3)

Ficus religiosa treated for 8 Days: The total protein level in *Ficus religiosa* extract (400 mg/kg body wt.) treated rat decreased up to 63.82 mg/dl as comparison to control (Table No.3)

Ficus religiosa treated for 12 Days: The total protein level in *Ficus religiosa* extract (400 mg/kg body wt.) treated rat decreased up to 42.45 mg/dl as comparison to control (Table No. 3)

HDL

Table 4 : Showing variation of HDL of control, Paracetamol and *F. religiosa* treated R*attus norvegicus*. (n=6)

S. No.	Sample	Mean value ± SD (mg/dl)
1.	Control	88.95 ± **0.38**
2.	Paracetamol	182.03 ± **0.58**
3.	4 Days	9.5 ± **0.82**
4.	8 Days	8.17 ± **0.03**
5.	12 Days	5.66 ± **0.06**

Graph – 4

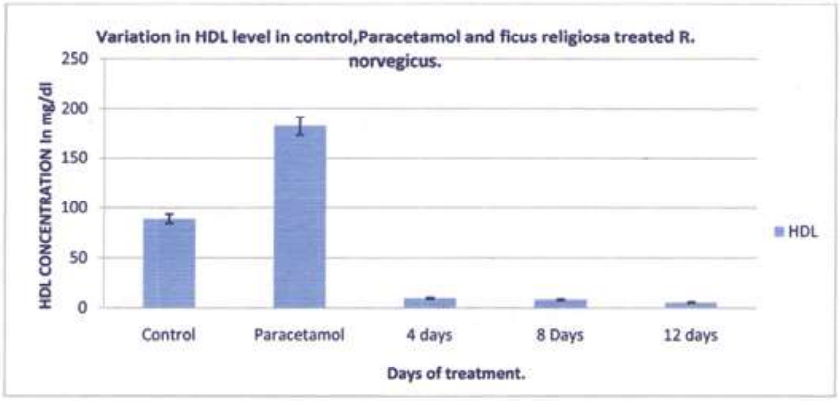

Paracetamol Treated

The total protein level in Paracetamol (1000 mg/kg Body) treated rat decreased up to 182.03 mg/dl as comparison to control (Table No. 4)

Ficus religiosa treated for 4 Days: The total protein level in *Ficus religiosa* extract (400 mg/kg body wt.) treated rat decreased up to 9.58 mg/dl as comparison to control (Table No. 4)

Ficus religiosa treated for 8 Days: The total protein level in *Ficus religiosa* extract (400 mg/kg body wt.) treated rat decreased up to 8.17 mg/dl as comparison to control (Table No.4)

Ficus religiosa treated for 12 Days: The total protein level in *Ficus religiosa* extract (400 mg/kg body wt.) treated rat decreased up to 5.66 mg/dl as comparison to control (Table No. 4)

Phytochemical Screening (Qualitative Estimation): Phytochemical screening of the ethanolic extract root bark of *Ficus religiosa* revealed following results

Phytochemicals	Present (+) / Absent (-)
Alkaloid	+
Phenolic compounds	Absent
Flavonoids compounds	++++

Test animal treated with *F. religiosa* extract showed positive effect which was visible through histopathological structure like decreasing of Sinusoidal space, regeneration of hepatic tissues and normal structure of central vein which is similar to the finding of Suryawanshi et. al 2011.

The serum cholesterol lowering effect of *Ficus religiosa* may be attributed to its ability to increase the excretion of cholesterol. Certain drugs/herbs has been reported to cause enhanced excretion of acidic and neutral.

These results suggest that *Ficus religiosa* can be used as antiatherogenic agent for the management of atherosclerosis in man (Brown et.al 1968). An increase of 1% serum cholesterol is reported to have resulted in a 3% increase in coronary heart disease (Govindrajan et.al 2005).

Our results show significant elevation of cholesterol and triglyceride in the liver of experimental rats compared to the control. Cholesterol and triglyceride are synthesized in the liver, this result demonstrate the ability of *Ficus religiosa* to influence live metabolism towards increased synthesis of lipids. The high levels of liver triglyceride may be due to a number of factors such as the increased availability of fatty acids for esterification (Khanb et. al 2011) reduced catabolism of LDL, inhibition of tissues lipases, activation of acetly – CoA carboxylase and production of triglycerides precursors such as acetyl-CoA and glycerol phosphatase (Joseph et.al 2010).

References

1. Adware EA, Afolyan AJ, A reveiw of Natural Products with Hepatoprotective Activity, Journal of Medicinal Plants Res. 2010, **4**(12) 1318-1334.
2. Brown RA. Hepatic and Renal Damage with paracetamol over doage, J. clin pathol 1968:6:793.
3. Govindarajan R, Pushpangadan, Vijaya Kumar M, Antioxitent approach to disease management and role of rasayana herbs of ayurveda. J. Ethnopharmacolgy 2005:**9**:131; 42.
4. Graham GG. Robins S-A, Bryant KJ, et.al Inhibition of prostaglandin synthesis in intact cell by Paracetamol (Acetaminophen). Inflammophormacol. 2001:**9**:131-42.

5. Husain A, Virmani OP, popli SP, Misara LN, Gupta MM, Srivasatava GN, Abaraham Z, Singh AK, Dictionary of Indian Medicinal Plants, CIMAP, Lucknow, India, 1992; 546.
6. Joseph Band Justin SR, Phytopharmcological and Phytochemical properties of three Ficus species an overview, international Journal of Pharma and Bio-Science, 2010 oct-dec. **1**(4).
7. Khanb MSA, Hussan SA, Jais AMM, Zakaria ZA, Khan M, Antiulcer activity of *Ficus religiosa* stem bark ethanolic extract in rats. J Medicinal Plants Research, 2011:**5**(3):354-59.
8. Pandey and Govind P. Pharmacological Studies of liver with special reference to liver function. MVSC & AH thesis. Jabalpur. MP. India; JNKVU:1980.
9. Pandey and Govind P. Hepatogenic effect of some indigenous drug on experimental liver damage PhD thesis. Jabalpur. MP. India; JNKVU:1990.
10. Parmar SR, Vashrambhi PH, Kaliak, Hepatoprotective activity of some plants Extract against Paracetamol induced Hepatotoxicity in rats, Journal of Herbal Medicinal and toxicologist, 2010, **4**(2);101-102.
11. Shandalik R. Ganthi G. Perucca E. Pharmacokinetics of sallying in bile following administration of silipide and Silymarin in cholecystectomy patients. Arzneim forsch. 1992, **42**: 964-968.
12. Verma, N, Chaudary S, Garg KU, TYAGIS, Anti-Inflammatory and Analgesic Activity of Methanolic Extract of stem bark of *Ficus religiosa*, international Journal of Pharma Professional Research. 2010. Oct. 2011.

Plate – I

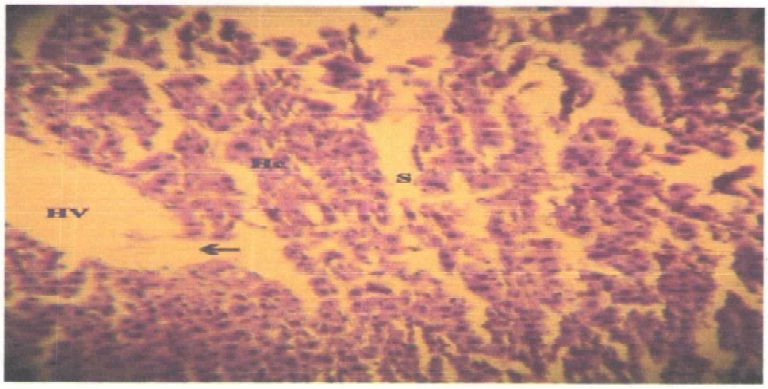

Fig 1 : Transverse section of rogor treated liver of mice showing degenerated hepatocytes (Hc), rupture (←) and widening of Hepatic vein (HV), widening of sinusoids (s) and acellularity. Some deposition in central vein (HV). × 100

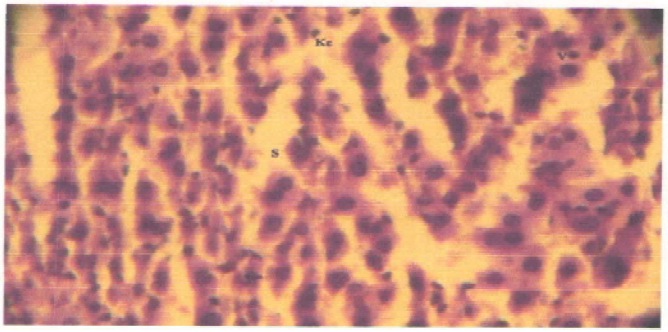

Fig 2 : Magnified view of the transverse section of paracetamol treated liver of rat showing Vaculation (v) in Hepatocytes, degenerated of nuclei (←), increase of sinusoid space (s) along with presence of Kuffper cell (kc). 400

Plate – II

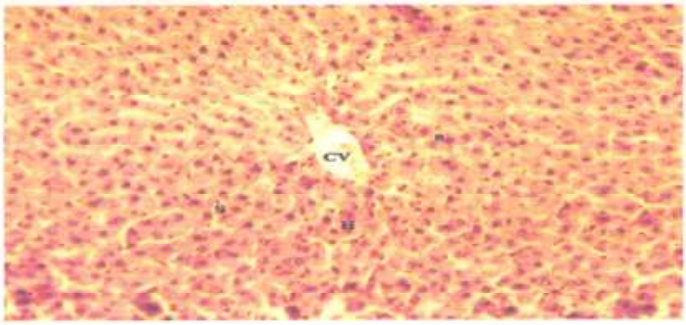

Fig 1 : Transverse section of liver of rat treated with **Ficus religiosa** *extract showing regeneration of hepatocytes (H) along with nucleus (N) decrease in sinusoidal space (S) and normal central vein (CV) 200*

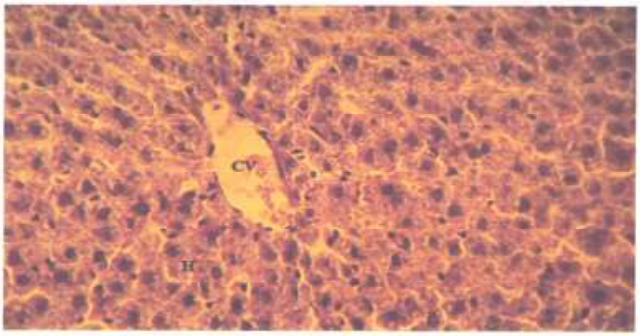

Fig 2 : Magnified view of transverse of **Ficus religiosa** *treated liver of rat showing regenerating Hepatocytes with central vein (CV) decreased insinusoidal space (s). 400*

Plate – III

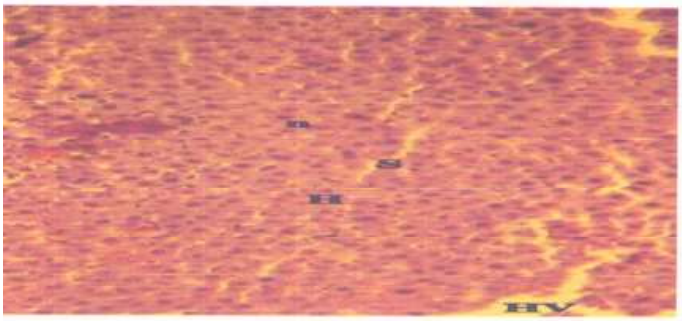

Fig 1 : Transverse section of **Ficus religiosa** *treated liver of rat showing regenerated Hepatocytes (H) and nucleus (N) less widening of Sinosoid (S) and hepatic vein (HV) 200*

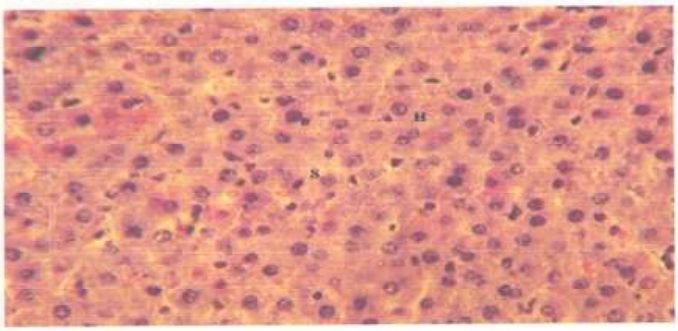

Fig 2 : Magnified view of transverse section of **Ficus religiosa** *treated liver of rat showing regenerating hepatocytes (H) and Nucleus (N). Decreased in sinusoid. 400*

Essence of Botany

Bhupendra Kumar Singh

Research Scholar, Monad University, Hapur

Bud

In botany, a bud is an undeveloped or embryonic shoot and normally occurs in the axil of a leaf or at the tip of the stem. Once formed, a bud may remain for some time in a dormant condition, or it may form a shoot immediately. Buds may be specialized to develop flowers or short shoots, or may have the potential for general shoot development. The term bud is also used in zoology, where it refers to an outgrowth from the body which can develop into a new individual.

Figure: *Flower buds have not yet bloomed into a full-size flower*

Overview

The buds of many woody plants, especially in temperate or cold climates, are protected by a covering of modified leaves called *scales* which tightly enclose the more delicate parts of the bud. Many bud scales are covered by a gummy substance which serves as added protection. When the bud develops, the scales may enlarge somewhat but usually just drop off, leaving on the surface of the growing stem a series of horizontally-elongated scars.

By means of these scars one can determine the age of any young branch, since each year's growth ends in the formation of a bud, the formation of which produces an additional group of bud scale scars. Continued growth of the branch causes these scars to be obliterated after a few years so that the total age of older branches cannot be determined by this means.

In many plants scales are not formed over the bud, which is then called a naked bud. The minute underdeveloped leaves in such buds are often excessively hairy. Naked buds are found in some shrubs, like some species of the Sumac and Viburnums (*Viburnum alnifolium* and *V. lantana*) and in

herbaceous plants. In many of the latter, buds are even more reduced, often consisting of undifferentiated masses of cells in the axils of leaves. A terminal bud occurs on the end of a stem and lateral buds are found on the side. A head of cabbage is an exceptionally large terminal bud, while Brussels sprouts are large lateral buds.

Figure: *On the left is an opening influorescence bud, that will develop like the one to the right.*

Since buds are formed in the axils of leaves, their distribution on the stem is the same as that of leaves. There are alternate, opposite, and whorled buds, as well as the terminal bud at the tip of the stem. In many plants buds appear in unexpected places: these are known as adventitious buds. Often it is possible to find a bud in a remarkable series of gradations of bud scales. In the buckeye, for example, one may see a complete gradation from the small brown outer scale through larger scales which on unfolding become somewhat green to the inner scales of the bud, which are remarkably leaf-like. Such a series suggests that the scales of the bud are in truth leaves, modified to protect the more delicate parts of the plant during unfavourable periods.

Types of Buds

Buds are often useful in the identification of plants, especially for woody plants in winter when leaves have fallen. Buds may be classified and described according to different criteria: location, status, morphology, and function.

Botanists commonly use the following terms:

- for location:
  - terminal, when located at the tip of a stem (apical is equivalent but rather reserved for the one at the top of the plant);
  - axillary, when located in the axil of a leaf (lateral is the equivalent but some adventitious buds may be lateral too);
  - adventitious, when occurring elsewhere, for example on trunk or on roots (some adventitious buds may be former axillary ones reduced and hidden under the bark, other adventitious buds are completely new formed ones).

- for status:
  - o accessory, for secondary buds formed besides a principal bud (axillary or terminal);
  - o resting, for buds that form at the end of a growth season, which will lie dormant until onset of the next growth season;
  - o dormant or latent, for buds whose growth has been delayed for a rather long time. The term is usable as a synonym of *resting*, but is rather employed for buds waiting undeveloped for years, for example epicormic buds;
  - o pseudoterminal, for an axillary bud taking over the function of a terminal bud (characteristic of species whose growth is sympodial: terminal bud dies and is replaced by the closer axillary bud, for examples beech, persimmon, *Platanus* have sympodial growth).
- for morphology:
  - o naked, when not covered by scales;
  - o scaly or covered, when scales (which are in fact transformed and reduced leaves) cover and protect the embryonic parts;
  - o hairy, when also protected by hairs (it may apply either to scaly or to naked buds).
- for function:
  - o vegetative, if only containing vegetative pieces: embryonic shoot with leaves (a leaf bud is the same);
  - o reproductive, if containing embryonic flower(s) (a flower bud is the same);
  - o mixed, if containing both embryonic leaves and flowers.

Within Zoology

The term bud (as in budding) is used by analogy within zoology as well, where it refers to an outgrowth from the body which develops into a new individual. It is a form of asexual reproduction limited to animals or plants of relatively simple structure. In this process a portion of the wall of the parent cell softens and pushes out. The protuberance thus formed enlarges rapidly while at this time the nucleus of the parent cell divides. One of the resulting nuclei passes into the bud, and then the bud is cut off from its parent cell and the process is repeated. Often the daughter cell will begin to bud before it becomes separated from the parent, so that whole colonies of adhering cells may be formed. Eventually cross walls cut off the bud from the original cell.

Chlorophyll

Chlorophyll (also chlorophyl) is a green pigment found in almost all plants, algae, and cyanobacteria. Chlorophyll is an extremely important

biomolecule, critical in photosynthesis, which allows plants to absorb energy from light. Chlorophyll absorbs light most strongly in the blue portion of the electromagnetic spectrum, followed by the red portion. However, it is a poor absorber of green and near-green portions of the spectrum, hence the green colour of chlorophyll-containing tissues. Chlorophyll was first isolated by Joseph Bienaimé Caventou and Pierre Joseph Pelletier in 1817.

Chlorophyll and Photosynthesis

Chlorophyll is vital for photosynthesis, which allows plants to absorb energy from light. Chlorophyll molecules are specifically arranged in and around photosystems that are embedded in the thylakoid membranes of chloroplasts. In these complexes, chlorophyll serves two primary functions. The function of the vast majority of chlorophyll (up to several hundred molecules per photosystem) is to absorb light and transfer that light energy by resonance energy transfer to a specific chlorophyll pair in the reaction centre of the photosystems.

The two currently accepted photosystem units are Photosystem II and Photosystem I, which have their own distinct reaction centre chlorophylls, named P680 and P700, respectively. These pigments are named after the wavelength (in nanometers) of their red-peak absorption maximum. The identity, function and spectral properties of the types of chlorophyll in each photosystem are distinct and determined by each other and the protein structure surrounding them. Once extracted from the protein into a solvent (such as acetone or methanol), these chlorophyll pigments can be separated in a simple paper chromatography experiment and, based on the number of polar groups between chlorophyll a and chlorophyll b, will chemically separate out on the paper.

References

Ackerknecht, Erwin H.: *Medicine and Ethnology*. Johns Hopkins Press, Baltimore, 1971.

Capon, Brian: *Botany for Gardeners,* Timber Publishing, Portland, OR, 2005.

Hellebust, J. A. and J. S. Craigie: *Handbook of Phycological Methods. Physiological and Biochemical Methods*. Cambridge University Press, Cambridge, England, 1978.

Iyer, Meena: *Faith & Philosophy of Zoroastrianism*, Kalpaz Publications, Delhi, India, 2009.

Jeanness, Diamond: *The People of the Twilight*. V. Chicago Press, Chicago, 1959.

King, John: *Reaching for the Sun: How Plants Work*. Cambridge University Press, Cambridge, 1997.

Lloyd, John U.: *Origin and History of all the Pharmacopoeial Vegetable Drugs*, *Chemicals, and Preparations*, The Caxton Press, Cincinnati, 1998.

Martin, A. C. & W. D. Barkley: *Seed Identification Manual.* U. Cal. Press, Berkeley, 1961.

Pakenham, Thomas: *Remarkable Trees of the World*, W. W. Norton, London, 2002.

Medicinal Plants

Om Prakash Singh
Assistant Professor, Department of Botany, RKS College, Dalmia Nagar, Rohtas, Bihar

Medicinal plants are various plants used in herbalism and thought by some to have medicinal properties. Few plants or their phytochemical constituents have been proven to have medicinal effects by rigorous science or have been approved by regulatory agencies such as the United States Food and Drug Administration or European Food Safety Authority.

The articles in this category can be about traditional healing uses of plants, allopathic medicines derived from plants, and pharmacological research results about a plant.

Pharmacognosy is the study of medicines derived from natural sources, including plants. The American Society of Pharmacognosy as "the study of the physical, chemical, biochemical and biological properties of drugs, drug substances or potential drugs or drug substances of natural origin as well as the search for new drugs from natural sources."

Economic Plants

Our daily dependence on plant products of tropical origin is astounding. For instance, Latin America and Africa are major suppliers of coffee and cacao (from which we derive chocolate), while Asia produces most of our rice and natural rubber. Our lives are enriched by beautiful hardwoods, spices, essential oils and fruits. In addition, tropical countries export many fibres, gums, resins, dyes, and plant essences that we may never see directly, but which are widely used in medicine and industry. This section highlights some of these important plants.

The Tropics in World Trade

Plant products like those just mentioned are often referred to as "commodities" or "cash crops." Unlike many exports from the industrialized economies, commodities are usually exported in minimally processed states as raw materials. Whether tropical nations should continue to rely extensively on these exports to fuel their emerging economies is a hotly debated subject, with critics maintaining that overproduction depresses world prices of these materials and diverts arable land from food production for local markets. Regardless, patterns of trade in commodities are not likely to change significantly in the near future.

Trade vs. Environmental Concerns

As tropical nations seek to increase their share in the world marketplace, a key question is the best way to balance these strategies with the needs to conserve and manage remaining forested areas. Indiscriminate harvesting techniques and clearing large tracts for cultivation or ranching have been all too characteristic of the past.

The future will require more appropriate means of extracting plants or their products if we are not to lose the many thousands of other tropical species holding genetic "blueprints" important to our future. This will require strong international leadership on economic and environmental fronts and, for all citizens of the world, a willingness to rethink our use of the Earth's resources.

Native Origins of Economic Plants

Plants listed below are native to these regions. Many are now grown in other areas of the tropics also.

Essential Oils

Essential oils, or volatile oils, are found in many different plants. These oils are different from fatty oils because they evaporate or volatilize on contact with the air and they possess a pleasant taste and strong aromatic odor. They are readily removed from plant tissues without any change in composition. Essential oils are very complex in their chemical nature. The two main groups are the hydrocarbon terpenes and the oxygenated and sulphured oils.

These oils do not have any obvious physiological significance for the plant. They may represent byproducts or metabolism rather than foods. The characteristic flavour and aroma that they impart are probably to some advantage in attracting insects and other animals, which play a role in pollination or in the dispersal of the fruits and seeds. When in high concentration, these same odors may serve to repel enemies of the plants.

The oils may also have some antiseptic and bactericidal value. There is some evidence that they play an even more vital role as hydrogen donors in oxidoreduction reactions, as potential sources of energy, or in affecting transpiration and other physiological processes (Hill 1952).

All the distinctly aromatic plants contain essential oils. They occur in over 60 families and are especially typical of the Lauraceae, Myrtaceae, Umbelliferae, Labiatae and Compositae. The quantity of oil varies from a very small amount to as much as 1-2 percent. The oils are secreted by internal glands or in hair like structures. Sometimes, as in wintergreen and mustard, the oil is not present in the plant but develops only as the result of chemical action when the ground-up plant tissue is extracted

with water. Almost any organ of a plant may be the source of the oil. Examples are flowers (rose), leaves (mint), fruits (lemon), bark (cinnamon), wood (cedar), root (ginger) or seeds (cardamom), and many resinous exudations as well.

These oils are extracted from the plant tissues in different ways depending on the quantity and stability of the compound. Three principal methods are: expression, distillation and extraction by solvents.

Perfumes

The history of civilization is directly connected with that of perfumes. Perfumes have been in widespread use since the earliest recorded times. The Egyptians and ancient Hebrews used them for both personal and religious purposes. They played an important role in the life of the Romans and Greeks, reaching such a high degree of specialization with the Greeks that a special perfume was required for each part of the body. Later Catherine de' Medici knew as much about perfumes as she did about poisons. In the time of Queen Elizabeth a gift of rare perfumes was a definite way to win the royal favour, while the court of Louis XIV at Versailles had a particular perfume for each day of the year, the preparation of which was supervised by the king himself.

In those days perfumes were of hygienic as well as aesthetic value for they acted as true antiseptics and deodorants and masked offensive odors at a time when bathing was infrequent. Perfumes have continued to be in great demand to the present day. The consumption of the natural products has gradually increased in spite of the many synthetic substitutes that chemists have placed on the market. Synthetics are not as long lasting as those obtained directly from the plants.

The most valuable perfumes are combinations of several essential oils. Frangipani, for example, contains sandalwood, sage, neroli, orris root, and musk, while one of the formulas for Eau de Cologne, which dates from 1709, calls for neroli, rosemary, lemon and bergamot dissolved in pure alcohol and aged. "The expert perfumer must be able to blend the several oils at his command as an orchestra leader combines the various instruments into a perfect whole" (Hill 1952).

Perfumes also contain fixatives, which are substances that are less volatile than the oils and which delay and so equalize evaporation. These may be of plant or animal origin. Musk, ambergris, and civet are frequently used for this purpose. Balsams and oleoresins, such as benzoin, styrax, and oak moss; essential oils with a low rate of evaporation like orris, patchouli, elary sage, and sandalwood; and various synthetic materials are also used.

Perfume plants are cultivated for the most part in areas bordering on the Mediterranean Sea and the Indian Ocean. Most of the natural perfumes are made in southern France in the region around Grasse and Cannes near the French Riviera. Here garden flowers are cultivated on a large scale, and from 10-12 billion pounds were being gathered annually by the mid 1950's. These included over 5 million pounds of orange blossoms, over 4 million pounds of roses, 440 thousand pounds of jasmine and 330 thousand pounds of violets. Large quantities of tuberoses, cassie, jonquils, thyme, rosemary, lavender and geraniums are grown and many other fragrant species to a lesser degree. Flowers are also grown for the perfume industry to some extent in Reunion, North Africa, England and various European, Pacific and Asiatic areas. When supplies were reduced during World War II, the United States developed substitutes and initiated or increased the cultivation of several essential oil plants in Central America. Of the 75 essential oils regularly used in the industry only eight are normally produced in the Western Hemisphere, and only oil of petitgrain is of much importance.

References

Anderson, Edgar: *Plants, Man and Life*. U. Calif. Press, Berkeley, 1967.

Barrows, D. P.: *The Ethno-Botany of the Coahuilla Indians of Southern California*. Univ. Chicago Press, 1900.

Bellamy, David: *Bellamy on Botany*, Edbury Publishing - BBC Books, London, 1972.

Capon, Brian: *Botany for Gardeners,* Timber Publishing, Portland, OR, 2005.

Dallal, Ahmad: *Islam, Science, and the Challenge of History*, Yale University Press, New Haven, CT, 2010.

Gantt, Elisabeth: *Handbook of Phycological Methods. Developmental and Cytological Methods.* Cambridge University Press, Cambridge, England, 1980.

Halle, Francis: *In Praise of Plants*, Timber Publishing, Portland, OR, 2002.

Jeanness, Diamond: *The People of the Twilight*. V. Chicago Press, Chicago, 1959.

King, John: *Reaching for the Sun: How Plants Work*. Cambridge University Press, Cambridge, 1997.

Lloyd, John U.: *Origin and History of all the Pharmacopoeial Vegetable Drugs*, *Chemicals, and Preparations*, The Caxton Press, Cincinnati, 1998.

Rutsch, E. S.: *Smoking technology of the aborigines of the Iroquois area*, Associated Univ. Press, NY,1973.

Thomas, Barry A.: *The Evolution of Plants and Flowers*, St. Martin's Press, New York, 1981.

Walker, David: *Energy, Plants and Man,* Oxygraphics Ltd., Sheffield, England, 1999.

Anatomy and Physiology of Animals Sensitive Organs

Menka Sisodia

Research Scholar, Department of Zoology, Kolhan University, Chaibasa

Cardiovascular System/Blood Circulation

The circulatory system is the continuous system of tubes through which the blood is pumped around the body. It supplies the tissues with their requirements and removes waste products. In mammals and birds the blood circulates through two separate systems - the first from the heart to the lungs and back to the heart again (the pulmonary circulation) and the second from the heart to the head and body and back again.

The tubes through which the blood flows are the arteries, capillaries and veins. The heart pumps blood into arteries that carry it away from the heart. The arteries divide into very thin vessels called capillaries that form a network between the cells of the body. The capillaries then join up again to make veins that return the blood to the heart.

Arteries

Arteries carry blood away from the heart. They have thick elastic walls that stretch and can withstand the surges of high pressure blood caused by the heartbeat (the pulse). The arteries divide into smaller vessels called arterioles. The hole down the centre of the artery is called the lumen.

There are three layers of tissue in the walls of an artery. It is lined with squamous epithelial cells. The middle layer is the thickest layer. It made of elastic fibres and smooth muscle to make it stretchy. The outer fibrous layer protects the artery. The pulse is only felt in arteries.

The Pulse

The pulse is the spurt of high pressure blood that passes along the aorta and arteries when the left ventricle contracts. As the pulse of blood passes along an artery the elastic walls stretch. When the pulse has passed the walls contract and this helps push the blood along. The pulse is easily felt at certain places where an artery passes near the surface of the body. It is strongest near the heart and becomes weaker as it travels away from the heart. The pulse disappears altogether in the capillaries.

Capillaries

Arterioles divide repeatedly to form a network penetrating between the cells of all tissues of the body. These small vessels are called capillaries. The walls are only one cell thick and some capillaries are so narrow that red blood cells have to fold up to pass through them. Capillaries form networks in tissues called capillary beds. The capillary networks in capillary beds are so dense that no living cell is far from its supply of oxygen and food.

Note: All arteries carry oxygenated blood except for the pulmonary artery that carries deoxygenated blood to the lungs.

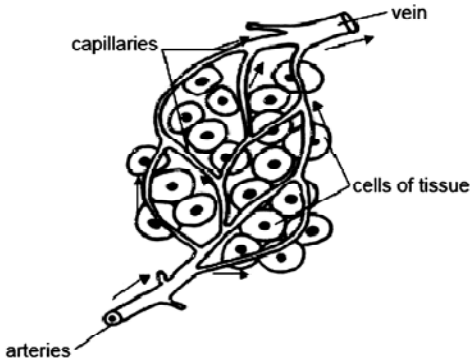

Figure: *A capillary bed*

The Formation of Tissue Fluid and Lymph

The thin walls of capillaries allow water, some white blood cells and many dissolved substances to diffuse through them. These form a clear fluid called tissue fluid (or extracellular fluid or interstitial fluid) that surrounds the cells of the tissues. The tissue fluid allows oxygen and nutrients to pass from the blood to the cells and carbon dioxide and other waste products to be removed from the tissues.

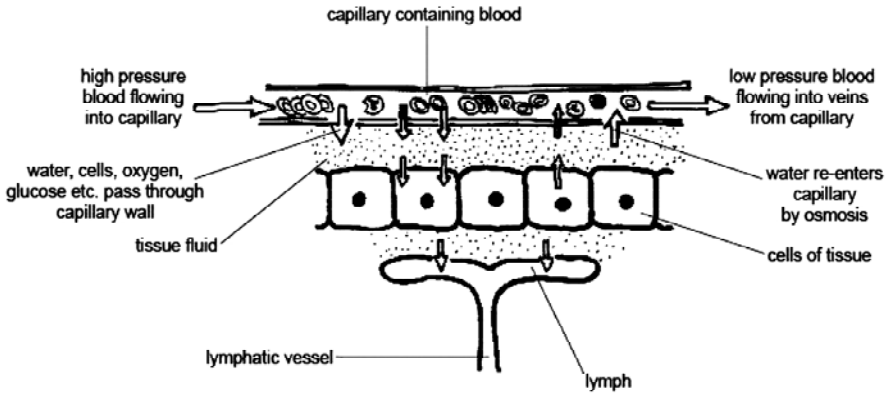

Figure: *The formation of tissue fluid and lymph from blood*

Some tissue fluid finds its way back into the capillaries and some of it flows into the blind-ended lymphatic vessels that form a network in the tissues. Once the tissue fluid has entered the lymphatics it is called lymph although its composition remains the same. The lymph vessels have walls that are even thinner than the capillaries. This means that molecules and particles that are larger than those that can pass into the blood stream e.g. cancer cells and bacteria can enter the lymphatic system. These are then filtered out as the lymph passes through lymph nodes.

Veins

Capillaries unite to form larger vessels called venules that join to form veins. Veins return blood to the heart and since blood that flows in veins has already passed through the fine capillaries, it flows slowly with no pulse and at low pressure. For this reason veins have thinner walls than arteries although there have the same three layers in them as arteries. As there is no pulse in veins, the blood is squeezed along them by the contraction of the skeletal muscles that lay alongside them. Veins also have valves in them that prevent blood flowing backwards.

The pulmonary vein that carries oxygenated blood from the lungs to the left atrium of the heart is an exception.

Regulation of Blood Flow

The flow of blood along arteries, arterioles and capillaries is not constant but can be controlled depending upon the requirements of the body. For example more blood is directed to the skeletal muscles, brain or digestive system when they are active. Regulation of the blood flow to the arterioles of the skin is also important in controlling body temperature. The size of the vessels is adjusted by the contraction or relaxation of smooth muscle fibres in their walls.

Oedema and Fluid Loss

Oedema is the swelling of the tissues due to the accumulation of tissue fluid. This may occur because the tissue fluid is prevented from returning to the bloodstream and accumulates in the tissues. This may be caused by physical inactivity (e.g. long car or plane trips in humans) or because of imbalances in the proteins in the blood. This is what causes the "potbelly" of the malnourished child or worm-infested puppy.

Loss of body fluid can be caused not only by drinking insufficient liquid but also through diarrhea and vomiting or sudden loss of blood due to haemorrhage. The effect is to reduce the volume of the blood which decreases the blood pressure. This could be dangerous because the supply of adequate blood to the brain depends upon maintaining the blood pressure at a constant level. To compensate for the loss of fluid various

mechanisms come into play. First of all the blood vessels contract in order to try and maintain the pressure. Then, since the loss of fluid tends to make the blood more concentrated and increases its osmotic pressure, fluid is drawn into the blood from the tissues by osmosis.

The Spleen

The spleen is situated near the stomach. It has a rich blood supply and acts as a reservoir of red blood cells. When there is a sudden loss of blood, as happens when a haemorrhage occurs, the spleen contracts to release large numbers of red blood cells into the circulation. The spleen also destroys old red cells and makes new lymphocytes but it is not an essential organ because its removal in adult life seems to cause few problems. In the foetus, the spleen makes both red and white cells.

Important Blood Vessels of The Systemic (Body) Circulation

Blood is pumped out into the body via the main artery, the aorta. This takes the blood to the head, the limbs and all the body organs. After passing through a network of fine capillaries, the blood is returned to the heart in the largest vein, the vena cava.

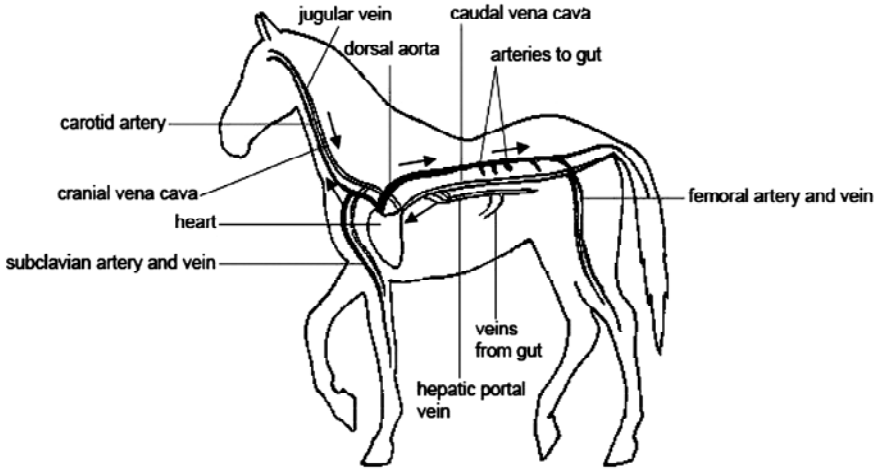

Figure: *The main arteries and veins of the horse*

Arteries and veins to and from many organs often run alongside each other and have the same name e.g. the renal artery and vein serve the kidney, the femoral artery and vein serve the hind limbs and the subclavian artery and vein serve the forelimbs. However, blood to the head passes along the carotid artery and returns to the cranial vena cava via the jugular vein.

One variation on this arrangement is found in the blood vessels that serve the digestive tract. A variety of arteries take blood from the aorta to the intestines but blood from the intestines is carried by the hepatic portal

vein to the liver where the digested food can be processed. This vessel is unlike others in that it transports blood from one organ to another rather than to or from the heart like arteries or veins.

Blood Pressure

The blood pressure is the pressure of the blood against the walls of the main arteries. The pressure is highest as the pulse produced by the contraction of the left ventricle passes along the artery. This is known as the systolic pressure. Pressure is much lower between pulses. This is known as the diastolic pressure. Blood pressure is measured in millimetres of mercury. A blood pressure that is higher than expected is known as hypertension while a pressure lower than expected is known as hypotension.

- The circulatory system is double with the blood passing through the heart twice.
- Arteries carry blood away from the heart. They have thick elastic walls that stretch and can withstand the high pressure of the pulse.
- Capillaries are small, thin walled vessels that form a network between the cells of the tissues.
- Veins return low pressure blood to the heart. They have thinner walls than arteries.
- The pulse is the spurt of high pressure blood that passes along the arteries when the left ventricle contracts. It can be felt where arteries pass close to the body surface.
- Tissue fluid is the clear fluid that leaks from the capillaries and surrounds the cells of the tissues. Lymph forms when tissue fluid enters lymphatics.
- Important blood vessels include the vena cava, aorta, pulmonary artery, carotid artery, jugular vein, renal artery and vein and hepatic portal vessel.

Respiratory System

Animals require a supply of energy to survive. This energy is needed to build large molecules like proteins and glycogen, make the structures in cells, move chemicals through membranes and around cells, contract muscles, transmit nerve impulses and keep the body warm. Animals get their energy from the large molecules that they eat as food. Glucose is often the energy source but it may also come from other carbohydrates, as well as fats and protein. The energy is made by the biochemical process known as cellular respiration that takes place in the mitochondria inside every living cell.

The overall reaction can be summarised by the word equation given below.

Charbohydrate Food (glucose) + Oxygen = Carbon Dioxide + Water + energy

As you can see from this equation, the cells need to be supplied with oxygen and glucose and the waste product, carbon dioxide, which is poisonous to cells, needs to be removed. The way the digestive system provides the glucose for cellular respiration will be described in Chapter 5, but here we are only concerned with the two gases, oxygen and carbon dioxide, that are involved in cellular respiration.

These gases are carried in the blood to and from the tissues where they are required or produced. Oxygen enters the body from the air (or water in fish)and carbon dioxide is usually eliminated from the same part of the body. This process is called gas exchange. In fish gas exchange occurs in the gills, in land dwelling vertebrates lungs are the gas exchange organs and frogs use gills when they are tadpoles and lungs, the mouth and the skin when adults.

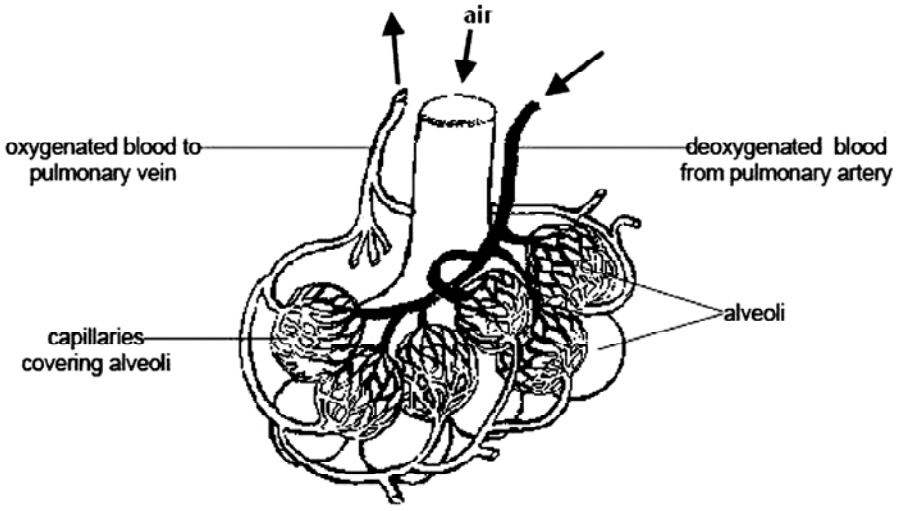

Figure: *Alveoli with blood supply*

Mammals (and birds) are active and have relatively high body temperatures so they require large amounts of oxygen to provide sufficient energy through cellular respiration. In order to take in enough oxygen and release all the carbon dioxide produced they need a very large surface area over which gas exchange can take place. The many minute air sacs or alveoli of the lungs provide this. When you look at these under the microscope they appear rather like bunches of grapes covered with a dense network of fine capillaries. A thin layer of water covers the inner surface

of each alveolus. There is only a very small distance -just 2 layers of thin cells - between the air in the alveoli and the blood in the capillaries. The gases pass across this gap by diffusion.

References

Agamben, Giorgio: *The Open: Man and Animal,* Stanford University Press, UK, 2004.

Alger, Janet and Steven Alger: *Cat Culture: The Social World of a Cat Shelter,* Temple University Press, Philadelphia, 2003.

Brown, L.: *Cruelty to Animals: The Moral Debt*, MacMillan, London, 1988.

Budiansky, S.: *The Covenant of the Wild: Why Animals Chose Domestication*, Morrow, New York, 1992.

Calarco, Matthew, and Peter Atterton: *Animal Philosophy: Essential Readings in Continental Thought,* Continuum, London, 2004.

Fudge, Erica: *Brutal Reasoning: Animals, Rationality and Humanity in Early Modern England,* Cornell University Press, Ithaca, 2006.

Gates, P.: *Animal Communication,* Cambridge University Press, Cambridge, 1997.

Harris, Marvin: *The Sacred Cow and the Abominable Pig: Riddles of Food and Culture*, Touchstone Books, New York, 1987.

Ucko, Peter J. and G.W. Dimbleby: *The Domestication and Exploitation of Plants and Animals*, Aldine Publishing Company, Chicago, IL, 1969.

Yarri, Donna: *The Ethics of Animal Experimentation: A Critical Analysis And Constructive Christian Proposal,* Oxford University Press, Oxford, 2005.

Zeuner, Frederick E.: *A History of Domesticated Animals*, Hutchinson, London, 1963.

Geotechnical Investigation

Naveen Kumar Jha
Assistant Professor, Department of Civil Engineering,
Noida International University, Noida

Geotechnical investigations are performed by geotechnical engineers or engineering geologists to obtain information on the physical properties of soil and rock around a site to design earthworks and foundations for proposed structures and for repair of distress to earthworks and structures caused by subsurface conditions. A geotechnical investigation will include surface exploration and subsurface exploration of a site. Sometimes, geophysical methods are used to obtain data about sites. Subsurface exploration usually involves soil sampling and laboratory tests of the soil samples retrieved. Surface exploration can include geologic mapping, geophysical methods, and photogrammetry, or it can be as simple as a geotechnical professional walking around on the site to observe the physical conditions at the site.

To obtain information about the soil conditions below the surface, some form of subsurface exploration is required. Methods of observing the soils below the surface, obtaining samples, and determining physical properties of the soils and rocks include test pits, trenching (particularly for locating faults and slide planes), boring, and in situ tests.

Soil Sampling

Borings come in two main varieties, large-diameter and small-diameter. Large-diameter borings are rarely used due to safety concerns and expense, but are sometimes used to allow a geologist or engineer to visually and manually examine the soil and rock stratigraphy in-situ. Small-diameter borings are frequently used to allow a geologist or engineer examine soil or rock cuttings or to retrieve samples at depth using soil samplers, and to perform in-place soil tests.

Soil samples are often categorised as being either "disturbed" or "undisturbed;" however, "undisturbed" samples are not truly undisturbed. A disturbed sample is one in which the structure of the soil has been changed sufficiently that tests of structural properties of the soil will not be representative of in-situ conditions, and only properties of the soil grains (e.g., grain size distribution, Atterberg limits, and possibly the water content) can be accurately determined. An undisturbed sample is one where the condition of the soil in the sample is close enough to the conditions of the soil in-situ to allow tests of structural properties of the soil to be used to approximate the properties of the soil in-situ.

Offshore soil collection introduces many difficult variables. In shallow water, work can be done off a barge. In deeper water a ship will be required. Deepwater soil samplers are normally variants of Kullenberg-type samplers, a modification on a basic gravity corer using a piston (Lunne and Long, 2006). Seabed samplers are also available, which push the collection tube slowly into the soil.

Soil Samplers

Soil samples are taken using a variety of samplers; some provide only disturbed samples, while others can provide relatively undisturbed samples.

Shovel: Samples can be obtained by digging out soil from the site. Samples taken this way are disturbed samples.

Hand/Machine Driven Auger: This sampler typically consists of a short cylinder with a cutting edge attached to a rod and handle. The sampler is advanced by a combination of rotation and downward force. Samples taken this way are disturbed samples.

Continuous Flight Auger: A method of sampling using an auger as a corkscrew. The auger is screwed into the ground then lifted out. Soil is retained on the blades of the auger and kept for testing. The soil sampled this way is considered disturbed.

Split-spoon / SPT Sampler: Utilised in the 'Standard Test Method for Standard Penetration Test (SPT) and Split-Barrel Sampling of Soils' (ASTM D 1586). This sampler is typically a 18"-30" long, 2.0" outside diameter (OD) hollow tube split in half lengthwise. A hardened metal drive shoe with a 1.375" opening is attached to the bottom end, and a one-way valve and drill rod adapter at the sampler head. It is driven into the ground with a 140-pound (64 kg) hammer falling 30". The blow counts (hammer strikes) required to advance the sampler a total of 18" are counted and reported. Generally used for non-cohesive soils, samples taken this way are considered disturbed.

Modified California Sampler: Similar in concept to the SPT sampler, the sampler barrel has a larger diameter and is usually lined with metal tubes to contain samples. Samples from the Modified California Sampler are considered disturbed due to the large area ratio of the sampler (sampler wall area/sample cross sectional area).

Shelby Tube Sampler: Utilised in the 'Standard Practice for Thin-Walled Tube Sampling of Soils for Geotechnical Purposes' (ASTM D 1587). This sampler consists of a thin-walled tube with a cutting edge at the toe. A sampler head attaches the tube to the drill rod, and contains a check valve and pressure vents. Generally used in cohesive soils, this sampler is

advanced into the soil layer, generally 6" less than the length of the tube. The vacuum created by the check valve and cohesion of the sample in the tube cause the sample to be retained when the tube is withdrawn. Standard ASTM dimensions are; 2" OD, 36" long, 18 gauge thickness; 3" OD, 36" long, 16 gauge thickness; and 5" OD, 54" long, 11 gauge thickness. It should be noted that ASTM allows other diameters as long as they are proportional to the standardised tube designs, and tube length is to be suited for field conditions. Soil sampled in this manner is considered undisturbed.

Piston Samplers: These samplers are thin-walled metal tubes which contain a piston at the tip. The samplers are pushed into the bottom of a borehole, with the piston remaining at the surface of the soil while the tube slides past it. These samplers will return undisturbed samples in soft soils, but are difficult to advance in sands and stiff clays, and can be damaged (compromising the sample) if gravel is encountered. The Livingstone corer, developed by D. A. Livingstone, is a commonly used piston sampler. A modification of the Livingstone corer with a serrated coring head allows it to be rotated to cut through subsurface vegetable matter such as small roots or buried twigs.

Pitcher Barrel Sampler: This sampler is similar to piston samplers, except that there is no piston. There are pressure-relief holes near the top of the sampler to prevent pressure buildup of water or air above the soil sample.

In-situ Tests

A standard penetration test (SPT) is an in-situ dynamic penetration test designed to provide information on the properties of soil, while also collecting a disturbed soil sample for grain-size analysis and soil classification. A cone penetration test (CPT) is performed using an instrumented probe with a conical tip, pushed into the soil hydraulically at a constant rate. A basic CPT instrument reports tip resistance and shear resistance along the cylindrical barrel. CPT data has been correlated to soil properties. Sometimes instruments other than the basic CPT probe are used, including:

CPTu - Piezocone Penetrometer: This probe is advanced using the same equipment as a regular CPT probe, but the probe has an additional instrument which measures the groundwater pressure as the probe is advanced.

SCPTu - Seismic Piezocone Penetrometer: This probe is advanced using the same equipment as a CPT or CPTu probe, but the probe is also equipped with either geophones or accelerometers to detect shear waves and/or pressure waves produced by a source at the surface.

Full Flow Penetrometers - T-bar, Ball, and Plate: These probes are used in extremely soft clay soils (such as sea-floor deposits) and are

advanced in the same manner as the CPT. As their names imply, the T-bar is a cylindrical bar attached at right angles to the drill string forming what look likes a T, the ball is a large sphere, and the plate is flat circular plate. In soft clays, soil flows around the probe similar to a viscous fluid.

The pressure due to overburden stress and pore water pressure is equal on all sides of the probes (unlike with CPT's), so no correction is necessary, reducing a source of error and increasing accuracy. Especially desired in soft soils due to the very low loads on the measuring sensors. Full flow probes can also be cycled up and down to measure remolded soil resistance. Ultimately the geotechnical professional can use the measured penetration resistance to estimate undrained and remolded shear strengths.

Flat Plate Dilatometer Test (DMT) is a flat plate probe often advanced using CPT rigs, but can also be advanced from conventional drill rigs. A diaphragm on the plate applies a lateral force to the soil materials and measures the strain induced for various levels of applied stress at the desired depth interval.

Laboratory Tests

A wide variety of laboratory tests can be performed on soils to measure a wide variety of soil properties. Some soil properties are intrinsic to the composition of the soil matrix and are not affected by sample disturbance, while other properties depend on the structure of the soil as well as its composition, and can only be effectively tested on relatively undisturbed samples. Some soil tests measure direct properties of the soil, while others measure "index properties" which provide useful information about the soil without directly measuring the property desired.

Atterberg Limits

The Atterberg limits define the boundaries of several states of consistency for plastic soils. The boundaries are defined by the amount of water a soil needs to be at one of those boundaries. The boundaries are called the plastic limit and the liquid limit, and the difference between them is called the plasticity index. The shrinkage limit is also a part of the Atterberg limits. The results of this test can be used to help predict other engineering properties.

California Bearing Ratio

ASTM D 1883. A test to determine the aptitude of a soil or aggregate sample as a road subgrade. A plunger is pushed into a compacted sample, and its resistance is measured. This test was developed by Caltrans, but it is no longer used in the Caltrans pavement design method. It is still used as a cheap method to estimate the resilient modulus.

Direct Shear Test

ASTM D3080. The direct shear test determines the consolidated, drained strength properties of a sample. A constant strain rate is applied to a single shear plane under a normal load, and the load response is measured. If this test is performed with different normal loads, the common shear strength parameters can be determined.

Expansion Index Test

This test uses a remolded soil sample to determine the Expansion Index (EI), an empirical value required by building design codes, at a water content of 50% for expansive soils, like expansive clays.

Hydraulic Conductivity Tests

There are several tests available to determine a soil's hydraulic conductivity. They include the constant head, falling head, and constant flow methods. The soil samples tested can be any type include remolded, undisturbed, and compacted samples.

Oedometer Test

This can be used to determine consolidation (ASTM D2435) and swelling (ASTM D4546) parameters.

Particle-size Analysis

This is done to determine the soil gradation. Coarser particles are separated in the sieve analysis portion, and the finer particles are analysed with a hydrometer. The distinction between coarse and fine particles is usually made at 75 ìm. The sieve analysis shakes the sample through progressively smaller meshes to determine its gradation. The hydrometer analysis uses the rate of sedimentation to determine particle gradation.

R-Value Test

California Test 301 This test measures the lateral response of a compacted sample of soil or aggregate to a vertically applied pressure under specific conditions. This test is used by Caltrans for pavement design, replacing the California bearing ratio test.

Soil Compaction Tests

Standard Proctor (ASTM D698), Modified Proctor (ASTM D1557), and California Test 216. These tests are used to determine the maximum unit weight and optimal water content a soil can achieve for a given compaction effort.

Soil Suction Tests

ASTM D5298.

Triaxial Shear Tests

This is a type of test that is used to determine the shear strength properties of a soil. It can simulate the confining pressure a soil would see deep into the ground. It can also simulate drained and undrained conditions.

Unconfined Compression Test

ASTM D698. This test compresses a soil sample to measure its strength. The modifier "unconfined" contrasts this test to the triaxial shear test.

Water Content

This test provides the water content of the soil, normally expressed as a percentage of the weight of water to the dry weight of the soil.

Geophysical Exploration

Geophysical methods are used in geotechnical investigations to evaluate a site's behaviour in a seismic event. By measuring a soil's shear wave velocity, the dynamic response of that soil can be estimated. There are a number of methods used to determine a site's shear wave velocity:

- Crosshole method
- Downhole method (with a seismic CPT or a substitute device)
- Surface wave reflection or refraction
- Suspension logging (also known as P-S logging or Oyo logging)
- Spectral analysis of surface waves (SASW)
- Modal Analysis of Surface waves (MASW)
- Reflection microtremor (ReMi).

Ambient Vibrations

Various types of vibration sources are always producing so called Ambient Vibrations on the Earth ground (also called ambient noise). These vibrations are mostly surface waves (Rayleigh waves, Love waves) propagating on the surface. Low frequency waves (below 1 Hz) are generally called microseisms and high frequency waves (above 1 Hz) are called microtremors. These ambient vibrations are used in practice to derive the elastic properties of the ground and the low-strain dynamic properties of civil-engineering structures (bridges, buildings, dams...). This information is useful for different purposes : fundamental seismology, engineering seismology, Earthquake engineering, Seismic microzonation, Structural health monitoring, but also Hydrology, Geotechnical Engineering, etc.

Physical Origin of the Ambient Vibrations

Bonnefoy-Claudet et al. reviewed the scientific work studying the origin of the noise wavefield. At low frequency (below 1 Hz), the noise sources are natural and mostly due to ocean waves. In particular the peak

between 0.1 and 0.3 Hz is clearly associated with the interaction of water waves of nearly equal frequencies but opposite directions. At high frequency (above 1 Hz), the wavefield is mainly produced by human activities (road traffic, industrial work...) but there are also natural sources like rivers. Around 1 Hz, the local atmospheric conditions (wind...) are also a major source of ground vibrations.

The amplitude of ground ambient vibrations is typically in the range of 1e-6 m, i.e. in the order of the tenth of micrometers to tens of micrometers. Peterson provided high and low noise models as a function of frequency. The ambient wave field is made of a small amount of body waves (P- and S-waves), and a most generally predominant part ofsurface waves, i.e. Love and Rayleigh waves. Theses waves are dispersive, i.e. their phase velocity varies with frequency (most generally, it decreases with increasing frequency). The dispersion curve (phase velocity or slowness as a function of frequency) is tightly related to the variations of the shear-wave velocity with depth in the different ground layers: it can thus be used as a non-invasive tool to investigate the underground structure.

References

Barnes, Thomas G. : *Origin and Destiny of the Earth's Magnetic Field,* Creation Research Society, London, 1983.

Berlin, G.L.: *Earthquakes and the Urban Environment,* CRC Press, Boca Raton, FL, 1980.

Curtis, L. F. : *Introduction to Environmental Remote Sensing*, London, New York, 1992.

David E.: *Earthquakes*, Franklin Watts, New York, 1993.

Freeman, J.R.: *Earthquake Damage and Earthquake Insurance: Studies of a Rational Basis for Earthquake Insurance, also Studies of Engineering Data for Earthquake-resisting Construction*, McGraw-Hill Books, New York, 1932.

Geist, Helmut: *The Causes and Progression of Desertification*, Ashgate Publishing, Delhi, 2005.

Knight, Linsay: *Volcanoes & Earthquakes*, Time-Life Books, Alexandria, VA. 1995.

Langran, G.: *Time in Geographic Information Systems.* Bristol: Taylor & Francis, 1992.

Macdonald, Gordon A.: *Volcanoes*, Prentice-Hall, Englewood Cliffs, NJ, 1972.

Mack, Pamela Etter : *Viewing the Earth: The Social Construction of the Landsat Satellite System*, Cambridge, MIT Press, 1900.

Summerfield, Mike: *Global Geomorphology*, Longman, London, 1991.

Thompson, Dick: *Volcano Cowboys: The Rocky Evolution of a Dangerous Science*, St. Martin's Press, New York, 2000.

Tilling, Robert I.: *Volcanoes*, General Interest Publications of the USGS, US, 1997

Modelling of Prime Movers and Generators

Sujata Arora

Research Scholar, Department of Electrical and Electronics Engineering, Manav Rachna International University

In engineering, a prime mover is an engine that converts fuel to useful work. In locomotives, the prime mover is thus the source of power for its propulsion. The term is generally used when discussing any locomotive powered by an internal combustion engine. The term is also applied to engine-generator sets, where the engine is termed the prime mover, as distinct from the generator.

In a diesel-mechanical locomotive, prime mover refers to the diesel engine that is mechanically coupled to the driving wheels (drivers). In a diesel-electric locomotive, prime mover refers to the diesel engine that rotates the main generator responsible for producing electricity to power the traction motors that are geared to the drivers. The prime mover can also be a gas turbine instead of a diesel engine. In either case, the generator, traction motors and interconnecting apparatus are considered to be the power transmission system and not part of the prime mover. A wired-electric or battery-electric locomotive has no on-board prime mover, instead relying on an external power station.

Power Unit

The term *power unit* is also sometimes used in application to diesel locomotives, with a similar meaning. Where the engine and generator set of a diesel-electric locomotive are removable as a unit, it is usual to term the coupled pair of them as "the power unit", but "prime mover" is applied to the diesel engine alone.

Figure: *Power unit (engine and generator right) from a diesel-electric locomotive*

Electric Generator

In electricity generation, an electric generator is a device that converts mechanical energy to electrical energy. A generator forces electric current to flow through an external circuit. The source of mechanical energy may be a reciprocating or turbine steam engine, water falling through a turbine or waterwheel, an internal combustion engine, a wind turbine, a hand crank, compressed air, or any other source of mechanical energy. Generators provide nearly all of the power for electric power grids.

The reverse conversion of electrical energy into mechanical energy is done by an electric motor, and motors and generators have many similarities. Many motors can be mechanically driven to generate electricity and frequently make acceptable generators. Before the connection between magnetism and electricity was discovered, electrostatic generators were used. They operated on electrostatic principles. Such generators generated very high voltage and low current. They operated by using moving electrically charged belts, plates, and disks that carried charge to a high potential electrode. The charge was generated using either of two mechanisms:

- Electrostatic induction
- The triboelectric effect, where the contact between two insulators leaves them charged.

Because of their inefficiency and the difficulty of insulating machines that produced very high voltages, electrostatic generators had low power ratings, and were never used for generation of commercially significant quantities of electric power. The Wimshurst machine and Van de Graaff generator are examples of these machines that have survived.

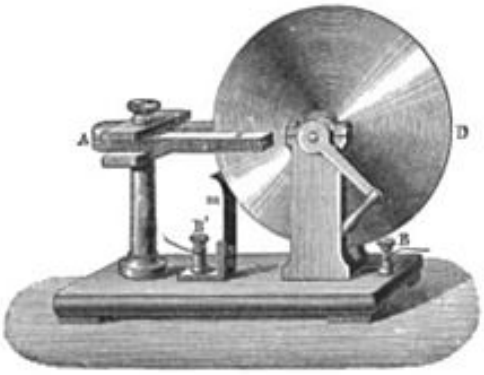

Figure: *Faraday disk, the first electric generator. The horseshoe-shaped magnet* (A) *created a magnetic field through the disk* (D). *When the disk was turned, this induced an electric current radially outward from the centre toward the rim. The current flowed out through the sliding spring contact* m, *through the external circuit, and back into the centre of the disk through the axle.*

In 1827, Hungarian Anyos Jedlik started experimenting with the electromagnetic rotating devices which he called electromagnetic self-rotors, now called the Jedlik's dynamo.

In the prototype of the single-pole electric starter (finished between 1852 and 1854) both the stationary and the revolving parts were electromagnetic. He formulated the concept of the dynamo at least 6 years before Siemens and Wheatstone but didn't patent it as he thought he wasn't the first to realise this. In essence the concept is that instead of permanent magnets, two electromagnets opposite to each other induce the magnetic field around the rotor. It was also the discovery of the principle of self-excitation.

In the years of 1831–1832, Michael Faraday discovered the operating principle of electromagnetic generators. The principle, later called Faraday's law, is that an electromotive force is generated in an electrical conductor which encircles a varying magnetic flux. He also built the first electromagnetic generator, called the Faraday disk, a type of homopolar generator, using a copper disc rotating between the poles of a horseshoe magnet. It produced a small DC voltage.

This design was inefficient, due to self-cancelling counterflows of current in regions that were not under the influence of the magnetic field. While current was induced directly underneath the magnet, the current would circulate backwards in regions that were outside the influence of the magnetic field. This counterflow limited the power output to the pickup wires, and induced waste heating of the copper disc. Later homopolar generators would solve this problem by using an array of magnets arranged around the disc perimeter to maintain a steady field effect in one current-flow direction.

Another disadvantage was that the output voltage was very low, due to the single current path through the magnetic flux. Experimenters found that using multiple turns of wire in a coil could produce higher, more useful voltages. Since the output voltage is proportional to the number of turns, generators could be easily designed to produce any desired voltage by varying the number of turns. Wire windings became a basic feature of all subsequent generator designs.

The dynamo was the first electrical generator capable of delivering power for industry. The dynamo uses electromagnetic induction to convert mechanical rotation into direct current through the use of a commutator. The first dynamo was built by Hippolyte Pixii in 1832.

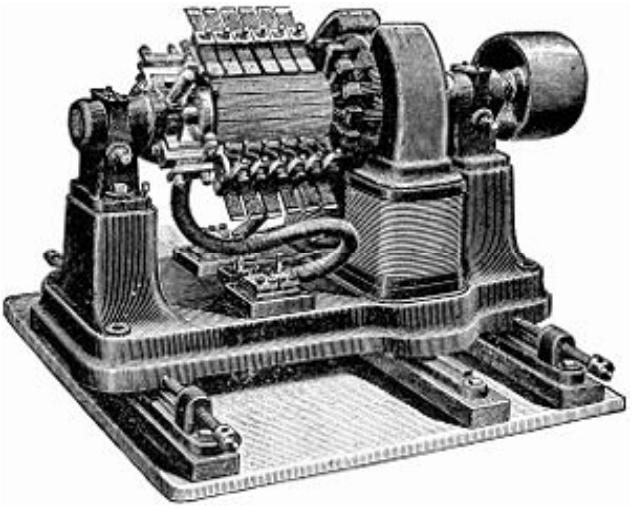

Figure: *Dynamos are no longer used for power generation due to the size and complexity of the commutator needed for high power applications. This large belt-driven high-current dynamo produced 310 amperes at 7 volts, or 2,170 watts, when spinning at 1400 RPM.*

A dynamo machine consists of a stationary structure, which provides a constant magnetic field, and a set of rotating windings which turn within that field. On small machines the constant magnetic field may be provided by one or more permanent magnets; larger machines have the constant magnetic field provided by one or more electromagnets, which are usually called field coils.

Through a series of accidental discoveries, the dynamo became the source of many later inventions, including the DC electric motor, the AC alternator, the AC synchronous motor, and the rotary converter.

Alternating current generating systems were known in simple forms from the discovery of the magnetic induction of electric current. The early machines were developed by pioneers such as Michael Faraday and Hippolyte Pixii.

Faraday developed the "rotating rectangle", whose operation was *heteropolar* - each active conductor passed successively through regions where the magnetic field was in opposite directions. The first public demonstration of a more robust "alternator system" took place in 1886. Large two-phase alternating current generators were built by a British electrician, J.E.H. Gordon, in 1882. Lord Kelvin and Sebastian Ferranti also developed early alternators, producing frequencies between 100 and 300 Hz. In 1891, Nikola Tesla patented a practical "high-frequency"

alternator (which operated around 15 kHz). After 1891, polyphase alternators were introduced to supply currents of multiple differing phases.

Later alternators were designed for varying alternating-current frequencies between sixteen and about one hundred hertz, for use with arc lighting, incandescent lighting and electric motors.

Large power generation dynamos are now rarely seen due to the now nearly universal use of alternating current for power distribution. Before the adoption of AC, very large direct-current dynamos were the only means of power generation and distribution. AC has come to dominate due to the ability of AC to be easily transformed to and from very high voltages to permit low losses over large distances.

Electromagnetic Generators

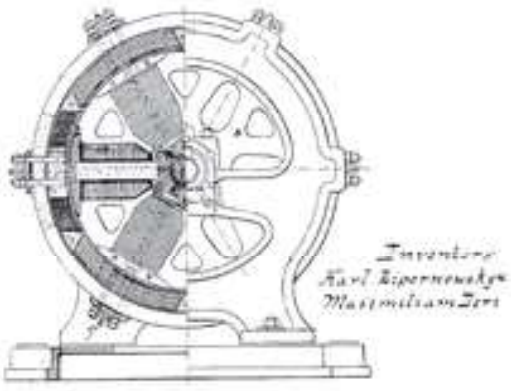

Figure: *"Dynamo Electric Machine" (end view, partly section, U.S. Patent 284,110), 1883*

Dynamo: A dynamo is an electrical generator that produces direct current with the use of a commutator. Dynamos were the first electrical generators capable of delivering power for industry, and the foundation upon which many other later electric-power conversion devices were based, including the electric motor, the alternating-current alternator, and the rotary converter.

Today, the simpler alternator dominates large scale power generation, for efficiency, reliability and cost reasons. A dynamo has the disadvantages of a mechanical commutator. Also, converting alternating to direct current using power rectification devices (vacuum tube or more recently solid state) is effective and usually economic.

References

Appleyard, Rollo: *Charles Parsons, his Life and Work*, Constable & Co., Ltd., London, 1933.

Armstrong, Christopher, and H. V. Nelles: *Monopoly's Moment: The Organization and Regulation of Canadian Utilities, 1830-1930*, University of Toronto Press, Toronto, 1986.

Baldwin, Neil: *Edison: Inventing the Century*, Hyperion, New York, 1995.

Bird, John: *Electrical and Electronic Principles and Technology,* Newnes, UK, 2007.

Bonbright, James C.: *Principles of Public Utility Rates,* Columbia University Press, New York, 1961.

Cantelon, Philip, and Robert C. Williams: *Crisis Contained: Department of Energy at Three Mile Island*, Southern Illinois University Press, Carbondale, IL, 1982.

Moorhouse, John C.: *Electric Power: Deregulation and the Public Interest,* Pacific Research Institute for Public Policy, San Francisco, 1986.

Nilsson, James; Riedel, Susan: *Electric Circuits*, Prentice Hall, London, 2007.

Nivola, Pietro S.: *The Politics of Energy Conservation,* Brooking Institution, Washington, DC, 1986.

Plummer, James and Troppmann, Susan: *Competition in Electricity: New Markets and New Structures,* Public Utilities Reports, Arlington, Va., 1990.

Plummer, James; Ferrar, Terry, and Hughes, William: *Electric Power Strategic Issues,* Public Utilities Reports, Inc., Arlington, VA, 1983.

Rudolph, Richard and Ridley, Scott, Power Struggle: *The Hundred-Year War Over Electricity,* Harper and Row, New York, 1986.

Sears, Francis W.: *University Physics,* Addison Wesley, NY, 1982.

Trebing, Harry M. and Mann, Patrick C.: *New Regulatory and Management Strategies in a Changing Market Environment,* Michigan State University, East Lansing, MI, 1987.

Chemical Industry

Smt. Nisha Kumari Mishra

(**M.Sc. Chemistry, M.U. Bodh Gaya,**
Principal, Sanjay Gandhi Mahila (Inter Section) Gosai Bagh, Gaya

The chemical industry comprises the companies that produce industrial chemicals. Central to the modern world economy, it converts raw materials (oil, natural gas, air, water, metals, and minerals) into more than 70,000 different products.

One of the first chemicals to be produced in large amounts through industrial process, was sulphuric acid. In 1736, the pharmacist Joshua Ward developed a process for its production that involved heating saltpeter and allowing the sulfur to oxidize and combine with water. It was the first practical production of sulfuric acid on a large scale. John Roebuck and Samuel Garbett were the first to establish a large scale factory in Prestonpans in 1749, which used leaden condensing chambers for the manufacture of sulphuric acid.

Expansion and Maturation

The late 19th century saw an explosion in both the quantity of production and the variety of chemicals that were manufactured. Large chemical industries also took shape in Germany and later in the United States.

Production of artificial manufactured fertilizer for agriculture was pioneered by Sir John Lawes at his purpose built Rothamsted Research facility. In the 1840s he established large works near London for the manufacture of superphosphate of lime. Processes for the vulcanization of rubber were patented by Charles Goodyear in the US and Thomas Hancock in England in the 1840s. The first synthetic dye was discovered by William Henry Perkin in London. He partly transformed aniline into a crude mixture which, when extracted with alcohol, produced a substance with an intense purple colour. He also developed the first synthetic perfumes. However, it was German industry that quickly began to dominate the field of synthetic dyes. The three major firms BASF, Bayer and Hoechst produced several hundred different dyes, and by 1913, the German industry produced almost 90 percent of the world supply of dyestuffs and sold about 80 percent of their production abroad.

The petrochemical industry can be traced back to the oil works of James Young in Scotland and Abraham Pineo Gesner in Canada. The first plastic

was invented by Alexander Parkes, an English metallurgist. In 1856, he patented Parkesine, a celluloid based on nitrocellulose treated with a variety of solvents. This material, exhibited at the 1862 London International Exhibition, anticipated many of the modern aesthetic and utility uses of plastics. The industrial production of soap from vegetable oils was started by William Lever and his brother James in 1885 in Lancashire based on a modern chemical process invented by William Hough Watson that used glycerin and vegetable oils.

By the 1920s, chemical firms consolidated into large conglomerates; IG Farben in Germany, Rhône-Poulenc in France and Imperial Chemical Industries in Britain. Dupont became a major chemicals firm in the early 20th century in America.

Products

Polymers and plastics, especially polyethylene, polypropylene, polyvinyl chloride, polyethylene terephthalate, polystyrene and polycarbonate comprise about 80% of the industry's output worldwide. Chemicals are used to make a wide variety of consumer goods, as well as thousands of inputs to agriculture, manufacturing, construction, and service industries. The chemical industry itself consumes 26 percent of its own output. Major industrial customers include rubber and plastic products, textiles, apparel, petroleum refining, pulp and paper, and primary metals. Chemicals are nearly a $3 trillion global enterprise, and the EU and U.S. chemical companies are the world's largest producers.[1]

Sales of the chemical business can be divided into a few broad categories, including basic chemicals (about 35 to 37 percent of the dollar output), life sciences (30 percent), specialty chemicals (20 to 25 percent) and consumer products (about 10 percent).

Basic Chemicals and Commodity Chemicals to Polymers and Speciality Chemicals

Basic chemicals or "commodity chemicals" are a broad chemical category including polymers, bulk petrochemicals and intermediates, other derivatives and basic industrials, inorganic chemicals, and fertilizers. Typical growth rates for basic chemicals are about 0.5 to 0.7 times GDP. Product prices are generally less than fifty cents per pound.

Polymers, the largest revenue segment at about 33 percent of the basic chemicals dollar value, includes all categories of plastics and man-made fibers. The major markets for plastics are packaging, followed by home construction, containers, appliances, pipe, transportation, toys, and games.

Chemicals in the bulk petrochemicals and intermediates are primarily made from liquefied petroleum gas (LPG), natural gas, and crude oil. Their

sales volume is close to 30 percent of overall basic chemicals. Typical large-volume products include ethylene, propylene, benzene, toluene, xylenes, methanol, vinyl chloride monomer (VCM), styrene, butadiene, and ethylene oxide. These basic or commodity chemicals are the starting materials used to manufacture many polymers and other more complex organic chemicals particularly those that are made for use in the specialty chemicals category.

Other derivatives and basic industrials include synthetic rubber, surfactants, dyes and pigments, turpentine, resins, carbon black, explosives, and rubber products and contribute about 20 percent of the basic chemicals' external sales.

Inorganic chemicals (about 12 percent of the revenue output) make up the oldest of the chemical categories. Products include salt, chlorine, caustic soda, soda ash, acids (such as nitric acid, phosphoric acid, and sulfuric acid), titanium dioxide, and hydrogen peroxide.

Fertilizers are the smallest category (about 6 percent) and include phosphates, ammonia, and potash chemicals.

Life Sciences

Life sciences (about 30 percent of the dollar output of the chemistry business) include differentiated chemical and biological substances, pharmaceuticals, diagnostics, animal health products, vitamins, and pesticides. While much smaller in volume than other chemical sectors, their products tend to have very high prices—over ten dollars per pound—growth rates of 1.5 to 6 times GDP, and research and development spending at 15 to 25 percent of sales. Life science products are usually produced with very high specifications and are closely scrutinized by government agencies such as the Food and Drug Administration. Pesticides, also called "crop protection chemicals", are about 10 percent of this category and include herbicides, insecticides, and fungicides.

Specialty Chemicals

Specialty chemicals are a category of relatively high valued, rapidly growing chemicals with diverse end product markets. Typical growth rates are one to three times GDP with prices over a dollar per pound. They are generally characterized by their innovative aspects. Products are sold for what they can do rather than for what chemicals they contain. Products include electronic chemicals, industrial gases, adhesives and sealants as well as coatings, industrial and institutional cleaning chemicals, and catalysts. In 2012, excluding fine chemicals, the $546 billion global speciality chemical market was 33% Paints, Coating and Surface

Treatments, 27% Advanced Polymer, 14% Adhesives and Sealants, 13% additives and 13% pigments and inks.

Speciality chemicals are sold as effect or performance chemicals sometimes they are mixtures of formulations unlike "fine chemicals" which are almost always single molecule products.

Consumer products

Consumer products include direct product sale of chemicals such as soaps, detergents, and cosmetics. Typical growth rates are 0.8 to 1.0 times GDP.

Consumers rarely if ever come into contact with basic chemicals but polymers and speciality chemicals are the materials that they will encounter everywhere in their every-day lives, such as in plastics, cleaning materials, cosmetics, paints & coatings, electronic gadgets, automobiles and the materials used to construct their homes. These speciality products are marketed by chemical companies to the downstream manufacturing industries as pesticides, speciality polymers, electronic chemicals, surfactants, construction chemicals, Industrial Cleaners, flavours and fragrances, speciality coatings, printing inks, water soluble polymers, food additives, paper chemicals, oil field chemicals, plastic adhesives, adhesives and sealants, cosmetic chemicals, water management chemicals, catalysts, textile chemicals. Chemical companies rarely supply these products directly to the consumer.

Every year, the American Chemistry Council tabulates the U.S. production volume of the top 100 basic chemicals. In 2000, the aggregate production volume of the top 100 chemicals totalled 502 million tons, up from 397 million tons in 1990. Inorganic chemicals tend to be the largest volume, though much smaller in dollar revenue terms due to their low prices. The top 11 of the 100 chemicals in 2000 were sulfuric acid (44 million tons), nitrogen (34), ethylene (28), oxygen (27), lime (22), ammonia (17), propylene (16), polyethylene (15), chlorine (13), phosphoric acid (13) and diammonium phosphates (12).

Companies

The largest corporate producers worldwide, each with plants in numerous countries, include BASF, Bayer, Ferro, Solvay, Braskem, Celanese/Ticona, Arkema, Degussa, Dow, DuPont, Eastman Chemical Company, ExxonMobil, Givaudan, INEOS, LG Chem, LyondellBasell, Mitsubishi, Monsanto, PPG Industries, SABIC, LANXESS, Shell, and Wanhua along with thousands of smaller firms.

In the U.S. there are 170 major chemical companies. They operate internationally with more than 2,800 facilities outside the U.S. and 1,700

foreign subsidiaries or affiliates operating. The U.S. chemical output is $750 billion a year. The U.S. industry records large trade surpluses and employs more than a million people in the United States alone. The chemical industry is also the second largest consumer of energy in manufacturing and spends over $5 billion annually on pollution abatement.

In Europe the chemical, plastics and rubber sectors are among the largest industrial sectors. Together they generate about 3.2 million jobs in more than 60,000 companies. Since 2000 the chemical sector alone has represented 2/3 of the entire manufacturing trade surplus of the EU.

In 2012 the chemical sector accounted for 12% of the EU manufacturing industry's added value. Europe remains world's biggest chemical trading region with 43% of the world's exports and 37%of the world's imports, although the latest data shows that Asia is catching up with 34% of the exports and 37% of imports. Even so Europe still has a trading surplus with all regions of the world except Japan and China where in 2011 there was a chemical trade balance. Europe's trade surplus with the rest of the world today amounts to 41.7 billion Euros.

Over the 20 years between 1991 and 2011 the European Chemical industry saw its sales increase 295 billion Euros to 539 billion Euros a picture of constant growth. Despite this the European industry's share of the world chemical market has fallen from 36% to 20%. This has resulted from the huge increase production and sales in the emerging markets like India and China. The data suggest that 95% of this impact is from China alone. In 2012 the data from the European Chemical Industry Council (CEFIC)shows that 5 European countries account for 71% of the EU's chemicals sales. These are Germany, France, United Kingdom, Italy and the Netherlands.

The industry includes manufacturers of inorganic- and organic-industrial chemicals, ceramic products, petrochemicals, agrochemicals, polymers and rubber (elastomers), oleochemicals (oils, fats, and waxes), explosives, fragrances and flavors.

Although the pharmaceutical industry is often considered a chemical industry , it has many different characteristics that puts it in a separate category. Other closely related industries include petroleum, glass, paint, ink, sealant, adhesive, and food processing manufacturers.

Though the business of chemistry is worldwide in scope, the bulk of the world's $3.7 trillion chemical output is accounted for by only a handful of industrialized nations. The United States alone produced $689 billion, 18.6 percent of the total world chemical output in 2008.

References

1. Derry, Thomas Kingston; Williams, Trevor I. (1993). *A Short History of Technology: From the Earliest Times to A.D. 1900*. New York: Dover.
2. Kiefer, David M. (2001). "Sulfuric Acid: Pumping Up the Volume". American Chemical Society. Retrieved 2008-04-21.
3. "The Chemical Industries In The UK". American Chemical Society. Retrieved 2013-04-21.
4. Aftalion, Fred (1991). *A History of the International Chemical Industry*. Philadelphia: University of Pennsylvania Press. pp. 11–13. ISBN 0-8122-1297-5.
5. *A History of the International Chemical Industry*.
6. Aftalion 1991, p. 104, Chandler 2004, p. 475
7. UK Patent office (1857). *Patents for inventions*. UK Patent office. p. 255.
8. Jeannifer Filly Sumayku, Unilever: Providing Enjoyable and Meaningful Life to Customers, *The President Post, 22 March 2010*
9. "Sectors of Chemical Industry". Technofunc. Retrieved 16 September 2013.

GPS Navigation Device

Vikram Singh Soni

Research Scholar, Department of Electronics, CMJ University, Meghalaya

The Global Positioning System (GPS) is a satellite-based navigation system made up of a network of 24 satellites placed into orbit by the U.S. Department of Defense. Military actions was the original intent for GPS, however in the 1980s, the U.S. government decided to allow the GPS programme to be used by civilians. Weather conditions do not affect the ability for GPS to work. The systems works 24/7 anywhere in the world. There are no subscription fees or setup charges to use GPS.

GPS devices may have capabilities such as:

- maps, including streets maps, displayed in human readable format via text or in a graphical format,
- turn-by-turn navigation directions to a human in charge of a vehicle or vessel via text or speech,
- directions fed directly to an autonomous vehicle such as a robotic probe,
- traffic congestion maps (depicting either historical or real time data) and suggested alternative directions,
- information on nearby amenities such as restaurants, fueling stations, and tourist attractions.

GPS may be able to answer:

- the roads or paths available,
- traffic congestion and alternative routes,
- roads or paths that might be taken to get to the destination,
- if some roads are busy (now or historically) the best route to take,
- the location of food, banks, hotels, fuel, airports or other places of interests,
- the shortest route between the two locations,
- the different options to drive on highway or back roads.

Dedicated GPS Navigation Devices

Dedicated devices have various degrees of mobility. *Hand-held*, *outdoor*, or *sport* receivers have replaceable batteries that can run them for several hours, making them suitable for hiking, bicycle touring and other activities far from an electric power source. Their screens are small, and some do

not show colour, in part to save power. Some use transflective liquid-crystal displays, allowing use in bright sunlight. Cases are rugged and some are water resistant.

Other receivers, often called *mobile* are intended primarily for use in a car, but have a small rechargeable internal battery that can power them for an hour or two away from the car. Special purpose devices for use in a car may be permanently installed and depend entirely on the automotive electrical system.

The pre-installed embedded software of early receivers did not display maps; 21st century ones commonly show interactive street maps (of certain regions) that may also show points of interest, route information and step-by-step routing directions, often in spoken form with a feature called "text to speech".

Due in part to regulations encouraging mobile phone tracking, including E911, the majority of GPS receivers are built into mobile telephones, with varying degrees of coverage and user accessibility. Commercial navigation software is available for most 21st-century smartphones as well as some Java-enabled phones that allows them to use an internal or external GPS receiver (in the latter case, connecting via serial or Bluetooth). Some phones using assisted GPS (A-GPS) function poorly when out of range of their carrier's cell towers. Others can navigate worldwide with satellite GPS signals as well as a dedicated portable GPS receiver does, upgrading their operation to A-GPS mode when in range. Still others have a hybrid positioning system that can use other signals when GPS signals are inadequate.

More bespoke solutions also exist for smartphones with inbuilt GPS capabilities. Some such phones can use tethering to double as a wireless modem for a laptop, while allowing GPS-navigation/localisation as well. One such example is marketed by Verizon Wireless in the United States, and is called VZ Navigator. The system uses gpsOne technology to determine the location, and then uses the mobile phone's data connection to download maps and calculate navigational routes. Other products including iPhone are used to provide similar services. Nokia gives Ovi Maps free on its smartphones and maps can be preloaded.

According to market research from the independent analyst firm Berg Insight, the sales of GPS-enabled GSM/WCDMA handsets was 150 million units in 2009, while only 40 million separate GPS receivers were sold.

GPS navigation applications for mobile phones include on-line (e.g. Waze, Google Maps Navigation) and off-line (e.g. iGo for Android,

Maverick and Here (Nokia) for Windows Phone) navigation applications. Google Maps Navigation, which is included with Android, means most smartphone users only need their phone to have a personal navigation assistant.

Many Android smartphones have an additional GPS feature, called EPO (Extended Prediction Orbit). The phone downloads a file to help it locate GPS satellites more quickly and reduce the Time To First Fix.

Palm, Pocket and Laptop PC

Software companies have made available GPS navigation software programmes for in-vehicle use on laptop computers. Benefits of GPS on a laptop include larger map overview, ability to use the keyboard to control GPS functions, and some GPS software for laptops offers advanced trip-planning features not available on other platforms, such as midway stops, capability of finding alternative scenic routes as well as only highway option.

Palms and Pocket PC's can also be equipped with GPS navigation. A pocket PC differs from a dedicated navigation device as it has an own operating system and can also run other applications.

GPS modules

Other GPS devices need to be connected to a computer in order to work. This computer can be a home computer, laptop, PDA, digital camera, or smartphones. Depending on the type of computer and available connectors, connections can be made through a serial or USB cable, as well as Bluetooth, CompactFlash, SD, PCMCIA and the newer ExpressCard. Some PCMCIA/ExpressCard GPS units also include a wireless modem.

Devices usually do not come with pre-installed GPS navigation software, thus, once purchased, the user must install or write their own software. As the user can choose which software to use, it can be better matched to their personal taste. It is very common for a PC-based GPS receiver to come bundled with a navigation software suite. Also, GPS modules are significantly cheaper than complete stand-alone systems (around €50 to €100). The software may include maps only for a particular region, or the entire world, if software such as Google Maps, Networks in Motion's AtlasBook mobile navigation platform, etc., are used.

Privacy Concern

Due to the popularity of GPS devices, privacy of the user becomes a subject of debate. This is because GPS devices can give geo-location

information of the user. This is considered as private information and nobody should violate private information without legal approval. However, there were several incidents where the privacy of GPS devices was questioned.

Advertisement

Since GPS devices can give the user's exact location, this helps advertising agents to give more relevant advertisement to the users based on their current location. The agencies might promote shops which are nearby to the users, rather than totally irrelevant shops. The advertising agency also will store the user's location for the agency's future uses. However, the regulatory agents all around the world (especially USA and Europe) start to consider whether geo-location data should be a sensitive data or not. If the data is sensitive data, the marketing team of an agency can not store geo-location of people since this amounts to a privacy violation. However, if the regulatory agents choose to consider geo-location as non-sensitive data, then private companies can have permission to store the user's location in their database.

Surveillance

Privacy concerns also arise when employers use GPS tracking units to track their employees' location, for example using vehicle tracking systems. This raises a major question about whether this violates personal privacy of employees. It raises a lot more concern for privacy violation if the employers collect geo-location data of their employee after work hours and during their holidays. In 2010, New York Civil Liberties Union filed a case against the Labor Department for firing Michael Cunningham after tracking Michael Cunningham's daily activity and locations using a GPS device that was attached to his car. This raises a few questions regarding the limit of surveillance. The worst privacy violation was committed by the FBI when they tracked down Antoine Jones's GPS devices, even without any search warrants. Later the Federal Appeal Court rejected the FBI's surveillance data as evidence against Antoine Jones.

Stalking

GPS devices are also used by private investigators in order to give more information to their clients. They will plant their own GPS devices in order to know more about their target. Moreover, some rental car services use the same technique to prevent their customers from going out of their targeted area. They charge additional fees for those who violate their rules. They get this information by using the car's GPS devices.

References

1. Parks, Garrett. "What is GPS". Retrieved February 26, 2014.
2. Motion X, Garmin, and Navigon GPS navigation software for smartphone
3. Example of hook-up of GPS-phone as wireless modem and GPS receiver
4. "GPS and Mobile Handsets - 4th edition" (PDF). Retrieved 2012-02-01.
5. Kevin J. O'Brien, New York Times, 2010 Nov 15 Smartphone Sales Taking Toll on G.P.S. Devices
6. Extended Prediction Orbit GPS data logger software
7. "List of laptop GPS navigation software programmes and reviews". Laptopgpsworld.com. 2008-07-27. Retrieved 2012-02-01.
8. GPS navigation software for Palm
9. GPSS for Pocket PC
10. "PCMCIA GPS adaptors". Web.archive.org. 2008-06-05. Retrieved 2012-02-01.
11. GPS ExpressCard with wireless modem.

Analysis of Hierarchies for Object Recognition Techniques

Neeraj Aggarwal

Research Scholar, Department of Computer/IT, CMJ University, Meghalaya

Every day we recognize a multitude of familiar and novel objects. We do this with little effort, despite the fact that these objects may vary somewhat in form, colour, texture, etc. Objects are recognized from many different vantage points (from the front, side, or back), in many different places, and in different sizes. Objects can even be recognized when they are partially obstructed from view.

While it may be obvious that people are capable of recognizing objects under many variations in conditions, it has been thought that pigeons may not possess the same range of capabilities. It has been proposed that pigeons act as "perceptrons," by analyzing simple features of objects and using those features to recognize objects. If the pigeon were a perceptron, then it would not be able to recognize an object that varied slightly in form or was seen from a novel viewpoint because the features would be altered. Moreover, a pigeon would be unable to discriminate between two objects that contained the same features, but with a different organization.

Object recognition is the ability to perceive an object's physical properties (such as shape, colour and texture) and apply semantic attributes to the object, which includes the understanding of its use, previous experience with the object and how it relates to others.

One model of object recognition, based on neuropsychological evidence, provides information that allows us to divide the process into four different stages.

Stage 1 Processing of basic object components, such as colour, depth, and form.

Stage 2 These basic components are then grouped on the basis of similarity, providing information on distinct edges to the visual form. Subsequently, figure-ground segregation is able to take place.

Stage 3 The visual representation is matched with structural descriptions in memory.

Stage 4 Semantic attributes are applied to the visual representation, providing meaning, and thereby recognition.

It should be noted that, within these stages, there are more specific processes that take place to complete the different processing components. In addition, other existing models propose integrative hierarchies (top-down and bottom-up), as well as parallel processing, as opposed to this general bottom-up hierarchy.

Visual recognition processing has been typically viewed as a bottom-up hierarchy in which information is processed sequentially with increasing complexities, where lower-level cortical processors, such as the primary visual cortex, are at the bottom of the processing hierarchy and higher-level cortical processors, such as the inferotemporal cortex (IT), are at the top, where recognition is facilitated. A most recognized bottom-up hierarchical theory is David Marr's theory of vision. In contrast, an increasingly popular recognition processing theory, is that of top-down processing. One model, proposed by Moshe Bar (2003), describes a "shortcut" method in which early visual inputs are sent, partially analyzed, from the early visual cortex to the prefrontal cortex (PFC). Possible interpretations of the crude visual input is generated in the PFC and then sent to the inferotemporal cortex (IT) subsequently activating relevant object representations which are then incorporated into the slower, bottom-up process. This "shortcut" is meant to minimize the amount of object representations required for matching thereby facilitating object recognition. Lesion studies have supported this proposal with findings of slower response times for individuals with PFC lesions, suggesting use of only the bottom-up processing.

A significant aspect of object recognition is that of object constancy: the ability to recognize an object across varying viewing conditions. These varying conditions include object orientation, lighting, and object variability (size, colour, and other within-category differences). For the visual system to achieve object constancy, it must be able to extract a commonality in the object description across different viewpoints and the retinal descriptions.

The Object Recognition module provides a way to identify specific trained objects within the current image. Once the module is trained with sample template images it will identify those objects within the current image depending on the filtered parameters of confidence, size, rotation, etc.

Serveral of the techniques will account for different object sizes, location and in plane rotation (roll) of the object aswell as variations in lighting and contrast. It will NOT account for significant rotation of the object in the X and Y (pan and tilt) directions. Should you need to identify

a 3D object in any orientation you will need to include template examples of each orientation.

Templates are created by including images into a folder that is used as the training samples for this module. Thus you can use any image editing application to edit and manage those templates as needed. Note, it is always best just to include the object to be identified without any background parts of the image. Only one folder at a time can be selected into a single object Recognition module. By changing the folder you change those objects that are to be identified. Note that you can also use more than one Object Recognition module within the pipeline.

It is recommended to use as large a template image as possible that will appear in the scene. One that encompasses as much of the image size as possible is best. This is because the Object Recognition module will only seek out objects from the template size down to a minimum of 1/3th the template size. Thus having the template contain the most amount of detail will provide the best results. If you specify too large an object then smaller versions of the objects may not be recognized as they may fall below the 30% size limit.

Several recognition methods are provided. As many objects/ environments differ in task the module provides various methods that can be switched between in order to determine the best technique for your use. Note that while you can switch between the techniques by selecting the appropriate radio button the module will NOT update the template database when you switch to that method. Thus if you add a new image and want to experiment with all techniques you will have to switch to each method and you MUST press the Train button in order to ensure that the template database is up-to-date.

Feature Points

This method will identify interesting points within the template using a modified fast Harris feature detector and match those points with those detected within the current image. The identified points are typically corner-like points that exhibit restraining forces in each direction (i.e. the highest edge signal in both X and Y directions will be maximal at the point's position). This helps to stabilize point choices in both the template and image such that most (but not all) points will be detected between the template and image. Once this correlation has been done the most likely template is then tested for at that location using a slower cross correlation technique. This technique is a good standard technique assuming there is enough internal texture within the object (think of a book cover) and is fast enough for most purposes.

Keep in mind that as this technique mainly uses corners as features motion blur will cause all those features to disappear and therefore not match correctly. Thus if you have a lot of motion blur within images you wish to match against you may need to decide on an alternative technique.

Objects to be detected MUST have internal texture as this module relies in inner feature points as the primary object identification technique. If you are interested in just the shape of an object the Shape Matching module will be of better use or the Shape method mentioned below.

This method will check for translation, scale and orientation.

Shape

The shape matching method is similar to the Shape Matching module but this method works on intensity images contrary to the Shape Matching module which uses binary (Black&White) images. The shape method will analyze the template and current image for correspondences in shape and determine which parts of the image best contain a particular template.

Due to its reliance on shape the shape matching method can determine any size and orientation (including X and Y location) of the template image within the current image in about the same time as the cross correlation method does just X and Y location. Its speed and flexibility make the shape matching method very useful when limited internal template texture is available. For example, labels, street signs, text, logos, fiducials, etc. are all ideal templates for the shape matching method as they consist of non-textured areas and rely on shape as their primary form of identification.

It is recommended to use templates that are as large as possible with regards to what may be seen in the current image. If small templates are used and matching to larger possible targets in the current image is attempted a mismatch will occur as more detail will be in the current image than what is contained within the template. Thus it is important to use a template by cropping the largest size seen of the template in any test or production images.

This method will check for translation, scale and orientation.

Haar

A very popular face recognition technique uses Haar like filters to determine a set of pixels comparisons that best represents the concept of a face. While this has its uses the Haar technique can also be applied to specific object recognition. In this scenario many high intensity versus low intensity checks are created that when run in sequence will identify a template with a high probability. These checks can be run across the image

very quickly and even adapt to size differences but they cannot be quickly rotated and thus are restricted to a single orientation.

Note that contrary to typical Haar training this method only requires ONE sample image to recognize the image and does NOT create a generic class based on that image. Thus if you want to recognize a class of objects you will need to include a couple images to best represent that class.

This method will check for translation and scale.

Cross Correlation

This method uses a well known and established technique for object recognition. The normalized cross correlation method has been widely used in many applications and can be one of the more stable techniques to use. The algorithm behind the cross correlation technique is, unfortunately, very CPU intensive and therefore should be used with care otherwise significant time may be spent on searching for objects within an image.

The cross correlation algorithm will use the template as saved in the trained folder and compare the template pixel by pixel at each pixel location within the current image. For example, if your template is 50x50 pixels large and your current image is 320x240 large this will mean there are approximately 2500x76800 = 192,000,000 pixel comparisons to make. This brute force method is entirely too slow for reasonable usage so tradeoffs between the size of the template versus the size of the image is made in order to speed up comparisons. While this does significantly speed up the algorithm some accuracy is forfeited as a result of that speed.

While normalized cross correlation does attempt to best deal with lighting changes between the template and the current image it is not performed within the image itself, thus while the template and current test image can be overall darker or lighter if a shadow is cast across the template that is not also within the current image the recognition process will fail.

To further reduce performance requirements the cross correlation method ONLY checks for templates of the same size AND orientation. Thus a template is only searched in the X and Y direction. If the current image contains the template at a different size it will NOT be recognized (but can still be tracked). If this is a requirement for your project and you decide to use cross correlation you will need to add the template in different sizes to the training folder. We recommend changing template sizes in increments of 10% which typically will provide adequate coverage.

If orientation is required you may attempt to use the Orient Image module prior to cross correlation which will help to specify a standard

orientation prior to matching. Note that you will need to add the 180deg rotated template within the training folder if you decide on this direction as the Orient Image will most likely have a 180deg symmetry and therefore not always align to the same 180 direction.

For comparisons that are image to image (meaning NO change in X or Y) the cross correlation technique can be one of the fastest. Thus if you goal is to find an image that exists within a known database without any size, orientation, horizontal or vertical shifts the cross correlation technique is a good technique to attempt.

In data mining, hierarchical clustering is a method of cluster analysis which seeks to build a hierarchy of clusters.

In order to decide which clusters should be combined (for agglomerative), or where a cluster should be split (for divisive), a measure of dissimilarity between sets of observations is required. In most methods of hierarchical clustering, this is achieved by use of an appropriate metric (a measure of distance between pairs of observations), and a linkage criterion which specifies the dissimilarity of sets as a function of the pair-wise distances of observations in the sets.

Most object detection tasks in computer vision are computationally expensive because of a) the large amount of input data that has to be processed and b) the use of complex classifiers that are robust against pose and illumination changes. Speeding-up the classification is therefore of major concern when developing systems for real-world applications. In the following we investigate two methods for speed-ups: feature reduction and hierarchical classification.

There are basically two types of feature selection methods in the literature: filter and wrapper methods. Filter methods are preprocessing steps performed independently of the classification algorithm or its error criteria; PCA is an example of a filter method. Wrapper methods attempt to search through the space of feature subsets using the criterion of the classification algorithm to select the optimal feature subset. Wrapper methods can provide more accurate solutions than filter methods, but in general are more computationally expensive. We present a new wrapper method to reduce the dimensions of both input and feature space of an SVM. An alternative approach for speeding-up SVM classification has been proposed in by reducing the number of support vectors.

Feature reduction is a generic tool that can be applied to any classification problem. When dealing with a specific classification task we can use prior knowledge about the type of data to speed-up classification. Two assumptions hold for most vision-based object detection

tasks: a) The vast majority of the analyzed patterns in an image belongs to the background class and b) most of the background patterns can be easily distinguished from the objects. Based on these two assumptions it is sensible to apply a hierarchy of classifiers. Fast classifiers remove large parts of the back-groundon the bottom and middle levels of the hierarchy and a more accurate but slower classifier performs the final detection on the top level. This idea falls into the framework of coarse-to-fine template matching and is also related to biologically motivated work on attention-based vision.

More recently a cascade of linear classifiers that have been trained using Ada Boost has been proposed in for frontal face detection. This idea is related to ours in the sense that it combines hierarchical classification with feature selection. However, in our approach the complexity of the classifiers in the hierarchy is not only controlled by the number of features (image resolution) but also by the class of decision functions (i.e. class of SVM kernel functions).

The bottom level of our hierarchy consists of a linear classifier that operates on low resolution patterns (9x9) while the top level consists of a non-linear classifier operating on higher resolution patterns (19x19).

References

1. Saaty, Thomas L.; Peniwati, Kirti (2008). *Group Decision Making: Drawing out and Reconciling Differences*. Pittsburgh, Pennsylvania: RWS Publications. ISBN 978-1-888603-08-8.
2. Saaty, Thomas L. (June 2008). "Relative Measurement and its Generalization in Decision Making: Why Pairwise Comparisons are Central in Mathematics for the Measurement of Intangible Factors – The Analytic Hierarchy/Network Process". *Review of the Royal Academy of Exact, Physical and Natural Sciences, Series A: Mathematics (RACSAM)* 102 (2): 251–318. doi:10.1007/bf03191825. Retrieved 2008-12-22.
3. Bhushan, Navneet; Kanwal Rai (January 2004). *Strategic Decision Making: Applying the Analytic Hierarchy Process*. London: Springer-Verlag. ISBN 1-85233-756-7.
4. Forman, Ernest H.; Saul I. Gass (July 2001). "The analytical hierarchy process—an exposition". *Operations Research* 49 (4): 469–487. doi:10.1287/opre.49.4.469.11231.
5. M. J. Swain and D. H. Ballard "Colour indexing", International Journal of Computer Vision, 7:1, 11-32, 1991.
6. B. Schiele and J. L. Crowley "Recognition without correspondence using multidimensional receptive field histograms", International Journal of Computer Vision, 36:1, 31-50, 2000
7. O. Linde and T. Lindeberg "Object recognition using composed receptive field histograms of higher dimensionality", Proc. International Conference on Pattern Recognition (ICPR'04), Cambridge, U.K. II:1-6, 2004.

Drugs and their Side Effects

Sayed Azeem Haider Abidi

Research Scholar, Department of Pharmecy,
Shri Venkateshwara University, Gajraula, UP

In medicine, a side effect is an effect, whether therapeutic or adverse, that is secondary to the one intended; although the term is predominantly employed to describe adverse effects, it can also apply to beneficial, but unintended, consequences of the use of a drug.

Occasionally, drugs are prescribed or procedures performed specifically for their side effects; in that case, said side effect ceases to be a side effect, and is now an intended effect. For instance, X-rays were historically (and are currently) used as an imaging technique; the discovery of their oncolytic capability led to their employ in radiotherapy (ablation of malignant tumours).

If it results from an unsuitable or incorrect dosage or procedure, this is called a medical error and not a complication. Adverse effects are sometimes referred to as "iatrogenic" because they are generated by a physician/treatment. Some adverse effects only occur only when starting, increasing or discontinuing a treatment.

Using a drug or other medical intervention which is contraindicated may increase the risk of adverse effects. Adverse effects may cause complications of a disease or procedure and negatively affect its prognosis. They may also lead to non-compliance with a treatment regimen.

The harmful outcome is usually indicated by some result such as morbidity, mortality, alteration in body weight, levels of enzymes, loss of function, or as a pathological change detected at the microscopic, macroscopic or physiological level. It may also be indicated by symptoms reported by a patient. Adverse effects may cause a reversible or irreversible change, including an increase or decrease in the susceptibility of the individual to other chemicals, foods, or procedures, such as drug interactions.

Classification

In terms of drugs, adverse events may be defined as: "Any untoward medical occurrence in a patient or clinical investigation subject administered a pharmaceutical product and which does not necessarily have to have a causal relationship with this treatment."

In clinical trials, a distinction is made between adverse events and serious adverse events. Generally, any event which causes death, permanent damage, birth defects, or requires hospitalization is considered an SAE. The results of these trials are often included in the labelling of the medication to provide information both for patients and the prescribing physicians.

The term "life-threatening" in the definition of "serious" refers to an event in which the patient was at risk of death at the time of the event; it does not refer to an event which hypothetically might have caused death if it were more severe.

Reporting Systems

In many countries, adverse effects are required by law to be reported, researched in clinical trials and included into the patient information accompanying medical devices and drugs for sale to the public. Investigators in human clinical trials are obligated to report these events in clinical study reports. Research suggests that these events are often inadequately reported in publicly available reports. Because of the lack of these data and uncertainty about methods for synthesising them, individuals conducting systematic reviews and meta-analyses of therapeutic interventions often unknowingly overemphasise health benefit. To balance the overemphasis on benefit, scholars have called for more complete reporting of harm from clinical trials.

United Kingdom

The Yellow Card Scheme is a United Kingdom initiative run by the Medicines and Healthcare products Regulatory Agency (MHRA) and the Commission on Human Medicines (CHM) to gather information on adverse effects to medicines. This includes all licensed medicines, from medicines issued on prescription to medicines bought over the counter from a supermarket. The scheme also includes all herbal supplements and unlicensed medicines found in cosmetic treatments. Adverse drug reactions (ADRs) can be reported by a number of health care professionals including physicians, pharmacists and nurses, as well as patients.

United States

In the United States several reporting systems have been built, such as the Vaccine Adverse Event Reporting System (VAERS), the Manufacturer and User Facility Device Experience Database (MAUDE) and the Special Nutritionals Adverse Event Monitoring System. MedWatch is the main reporting center, operated by the Food and Drug Administration.

Australia

In Australia, adverse effect reporting is administered by the Adverse Drug Reactions Advisory Committee (ADRAC), a subcommittee of the Australian Drug Evaluation Committee (ADEC). Reporting is voluntary, and ADRAC requests healthcare professionals to report all adverse reactions to its current drugs of interest, and serious adverse reactions to any drug. ADRAC publishes the Australian Adverse Drug Reactions Bulletin every two months.The Government's Quality Use of Medicines programme is tasked with acting on this reporting to reduce and minimize the number of preventable adverse effects each year.

New Zealand

Adverse reaction reporting is an important component of New Zealand's pharmacovigilance activities. The Centre for Adverse Reactions Monitoring (CARM) in Dunedin is New Zealand's national monitoring centre for adverse reactions. It collects and evaluates spontaneous reports of adverse reactions to medicines, vaccines, herbal products and dietary supplements from health professionals in New Zealand. Currently the CARM database holds over 80,000 reports and provides New Zealand-specific information on adverse reactions to these products, and serves to support clinical decision making when unusual symptoms are thought to be therapy related

Canada

In Canada, adverse reaction reporting is an important component of the surveillance of marketed health products conducted by the Health Products and Food Branch (HPFB) of Health Canada. Within HPFB, the Marketed Health Products Directorate leads the coordination and implementation of consistent monitoring practices with regards to assessment of signals and safety trends, and risk communications concerning regulated marketed health products.

MHPD also works closely with international organizations to facilitate the sharing of information. Adverse reaction reporting is mandatory for the industry and voluntary for consumers and health professionals.

Limitations

In principle, medical professionals are required to report all adverse effects related to a specific form of therapy. In practice, it is at the discretion of the professional to determine whether a medical event is at all related to the therapy. For example, a leg fracture in a skiing accident in a patient who years before took antibiotics for pneumonia is not likely to get reported.

As a result, routine adverse effects reporting often may not include long-term and subtle effects that may ultimately be attributed to a therapy.

Part of the difficulty is identifying the source of a complaint. A headache in a patient taking medication for influenza may be caused by the underlying disease or may be an adverse effect of the treatment. In patients with end-stage cancer, death is a very likely outcome and whether the drug is the cause or a bystander is often difficult to discern.

Adverse Effects by Situation

Adverse Effects of Medical Procedures

Surgery may have a number of undesirable or harmful effects, such as infection, hemorrhage, inflammation, scarring, loss of function, or changes in local blood flow. They can be reversible or irreversible, and a compromise must be found by the physician and the patient between the beneficial or life-saving consequences of surgery versus its adverse effects. For example, a limb may be lost to amputation in case of untreatable gangrene, but the patient's life is saved. Presently, one of the greatest advantages of minimally invasive surgery, such as laparoscopic surgery, is the reduction of adverse effects.

Other nonsurgical physical procedures, such as high-intensity radiation therapy, may cause burns and alterations in the skin. In general, these therapies try to avoid damage to healthy tissues while maximizing the therapeutic effect.

Vaccination may have adverse effects due to the nature of its biological preparation, sometimes using attenuated pathogens and toxins. Common adverse effects may be fever, malaise and local reactions in the vaccination site. Very rarely, there is a serious adverse effect, such as eczema vaccinatum, a severe, sometimes fatal complication which may result in persons who have eczema or atopic dermatitis.

Diagnostic procedures may also have adverse effects, depending much on whether they are invasive, minimally invasive or noninvasive. For example, allergic reactions to radiocontrast materials often occur, and a colonoscopy may cause the perforation of the intestinal wall.

Adverse Effects of Drugs

Adverse effects can occur as a collateral or side effect of many interventions, but they are particularly important in pharmacology, due to its wider, and sometimes uncontrollable, use by way of self-medication. Thus, responsible drug use becomes an important issue here. Adverse

effects, like therapeutic effects of drugs, are a function of dosage or drug levels at the target organs, so they may be avoided or decreased by means of careful and precise pharmacokinetics, the change of drug levels in the organism in function of time after administration.

Adverse effects may also be caused by drug interaction. This often occurs when patients fail to inform their physician and pharmacist of all the medications they are taking, including herbal and dietary supplements. The new medication may interact agonistically or antagonistically (potentiate or decrease the intended therapeutic effect), causing significant morbidity and mortality around the world. Drug-drug and food-drug interactions may occur, and so-called "natural drugs" used in alternative medicine can have dangerous adverse effects. For example, extracts of St John's wort (*Hypericum perforatum*), a phytotherapic used for treating mild depression are known to cause an increase in the cytochrome P450 enzymes responsible for the metabolism and elimination of many drugs, so patients taking it are likely to experience a reduction in blood levels of drugs they are taking for other purposes, such as cancer chemotherapeutic drugs, protease inhibitors for HIV and hormonal contraceptives.

The scientific field of activity associated with drug safety is increasingly government-regulated, and is of major concern for the public, as well as to drug manufacturers. The distinction between adverse and nonadverse effects is a major undertaking when a new drug is developed and tested before marketing it. This is done in toxicity studies to determine the nonadverse effect level (NOAEL). These studies are used to define the dosage to be used in human testing (phase I), as well as to calculate the maximum admissible daily intake. Imperfections in clinical trials, such as insufficient number of patients or short duration, sometimes lead to public health disasters, such as those of fenfluramine (the so-called fen-phen episode), thalidomide and, more recently, of cerivastatin (Baycol, Lipobay) and rofecoxib (Vioxx), where drastic adverse effects were observed, such as teratogenesis, pulmonary hypertension, stroke, heart disease, neuropathy, and a significant number of deaths, causing the forced or voluntary withdrawal of the drug from the market.

Most drugs have a large list of nonsevere or mild adverse effects which do not rule out continued usage. These effects, which have a widely variable incidence according to individual sensitivity, include nausea, dizziness, diarrhea, malaise, vomiting, headache, dermatitis, dry mouth, etc. These can be considered a form of pseudo-allergic reaction, as not all users experience these effects; many users experience none at all.

Drugs contain side effects which is the reason why commercials or advertisements put many disclaimers about the unwanted symptoms after taking the drug(s).

Examples of adverse effects associated with specific medications

- Abortion, miscarriage or uterine hemorrhage associated with misoprostol (Cytotec), a labor-inducing drug (this is a case where the adverse effect has been used legally and illegally for performing abortions)
- Addiction to many sedatives and analgesics, such as diazepam, morphine, etc.
- Birth defects associated with thalidomide
- Bleeding of the intestine associated with aspirin therapy
- Cardiovascular disease associated with COX-2 inhibitors (i.e. Vioxx)
- Deafness and kidney failure associated with gentamicin (an antibiotic)
- Death, following sedation, in children using propofol (Diprivan)
- Depression or hepatic injury caused by interferon
- Diabetes caused by atypical antipsychotic medications (neuroleptic psychiatric drugs)
- Diarrhea caused by the use of orlistat (Xenical)
- Erectile dysfunction associated with many drugs, such as antidepressants
- Fever associated with vaccination
- Glaucoma associated with corticosteroid-based eye drops
- Hair loss and anemia may be caused by chemotherapy against cancer, leukemia, etc.
- Headache following spinal anaesthesia
- Hypertension in ephedrine users, which prompted FDA to remove the dietary supplement status of ephedra extracts
- Insomnia caused by stimulants, methylphenidate (Ritalin), Adderall, etc.
- Lactic acidosis associated with the use of stavudine (Zerit, for HIV therapy) or metformin (for diabetes)
- Mania caused by corticosteroids
- Liver damage from paracetamol

- Melasma and thrombosis associated with use of estrogen-containing hormonal contraception, such as the combined oral contraceptive pill
- Priapism associaded with the use of sildenafil
- Rhabdomyolysis associated with statins (anticholesterol drugs)
- Seizures caused by withdrawal from benzodiazepines
- Drowsiness or increase in appetite due to antihistamine use. Some antihistamines are used in sleep aids explicitly because they cause drowsiness.
- Stroke or heart attack associated with sildenafil (Viagra), when used with nitroglycerin
- Suicide, increased tendency associated to the use of fluoxetine and other selective serotonin reuptake inhibitor (SSRI) antidepressants
- Tardive dyskinesia associated with long-term use of metoclopramide and many antipsychotic medications

Controversies

Sometimes, putative medical adverse effects are regarded as controversial and generate heated discussions in society and lawsuits against drug manufacturers. One example is the recent controversy as to whether autism was linked to the MMR vaccine (or by thiomersal, a mercury-based preservative used in some vaccines). No link has been found in several large studies, and despite removal of thimerosal from vaccines a decade ago the rate of autism has not decreased as would be expected if it had been the causative agent.

Another instance is the potential adverse effects of silicone breast implants, which led to hundreds of thousands of litigations against manufacturers of gel-based implants, due to allegations of damage to the immune system which have not yet been conclusively proven.

Due to the exceedingly high impact on public health of widely used medications, such as hormonal contraception and hormone replacement therapy, which may affect millions of users, even marginal probabilities of adverse effects of a severe nature, such as breast cancer, have led to public outcry and changes in medical therapy, although its benefits largely surpassed the statistical risks.

References

1. Expert Working Group (Efficacy) of the International Conference on Harmonisation of Technical Requirements for Registration of Pharmaceuticals for Human Use (ICH). (August 25, 2007). "Guideline for Industry - Clinical safety data management:

definitions and standards for expedited reporting." (PDF). FDA Center for Drug Evaluation and Research.

2. Expert working group (efficacy) of the international conference on harmonization of technical requirements for registration of pharmaceuticals for human use. (August 25, 2007). "Guideline for Industry Structure and Content of Clinical Study Reports." (PDF). FDA Center for Drug Evaluation and Research.
3. Ioannidis JP, Lau J. (2001). "Completeness of safety reporting in randomized trials: an evaluation of 7 medical areas.". *JAMA* 285 (4): 437–43. doi:10.1001/jama.285.4.437. PMID 11242428.
4. Chou R, Helfand M. (2005). "Challenges in systematic reviews that assess treatment harms.". *Ann Intern Med* 142 (12 Pt 2): 1090–0. doi:10.7326/0003-4819-142-12_part_2-200506211-00009. PMID 15968034.
5. Ioannidis JP, Evans SJ, Gøtzsche PC, O'Neill RT, Altman DG, Schulz K, Moher D; CONSORT Group. (2004). "Better reporting of harms in randomized trials: an extension of the CONSORT statement.". *Ann Intern Med* 141 (10): 781–8. PMID 15545678.
6. "Mifepristone and Misoprostol for Abortion". *WebMD*. Retrieved March 20, 2013.
7. "Morphine Addiction Withdrawal Symptoms and Treatment". *rehabinfo*. Retrieved March 20, 2013.
8. "Even Low Dose of Aspirin Can Cause Intestinal Bleeding". *WebMD News*. November 9, 2000. Retrieved March 20, 2013.
9. "Coronary Heart Disease". *Weitz & Luxenberg P.C*. Retrieved March 20, 2013.
10. "The Antibiotic Gentamycin Can Cause Hearing Loss, Deafness, and "Wobblers"". *The Beasley Firm LLC*. Retrieved March 20, 2013.
11. "Kidney Damage". *Gentamicin Information Center*.
12. Boseley, Sarah (2006-06-17). "Drugs firm blocks cheap blindness cure". *The Guardian* (London). Retrieved 2010-05-20.

Study on Electroosmotic Fluids in Nanofluidic Channels

Indu Kumari

Dept. of Mathematics, V.K.U.Ara

Dr. Ujjwal Kanti Ghoshal

Asst. Professor, Dept. of Math,S.P. Jian College ,Sasaram

Abstract

We report the measurement of electroosmotic mobilities in nanofluidic channels with rectangular cross sections and compare our results with theory. Nanofluidic channels were milled directly into borosilicate glass between two closely spaced microchannels with a focused ion beam instrument, and the nanochannels had half-depths (h) of 27, 54, and 108 nm and the same half-width of 265 nm. We measured electroosmotic mobilities in NaCl solutions from 0.1 to 500 mM that have Debye lengths $\left(\kappa^{-1}\right)$ from 30 to 0.4 nm, respectively. The experimental electroosmotic mobilities compare quantitatively to mobilities calculated from a nonlinear solution of the Poisson–Boltzmann equation for channels with a parallel-plate geometry. For the calculations, ζ-potentials measured in a microchannel with a half-depth of 2.5 μm are used and range from –6 to –73 mV for 500 to 0.1 mM NaCl, respectively. For $\kappa h > 50$, the Smoluchowski equation accurately predicts electroosmotic mobilities in the nanochannels. However, for $\kappa h < 10$, the electrical double layer extends into the nanochannels, and due to confinement within the channels, the average electroosmotic mobilities decrease. At $\kappa h \approx 4$, the electroosmotic mobilities in the 27, 54, and 108 nm channels exhibit maxima, and at 0.1 mM NaCl, the electroosmotic mobility in the 27 nm channel $(\kappa h = 1)$ is 5-fold lower than the electroosmotic mobility in the 2.5 μm channel $(\kappa h = 100)$.

Nanofluidic devices have received considerable attention due to their unique ion and fluid transport properties and applications in chemical analysis. Small lateral dimensions, surface charge, and geometric asymmetry contribute to many of these interesting transport phenomena. Nanochannel devices exhibit concentration polarization and are able to concentrate small molecules and peptides and proteins at the nanochannel and microchannel interface. Electrokinetically mediated transport through nanoporous membranes can be used to create chemical gradients, concentrate mass-limited samples, and stack samples across microfluidic

layers separated by a membrane. When the nanoscale conduit has a geometric asymmetry, ion current rectification occurs in quartz nanopipettes, track-etched polymer membranes, silicon-based nanochannels, and nanoscale funnels. Conical nanopores can electrokinetically trap and concentrate particles due to the high electric field strength at the tips of the pores. Within nanochannel devices, enhanced channel conductance and reduced electrokinetic mobilities of small molecules and DNA are observed. Nanochannel devices are also used for resistive-pulse sensing of single molecules, ion current rectification-based sensing, and separations based on entropic sieving, liquid chromatography, electrophoresis, and continuous-flow Ogston and entropic sieving.

Nanofluidic devices with in-plane nanochannels have been fabricated in a variety of materials by techniques such as wet chemical etching, double thermal oxidation and wet chemical etching, sacrificial layer deposition, nanoimprint lithography, focused ion beam (FIB) milling, electron-beam (e-beam) lithography with reactive-ion etching, and e-beam lithography and polymer replication. Fabrication techniques, such as e-beam lithography and FIB milling, are able to create channels confined to nanometer dimensions in both lateral dimensions, e.g., width and depth, and to generate any two-dimensional channel pattern on the substrate surface. FIB milling has the added advantage to directly mill channels with three-dimensional topography during a single fabrication step. We milled the nanofluidic channels directly into borosilicate glass with an FIB instrument, which uses an electron flood gun to minimize surface charge generated by the ion beam. Use of the electron flood gun circumvented the need for a conductive film, e.g., metal, on the glass surface to dissipate charge buildup.

In particular, we are interested in electroosmotic flow in nanochannels when κh is small, where ê is the Debye–Hückel parameter and h is the channel half-depth. Electroosmotic mobility decreases as the channel dimension (e.g., h) becomes small, the Debye length $\left(\kappa^{-1}\right)$ becomes large, or both. As the double layer extends into the channel, the profile for electroosmotic flow goes from having a uniform velocity profile to a nonuniform profile with a reduced average velocity. As κh approaches 1, double layer overlap occurs, the flow profile becomes parabolic, and electroosmotic mobility reaches a minimum for a given Debye length. This theory was extended to include an analytical solution for a cylindrical capillary and parallel-plate channel.

Subsequent work about electroosmotic flow in nanochannels is mostly theoretical. Numerical simulations of electrokinetically driven fluids

address the influence of channel dimensions, double layer thickness and electrostatic potential distribution, surface potential, and ion valence on electroosmotic flow. Similar to early work, finite element analysis predicts the reduction of electroosmotic velocities when there is double layer overlap in the channel. Simulations also study the validity of common approximations, in particular, the linear solution of the Poisson–Boltzmann equation to calculate potential distributions when the surface potential is relatively high or the electrostatic potential in the center of the channel is zero. Two-dimensional flow profiles are generated for cases in which there is significant double layer overlap in nanochannels to account for sidewall effects. Reduction of electroosmotic velocity due to the double layer extending into the nanochannel is observed experimentally at low buffer concentrations in high aspect ratio channels. Also, electroosmotic flow is measured in nanochannels with no double layer overlap by a current-monitoring technique.

We measured the average electroosmotic mobilities and ionic conductivities in channels with half-depths of 27 nm, 54 nm, 108 nm, and 2.5 ìm for NaCl concentrations from 0.1 to 500 mM. From these micro- and nanochannels measurements, specific surface charge, zeta (ζ) potentials, and electroosmotic mobilities are extracted directly from the experimental data. The experimental electroosmotic mobilities compare quantitatively to mobilities calculated from a nonlinear solution of the Poisson–Boltzmann equation for channels with a parallel-plate geometry. For the calculations, ζ-potentials measured in the 2.5 μm channel are used and range from –6 to –73 mV for 500 to 0.1 mM NaCl, respectively. For $\kappa h > 50$, electroosmotic mobilities in the nanochannels are accurately predicted by the Smoluchowski equation. However, for $\kappa h < 10$, the electrical double layer extends into the nanochannels, and due to confinement in the channels, average electroosmotic mobilities decrease. At $\kappa h \approx 4$, electroosmotic mobilities in the 27, 54, and 108 nm channels exhibit maxima, and at 0.1 mM NaCl, the electroosmotic mobility in the 27 nm channel $(\kappa h = 1)$ is 5-fold lower than the electroosmotic mobility in the 2.5 μm channel $(\kappa h = 100)$.

Experimental Section

Materials

We purchased chromium etchants 1020 and 8002-A and buffered oxide etchant (BOE) from Transene Co.; Microposit MF 319 developer from MicroChem Corp.; D263 glass substrates with a 530 nm thick layer of photoresist and a 120 nm thick layer of chromium from Telic Co.; No. 1.5 cover glass from VWR; rhodamine B and disodium fluorescein from

Sigma-Aldrich Co.; NaCl and NaOH from Mallinckrodt, Inc.; methanol from EMD Millipore, Inc.; and 353NDT Epoxy from Epoxy Technology, Inc.

Microchannel Fabrication

We fabricated microfluidic devices with and without integrated nanochannels. For the devices with nanochannels, two V-shaped microchannels were fabricated in a glass substrate by conventional photolithography and wet chemical etching, and the nanochannel was milled into the substrate to bridge the gap between the two microchannels (Figure 1). The V-shaped microchannel design was transferred into the photoresist layer by UV exposure (200 mJ/cm^2) through a photomask (HTA Photomask). After development of the photoresist, the chromium layer was etched with chromium etchant 8002-A, and the microchannels were etched into the glass substrate with BOE. The microchannels were measured with a stylus-based profiler (Dektak 6M, Veeco Instruments, Inc.) and had a half-depth of 2.55 ± 0.2 μm and a width of 31 ± 2 μm. Holes were sandblasted into the backside of the substrate for fluid and electrical access at the ends of the microchannels. Remaining photoresist and chromium were then removed with acetone and chromium etchant 1020, respectively, and the glass surfaces were cleaned in an ammonium hydroxide, hydrogen peroxide, and water solution (2:1:2), rinsed with water, and dried before FIB milling as described below. For microfluidic devices without nanochannels, microchannels with a cross pattern were fabricated by the same process as above. The cross-shaped microchannels had a half-depth of 2.52 ± 0.2 μm and a width of 42 ± 2 μm.

Figure 1

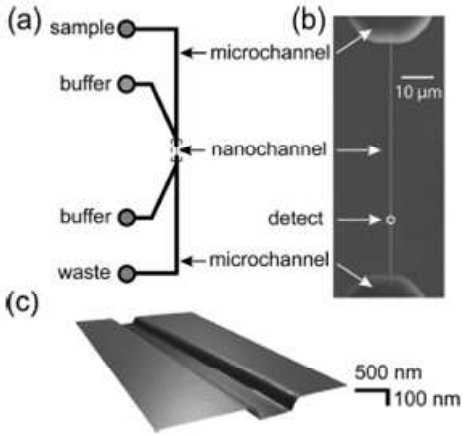

Figure 1. (a) Schematic of a nanochannel device used for electroosmotic mobility and conductivity measurements. Two V-shaped microchannels

(represented by thick black lines) are bridged by a nanochannel milled with a focused ion beam (FIB) instrument. (b) Scanning electron microscope (SEM) image of an FIB-milled nanochannel with a half-depth of 54 nm, half-width of 265 nm, and length of 76 μm that bridges two microchannels etched into the glass substrate. Arrival of rhodamine B dye is detected 60 μm from the top micro- and nanochannel junction at the "detect" location. (c) Atomic force microscope (AFM) image of a nanochannel with a half-depth of 54 nm and half-width of 265 nm.

Nanochannel Fabrication

Nanochannels were milled between the two V-shaped microchannels with a dual-beam FIB instrument (AURIGA 60, Carl Zeiss, Inc.). Nanochannels with a rectangular design were created in the NanoPatterning and Visualization Engine (FIBICS Corp.), and a 30 kV gallium ion beam at 50 pA milled the pattern directly into the glass while an electron flood gun bathed the substrate surface with electrons to compensate for charge buildup. After FIB milling, the nanochannels were characterized with the scanning electron microscope (SEM) on the FIB instrument and an atomic force microscope (AFM; MFP-3D, Asylum Research) to determine the nanochannel dimensions. All of the nanochannels had a length of 76 ± 2 μm (i.e., the distance between the two V-shaped microchannels) and half-widths of 265 ± 10 nm. We fabricated three nanochannel devices with half-depths of 27 ± 2 nm, four nanochannel devices with half-depths of 54 ± 3 nm, and two nanochannel devices with half-depths of 108 ± 5 nm.

Device Bonding

Substrates with and without integrated nanochannels and No. 1.5 cover glass were soaked in 1 M NaOH at 60 °C for 20 min, sonicated in water for 10 min, rinsed with water, and brought into contact with each other while wet. The bonded devices were dried in an oven at 90 °C overnight and annealed in a furnace at 545 °C for 12 h. Glass reservoirs (6 mm o.d. × 4 mm i.d. × 6 mm tall) were attached over the sandblasted holes with epoxy to hold the solutions and make electrical connections to the micro- and nanochannels.

Nanochannel Conditioning

After bonding, micro- and nanochannels in the devices were sequentially rinsed with methanol, 1:1 methanol in water, water, 1 M NaOH, and water. Solutions were drawn through the channels with vacuum for 15 min each. Devices filled with water were stored for at least 4 days before measurements were made to ensure reproducible electroosmotic flow. Electroosmotic flow increased slightly from days 1

to 3, but by day 4, no significant change in electroosmotic mobility was observed. The change in mobility is presumably due to the dissolution of Ga ions at the glass surface that were deposited during the FIB milling process.

Conductivity Measurements

Channel conductivities for each device were measured with a picoammeter/voltage source (6487 Keithley Instruments, Inc.). Silver–silver chloride electrodes were prepared by sanding a 10 mm section of a 2 mm diameter piece of silver wire and immersing this section of wire in an $FeCl_3$ chloridizing solution overnight. The chloridized sections of the electrodes were placed in the solution-filled reservoirs, and the nonchloridized sections were wired to the voltage source. With 1 V applied through silver–silver chloride electrodes, the current was measured between each pair of reservoirs on a device, and channel conductance was calculated from the average current for each micro- and nanochannel by a least-squares method. Channel conductivities were then calculated with the channel length and cross-sectional area. We tested NaCl solutions of 0.1, 1, 10, 100, 500, and 1000 mM (pH 5.1–5.5). Channel conductivities were measured on three 27 nm channels, four 54 nm channels, two 108 nm channels, and two 2.5 μm channels. The bulk conductivity of each solution was measured with a standard conductivity meter (1026, VWR, Inc.).

Electroosmotic Flow Measurements

In the nanochannel devices, we measured the electroosmotic velocity by monitoring the arrival time of a zwitterionic dye (rhodamine B) at a location 60 μm from the micro- and nanochannel junction (the location labeled "detect" in Figure 1b). The arrival time of the rhodamine B was monitored on an inverted optical microscope (IX71, Olympus, Inc.), and a green helium–neon laser focused to a spot with a 60× objective at the detection location was used to excite the dye. The fluorescence was collected by the objective, spectrally filtered with the bandpass filter in the TRITC filter cube (U-N41002, Olympus, Inc.), spatially filtered with a 100 μm pinhole, detected with a photomultiplier tube (H5783-01, Hamamatsu Photonics), amplified (SR570, Stanford Research Systems, Inc.), and recorded through a multifunction data acquisition card (PCI-6032, National Instruments Corp.) with a LabVIEW program (National Instruments Corp.).

A positive potential (0.3–5.2 V) from an analog output card (PCI-6713, National Instruments Corp.) controlled through the LabVIEW program was applied through a silver–silver chloride electrode to the sample

reservoir (see Figure 1a), and a silver–silver chloride electrode inserted into the waste reservoir was held at ground. For each set of measurements, the NaCl concentration was stepped from lowest (0.1 mM) to highest (500 mM), and the field strength was stepped from lowest (50 V/cm) to highest (250 V/cm). The arrival time distribution of the dye front in nanochannels was fitted with a sigmoidal curve, and the arrival time corresponded to the half-height of the curve. Arrival times of the rhodamine B solution at the detection point ranged from 70 ms to 1.40 s for the low-salt concentrations at high field strengths and the high-salt concentrations at low field strengths, respectively. The time for rhodamine B to diffuse 60 ìm is estimated to be ~4 s and did not impact the electroosmotic flow measurements.

To measure the electroosmotic mobility on the cross-shaped microchannel device, we used a pinched injection and monitored the arrival time of rhodamine B 4 mm downstream from the cross intersection. Potentials were applied to the reservoirs with a high-voltage power supply controlled by a LabVIEW program. For measurements made in both the nanochannel and microchannel devices, the electroosmotic mobility was calculated from a linear fit of electroosmotic velocity versus field strength. Similar to the conductivity measurements, electroosmotic mobilities were measured in three 27 nm channels, four 54 nm channels, two 108 nm channels, and two 2.5 μm channels. To check for concentration polarization, disodium fluorescein (10 μm) was added to the NaCl solutions and drawn into devices with the 27 nm channel for 15 min by vacuum. Potentials of 1 and 10 V, corresponding to field strengths of 120 and 1200 V/cm in the nanochannels, respectively, were applied, and the microchannel and nanochannel junctions were visualized on the inverted IX71 microscope by wide-field epifluorescence.

Results and Discussion

Nanochannel Fabrication

Rectangular nanochannels were fabricated in the gap between two closely spaced V-shaped microchannels (see Figure 1). The microchannels were fabricated by standard photolithography and wet chemical etching, and the nanochannels were milled into the glass substrate between the microchannels with a focused ion beam. We used an electron flood gun to minimize charge buildup at the substrate surface caused by the ion beam. Each of the milled nanochannels had a length of 76 ± 2 μm and width ($2w$) of 530 ± 10 nm, but had depths ($2h$) of 54 ± 4, 108 ± 6, or 216 ± 10 nm. We used an SEM to measure the nanochannel width and an AFM to determine the nanochannel depth. To facilitate comparison to theory, we refer to the channels by their half-depths (h) of 27, 54, and 108 nm. SEM

and AFM images of a nanochannel with a 54 nm half-depth are shown in Figure 1b,c.

Channel Conductivity

We measured the ionic conductivities in the nanochannels with half-depths of 27, 54, and 108 nm for NaCl solutions from 0.1 to 1000 mM and compared their conductivities with the conductivities of the bulk solutions and a microchannel with a half-depth of 2.5 μm. At a fixed potential of 1 V, currents in the micro- and nanochannels were measured, and channel conductance is calculated from these current measurements recorded for each reservoir pair. Channel conductivities are then calculated from the channel conductance and measured channel lengths and cross-sectional areas of the micro- and nanochannels.

Figure 2 shows the variation of the channel conductivity with NaCl concentration and bulk solution conductivity. As expected, at high salt concentrations, the nanochannel conductivities match the bulk solution conductivities. However, at low salt concentrations, the nanochannel conductivities deviate from linearity and are significantly higher than the conductivities in the microchannel and bulk solution. The deviation increases as the channel half-depth decreases, i.e., the shallowest nanochannel (h = 27 nm) has the highest conductivities for NaCl concentrations of 0.1, 1, and 10 mM. Deviation from linearity occurs because a significant portion of the current is carried through the nanochannel by surface charge. As the surface-to-volume ratio of the channel increases, surface charge contributes a much greater fraction of current transported, which results in higher channel conductivities.

Figure 2

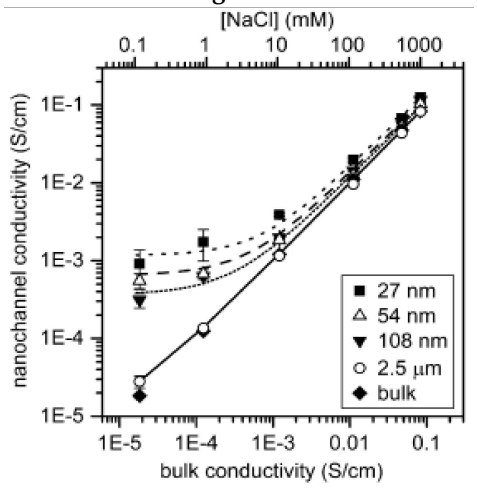

Figure 2. Variation of channel conductivity with bulk conductivity and NaCl concentration. Channel half-depths (h) are 27 nm, 54 nm, 108 nm, and 2.5 μm. Lines for each channel half-depth are calculated with eq 1 from the specific surface conductivities, bulk conductivities, and channel dimensions. Measurements were made on three devices with h = 27 nm, four devices with h = 54 nm, and two devices with h = 108 nm and 2.5 ìm. Error bars are $\pm \sigma$.

The experimental channel conductivities are in excellent agreement with the model presented by Hunter adapted to a channel with a rectangular cross-section. Equation 1 shows the channel conductivity,

$$\sigma_c = \sigma_b + \lambda_s\left(\frac{1}{h} + \frac{1}{w}\right) \qquad (1)$$

where σ_b is the bulk solution conductivity, λ_s is the specific surface conductivity, and w is the channel half-width. λ_s is calculated from eq 1 with an average of three conductivity measurements from each channel dimension at each salt concentration. Figure 3 shows the average λ_s for all channel depths, which ranged from 2.15 to 137 nS for NaCl concentrations of 0.1 to 1000 mM, respectively. When the channel cross-section is large, i.e., h and w are large, the second term of eq 1 for the contribution of the surface charge goes to zero, and the channel conductivity matches the bulk conductivity. However, when h and w are small, the second term becomes significant, and the channel conductivity is greater than the bulk conductivity. Equation 1 is used to calculate the channel conductivities from the specific surface conductivities, bulk conductivities, and channel dimensions for each channel half-depth, and the predicted values (lines in Figure 2) match the experimental data for all channel dimensions across all concentrations.

Figure 3

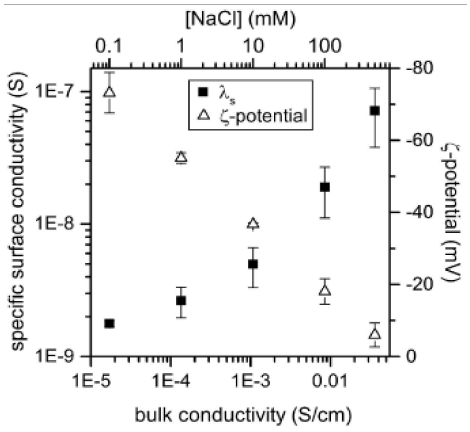

Figure 3. Variation of specific surface conductivity (λ_s) and zeta potential (ζ-potential) with bulk conductivity and NaCl concentration. The specific surface conductivities are an average for all nanochannel and microchannel devices and were measured on three devices with h = 27 nm, four devices with h = 54 nm, and two devices with h = 108 nm and 2.5 ìm. ζ-potentials were measured on two devices with h = 2.5 μm. Error bars are $\pm \sigma$.

Electroosmotic Mobility

The electroosmotic velocity was measured in the channels with h = 27 nm, 54 nm, 108 nm, and 2.5 μm. The zwitterionic dye, rhodamine B, was added to NaCl solutions of 0.1 to 500 mM and detected by laser-induced fluorescence. For the nanochannel devices, a front of the rhodamine B solution was introduced into the nanochannel, and the arrival time of the dye was detected 60 μm from the top micro- and nanochannel junction (the location labeled "detect" in Figure 1b).

For the microchannel devices, a pinched injection was used to introduce a plug of rhodamine B solution, and the arrival time of the rhodamine B plug was detected 4 mm downstream from the cross intersection. Over the range of electric field strengths used (50–250 V/cm), the electroosmotic velocity was linear with field strength for all NaCl concentrations. The slopes of the lines fitted to the velocity versus field strength data are the electroosmotic mobilities in the micro- and nanochannels. For the linear fits, $R^2 > 0.999$ for the experiments with the 0.1–100 mM NaCl solutions, and $R^2 > 0.998$ for the experiments with the 500 mM NaCl solution.

To evaluate whether concentration polarization might impact the conductivity and electroosmotic flow measurements, we imaged the transport of fluorescein through the nanochannels with applied potentials of 1 and 10 V, and enrichment or depletion of the fluorescein at the entrance or exit of the nanochannel was not observed. Although some concentration polarization may occur, the time scale for each electroosmotic flow measurement was relatively short, e.g., 1–5 s in duration, because the polarity of the power supply was switched frequently to move rhodamine B into the nanochannel and clear the dye from the nanochannel for the next measurement. In addition, the channel conductivities and electroosmotic mobilities in the nanochannels are consistent with values measured in the microchannels, for which concentration polarization is negligible.

Figure 4

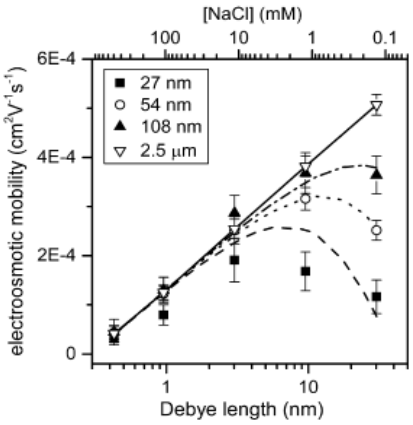

Figure 4. Variation of average electroosmotic mobility (μ_{eo}) with Debye length (κ^{-1}) for channel half-depths (h) of 27 nm, 54 nm, 108 nm, and 2.5 ìm and NaCl concentrations from 0.1 to 500 mM. Lines for each channel half-depth are calculated with eq 4. Measurements were made on three devices with h = 27 nm, four devices with h = 54 nm, and two devices with h = 108 nm and 2.5 μm. Error bars are $\pm \sigma$.

Figure 4 shows the variation of electroosmotic mobility with Debye length (κ^{-1}). For NaCl concentrations of 0.1 to 500 mM, the Debye lengths for a 1:1 electrolyte at 22 °C range from 30 to 0.4 nm, respectively. As expected, the electroosmotic mobilities in the 2.5 μm channel are linear over the entire NaCl concentration range. However, the electroosmotic mobilities in the three nanochannels at low salt concentrations (0.1, 1, and 10 mM) are significantly reduced compared to the electroosmotic mobilities in the microchannel. Reduction of the electroosmotic mobility is most pronounced in the 27 nm channel with κ^{-1} = 30 nm for 0.1 mM NaCl, where double layer overlap results in a parabolic flow profile with a reduced average mobility compared to the flat-flow profile in microchannels with a higher average mobility. In addition, the electroosmotic mobilities in the nanochannels milled by the FIB instrument are in excellent agreement with the electroosmotic mobilities in the microchannels etched by a wet-chemical method. The electroosmotic mobilities in the 2.5 μm channel coincide with the electroosmotic mobilities in the 108 nm channel for NaCl concentrations ≥1 mM, in the 54 nm channel for NaCl concentrations ≥10 mM, and in the 27 nm channel for NaCl concentrations ≥100 mM. These results suggest that the FIB-milling process does not significantly impact the surface and ζ-potential of the nanochannels.

Theoretical electroosmotic mobilities are calculated from a nonlinear solution of the Poisson–Boltzmann equation for a channel with parallel-plate geometry. The equilibrium potential, $\psi(y)$, in the channel at position y perpendicular to the wall is calculated:

$$\psi(y) = \frac{4kT}{ze}\left[\tanh^{-1}\left(\tanh\left[\frac{ze\zeta}{4kT}\right]\exp(-\kappa y)\right)\right] + \frac{4kT}{ze}\left[\tanh^{-1}\left(\tanh\left[\frac{ze\zeta}{4kT}\right]\exp(-\kappa(2h-y))\right)\right] \quad (2)$$

where k is the Boltzmann constant, T is the temperature, z is the ion valence, and e is the electronic charge. The electroosmotic velocity, $u_{eo}(y)$, is calculated:

$$u_{eo}(y) = -\frac{\varepsilon\zeta E}{\eta}\left(1 - \frac{\psi(y)}{\zeta}\right) \quad (3)$$

where ε is the permittivity of the medium, η is the viscosity, and E is the electric field strength. ζ-potentials measured in the 2.5 μm channel ranged from –6 to –73 mV for NaCl concentrations from 500 to 0.1 mM, respectively (see Figure 3) and are used in these calculations.

The average electroosmotic mobility, μ_{eo}, is then calculated by eq 4:

$$\mu_{eo} = \frac{1}{2hE}\int_0^{2h} u_{eo}(y)\,dy \quad (4)$$

μ_{eo} is integrated from the channel wall ($y = 0$) across the entire channel depth ($y = 2h$). The permittivity of the medium and solution viscosity for water are used and assumed to be constant. Calculated values of μ_{eo} for each nanochannel half-depth are plotted as lines in Figures 4 and 5 and match the experimental data extremely well over the entire range of NaCl concentrations.

Figure 5

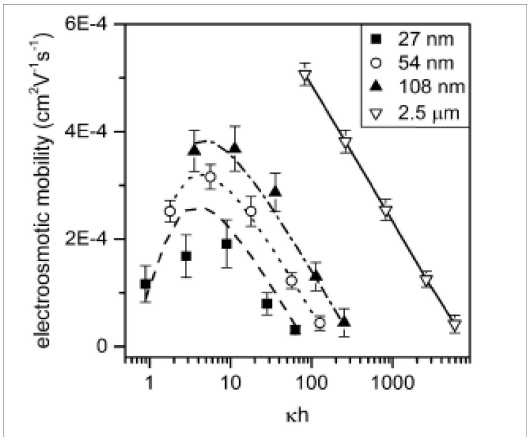

Figure 5. Variation of average electroosmotic mobility (μ_{eo}) with κh for channel half-depths (h) of 27 nm, 54 nm, 108 nm, and 2.5 μm and NaCl concentrations from 0.1 to 500 mM. Lines for each channel half-depth are calculated with eq 4. Measurements were made on three devices with h = 27 nm, four devices with h = 54 nm, and two devices with h = 108 nm and 2.5 μm. Error bars are $\pm \sigma$.

For large κh where κ is the Debye–Hückel parameter, the ratio $\psi(y)/\zeta$ goes to zero, and eq 3 for u_{eo} reduces to the Smoluchowski equation. For small κh, $\psi(y)/\zeta$ approaches 1, and u_{eo} is significantly reduced in the channel. Figure 5 shows the variation of electroosmotic mobility with κh. In the microchannel, $\kappa h > 100$ for all electroosmotic mobility measurements, and therefore, the electroosmotic mobilities are linear with κh. For $\kappa h > 50$, electroosmotic mobilities in the nanochannels are accurately predicted by the Smoluchowski equation. However, for $\kappa h < 10$, the electrical double layer extends into the nanochannel, and consequently, electroosmotic mobilities decrease as the nanochannel half-depths decrease. In Figure 5, maxima in the electroosmotic mobilities are observed at $\kappa h \approx 4$ for all three nanochannels, and the experimental data are in excellent agreement with predicted values. These maxima occur at different NaCl concentrations for all three nanochannels (see Figure 4) and indicate that the degree of double layer overlap depends on both channel dimensions and Debye length. Moreover, at $\kappa h \approx 4$ where the average electroosmotic mobilities exhibit maxima, the electrostatic potential in the center of the channel is zero. When κh goes from 4 toward 1, the electrostatic potential in the channel center becomes nonzero due to interaction between the electrical double layers, and consequently, the average electroosmotic mobilities decrease.

Equation 2 is a nonlinear solution of the Poisson–Boltzmann equation that assumes a two-dimensional flow field in channels with a parallel-plate geometry and neglects sidewall effects. Our nanochannels are shallow rectangles and have aspect ratios (w/h) of 9.8, 4.9, and 2.5 for channel half-depths of 27, 54, and 108 nm, respectively. The calculated electroosmotic mobilities match the experimental values for the 54 and 108 nm channels, which have the lower aspect ratios. The 27 nm channel has the highest aspect ratio of the channels tested, and except for one point at κh = 2.8, the calculated and experimental electroosmotic mobilities match. In our calculation, we use the ζ-potentials measured in the 2.5 μm channel and do not account for possible changes in the surface charge density as κh approaches 1. Consequently, suppression of the electroosmotic flow is simply due to geometric confinement of the electrical double layer in the shallow nanochannels. The model also assumes weak double layer overlap $(\kappa h \geq 2)$. This assumption is considered valid for

all of our electroosmotic flow measurements except two measurements made at 0.1 mM NaCl in the 27 nm channel ($\kappa h = 1$) and 54 nm channel ($\kappa h = 1.8$). However, as seen in Figures 4 and 5, the calculated and experimental values match well.

Conclusion

Nanochannels with rectangular cross sections fabricated in glass by FIB milling show enhanced ionic conductivities and reduced electroosmotic mobilities when compared to ion and electroosmotic transport in microchannels. These nanochannels have large surface-to-volume ratios, and consequently, the surface conductivity dominates the ionic conductivity in the channel. Also, as the Debye length becomes comparable to the channel half-depth (e.g., $\kappa h < 10$), the electrical double layer extends into the channel and significantly impacts the electroosmotic flow profile, which leads to a lower average electroosmotic velocity. The experimental electroosmotic mobilities match theoretical predictions, and both exhibit maxima at $\kappa h \approx 4$.

References

Schoch, R. B.; Han, J.; Renaud, P. Rev. Mod. Phys. 2008, 80, 839– 883

Zangle, T. A.; Mani, A.; Santiago, J. G. Chem. Soc. Rev. 2010, 39, 1014– 1035

Kovarik, M. L.; Jacobson, S. C. Anal. Chem. 2009, 81, 7133– 7140

Piruska, A.; Gong, M.; Sweedler, J. V.; Bohn, P. W. Chem. Soc. Rev. 2010, 39, 1060– 1072

Pu, Q.; Yun, J.; Temkin, H.; Liu, S. Nano Lett. 2004, 4, 1099– 1103

Wang, Y.-C.; Stevens, A. L.; Han, J. Anal. Chem. 2005, 77, 4293– 4299

Kim, S. J.; Wang, Y. C.; Lee, J. H.; Jang, H.; Han, J. Phys. Rev. Lett. 2007, 99, 044501

Kemery, P. J.; Steehler, J. K.; Bohn, P. W. Langmuir 1998, 14, 2884– 2889

Fa, K.; Tulock, J. J.; Sweedler, J. V.; Bohn, P. W. J. Am. Chem. Soc. 2005, 127, 13928– 13933

Kim, B. Y.; Swearingen, C. B.; Ho, J. A. A.; Romanova, E. V.; Bohn, P. W.; Sweedler, J. V. J. Am. Chem. Soc. 2007, 129, 7620– 7626

Zhou, K.; Kovarik, M. L.; Jacobson, S. C. J. Am. Chem. Soc. 2008, 130, 8614– 8616

Wei, C.; Bard, A. J.; Feldberg, S. W. Anal. Chem. 1997, 69, 4627– 4633

Umehara, S.; Pourmand, N.; Webb, C. D.; Davis, R. W.; Yasuda, K.; Karhanek, M. Nano Lett. 2006, 6, 2486– 2492

Siwy, Z.; Fulinski, A. Phys. Rev. Lett. 2002, 89, 198103

Siwy, Z. S. Adv. Funct. Mater. 2006, 16, 735– 746

Kovarik, M. L.; Zhou, K.; Jacobson, S. C. J. Phys. Chem. B 2009, 113, 15960– 15966

Karnik, R.; Duan, C.; Castelino, K.; Daiguji, H.; Majumdar, A. Nano Lett. 2007, 7, 547– 551

Perry, J. M.; Zhou, K.; Harms, Z. D.; Jacobson, S. C. ACS Nano 2010, 4, 3897– 3902

Lee, S.; Zhang, Y. H.; White, H. S.; Harrell, C. C.; Martin, C. R. Anal. Chem. 2004, 76, 6108– 6115

Kovarik, M. L.; Jacobson, S. C. Anal. Chem. 2008, 80, 657– 664

Stuy of Some New Insecticides against Brinjal Shoot Borer L. Orbonalis

Chandra Shekhar

Dept. of (Zoology), R.L.S.Y. College, Auragabad

ABSTRACT :

Food products derived from brinjal are extensively processed before the use for human consumption. Therefore, no intact protein or genetic materials are expected to be contained in food products derived from brinjal. Brinjal has a history of safe use as a source of food in India. Brinjal is a highly productive crop, the fruit are consumed as cooked vegetables in various ways, and dried shoots are used as fuel in rural areas. Brinjal is a good source of minerals and vitamins, and rich in total water soluble sugars, free reducing sugars, amide proteins among other nutrients. The fundamental principal of substantial equivalence when applied to Bt brinjal and its non-Bt counterpart has revealed that Bt brinjal is substantially equivalent in its composition to control brinjal and thus the food and feed derived from Bt brinjal will also be substantially equivalent to food and feed derived from non-Bt counterpart. In addition to compositional analysis the wholesomeness of feed from Bt brinjal was demonstrated in separate feeding studies with fish, chickens, cows, goats and rabbits.

Keywords: *Insecticides, Brinjal and Shoot Borer*.

INTRODUCTION :

Brinjal has been cultivated in the country for the last 4,000 years, although it is often thought of as a Mediterranean or mid-Eastern vegetable. Among the Solanaceous vegetables, brinjal, Solanum melongena Linn. is the most common, popular and principal vegetable crop grown in many geographical parts in India. The area under brinjal cultivation is estimated at 0.51 million ha. with total production of 8,200,000 Mt (FAO data, 2005, http://faostat.fao.org/). Brinjal is mainly cultivated on small family farms and it is a source of cash income for resource-poor farmers. This staple vegetable crop is extensively damaged by the insect brinjal fruit and shoot borer (*Leucinodes orbonalis*) and losses range from 50-70%. The young larvae of the pest bore in to petioles and midribs of large leaves and tender shoots causing shoot tips to wilt and later they bore in to flower buds and fruits. The affected fruits loose their market value besides considerable reduction in yield. The pest poses a serious problem because

of its high reproductive potential, rapid turnover of generations and intensive cultivation of brinjal both in wet and dry seasons of the year. Farmers use large quantities of chemical insecticides singly or in combination to get blemish free fruits, which fetch premium prices in the market. Around 25 to 80 sprays are undertaken for effective control of brinjal fruit and shoot borer. This practice of indiscriminate use of insecticides leads to build up of pesticide residues in the produce, destruction of beneficial insects, pest resurgence, pesticide exposure to farm workers and environmental pollution. To reduce pest-linked damage in brinjal crop as well as to protect the environment from adverse effects of pesticides, deploying the lepidopteran specific cry1Ac gene under the control of enhanced CaMV 35S promoter for high level expression in brinjal would provide an effective built-in control for brinjal fruit and shoot borer as a insect resistance management strategy. This would result in bringing down the cultivation costs of brinjal, as contribution of chemical pesticides to brinjal cultivation is sizable.

EXPERIMENTAL WORKS :

Brinjal was developed by transforming the brinjal proprietary line of Mahyco. Bt brinjal contains the following three genes inserted via genetic engineering techniques:

The cry1Ac gene, which encodes for an insecticidal protein, Cry1Ac, derived from the common soil bacterium *Bacillus thuringiensis* subsp. kurstaki (B.t.k). The cry1Ac gene is driven by enhanced CaMV 35S promoter. The nptII gene which encodes the selectable marker enzyme neomycin phosphotransferase II (NPTII) was used to identify transformed cells that contained the Cry1Ac protein. It has no pesticidal properties. The nptII gene is derived from the prokaryotic transposon Tn5 (Beck *et. al*., 1982). The aad gene which encodes for the bacterial selectable marker enzyme 3"(9)-O- aminoglycoside adenyl transferase (AAD) allowed for the selection of bacteria containing the pMON 10518 plasmid on media containing spectinomycin or streptomycin. The aad gene is under the control of a bacterial promoter and hence not expressed in Bt brinjal. The aad gene was isolated from transposon Tn7 (Fling *et. al*., 1985).

The Bt transgene in the transgenic Bt brinjal behaves as a single gene, dominant Mendelian factor and is stably integrated in the plant genome. To be active against lepidopterans insects (brinjal fruit and shoot borer; fruit borer) the protein must be ingested. In the insect gut, the protein binds to specific receptors on the insect midgut, inserts into the membrane and forms ion specific pores. These events disrupt the digestive processes and cause death of the insect. The Cry1Ac protein produced in Bt brinjal is non-toxic to non-lepidopteran insects, birds, fish and mammals as these

species lack receptors for the proteins on the surface of their gut cells. Also the acidic medium in gut of these organisms also makes Cry1Ac protein inactive.

RESULT & DISCUSSION :

Acute oral toxicity study of transgenic Bt brinjal was conducted at INTOX PVT. LTD., India to assess the safety of Bt brinjal. Acute oral administration of transgenic Bt brinjal expressing Cry1Ac protein to Sprague Dawley rats at the limit dose of 5000mg/ kg did not cause any toxicity. Proteins that are non-toxic by the oral route are not expected to be toxic by the dermal or pulmonary route. Subchronic oral (90 Days) toxicity study of transgenic Bt brinjal in Sprague Dawley Rat was conducted at INTOX PVT. LTD., Pusa, Bihar, India. Based on the findings of this study, the no-observed-adverse-effect-level (NOAEL) of transgenic Bt brinjal expressing Cry1Ac protein in Sprague Dawley rat, following oral administration for 90 days was found to be more than 1000 mg/kg body weight. This study demonstrates that Bt brinjal expressing Cry1Ac protein is non-toxic to the study animal by oral route.

Assessment of the allergenicity of protein extract from transgenic Bt brinjal was conducted at Rallis India Limited, Bangalore, India. The objective of this study was to assess the relative allergenicity of transgenic Bt brinjal compared to the allergenicity of conventional brinjal (non-transgenic), as measured by active cutaneous anaphylaxis (ACA) in Brown Rats sensitized with brinjal. Six to seven weeks old Brown Rats were randomly selected and used for the studies. The animals were observed daily for signs of toxicity and pre-terminal deaths, weekly body weights and food consumption.

There were no clinical signs of toxicity and pre-terminal deaths (mortalities). The weekly mean body weights were increased in all the groups. There was no statistically significant intergroup difference in body weights between treatment and control groups. There were no significant differences in food consumption between treatment and control groups.

There were no differences between the skin reactions of each of the 4 extracts on the same animals. These observations suggest that there are no differences between the allergenicity or inflammatory characteristics of the 5 brinjal extracts tested including transgenic Bt brinjal and non transgenic brinjal.

Conclusion :

Brinjal (*Solanum melongena* L.) is one for the most popular vegetable, largely grown in almost all parts of India. India seems to be the original habitalt as the plant still exists here in the wild state. It is grown in all the

seasons. It has quite high nutritive value and holds a position nearly comparable to tomato. Its unpire violet, green or white coloured fruits contains vitamins A, B and C and also have Ayurvedic medicine properties. The white brinjal is said to be good for diabetic partients (Chaudhary, 1990).

REFERENCE:

1. Abrol DP and Singh JB, 2003, Relative efficacy of some insecticides against brinjal fruit and shoot borer, *Leucinodes orbonalis* Guenee, and their impact on fruit yield. *Journal of Asia Pacific Entomology* 6(1): 83-90. DOI: 10.1016/S1226-8615(08)60172-7
2. Adiroubane D and Raghuraman K 2004, Plant products and microbial formulation in the management of brinjal shoot and fruit borer, *Leucinodes orbonalis Guenee. Journal of Biopesticides* 1(2): 124-129.
3. Alam AZ and Sana DL, 1964, Biology of *Leucinodes orbonalis* Guen. In: Alam MZ and Sattar A (eds.). Review of research in East Pakistan, Division of Entomology (1947-1964): Agricultural Information Service East Pakistan. Agriculture Research Institute Dhaka. pp. 192-200.
4. Alam SN, Hossain MI, Rouf FMA, Jhala RC, Patel MG, Rath LK, Sengupta A, Baral K, Shylesha AN, Satpathy S, Shivalingaswamy TM, Cork A and Talekar NS, 2006, Implementation and promotion of an IPM strategy for control of eggplant fruit and shoot borer in South Asia. *Technical Bulletin No.* 36. AVRDC publication number 06-672. AVRDC - The World Vegetable Center, Shanhua, Taiwan. 74 p.
5. Alam SN, Rashid MA, Rouf FMA Jhala RC, Patel JR, Satpathy S, Shivalingaswamy TM, Rai S, Wahundeniya I, Cork A, Ammaranan C and Talekar NS, 2003 Development of an integrated pest management strategy for eggplant fruit and shoot borer in South Asia. *Technical Bulletin No*. 28. AVRDC Publication No. 03-548. AVRDC - The World Vegetable Center, Shanhua, Taiwan. 56 p.
6. Alpuerto AB, 1994, Ecological studies and management of brinjal fruit and shoot borer, *Leucinodes orbonalis* Guenee. *Indian Journal of Agricultural Sciences* 52(6): 391-395.
7. Atwal AS (1976) Agricultural pests of India and Southeast Asia. Kalyani Publishers. New Delhi, India. 529 p.
8. Harish, D.K., A.K. Agasimani, S.J. Imamsaheb and S. Patil Satish, 2002. Growth and yield parameters in brinjal as influenced by organic nutrient management and plant protection conditions. *Res. J. Agric. Sci.*, 2(2): 221-225.

Study On Air Quality In Smaller Towns In Indo-gangetic Plains

Kumari Samriddhi Singh

Research Scholar, Department of Chemistry, Sanskriti University, Mathura(U.P.) India

Dr. Durgesh Wadhwa

Head, Department of Chemistry, Sanskriti University, Mathura(U.P.) India

Abstract

This paper shows that the several bigger cities (like Delhi or Varanasi) have witnessed reduction in annual PM2.5 levels, smaller towns and cities (like Fatehabad or Moradabad) have seen an increase. Dramatic build-up in smaller towns like Hisar and Jind happened only during November, indicating the influence of stubble burning. Air quality got more toxic with the onset of winter: share of tinier PM2.5 in PM10 increased. Number of days in which PM2.5 levels met the standard was considerably lower this winter; more poor days this winter in the region. This reaffirms why air quality management requires regional approach to implement clean air action plans with speed, scale and urgency.

Introduction

New analysis of winter air pollution (till January 11, 2021) in the cities of Indo-Gangetic Plains (IGP), carried out by Centre for Science and Environment (CSE), shows how clean air gains of the lockdown and monsoon periods have been lost with the reopening of the economy and the hostile winter weather.

Interestingly, says the analysis, the rise in pollution levels has also been synchronised across the region with varying patterns.

While this was expected, the analysis of real-time data from monitoring stations outside the National Capital Region (NCR) in the larger Indo-Gangetic Plains shows newer patterns in winter pollution this year. Even though trapping of winter pollution in the IGP is high compared to other regions, it was not as high as that in the NCR – at the same time, it was alarmingly high and synchronised despite the large distances involved. This is the challenge of this landlocked region.

This analysis is part of CSE's air quality tracker initiative to get a deeper view of the changing patterns of air quality trends in the country. Says Anumita Roychowdhury, CSE's executive director in charge of research and advocacy: "This brings out the impact of the extraordinary disruption

that 2020 has caused. Despite the dramatic reduction in air pollution during the lockdown, pollution has bounced back across the region post-lockdown unmasking the high impacts of local and regional pollution with some variation in the pattern. This demands quicker regional reforms and action to curb pollution from vehicles, industry, power plants and waste burning to further bend the air pollution curve on a regional scale."

Higher $PM_{2.5}$ levels is a typical and predictable winter trend when continuous emissions from local sources including vehicles, industry, construction, and episodic pollution from biomass burning get trapped due to meteorological changes. Avikal Somvanshi, programme manager in CSE's Urban Lab team of the Sustainable Cities programme, says: "This year, this trend has set in almost two weeks earlier in the season. There is a clear difference in the winter pollution pattern between IGP regions north and south of the NCR. Even though the average level of PM2.5 for the summer and monsoon months in 2020 is considerably lower than the previous year's due to the summer lockdown, the $PM_{2.5}$ levels this winter have risen beyond the 2019 levels in almost all monitored cities in Punjab and Haryana (regions north of the NCR)."

Somvanshi adds: "Cities in central and eastern UP and Bihar (regions south of the NCR) also show high winter pollution, but the levels are similar or lower compared to 2019. Combination of the reopening of the economy and changing meteorology is responsible for high winter pollution, but this regional variation calls for a more nuanced and robust pollution control strategy. The region cannot rely only on action being taken in Delhi-NCR. This demands speed and scale of action.

Analysis of the Study

The analysis is based on publicly available granular real-time data (15-minute averages) from the Central Pollution Control Board's (CPCB) official online portal, the Central Control Room for Air Quality Management.

Twenty-six cities – Amritsar, Bhatinda, Jalandhar, Khanna, Ludhiana, Mandi Gobindgarh, Patiala, Rupnagar, Chandigarh, Ambala, Fatehabad, Hisar, Kaithal, Kurukshetra, Panchkula, Sirsa, Yamuna Nagar, Agra, Kanpur, Moradabad, Varanasi, Lucknow, Patna, Gaya, Muzaffarpur and Hajipur have been selected for this analysis because real-time data is available for these cities.

Analysis has been done of the data recorded by six air quality monitoring stations in Patna, five in Lucknow, two in Gaya and Muzaffarpur each, and one station each in the rest of the cities under the Continuous Ambient Air Quality Monitoring System (CAAQMS) of the

CPCB. Weather data for Amritsar, Ambala, Chandigarh, Lucknow, and Patna has been sourced from the weather stations of Indian Meteorological Department (IMD) located at the airports in each city.

Key Highlights of the Analysis

Annual average level of $PM_{2.5}$ not lower in many cities this year despite the lockdown — while several bigger cities have witnessed a reduction, many smaller towns and cities have experienced an increase: The 2020 average $PM_{2.5}$ level in many cities in upper IGP has climbed up to breach the average concentration recorded in 2019. Fatehabad in northern Haryana is the worst performer with a 35 per cent increase from 2019 level. It is followed by increases in Bhatinda (14 per cent), Agra (9 per cent), Khanna (7 per cent), Mandi Gobindgarh (6 per cent), Moradabad (5.5 per cent) and Kurukshetra (1 per cent). Jalandhar registered a less than 1 per cent change.

Most improvement has been noted in Sirsa which is closing 2020 with a 44 per cent lower $PM_{2.5}$. Varanasi with 31 per cent, Gaya with 27 per cent, Muzaffarpur with 15 per cent and Hisar with 12 per cent are the other top performers in the pool. Rest of the cities show improvement in the range of 4-12 per cent. For context, Delhi's 2020 average is 13 per cent lower than its 2019 level.

Bad November indicates influence of stubble burning: Fatehabad (the worst performer) and Sirsa (the best performer) are neighboring towns — just 40 km apart. Says Somvanshi: "Therefore, this massive variation cannot be attributed to meteorology and has to do with local factors. The annual average of these towns along with other smaller towns like Hisar and Jind in the north-west are heavily influenced by episodic pollution caused by burning of crop stubbles. The influence is so strong that it can elevate their monthly $PM_{2.5}$ levels for November to that of Delhi's, but unlike Delhi, these towns are directly exposed to the smoke. The elevated November levels do not linger on for the rest of the winter in these towns (as is the case in Delhi)."

Therefore, any change in stubble burning pattern – notes the CSE analysis — skews their annual average dramatically, which may possibly be the reason for the observed trends; further field investigation is needed to determine the real reasons.

Average level of $PM_{2.5}$ has been lowest during this summer and monsoon due to the lockdown, but this could not prevent the winter spike: The overall $PM_{2.5}$ average this summer and monsoon has been predictably lower compared to the previous year — largely because of the unprecedented economic disruption during the summer lockdown

and the phased unlocking. But reopening of the economy coinciding with the onset of the winter trapped the pollution — $PM_{2.5}$ levels rose starting October. From the respective cleanest week the weekly average of $PM_{2.5}$ in Amritsar rose 10 times, in Ambala nine times, Chandigarh six times, Lucknow 11 times, and Patna 11 times to the dirtiest week. These major cities recorded lesser deterioration than Delhi where weekly air quality worsened 14 times.

But the smaller towns have beaten the capital. Bhatinda deteriorated 23 times, Fatehabad 22 times, Muzaffarpur 19 times, Sirsa 17 times, Kanpur 16 times, and Hisar and Kaithal 15 times.

There is a marked difference between northern and eastern cities. The cities in the north recorded their dirtiest week in the first half of November (same as Delhi-NCR); eastern cities had their dirtiest week in December.

The dirtiest week for Khanna, Mandi Gobindgarh, Patiala, Rupnagar, Chandigarh, Ambala, Kaithal, Kurukshetra, Yamuna Nagar, Agra, and Moradabad was the week ending November 8, 2020. For Delhi, Amritsar, Bhatinda, Jalandhar, Ludhiana, Fatehabad, Hisar, Panchkula and Sirsa the dirtiest week was the week ending November 15, 2020. Hajipur, Patna and Muzaffarpur saw their dirtiest week in the week ending December 6, 2020. Kanpur, Varanasi and Lucknow had theirs in the week ending December 27, 2020. The dirtiest week for Gaya was the New Year's week.

The cleanest week for Khanna, Rupnagar, Ludhiana, and Panchkula was the week ending March 29, 2020. Amritsar and Jalandhar had their cleanest week in April. Patna had its cleanest week in June and July was the cleanest for Agra, Moradabad, Patiala, Chandigarh, Ambala, Kaithal, Kurukshetra, Yamuna Nagar, Delhi and Hisar. Kanpur, Varanasi, Lucknow and Muzaffarpur had their cleanest week in the week ending August 23, 2020. Mandi Gobindgarh and Fatehabad had their cleanest week in the week ending August 30, 2020. Bhatinda and Sirsa had theirs in the week ending September 6, 2020. Hajipur and Gaya had their cleanest in the week ending September 27, 2020.

Average November $PM_{2.5}$ levels considerably higher in the northern cities: November 2020 was dirtier across most cities in the IGP. The $PM_{2.5}$ average this November was 310 per cent higher in Fatehabad, 104 per cent in Agra and 57 per cent in Kaithal compared to November 2019. November was also same or dirtier in all Punjab and Haryana cities except Sirsa which registered a 16 per cent cleaner month. All cities in central and eastern UP and Bihar had a 4-48 per cent cleaner November. Also, August 2020 was cleaner in all these cities compared to August 2019 (except in Bhatinda, Mandi Gobindgarh, Patiala and Fatehabad).

Air quality gets more toxic with the onset of winter — share of tinier $PM_{2.5}$ in the PM_{10} increases: The share of tinier and finer particles in the overall coarser PM_{10} concentration determines the toxicity of air. When the overall share of tinier $PM_{2.5}$ in PM_{10} is higher, the air is more toxic as the tiny particles penetrate deep inside the lungs and cut through the blood barrier, thus increasing the health risk. Interestingly, during lockdown, when the overall suspended coarser particles had settled down reducing the PM_{10} levels, the $PM_{2.5}$ had also come down. But its share was 33 per cent in Amritsar, 39 per cent in Chandigarh and 38 per cent in Patna – still higher than it is usually noted during summer.

But with the onset of winter, the overall levels of both have gone up, as has the percentage share of $PM_{2.5}$ in overall $PM_{10.}$ This rose to the high 40s in October and remained high through November averaging at 55 per cent in Amritsar, 48 per cent in Chandigarh and 53 per cent in Patna. The share of $PM_{2.5}$ in PM_{10} is generally highest on Diwali – in 2020, it reached 64 per cent in Amritsar, 69 per cent in Chandigarh, and 62 per cent in Patna.

Dirtier Diwali in Lucknow, but Amritsar, Ambala, Chandigarh and Patna were cleaner: The average $PM_{2.5}$ level on Diwali day at Talkatora in Lucknow was 434 ìg/m^3 — up from 237 ìg/m^3 recorded in 2019. In 2020, there was an over 100 per cent higher rise in hourly $PM_{2.5}$ concentration between afternoon and night of Diwali (mostly caused due to firecracker busting). Amritsar was 7 per cent cleaner, Chandigarh 56 per cent, Ambala 57 per cent, and Patna 22 per cent. Diwali also occurred later in November in 2020 than in the previous year.

Bad air days started earlier in 2020 winter: The rolling weekly average rose over the 24-hour standard or 60 µ g/m^3 in Amritsar on October 6 (eight days earlier), Ambala on October 4 (eight days earlier), Lucknow on September 10 (29 days earlier), and Patna on October 1 (14 days earlier). Overall, the winter was dirtier all across. Chandigarh has had a relatively cleaner November with bad air setting in later this year compared to 2019.

Number of days with $PM_{2.5}$ concentration meeting the standard was considerably lower this winter — more 'poor' or 'worse' days: There have been 33 days of standard air days this winter compared to 41 recorded last year in Amritsar. Similarly, standard days have been lesser by 11 days in Ambala and four in Lucknow and Patna each. In fact, in Lucknow, not a single day met the standard since the beginning of October this winter; there were 19 days of 'severe' or 'worse' air quality — up from five last winter. Chandigarh bucks the trend and recorded 18 more days this winter with air quality meeting the standard.

The cyclical ups and down of pollution in the winter of 2020 has been less volatile – showing slower rise and fall than in previous winter: This inelastic behavior of $PM_{2.5}$ levels in IGP cities is in contrast to the trend seen in Delhi-NCR, where it has been more volatile during winter with frequent and quicker rise and drop. This cannot be the impact of meteorology as Delhi-NCR is exhibiting a different trend – therefore, it might be due to poor pollution control action among these cities. But more investigation is needed to understand the reasons for this.

Even with a comparatively cleaner air in 2020, most cities recorded daily spikes similar to those observed in 2019: CSE has compared the annual averages and peak 24-hour averages in these cities of the IGP between 2019 and 2020. This shows that the smaller towns even with much lower annual average levels of $PM_{2.5}$ have experienced almost same or higher maximum daily levels during winter when the entire region got air locked. Punjab cities have relatively lower daily peak compared to the rest.

Conclusion:

On the basis of above facts this paper concludes that to avoid winter pollution peaks and the varying pattern of annual rise in pollution across the Indo Gangetic Plain, the country and the region will require regional-scale action to reduce regional influences on local air pollution, as well as deep local cuts. It is clear that the region has to take forward its wins so far and raise the level of ambition to drive action across all key sectors of pollution and in the entire region. Enforce power plant standards across the state, minimise use of coal and other dirt fuels in the industry while improving emissions control, scale up public transport and vehicle restraint measures and manage waste to have a zero waste and zero landfill strategy.

References:

1. Cohen AJ, Brauer M, Burnett R, et al. Estimates and 25-year trends of the global burden of disease attributable to ambient air quality: an analysis of data from the Global Burden of Diseases Study 2015. *Lancet* 2017; **389:** 1907–18.
2. Landrigan PJ, Fuller R, Acosta NJR, et al. The *Lancet* Commission on quality and health. *Lancet* 2018; **391:** 462–512.
3. Manisalidis I, Stavropoulou E, Stavropoulos A, Bezirtzoglou E. Environmental and health impacts of air quality: a review. *Front Public Health* 2020; **8:** 14.
4. WHO. Air quality. https://www.who.int/health-topics/air-quality#tab=tab_1 (accessed Dec 11, 2020).
5. Zivin JG, Neidell M. The impact of quality on worker productivity. *Am Econ Rev* 2012; **102:** 3652–73.

6. Roth S. Air quality, educational achievements, and human capital formation. IZA World of Labor. August, 2017. https://wol.iza.org/ articles/air-quality-educational achievements-and-human-capital-formation/long (accessed Dec 11, 2020).
7. WHO. Sustainable Development Goals for household energy. http://www.who.int/ airquality/household/sustainable-development-goals/en/ (accessed Dec 11, 2020).
8. Central Quality Control Board, Ministry of Environment, Forest and Climate Change, Government of India. Air quality monitoring, emission inventory and source apportionment study for Indian cities—national summary report. New Delhi: CPCB. February, 2011. http://cpcb.nic.in/ displaypdf.php?id=RmluYWxOYXRpb25hbFN1b W1hcnkucGRm (accessed Dec 11, 2020).
9. Guttikunda SK, Goel R, Pant P. Nature of air quality, emission sources, and management in the Indian cities. *Atmos Environ* 2014; 501–10.
10. Sharma M, Dikshit O. Comprehensive study on air quality and green house gases (GHGs) in Delhi. Department of Environment, Government of NCT of Delhi. January, 2016.
11. Upadhyay A, Dey S, Chowdhury S, Goyal P. Expected health benefits from mitigation of emissions from major anthropogenic $PM_{2.5}$ sources in India: statistics at state level. *Environ Pollut* 2018;1817–26.

The Histological Examination of the Digestive Tract of *Poekilocerus Pictus,* An Orthopteran Insect Species

Harendra Kumar Singh[1]

S.N.P Yadav[2]

[1,2] **P.G Department of zoology, Magadh University, Bodh-Gaya, Bihar, India**

Abstract:

The *Poekilocerus pictus* species poses a significant threat to cultivation as a roaming caterpillar. The objective of this investigation is to comprehend the anatomical arrangements of the gastrointestinal systems of the aforementioned species. The G.I system is anatomically partitioned into three distinct regions, namely the foregut, midgut, and hindgut. The digestive tracts were extracted and the tissues were preserved using a 10% buffered neutral formalin solution for a duration of 24 hours during the dissection procedure. Following standard histological protocols, the tissue sections underwent staining with hematoxylin-eosin (H-E). The mid-gut is analysed with regard to various anatomical features such as the peritrophic membrane, epi-thelial tissue, cell size, nucleus size, circular and longitudinal muscles, connective tissue, regenerative cells, and cellular diversity. Understanding the histology of grasshoppers has the potential to enhance the efficacy of grasshopper control measures and facilitate the advancement of agricultural plant protection agents.

Keywords: *Poekilocerus pictus,* caterpillar, mid-gut, longitudinal muscles, regenerative cells,

Introduction:

Insects with a long history of existence on Earth exhibit a broad distribution. Regarding taxonomy, they represent the most prevalent taxonomic group within the Animalia kingdom. Currently, over 750,000 species have been identified and classified (1).

The order Orthoptera comprises over 22,000 species distributed across 30 families and has been documented to have a global distribution. The Orthoptera taxonomic classification comprises two sub-orders, namely Caelifera, which encompasses grasshoppers with short antennae, and Ensifera, which includes grasshoppers with long antennae. Grasshoppers exhibit hemimetabolous metamorphosis and possess elongated cylindrical

bodies of moderate size, with appendages that can extend up to 12 cm in length (2).Grasshoppers are characterised by their anatomical features, such as elongated hind legs that facilitate jumping, a downward-facing head, a chewing mouth, well-developed compound eyes, multi-segmented antennae, a large prothorax resembling a shield, a small mesothorax, and a large metathorax. Their wings are narrow in the front and wide in the rear, with numerous long veins that extend diagonally. The legs exhibit elongated and cylindrical morphology, characterised by an enlarged tarsus that may possess either one or four segments. The abdomen is comprised of eight or nine segments, with two or three of the terminal segments being reduced. Additionally, well-developed ovipositors have been documented (3).

Poekilocerus pictus is a species of grasshopper with elongated antennae that falls under the Ensifera sub-order and is classified within the Pyrgomorphidae family. Acrida. The present species exhibits compound eyes located on both the lateral and dorsal aspects of the cranium. *Poekilocerus pictus* possesses robust mandibles and exhibits a chewing mouthpart morphology, which is regarded as the fundamental insect mouth structure. The mandible is prominently developed, likely as an adaptation for plant feeding. *Poekilocerus pictus* exhibits the ability to engage in aerial locomotion. Due to this factor, it is widely acknowledged that *Poekilocerus pictus* exhibits the ability to migrate (citation 5). Currently, it is widely acknowledged that grasshoppers serve as a viable source of sustenance and are imported to foreign countries (3). The field of forensic entomology has established itself as a prominent discipline within the scientific community and has experienced significant advancements through the utilisation of insects in criminal investigations (6). Insects may pose a threat in a variety of circumstances, such as when they venture beyond their designated territory, when they are evading predators, or when they are being cultivated by humans. Insects are considered innocuous until they assume the role of a pathogen vector for a plant or animal, including humans. The harmful impact of insects can be attributed to the proliferation of plant and food resources within their respective habitats (3).

Most plant-feeding insects are considered agricultural pests. Familiarity with the histological and anatomical structures of insects facilitates the development of pesticides with greater precision and cost-effectiveness (7; 8; 9). Given this information, insects remain a topic of investigation in contemporary times. The *Poekilocerus pictus* exhibits a green hue and is raised on a grass-fed diet. The physical structure of *Poekilocerus pictus* is characterised by an elongated, tubular body that exhibits a high

degree of flexibility and softness in comparison to other members of the grasshopper family.

Materials and Methods:

The materials and methods employed in this study involved the removal of the digestive canal subsequent to dissection, followed by its placement in a fixation solution consisting of 10% buffered neutral formalin for a duration of 24 hours. Following standard histological protocol, paraffin blocks were sectioned using a Rotary microtome. These sections were subsequently stained with hematoxylin and eosin (H-E) and analysed to determine the histological composition of the midgut in question.

Histological assessments were conducted on hematoxylin and eosin (H-E) stained slides based on the quantity of cells and their staining condition. The enumeration of cells was conducted utilising a Leica DM1000 light microscope and camera. The counting field was established as a 33.28ìm square at 40X magnification, as depicted in Figure 1. During the measurement of tissue height, the segment of the epithelial tissue that extends from the baseline towards the apical direction was also assessed.

Results & Discussion :

The examination conducted under light microscopy revealed the presence of curved morphology in the digestive tract. The nuclei of the cylindrical epithelial cells were observed to be in a rigid state. The cellular composition of the epithelium was unilayered and consisted of prismatic cells. Microvilli were discernible and evident as depicted in Figure 2, Ab. The nuclei exhibit an oval shape and a dark appearance, as depicted in Figure 2, panel Aa.

Stem cell nests are observed in the epithelial region, where individual or clustered young cells are located at the base of the epithelium. The regeneration region is defined as depicted in Figure 2A and 2B.

The digestive tract cells and muscle structure of *Poekilocerus pictus* exhibit a thin morphology. The presence of secretory granules within the cell was also observed, as depicted in Figure 2Ag. Microvilli were observed as well, as depicted in Figure 2Ab. The goblet cells were observed to be situated amidst the prismatic epithelial cells. The nuclei exhibited an oval shape and displayed a significant degree of staining. The presence of longitudinal muscle cells was observed, as depicted in Figure 2Ad. The statistical analysis indicated that the mean count of epithelial cells in *Poekilocerus pictus* was not significantly different from the expected value ($P > 0.05$). The average measured value of the species' goblet number was significantly elevated.

The present investigation focused on the herbivorous species Poekilocerus pictus, wherein a high count of epithelial cells and goblet cells was observed. The present investigation aimed to make a contribution to the existing body of research on grasshoppers by examining the histological structural alterations resulting from feeding across various grasshopper species.

The digestive system of *Poekilocerus pictus* is characterised by a digestive tract that is lined with a single-row prismatic epithelial tissue, a thin layer of connective tissue, and striated muscles that exhibit both circular and longitudinal structures. Additionally, microvilli are present, as are one- way opening digestive canal valves and a peritrophic membrane. The primary histological structures that are examined in grasshoppers are as follows. Poekilocerus pictus, being a herbivorous species, exhibits a greenish hue as per observations. According to previous research (11), it is hypothesised that these particular colours are necessary for adaptation. In a recent investigation conducted by Bursalý (2012), the histological and histochemical composition of the digestive tract of Pezodrymedusa lata (Orthoptera: Tettigoniidae) was examined. The findings revealed the presence of a delicate connective tissue layer beneath the epithelial tissue. Demirsoy (2013) reported the presence of a subepithelial connective tissue layer and identified certain regions of the epithelial tissue as a regeneration disc. The findings of our investigation indicate that the grasshopper species under examination exhibits a comparable presence of a slender connective tissue beneath the epithelial tissue and regeneration site in the basal regions of prismatic epithelial tissue, as observed in previous studies. Ecevit et al. (11) have reported that the length of the digestive tract in insects is correlated with their dietary habits. Specifically, insects that consume protein-rich diets tend to have shorter digestive tracts compared to those that consume carbohydrate-rich diets. To clarify, carnivorous insects consume a diet rich in protein and solid nutrients, and possess a comparatively abbreviated digestive tract. Herbivorous insects consume a diet that is relatively low in protein but high in carbohydrates, and their digestive tracts are distributed throughout most of their body. As a result, the length of the digestive system in carnivorous grasshoppers is comparatively shorter than that of herbivorous grasshoppers. The herbivorous *Poekilocerus pictus* exhibited a high count of epithelial cells and goblet cells. The elongation of the digestive tract of *Poekilocerus pictus* was ascertained. The results of our study demonstrate a resemblance to the research conducted by Ecevit (11).

Undoubtedly, the comprehension of grasshopper histology and embryology will enhance the formulation of pesticides that are potent in

combating the menace of grasshoppers.

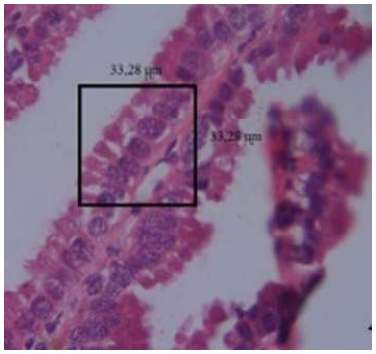

Fig-1: G.I tract epithelial & Goblet cell counting square

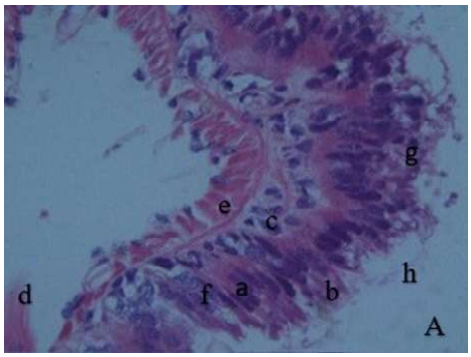

Fig-2A: G.I tract

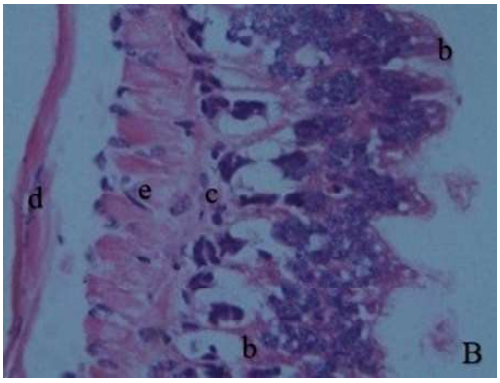

Fig-2B: G.I tract

References

1. Richards OW, Davies RG. Imms' general textbook of entomology (10th ed.). London: Chapman and Hall. ISBN978-0-412-15210-8, 1977.
2. Çýplak B, Demirsoy A. Arguvan (Malatya) ve çevresinde Orthoptera (Insecta) faunasýnýn incelenmesi. Turkish Journal of Zoology 1991; 15, 98-114.
3. Gök A. Böcekler. Nobel yayýnevi. ISBN: 978-605-133-324-3. Ankara, 2012

4. Çýplak B, Demirsoy A. Türkiye'de Ensifera (Orthoptera, Insecta) alt takýmýnýn endemizm açýsýndan deðerlendirilmesi. Turkish Journal of Zoology 1995; 19, 213-320.
5. Weber H. Biologie der Tiere Deutschlands. P. Schulze (ed), Berlin, 1922.
6. Zeybekoðlu Ü, Kartal V. Samsun Çevresindeki Philenus spumarius (Linnaeus, 1758) (Homoptera, Auchenorrhyncha, Cercopidae) Türünün Varyasyonlarý Üzerine Araþtýrma. IX. Ulusal Biyoloji Kongresi, Sivas, Cilt 2, 171-175, 21-23 Eylül, 1988.
7. Önalp B. Oedaleus decorus (Germar) (Orthoptera: Acrididae)'un Biyolojisi Üzerinde Çalýþmalar. Bitki Koruma Bülteni, Cilt 27, Sayý 1-2, 1987
8. Geyikoðlu, F, Akgül, Ü. Oedipode coerulescens'in diþisinde üreme sisteminin histolojik yapýsý. Turkish Journal of Biology 1993;17, 2,1-113.
9. Karaca Ý, Aslan B, Demirözen O, Karsavuran Y. Isparta Ýli Orthoptera Faunasý Üzerine Ön Bir Deðerlendirme, Süleyman Demirel Üniversitesi Ziraat Fakültesi Dergisi 2006; 1(2):49-52
10. Hunter P, Jones M. Rearing and breeding locust in the laboratory. Anti-locust Research Center. London, 1961.
11. Ecevit O, Akyazý F, Akyazý R. Böceklerde (Hexapoda: Arthropoda) Morfoloji, Fizyoloji ve Geliþim. Nobel Akademik Yayýncýlýk Eðitim Danýþmanlýk Ticaret Limited Þirketi. ISBN: 978- 605-133-358-8. Ankara, 2012.
12. Bursalý A. Pezodrymedusa Lata'nýn sindirim kanalýnýn histolojik ve histokimyasal yapýsýnýn araþtýrýlmasý. Gaziosmanpaþa Üniversitesi. Tokat. 1996.
13. Demirsoy A. Entomoloji. Meteksan Yayýn Evi. ISBN: 975-7746-02-9. Ankara, 2006.

Eco Friendly Control of MealyBugs by Different Plant Extracts

Abhishek Ranjan

Research Scholar, Department of Zoology, Patna University, Patna

Dr. Motilal Gupta

Associate Professor, B.N.College, (P.U.), Patna

Abstract:

This paper reveals that a field experiment was conducted under Patna university at Patna, Bihar to study seasonal occurrence of mealy bug (Maconellicoccus hirsutus Green) on som plant (Machilus bombycina King) and its management using bio-pesticides. The mealy bug was active throughout the year. The peak population of mealy bug (18.68/3 leaves) was recorded on 10th standard meteorological week i.e. on 2nd week of March. Correlation co-efficient (r) study between pest population with environmental parameter showed that there was significant positive (+) correlation with temperature difference and significant negative (-) correlation with temperature (minimum and average) and relative humidity (maximum, minimum and average). On the other hand, non-significant negative (-) correlation found between mealy bug population and maximum temperature. Bio-efficacy of different treatments against mealy bug showed that Imidacloprid (CONFIDOR 17.8 SL) 1 ml/ 5L was found superior for management of mealy bug (77.39% reduction of mealy bug population) followed by Azadirachtin (NIMARIN 1500 ppm) 2.5 ml/ L (57.38% reduction of mealy bug population). However botanical extract of tobacco 50.00 ml/L (5%) (50.48% reduction of mealy bug population), Garlic 50.00 ml/L (5%) (48.73% reduction of mealy bug population), Spilanthes 50.00 ml/L (5%) (45.40% reduction of mealy bug population), polygonum 50.00 ml/L (5%) (40.91% reduction of mealy bug population) and Pongamia 50.00 ml/L (5%) (30.37% reduction of mealy bug population) were found satisfactory to manage the pest.

Key words: Abiotic factors, Botanical extracts, Mealybug, Organic cultivation, Seasonal occurrence

Introduction:

Muga silk worm (Antheraea assama Westwood) primarily feeds on Som (Machilus bombycina King) plant (Bhattacharya et al. 1993, Tikader and Rajan 2012). The plant is very prone to attacked by different type of insect pests like gall insect, stem borer, leaf defoliating beetle, aphid, leaf

miner, leaf roller, red tree ant etc. (Borgohain 2015). Kumar et al. (2011) found that som plant is infested by shoot borer, trunk borer, leaf miner, leaf gall and mealy bug. Due to attack of insect-pests it becomes difficult for the farmers to conduct silk worm rearing (Singh et al. 2000). Application of insecticides for the insect-pests control is not advocated as their residual effects is harmful for the silk worm (Subharani and Jayaprakash 2015).

Botanical insecticide like onion, garlic, zinger, custard apple, turmeric, chrysanthemum, neem, pongamia, tobacco etc. have used for the management of insect-pest in sericulture (Singh and Saratchandra 2005). Ghosh and Senapati (2002) reported that Azadirachtin / neem found moderate control of flea beetle (41.70%) on eggplant in terai region of West Bengal, India. Azadirachtin and extracts of Polygonum were found moderate to higher flea beetle control, recording more than 50% mortality (Ghosh 2014). Polygonum, locally known as "Biskanthali" (Sarkar and Mukherjee 2005) and its crude leaf and flower extracts of Polygonum hydropiper are responsible for mortality of Heterotermes indicola and Coptotermes heimi (Badshah et al. 2005). Ghosh et al. (2009) found that Polygonum plant extracts provided 59.77% aphid suppression in ladys finger field. Nicotine is another promising botanical pesticide (Ujvary 1999) and found effective against Bemisia tabaci Genn. (Dhaliwal and Arora 2001). A rapid degradation of persistency was found in Imidacloprid which was very important for pest control (Ghosh et al. 2012). Considering the economic importance present studies on seasonal occurrence of mealy bug (Maconellicoccus hirsutus Green) on som plant (Machilus bombycina King) and its management using bio-pesticides were undertaken.

Materials And Methods:

The field experiment was conducted under Patna University, Patna, Bihar to study seasonal occurrence of mealy bug (Maconellicoccus hirsutus Green) on som plant (Machilus bombycina King) and its management using bio-pesticides for two years. The experimental area was situated between 25°57' and 27°N latitude and 88°25' and 89°54' E longitude at terai zone of Bihar. The soil of the experimental field was sandy loam with pH 6.9.

Analysis:

Seasonal incidence of mealy bug

To study the seasonal incidence of mealy bug on som plant and their influence on weather condition, some randomly selected som plants were taken. Som plants were grown under recommended agronomic practices

without adopting any plant protection measures. The plants were fertilized once a year (90 g Urea + 140 g Single Super Phosphate + 30 g Muriate of potash / plant) after the first rain and spacing was maintain as 3 m × 3 m in 5 m × 5 m sized plots containing 4 plants with three replications. Mealy bug population was recorded per 3 leaves basis from top, middle and bottom leaves from four randomly selected plants per replication at seven days interval (standard meteorological week) throughout the year. The readings were started in the month of January and ended in December in both the years. Recorded data were presented graphically with important weather parameters like temperature, relative humidity. Correlation co-efficient (r) was worked out between incidence of mealy bug and important weather parameters during the period to find out influence of weather on population fluctuation.

Bio-efficacy of plant extracts (botanicals) against mealy bug

To study bio-efficacy of plant extracts, there were seven pesticides were taken with three sprays at ten days interval was made for each pesticide. Spraying had been done in the month of March-April starting with the initiation of infestation of mealy bug. Som plants were grown under recommended agronomic practices. The plants were fertilized once a year (90 g Urea + 140 g Single Super Phosphate + 30 g Muriate of potash / plant) after the first rain and spacing was maintain as 3 m × 3 m in 5 m × 5 m sized plots containing 4 plants. The treatments were replicated three times in a randomized block design.

Treatments details are given here under

Treatments	Dose ml/L (%)
T_1: *Polygonum hydropiper*	50.00 ml/L (5%)
T_2: *Pongamia pinnata*	50.00 ml/L (5%)
T_3: Azadirachtin (NIMARIN 1500 ppm)	2.5 ml/L
T_4: Garlic (*Allium sativum*)	50.00 ml/L (5%)
T_5: Imidacloprid (CONFIDOR 17.8 SL)	1 ml/ 5L
T_6: Tobacco (*Nicotiana tabacum*)	50.00 ml/L (5%)
T_7: *Spilanthes paniculata*	50.00 ml/L (5%)
T_8: Untreated control	-

Five botanical extracts (prepared by following certain methodology), viz. Polygonum hydropiper floral parts, Pongamia pinnata leaves, Garlic bulb (Allium sativum), Tobacco (Nicotiana tabacum) leaves and Spilanthes paniculata floral parts, one plant based insecticide formulation, Azadirachtin (NIMARIN 1500 ppm) were evaluated and compared with the chemical insecticide, Imidacloprid (CONFIDOR 17.8 SL).

Preparation of Plant Extracts

Polygonum (Polygonum hydropiper) plants were collected from Patna University Campus. The floral parts of the plant were separated and dried

out in sunlight for three days. Then it was made powder form by a mixture grinder. 50 g of powder was taken into conical flask (500 ml) and mixed with 250 ml of methanol. The material was allowed to stand for 72 hours at room temperature with occasional stirring. After 72 hours the extract was filtered through Whatman 42 filter paper and residues was washed twice with methanol. Pongamia (Pongamia pinnata) leaves, garlic (Allium sativum), spilanthes (Spilanthes paniculata) (floral parts) were extracted in methanol in the same way. The tobacco (Nicotiana tabacum) leaves were extracted in water as follows. The leaves were dried and powdered in a grinder. The powdered sample (100 g) were transferred to a container and dipped in 1000 ml water. The material was allowed to stand for 72 hours at room temperature with occasional stirring. After 72 hours the extract was filtered through Whatman 42 filter paper and added 15 ml liquid soap.

Data Recording

To study bio-efficacy of plant extracts, mealy bug population were recorded 3, 6, and 9 days after each spraying. Total mealy bug population per 3 leaves from top, middle and bottom leaves from four randomly selected plants per replication was recorded. The results were expressed as mealy bug population reduction percentage compared to population recorded on control plot. Percent reduction of mealy bug population over control was calculated by the following formula (Abbott 1925).

$$PT = \frac{P_o - P_c}{100 - P_c} \times 100$$

Where, Pt = Corrected mortality, Po = Observed mortality and Pc = Control mortality.

Data were analyzed by using INDO-STAT software for analysis of variance following randomized block design treatment means were separated by applying CD Test (critical difference) at 5% level of significance.

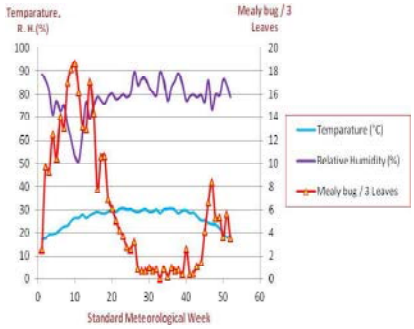

Seasonal incidence of mealy bug

The average data of mealy bug population for the two years found that the pest was active throughout the year. Higher population level of the pest was found during 2nd to 18th standard meteorological week i.e. 2nd week of January to 1st week of May and lower population level of the pest was found during 27th to 44th standard meteorological week

i.e. 1st week of July to 1st week of November. The peak population (18.68/3 leaves) was recorded on 10th standard week and it was on 2nd week of March (Fig 1).

Correlation between mealy bug and environmental parameters

Correlation studies (Table 1) between mealy bug population and environmental parameter revealed that mealy bug population had a significant positive (+) correlation with temperature difference while significant negative (-) correlation with temperature (minimum and average) and relative humidity (maximum, minimum and average). On the other hand, non-significant negative (-) correlation found between mealy bug population and maximum temperature. This indicates that activity of mealy bug population decreased with the rise of temperature and relative humidity.

Results And Discussion

Table 1 Correlation co-efficient between mealy bug and environmental parameters

Environmental parameter		Correlation co-efficient(r)	Co-efficient of determination (R^2)	Regression equation
Temperature °C	Maximum	-0.171	0.029	Y= -0.33x + 16.38
	Minimum	-0.435**	0.189	Y= -0.662x + 16.14
	Difference	0.577**	0.332	Y= 1.073x - 3.661
	Average	-0.352**	0.124	Y= -0.498x + 19.28
Relative humidity (%)	Maximum	-0.559**	0.312	Y= -0.449x + 43.55
	Minimum	-0.839**	0.703	Y= -0.457x + 39.72
	Average	-0.777**	0.603	Y= -0.540x + 48.44

*Significant at 5% level of significance; **Significant at 1% level of significance

Table 2 Efficacy of plant extracts against mealy bug on Som plant

Treatments	Dose ml/Liter (%)	Over all efficacy (% reduction or increase)1st Year					Over all efficacy (% reduction or increase)2nd Year				
		Pre-treatment Obs. mealy bug/3 leaves	3 DAT	6 DAT	9 DAT	Mean	Pre-treatment Obs. mealy bug/3 leaves	3 DAT	6 DAT	9 DAT	Mean
T1: Polygonum	50.00 ml/L	14.57	52.11	37.33	33.23	40.89	12.42	51.94	38.07	32.78	40.93
	(5 %)		(45.84)	(37.63)	(35.16)	(39.54)		(46.12)	(38.06)	(34.83)	(39.67)
T2: Pongamia	50.00 ml/L	15.83	31.51	30.63	29.63	30.59	10.56	31.15	30.64	28.70	30.16
	(5 %)		(34.13)	(33.54)	(32.89)	(33.52)		(33.90)	(33.53)	(32.33)	(33.25)
T3: Azadirachtin	2.5 ml/L	13.87	66.31	58.85	45.79	56.98	12.91	65.70	58.71	48.94	57.79
(NIMARIN 1500 ppm)			(54.57)	(50.11)	(42.56)	(49.08)		(54.23)	(50.04)	(44.38)	(49.55)
T4: Garlic	50.00 ml/L	12.89	53.52	50.97	43.66	49.38	11.53	52.65	48.23	43.40	48.09
	(5 %)		(47.03)	(45.56)	(41.32)	(44.64)		(46.52)	(43.99)	(41.14)	(43.88)
T5: Imidaclorprid	1 ml/ 5L	16.67	81.01	86.74	64.34	77.36	13.67	80.66	85.73	65.88	77.42
(CONFIDOR 17.8 SL)			(64.24)	(68.76)	(53.35)	(62.12)		(63.97)	(67.96)	(54.32)	(62.08)
T6: Tobacco	50.00 ml/L	15.52	52.18	50.31	48.56	50.35	10.53	51.44	50.74	49.66	50.61
	(5 %)		(46.26)	(45.18)	(44.17)	(45.20)		(45.84)	45.42)	(44.83)	(45.36)
T7: Spilanthes	50.00 ml/L	13.71	50.59	48.03	40.11	46.24	11.98	49.79	47.22	36.70	44.57
	(5 %)		(45.34)	(43.87)	(39.26)	(42.82)		(44.88)	(43.39)	(37.23)	(41.83)
T8: Untreated control	---	15.47	0.00	0.00	0.00	0.00	12.63	0.00	0.00	0.00	0.00
S Em (±)	---	---	1.67	1.66	1.77	---	---	1.91	2.18	2.33	---
CD at 5%	---	NS	5.15	5.13	5.46	---	NS	5.90	6.72	7.20	---

Bio-efficacy of plant extracts (botanicals) against mealy bug The different treatments and their persistence at different days after application varied significantly in their suppression of mealy bug populations (Table 2-3). Among the seven pesticides evaluated (Table 3) under the present investigation Imidaclorprid was found most effective against mealy bug providing 77.39% suppression, closely followed by Azadirachtin providing 57.38% suppression. Mandal et al. (2016) reported that Imidacloprid and Azadirachtin were found effective against sucking pest thrips on som plants recording 75.18% and 64.94% control respectively.

Ghosh et al. (2016) found that Imidacloprid and Azadirachtin were also very effective on another sucking pest aphid on som plant recording 82.46% and 71.62% control respectively. These results supported the present findings. From over all observation it was revealed that extracts of tobacco, extracts of garlic, extracts of Spilanthes and extracts of Polygonum plant gave satisfactory results, recording about 50.48%, 48.73%, 45.40% and 40.91% mealy bug suppression respectively. Mandal et al. (2016) also reported that plant extracts were found moderate thrips (sucking pest like mealy bug) control. Least effectiveness against mealy bug was recorded from Pongamia leaf extracts providing 30.37% suppression.

Table 3 Overall efficacy of plant extracts against mealy bug on Som plant (Grand Mean of Two years)

Treatments	Dose ml/Liter (%)	Over all efficacy (% reduction or increase)				
		Pre-treatment Obs. mealy bug / 3 leaves	3 DAT	6 DAT	9 DAT	Mean
T_1: Polygonum	50.00 ml /L (5 %)	13.49	52.02 (45.98)	37.70 (37.84)	33.00 (34.99)	40.91 (39.60)
T_2: Pongamia	50.00 ml/L (5%)	13.19	31.33 (34.01)	30.63 (33.53)	29.16 (32.61)	30.37 (33.38)
T_3: Azadirachtin (NIMARIN 1500 ppm)	2.5 ml/L	13.39	66.00 (54.40)	58.78 (50.07)	47.36 (43.47)	57.38 (49.31)
T_4: Garlic	50.00 ml/L (5%)	12.21	53.08 (46.77)	49.60 (44.77)	43.53 (41.23)	48.73 (44.26)
T_5: Imidaclorprid (C0NFIDOR 17.8 SL)	1 ml/ 5L	15.17	80.83 (64.10)	86.23 (68.36)	65.11 (53.83)	77.39 (62.10)
T_6: Tobacco	50.00 ml/L (5%)	13.02	51.81 (46.05)	50.52 (45.30)	49.11 (44.50)	50.48 (45.28)
T_7: Spilanthes	50.00 ml/L (5%)	12.84	50.19 (45.11)	47.62 (43.63)	38.40 (38.24)	45.40 (42.32)
T_8: Untreated control	---	14.05	0.00	0.00	0.00	0.00
S Em (±)	---	---	1.79	1.92	2.05	---
CD at 5%	---	NS	5.52	5.92	6.33	---

Mealy bug is a sucking pest and causes heavy damage to the leaves of the som plant through the year. Higher population level was maintained during 2nd standard week to 18th standard meteorological week i.e. 2nd week of January to 1st week of May and peak population (18.68/3 leaves) was recorded on 10th standard week that is on 2nd week of March. Correlation studies between mealy bug population and environmental parameter revealed that mealy bug population had a significant positive

(+) correlation with temperature difference while significant negative (-) correlation with temperature (minimum and average) and relative humidity (maximum, minimum and average). On the other hand, non-significant negative (-) correlation found between mealy bug population and maximum temperature.

Conclusion:

This paper concludes that activity of mealy bug population decreases with the rise of temperature and relative humidity. Imidaclorprid was found to be most effective against mealy bug providing more than 75% suppression however Tobacco leaf extracts gave a satisfactory mealy bug control, recording more than 50% suppression. But Imidaclorprid is a highly toxic synthetic insecticide, so there is a possibility to contaminate som plant leaf with the toxic chemicals, as som leaf is the major food component of muga silk worm rearing. Plant extracts are biological origin, eco-friendly and so can be incorporated in IPM programme against mealy bug on som plant.

Reference

Abbott W S. 1925. A method of computing the effectiveness of an insecticide. Journal of Economic Entomology 18: 265- 267.

Badshah H, Khan A S, Farid A and Khan A. 2005. Toxic effect of palpoluck (Polygonum hydropiper L.) plant extract against termites (Heterotermes indicola Was. and Coptotermes heimi Was.). Songklanakarin Journal of Science and Technology 27: 705-710.

Bhattacharya A, Saikia S K and Goswami D. 1993. Scientific inference to the traditional muga rearing. Indian Silk 32: 35-41. Borgohain A. 2015. Different insect pests in muga host plant som (Persea bombycina) ecosystem. International Journal of Development Research 5(7): 4895-4896.

Dhaliwal G S and Arora R. 2001. Role of phytochemicals in integrated pest management. In: Phytochemical Biopesticides (Eds) Koul O and Dhaliwal G S. Harwood Academic Publishers, Amsterdam, The Netherlands. pp 97-117.

Ghosh S K and Senapati S K. 2002. Field evaluation of pesticides from different origin against pest complex of brinjal/eggplant under terai region of West Bengal. Crop Research 23(1): 108-115.

Ghosh S K, Mahapatra G S S and Chakraborty G. 2009. Field efficacy of plant extracts and microbial insecticides against aphid (Aphis gossypii) infesting okra (Abelmoschus esculentus). Redia, Itali XC11: 249-252. (with sub-title Journal of Entomology).

Ghosh S K, Mandal T and Chakraborty K. 2016. Population fluctuation of aphid (Aphis craccivora Koch.) infesting Som plant leaves (Machilus bombycina King.) and its management. Journal of Entomological Research 40(3): 235-240.

Ghosh S K, Mandal T, Biswas S and Chakraborty K. 2012. Field evaluation of cultivars and bio-efficacy of insecticides against pest complex of ladysfinger (Abelmoschus esculentus L.). Journal of Applied Zoological Research 23(2): 121- 128.

Ghosh S K. 2014. Population dynamics of different species of flea beetle infesting ladysfinger (Abelmoschus esculentus L.) and their sustainable management. Journal of Applied Zoological Research 25(2): 121-128.

Kumar R, Rajkhowa G, Dhar N J and Rajan R K. 2011. A new record of Xylotrupes gideon (Linnaeus) (Coleoptera: Scarabaeidae) on Persia bombycina, Kost. from India. Munis Entomology and Zoology 6(1): 173-175.

Mandal T, Ghosh S K and Chakraborty K. 2016. Seasonal incidence of thrips (Thrips tabaci L.) infesting som plant leaves (Machilus bombycina King.) and their management using bio-pesticides. International Journal of Science Environment and Technology 5(4): 2245-2256.

Mandal T. 2013. Studies on improvement of host plant (som, Machilus bombycina King) and rearing of Muga silk worm (Antheraea assama Westwood). Ph. D. Thesis, Uttar Banga Krishi Viswavidyalaya, Pundibari, Coochbehar, West Bengal, India. pp 100, 132-133.

Sarkar A and Mukherjee P K. 2005. Ecology of Polygonum: A predominant weed in terai Agro-climatic region of West Bengal. Annals of Agricultural Research 26: 462-463.

Singh R N and Saratchandra B. 2005. The development of botanical products with special reference to seri-ecosystem. Caspian Journal of Environment Science 3: 1-8.

Singh R N, Samson M V and Dutta R K. 2000. Pest Management in Sericulture. Indian Publishers Distribution. pp 50-270. Subharani S and Jayaprakash P. 2015. Biodiversity of insect pests complex in Muga ecosystem in Narayanpur, Assam, India.

International Journal of Current Microbiology and Applied Sciences 4(12): 209-214.

Tikader A and Rajan R K. 2012. Utilization of Muga host plants for cocoon crop improvement. In: National Seminar on Recent Trends in Research and Development in Muga culture- Ideas to action (Eds). Guwahati, India, 3-4th May 2012. pp 68-71.

Ujvary I. 1999. Nicotine and other insecticidal alkaloids. In: Nicotinoid Insecticide and the Nicotinic Acetylcholine Receptor (Eds) Yamamoto I and Casida J E. Springer-Verlag, Tokyo. pp 229-269.

Operation of Low-voltage, Energy-independent, Compound Semiconductor Memory Cells at Room Temperature

Vishwajeet Kumar Chandel

Research Scholar, Dept. of Physics, J.P. University, Chapra

Abstract

While various forms of conventional (rechargeable) memories are well suited for their individual roles in computers and other electronic devices, deficiencies in their properties mean that intensive research into alternative or emerging memories continues. In particular, the goal of simultaneously achieving the conflicting requirements of non-volatility and fast low-voltage (low-energy) switching has proven challenging. Here, we report an oxide-free floating-gate memory cell based on III-V semiconductor heterostructures with discontinuous channel and non-destructive readout of stored data. Permanent data retention of at least 104s combined with switching at $\leq$2.6 V is achieved by using extraordinary 2.1 eV conduction band shifts of InAs/AlSb and a three-barrier resonant tunneling structure. The combination of low-voltage operation and small capacity implies an intrinsic switching energy per unit area that is 100 times and 1000 times smaller than that of dynamic direct access memory and Flash. The device can thus be considered an emerging memory with considerable potential.

Introduction

Static Random Access Memory (SRAM), Dynamic Random Access Memory (DRAM), and Flash have complementary properties that make them well suited for their specialized roles in cache, active memory, and data storage. Nevertheless, each of them has its disadvantages. Flash memories, first introduced in 1984, are essentially metal-oxide-semiconductor field-effect transistors (MOSFETs) with an additional floating gate (FG) for charge storage1. The data is represented by the amount of charge held in the FG, which is isolated by the oxide layers. However, the robust charge storage required for non-volatility comes at a cost. Writing and erasing requires the application of a high voltage to the control gate (CG), typically ±20 V. The process is slow and induces voltage-accelerated failure mechanisms in the oxide, which limits device lifetime.

On the other hand, only small voltages are needed to read data by testing channel conductivity. This is efficient and leaves the data intact, which is known as a non-destructive read. Unlike Flash, all single-bit DRAM operations are relatively fast, making it a powerhouse of active memory. However, data is lost from DRAM cells when read.

In addition, there is charge leakage from the capacitors used to store data, so DRAM also has to be refreshed every few tens of ms. SRAM is the fastest conventional memory and has relatively good data retention compared to DRAM, but it typically uses six transistors per cell and therefore requires a large chip footprint. These problems mean that, despite the evident long-term success of conventional memories, the search for alternatives, so-called emerging memories, continues. Charge-trap memory, phase-change memory, ferroelectric RAM, resistive RAM, conductive bridge RAM, and magnetoresistive RAM, collectively called storage-class memory (SCM), are all examples of emerging memories that have been the subject of intense research activity.

Here, we report the concept, design, modeling, fabrication, and room-temperature operation of a novel, low-voltage, compound semiconductor, charged, nonvolatile memory device with a compact form factor. The use of a spectacular AlSb/InAs conduction band array to retain charge and to create a resonant tunneling barrier allowed us to demonstrate the opposing characteristics of low-voltage (low-energy) operation and non-volatile storage.

The device is an FG memory structure formed from InAs/AlSb/GaSb heterostructures, with InAs used as both the FG and the junctionless channel. Simulations are performed to demonstrate the concept of device operation, while key memory properties of our device, such as the retention characteristics of programmed/erased states, are presented as experimental results on fully functional single-cell devices.

Operational Concept

Figure 1 is a schematic representation of the memory cell along with a transverse, high-angle, annular, dark-field scanning transmission electron microscopy (HAADF-STEM) image of the epitaxially grown material used in this work. Like Flash, the charge is stored in FG. However, there are no oxide barriers. Instead, we took advantage of conduction band offsets in the so-called 6.1-Å family of semiconductors.

Thus, the device below the memory cell is more similar to a high electron mobility transistor (HEMT) than a MOSFET. The channel is made

of InAs, which does not contain any junctions or doping concentration gradients. However, it is n-doped to compensate for unintentional background doping and internal Ga vacancies and antisit defects in the underlying GaSb, both of which make the layers inherently p-type. Figure 2a shows the simulated band alignment along with the electron and hole density in the layers in the absence of bias. As shown in the figure and well documented in the literature, at the InAs/GaSb interface, the conductivity of InAs is located below the valence band of GaSb, resulting in electron flow from GaSb to InAs, leaving holes in GaSb.

Accumulated electrons/holes can be seen at the InAs/GaSb interface, however, electrons in the InAs channel are not bound to the InAs/GaSb interface and there is significant electron density throughout the InAs channel. The conductivity of the entire channel is dominated by electrons in InAs, which will have higher mobility and higher areal density (due to doping) than holes in GaSb.

The native InAs FG is isolated from the InAs channel by a 15nm AlSb barrier, while double InAs quantum wells (QWs) with triple AlSb barriers serve as a resonant tunneling barrier between the FG and the n-doped InAs CG.

Thus, in our devices, electrons stored in InAs FG are isolated by an anomalously large conduction band discontinuity with AlSb, a charge confinement system predicted to have a thermally activated storage lifetime at room temperature of an extraordinary 1014 years.

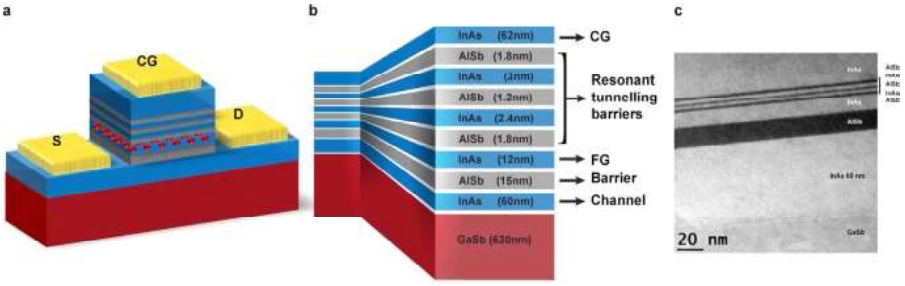

Figure 1: *Device structure. (a) Schematic of the processed device with control gate (CG), source (S) and drain (D) contacts (gold). The red spheres represent stored charge in the floating gate (FG). (b) Details of the layer structure within the device. In both (a,b) InAs is coloured blue, AlSb grey and GaSb dark red. (c) Cross-sectional scanning transmission electron microscopy image showing the high quality of the epitaxial material, the individual layers and their heterointerfaces.*

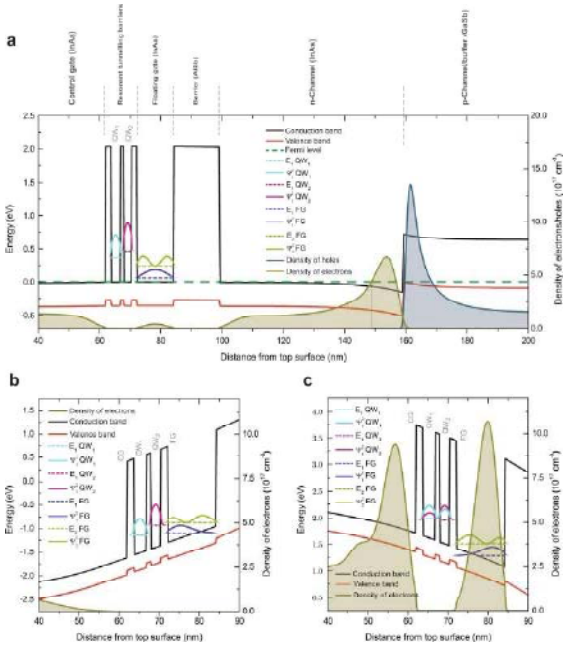

Figure 2: *Calculated band diagram vertically through the structure. The black and red lines represent the bottom of the conduction band and the top of the valence band respectively, whilst the green long-dashed line is the Fermi-level. Short-dashed lines represent energies of the lowest confined states in the quantum wells (QWs) of the resonant-tunnelling structure, and the ground and the first excited-states in the floating gate (FG). The probability densities,* $|\Psi|2$, *for the position of the electrons in the QWs and the FG are plotted in arbitrary units. The densities of electrons and holes are plotted as olive and blue shaded areas respectively. (a) In the absence of bias across the device. (b) At the end of the erase process with* $V^{E}CG"S$ *=+2.6V, showing the depletion of the FG of electrons. (c) At the end of the write process when* $V^{W}CG"S$*="2.6V. This results in a significant density of electrons in the FG.*

A crucial aspect of the device design and operation is that the two QWs (QW1 and QW2) in the triple resonant tunneling barrier have different thicknesses, i.e. confined states with different energies 21, as shown in Fig. 2a. Because QW2 is thinner than QW1, the only available energy level for electrons in QW2 has a higher energy than the equivalent in QW1. In addition, the state in QW1 is at significantly higher energy than the state in the neighboring CG region. This prevents direct tunneling of electrons between CG and FG, so that when the system is unbiased, the barrier to electron passage from CG to FG (or vice versa) is given by the InAs/AlSb conduction band offset of 2.1eV, i.e. charge will flow into (or out of) FG. Likewise, the ground and first excited states in FG are located well below the energy states in QW. Therefore, when no voltage is applied,

the electrons are confined inside the FG, the triple resonant tunneling barrier is opaque to the passage of electrons into or out of the FG, and non-volatility is achieved. On the other hand, the application of a small voltage to the CG enables a tunable coupling of energy states inside the resonant tunneling barrier such that electrons pass from (Fig. 2b) or into (Fig. 2c) the FG as required. In this work, read, write, and erase operations were performed on a number of $10\ \mu\text{m} \times 10\mu\text{m}$ (gate size) cells in an electrostatically shielded dark box at room temperature. All processes, including writing and erasing, were performed with a bias voltage of d"2.6 V, which is about an order of magnitude lower than that required to fully operate the Flash cell. Clearing was performed by applying a CG bias, VECG"S, +2.5 or +2.6V between the CG and the source, resulting in a "0" state. Figure 2b shows the calculated band alignments resulting from applying a $\leq$2.6V smear voltage. Under such circumstances, the calculated electron energy level in QW1 is lower than that in QW2, while both are below the first excited state and close to the ground energy level in FG. Furthermore, the calculated electron probability density for the ground state in FG predicts a high electron accumulation at the interface with a resonant tunneling barrier and a decaying tail extending into the first AlSb barrier (left). Thus, the net effect of erasure is a flow of electrons from FG to CG, which depletes FG. Similarly, write used VWCG–S=–VECG–S to increase the charge in FG (state "1"). Figure 2c shows the calculated band diagram when the CG bias VWCG–S =–2.6V is used to write the data. In this case, the energy levels in QW1 and QW2 are almost identical, leading to strong coupling of these states, resonant tunneling and flux of electrons from CG to FG, thereby charging FG.

Because of capacitive coupling, the channel conductance depends on the amount of charge stored in the FG, so data is read by measuring the source-drain current, IS-D, for a fixed source-drain voltage, VS-D. The "1" state, defined as an increased charge in the FG, decreases the charge in the channel and thus its conductance. Conversely, the "0" state increases the channel conductivity. Data can be read in the absence of any bias to the CG, but such a voltage would be required to select individual devices (bits) in the cell array and would generate an electric field across the resonant tunneling barrier, which is insufficient. allow the charge to pass into or out of the FG. Using $\sim 2.5\text{V}$ between the center of gravity and the common back gate this can be conveniently achieved.

Characteristics of Memory

For the results presented here, the reading was taken with zero bias at CG and VS-D=1.0 V, although significantly smaller VS-D can easily be used. Figure 3a shows a series of erase-read-write-read operations in which

each write or erase is followed by a single read. A portion of a substantially extended sequence of erase-read-write-read operations is shown in Fig. 3b, with several reads after each write or erase. This clearly demonstrates the non-destructive nature of the read operation. A clear differentiation between the "0" and "1" states is preserved in both sequences, although in Fig. 3b there is an undesirable but almost symmetric upward shift in IS-D with increasing number of operations. The reason for this requires further investigation, but it is likely to be an asymmetry in the write and erase process, so that each erase removes slightly more charge from the FG than the write adds. There is no such drift in Fig. 3a, where the write/ erase voltages are slightly lower. After several hundred write and erase operations and many more reads in various experiments, there were no signs of damage to the device. Research is currently underway into the automated characterization of single-cell device resilience and the definition of suitable architectures and operational processes for memory cell arrays.

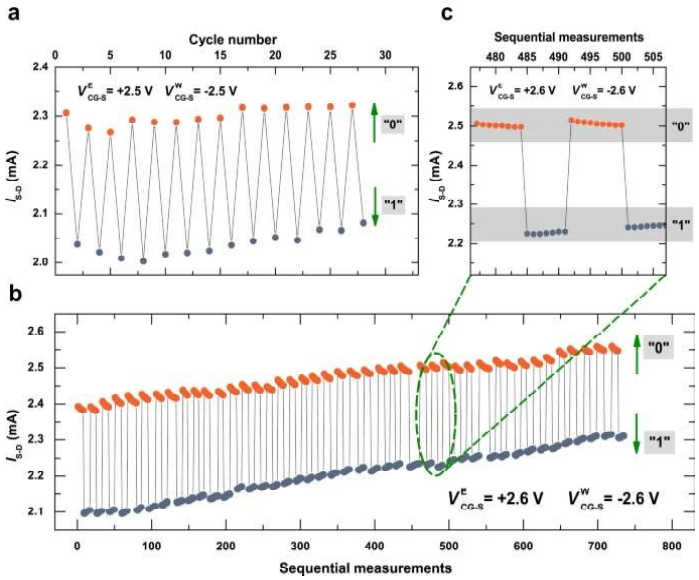

Figure 3: *Erase-read-write-read cycles. "0" and "1" states are prepared by application of erase and write voltages, VECG"S and VWCG"S, respectively, and read via the source-drain current, I_{S-D}, with 1.0 V bias across the channel and zero bias on the control gate. (a) Single read measurements subsequent to each erase or write. (b) Part of an extended measurement with multiple reads (every 1 s) following each erase or write operation (>80 cycles shown). (c) A detail of a portion of the data in b showing a slight convergence of I_{S-D} for "0" and "1" states following erase and write. In (b,c) the number of reads following each write or erase is arbitrary.*

In addition to non-volatility and low-voltage write and erase, a low switching energy is an important characteristic of a memory, and one which emerging memories have struggled to compete with DRAM and Flash. In common with those conventional memories, our devices are also based on charge storage, so the switching energy is given by the capacitive charging energy: low-voltage switching is synonymous with low-energy switching. Indeed, since our devices have a similar structure to Flash, simply assuming the same capacitance for the same gate dimension, infers that the switching energy is ~$(20/2.5)^2$=64 times less than Flash, which also puts it lower than the switching energy for DRAM (for a given device size). Theoretical evaluations suggest a CG-FG capacitance of the order of 10^{-12} F for a $10\mu m \times 10\mu m$ (gate dimension) device, and a switching energy of $\sim 2\times10^{-12}$ J. Shrinking the device dramatically decreases this number, such that the switching energy is of the order of 10^{-17} J for the 20nm node, which is 100 and 1000 times smaller than for DRAM and Flash respectively. This potential for ultra-low switching energy in an emerging memory is, to the best of the authors' knowledge, unique.

Retention

Figure 3c shows a detail of some of the write-erase operations in Fig. 3b, revealing a different variation in the "0" and "1" states: successive read measurements following an erase yield a slightly smaller $I_{S\text{-}D}$ for the "0" state. Similarly, for successive read measurements following a write, $I_{S\text{-}D}$ is slightly larger. This effect is thus different to the upward drift in $I_{S\text{-}D}$ discussed above, and is related to the volatility of the data. To investigate this further we performed successive read operations over extended periods for each memory state. Examples of such measurements are shown in Fig. 4, where the retention characteristics of the memory cells were studied by monitoring their time-dependent behaviour at a constant $V_{S''D}$ =1.0V. For this purpose, a read was performed every second for about an hour following an erase pulse (*VECG"S*=+2.6V, pulse duration 1.0s). After this experiment, the memory was programmed to the "1" state by a write voltage pulse (*VWCG"S*="2.6V, pulse duration 1.0s), and the data was read in the same way. Both "0" and "1" states exhibit an initial rapid decay that is consistent with that seen in Fig. 3c. However, for both memory states the initial rapid decay is followed by much slower changes, such that during the entire observation time, the corresponding "0" and "1" states are clearly distinguishable. To further investigate the retention properties of these memory devices, a separate experiment was performed on the same device for an extended period of time. This is illustrated in the inset

of Fig. 4, showing the ultimate saturation of the exponential decays and distinct "0" and "1" states over time. Such a storage time is at least 10^6 times longer than the refresh time required for DRAM.

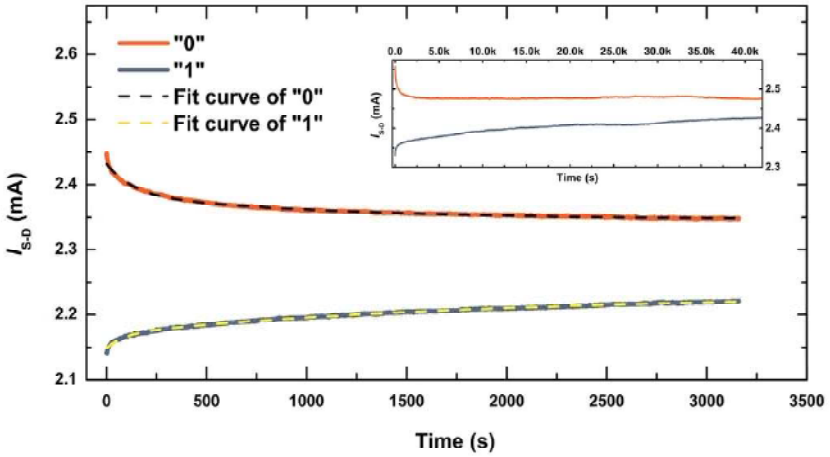

Figure 4: Data retention following write and erase. Time evolution of the "0" and "1" states as measured by the source-drain current, $I_{S\text{-}D}$, (solid orange and navy lines, respectively) follow double-exponential decay (dashed lines) with asymptotic values that do not converge. Data was taken with 1.0V source-drain bias and zero bias on the control gate. The inset shows an example of an overnight measurement (>12hours).

Fitting the data in Fig. 4 with double exponential decay functions reveals that the initial 'fast' component has a time constant of $\sim$100s, while the time constant for the 'slow' component is approximately an order of magnitude longer, for both states. The existence of double exponential decay implies that there are at least two mechanisms behind the degradation of the states. Candidates include tunnelling through defect states in the AlSb barriers, thermal excitation of electrons across the narrow InAs bandgap and recombination with thermally-generated holes. Crucially, the asymptotic values of the "1" and "0" states are 2.232 ± 0.0002 and 2.346 ± 0.000 1mA respectively, indicating that discernible "1" and "0" states could endure indefinitely, *i.e.* the data in Fig. 4 are consistent with non-volatility. We note that even though these states are clearly distinguishable in this experiment, a larger contrast is required for implementation in a practical device. From consideration of the capacitance of the device and the applied write/erase voltage, we estimate that write and erase transfer ~10^7 electrons to or from the FG. Despite the fact that this is a large number, it has a small effect on the conductivity of the laterally-junctionless InAs channel. This is mainly due to the Fermi-

level pinning above the conduction band of the highly doped InAs channel which makes it always conductive and very hard to deplete. Furthermore, the In As channel is 5 times thicker than the FG, leading to a higher level of intrinsic or thermally-generated carriers in this layer. This can be resolved by making the channel thin and narrow enough to allow for full depletion of carriers when the memory is in the "1" state. Strong quantum confinement and, thus, heavy quantisation is expected at sub-20-nm thicknesses.

Conclusions

We have demonstrated room-temperature operation of non-volatile, charge-based memory cells with compact design, low-voltage write and erase and non-destructive read. The contradictory requirements of non-volatility and low-voltage switching, are achieved by exploiting the quantum-mechanical properties of an asymmetric triple resonant-tunnelling barrier. The compact configuration and junctionless channel with uniform doping suggest good prospects for device scaling, whilst the low-voltages, non-volatility and non-destructive read will minimise the peripheral circuity required in a complete memory chip. These devices thus represent a promising new emerging memory concept.

Methods

Simulations

The nextnano software package was utilised for mathematically modelling the energy band diagram of the memory device structure reported here, taking into account strain and piezoelectricity. Within this work, a self-consistent Schrödinger solver was used along with the Poisson and drift–diffusion equations to calculate the electron densities at equilibrium and under bias.

Molecular Beam Epitaxy

The InAs/AlSb/GaSb heterostructures were grown on a semi-insulating, undoped, 2-inch GaAs wafers using molecular beam epitaxy (MBE). A GaAs substrate was chosen because of the long-term need for low-cost manufacture, even though the resulting mismatched epitaxy reduced device yield in the present work. First, the (100) GaAs substrate was annealed for 15minutes at 600°C to remove the native oxide layer. After oxide desorption, the substrate was cooled down to 570°C and the growth initiated with a 50-nm GaAs buffer layer followed by a 250-nm-thick n-type ($5\times10^{17}cm^{-3}$ Si-doped) GaAs layer. This doped layer forms a buried back-gate, but was not used in the experiments reported here. A SUMO® K-cell was used as the Ga source, along with a valved cracker

source configured for As dimers. Next, a 100-nm $Al_{0.8}Ga_{0.2}As$ layer was grown with an Al SUMO® K-cell at the same substrate temperature to separate the GaAs back-gate from the other active layers, in both the processing and electrical measurements of devices. After the growth of a further GaAs buffer layer of 10nm, the As source was shut for 1 minute to minimise the As background, followed by a 10s growth interrupt to desorb the As surface layer from the sample. This was in preparation for the growth of the GaSb via the interface misfit method, needed for the transition to the ~6.1Å lattice constant of the active layers of the device. Following the initial introduction of Sb_2 flux from a valved cracker source, the substrate temperature was decreased to 500 °C and a 630-nm-thick GaSb layer was grown. The substrate temperature was further decreased to 440 °C for the growth of the n-type InAs channel ($5 \times 10^{17} cm^{-3}$ Si-doped). Due to the use of radiative heating in the MBE reactor and an undoped substrate, infrared absorption within the narrow-bandgap epilayer led to an increase in surface temperature to an estimated 470°C during the growth of the InAs channel. The 15-nm-thick AlSb charge-blocking-barrier layer, the 12-nm-thick InAs floating gate and the AlSb/InAs resonant-tunnelling barrier were grown with InSb-like interfaces to ensure abrupt boundaries between materials and good electrical characteristics. Finally, the control gate was grown with a 7-nm-thick cap layer of intrinsic InAs followed by 55 nm of heavily-doped (1×10^{18} cm^{-3} Si) n-type InAs.

Device Processing

A top-down processing procedure was employed to fabricate the memory devices with gate dimension of $10\ \mu m \times 10\ \mu m$. In this device design, there are four different electronic terminals: the GaAs back-gate, the source and drain terminals on the InAs channel, and the control gate on the top InAs layer. Separate UV lithography stages were used to pattern the back gate, device mesa and source/drain areas. At each step, excess material was dry etched with an Oxford Instruments Plasma Lab 100 inductively-coupled plasma (ICP) machine. The etching process was carried out using a $BCl_3/Cl_2/Ar$ (8.5/2.5/5 sccm) gas mixture and a chamber pressure of 4 mTorr, with an ICP power of 120 W and an RF power of 25W. During the process, the sample holder temperature was kept at 10°C by the combination of helium flow and the use of FOMBLIN vacuum oil to achieve the desired thermal conductivity between the substrate and the sample holder. After sculpting the surface of the grown wafer, a 200-nm SiO_2 layer was deposited on the sample using an Oxford Instruments plasma-enhanced chemical vapour deposition machine. The SiO_2 layer provides device isolation, and prevents any shorts between the subsequent metal contacts in the probing areas and underside layers. In order to attain

good adhesion between the hydrophobic SiO_2 layer and the photoresist, a thin discontinuous layer of Al_2O_3 was thermally grown on the surface of the sample. However, to get access to the top and back gates, the source and the drain, the oxide layer was chemically etched (using buffered oxide etch, 10:1) in the contact areas, which were exposed through openings in the photoresist provided by UV lithography. A hard-baked positive photoresist lifting layer was then patterned on one edge of the devices by UV lithography. This enabled deposition of continuous contacts, and at the same time, prevented any shorts between the metal and the layers (other than the desired ones) in regions where the oxide was possibly partly over-etched. To form ohmic contacts to InAs (control gate, source and drain) and GaAs (back gate), saturated ammonium polysulphide ($(NH_4)_2S:S_x$) was used to remove the native oxide with minimal semiconductor material removal and to passivate the semiconductor surface in the contact areas. Finally, the metal contacts were formed by deposition of 20/100nm Ti/Au with an e-beam evaporator.

Electrical Measurements

Current-voltage measurements were carried out on individual devices using a dual-channel Keithley 2634B source meter unit. Memory chips were mounted on to a ceramic chip holder, with connections formed by gold wire attached between bond pads and the chip holder. Semi-automated measurements using custom-made software were performed in darkness at room temperature and pressure, with the sample in an electrically-shielded switching box. All measurements reported here were on $10\ \mu m \times 10\ \mu m$ devices. Erase was performed with *VECG–S* of +2.5 or +2.6V applied between the control gate and the channel, with source and drain grounded, and similarly for write, with *VWCG"S*=–*VECG–S*. Read was performed by measuring $I_{S\text{-}D}$ with $V_{S\text{-}D}$ =1 V and the control gate grounded. Write and erase pulses were 1s in duration, while read pulses were 10ms. The back gate was not used, and remained grounded. No bias was required to retain the charge in the floating gate.

Transmission Electron Microscopy Measurements

A conventional method was used to prepare the specimen in cross section for the analysis by HAADF-STEM. This consisted of mechanical thinning by SiC sandpaper to a thickness of 30μm, followed by Ar^+ milling using a precision ion-polishing system to create a hole. The area suitable for study is located at the edges of the hole. The beam energy during milling has to be controlled carefully to obtain a high-quality electron-transparent sample; 3.5kV was used at the beginning, and 2kV at the last

step, to get a clean and smooth surface. The HAADF-STEM study was carried out using a JEOL 2010 F at 200kV.

References

1. Bez, R., Camerlenghi, E., Modelli, A. & Visconti, A. Introduction to flash memory. *Proc. IEEE* **91**, 489–502 (2003).
2. Aritome, S. *Nand Flash Memory Technologies*. (John Wiley & Sons, Inc. https://doi.org/10.1002/9781119132639 (2015).
3. Aritome, S., Shirota, R., Hemink, G., Endoh, T. & Masuoka, F. Reliability issues of flash memory cells. *Proc. IEEE* **81**, 776–788 (1993).
4. Chen, J. J., Mielke, N. R. & Hu, C. C. *Nonvolatile Memory Technologies with Emphasis on Flash*. *Nonvolatile Memory Technologies with Emphasis on Flash: A Comprehensive Guide to Understanding and Using Flash Memory Devices* (John Wiley & Sons, Inc. https://doi.org/10.1002/9780470181355 (2007)
5. Jacob, B., Ng, S. W. & Wang, D. *Memory Systems - Cache, DRAM, Disk*. (Morgan Kaufmann Publishers Inc., 2007).
6. Akerman, J. Toward a Universal Memory. *Science (80-.).* **308**, 508–510 (2005).
7. Wong, H.-S. P. & Salahuddin, S. Memory leads the way to better computing. *Nat. Nanotechnol.* **10**, 191–194 (2015).
8. Tian, H. *et al*. A Dynamically Reconfigurable Ambipolar Black Phosphorus Memory Device. *ACS Nano* **10**, 10428–10435 (2016).
9. Zhang, E. *et al*. Tunable Charge-Trap Memory Based on Few-Layer MoS 2. *ACS Nano* **9**, 612–619 (2015).
10. Wong, H.-S. P. *et al*. Phase Change Memory. *Proc. IEEE* **98**, 2201–2227 (2010).
11. Koelmans, W. W. *et al*. Projected phase-change memory devices. *Nat. Commun.* **6**, 8181 (2015).
12. Guo, R. *et al*. Non-volatile memory based on the ferroelectric photovoltaic effect. *Nat. Commun.* **4**, 1990 (2013).
13. Lee, Y. T. *et al*. Nonvolatile Ferroelectric Memory Circuit Using Black Phosphorus Nanosheet-Based Field-Effect Transistors with P(VDF-TrFE) Polymer. *ACS Nano* **9**, 10394–10401 (2015).
14. Yang, J. J., Strukov, D. B. & Stewart, D. R. Memristive devices for computing. *Nat. Nanotechnol.* **8**, 13–24 (2012).
15. Baeumer, C. *et al*. Spectromicroscopic insights for rational design of redox-based memristive devices. *Nat. Commun.* **6**, 8610 (2015).
16. Cappelletti, P. Non volatile memory evolution and revolution. In *2015 IEEE International Electron Devices Meeting (IEDM)* **2016–Febru**, 10.1.1-10.1.4 (IEEE, 2015).
17. Kwon, K.-C. *et al*. Nanoscale CuO solid-electrolyte-based conductive-bridging-random-access-memory cell operating multi-level-cell and 1selector1resistor. *J. Mater. Chem. C* **3**, 9540–9550 (2015).
18. Chappert, C., Fert, A. & Van Dau, F. N. The emergence of spin electronics in data storage. *Nat. Mater.* **6**, 813–823 (2007).
19. Hu, J.-M., Li, Z., Chen, L.-Q. & Nan, C.-W. High-density magnetoresistive random access memory operating at ultralow voltage at room temperature. *Nat. Commun.* **2**, 553 (2011).

20. Freitas, R. F. & Wilcke, W. W. Storage-class memory: The next storage system technology. *IBM J. Res. Dev.* **52**, 439–447 (2008).
21. Hayne, M. Electronic memory devices. Patent US10243086B2.
22. Kroemer, H. The 6.1 Å family (InAs, GaSb, AlSb) and its heterostructures: a selective review. *Phys. E Low-dimensional Syst. Nanostructures* **20**, 196–203 (2004).
23. Dutta, P. S., Bhat, H. L. & Kumar, V. The physics and technology of gallium antimonide: An emerging optoelectronic material. *J. Appl. Phys.* **81**, 5821–5870 (1997).
24. Nowozin, T., Bimberg, D., Daqrouq, K., Ajour, M. N. & Awedh, M. Materials for Future Quantum Dot-Based Memories. *J. Nanomater.* **2013**, 1–6 (2013).

Machine Learning-driven Discovery of a new Thermoelectric Material

Dheeraj Kumar Singh

Research Scholar, Dept. of Physics, J.P. University, Chapra

Abstract

Thermoelectric technologies are becoming indispensable in the search for a sustainable future. Recently, an emerging phenomenon, the spin-controlled thermoelectric effect (STE), has attracted much attention as a promising route to a low-cost and versatile thermoelectric technology with easily scalable fabrication. However, progress in the development of STE devices is hindered by a lack of understanding of the fundamental physical and material properties responsible for this effect. In such a nascent scientific field, data-driven approaches that rely on statistics and machine learning instead of more traditional modeling methods can show their full potential. Here, we use machine learning modeling to determine the key physical parameters governing STEs. Based on the models, we performed a real material synthesis that led to the identification of a new STE material with a thermal strength an order of magnitude greater than that of the current generation of STE devices.

Introduction

Waste heat is ubiquitous in modern society, and thermoelectric technologies based on the Seebeck effect have been seen as a central route to a sustainable future. Unfortunately, conventional thermoelectric (TE) devices suffer from high manufacturing costs due to their complex structure, in which p-type and n-type thermoelectric materials are cascaded in an alternating manner. The emergence of new thermoelectric devices based on spin controlled thermoelectric phenomena (STE) offers a potential solution to this problem. Unlike conventional TE devices, STE devices consist of simple layered structures and can be fabricated by straightforward processes such as sputtering, coating, and plating, resulting in lower manufacturing costs. Another advantage of STE devices is that they can double their function as heat flow sensors due to their flexible design and lower thermal resistance.

STE devices utilize the spin-Seebeck effect (SSE) and the anomalous Nernst effect (ANE). SSE generates a spin current from a temperature gradient in the magnetic material. By attaching a metal film with a large spin-orbit interaction (such as Pt) to a magnetic material, it is possible to convert the spin current into an electric current via the inverse spin-Hall

effect (ISHE). SSE-based thermoelectric conversion may lead to a whole new class of low-cost and versatile thermoelectric devices. Unfortunately, progress in device development is hindered by a lack of understanding of the fundamental mechanism of SSE and the materials parameters that control it. Several different theories have been put forward to explain this phenomenon, but a unified picture of its mechanism is yet to emerge. The key material parameters determining SSE have not yet been identified and there are no clear pathways to increase thermal strength and related values.

But in areas where basic understanding is still too unreliable to drive progress, data-driven approaches using statistical modeling and machine learning can be used to uncover hidden links and correlations. Machine learning methods are becoming indispensable tools for studying materials. These methods are now commonly used to address many key questions in materials science. In particular, machine learning-based models are being used to search for new materials, including potential magnets, ferroelectrics and superconductors. Although machine learning-driven material synthesis has been relatively rare so far, it is very likely to become commonplace in the future.

Using these methods, we developed a systematic approach to reveal the main material variables that control SSE. We combine machine learning modeling with high-throughput experimentation and use the modeling results to design combinatorial libraries. We have successfully used machine learning-based knowledge of the dependence of SSE on material parameters to arrive at a novel and high-performance STE material using ANE that converts thermal current to electric current via spin-orbit interaction in a single ferromagnetic material. From a number of proposed material systems, the expansion of the composition of one ternary system led to the identification of Fe0.665Pt0.27Sm0.065, which exhibits a thermal strength of up to 11.12 μV/K.

Results

Material Data Collection

First, we performed experiments to collect STE data for various materials. Figure 1a shows the general configuration of one of the STE devices using the spin-Seebeck effect (SSE). It is composed of a paramagnetic conductive layer, a magnetic layer, and a single crystal substrate. We adopted a bilayer consisting of platinum (Pt) and rare-earth-substituted yttrium iron garnet ($R_1Y_2Fe_5O_{12}$, referred to as R:YIG), where R stands for a rare-earth element. When a temperature difference Ä*T* and a magnetic field *H* are applied along the z and the x direction, respectively,

one can detect the thermopower S_{STE} along the y direction. Therefore, this device converts electric energy into thermal energy. The details of the STE device are shown in the Supplementary Information 1.

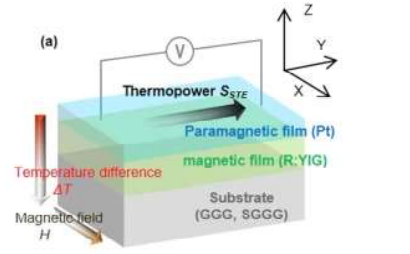

(c)

	Δa	n_R	S_R	L_R	S_{STE}
Δa	1				
n_R	-0.576	1			
S_R	-0.373	0.366	1		
L_R	-0.323	0.334	0.309	1	
S_{STE}	-0.301	0.453	-0.269	0.452	1

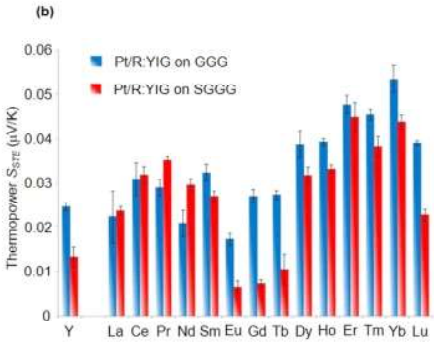

Figure 1: *Data of spin-driven thermoelectric materials. (a) Schematic of the spin-driven thermoelectric (STE) device using spin-Seebeck effect (SSE) consisting of a Pt layer, a rare-earth substituted yttrium iron garnet ($R_1Y_2Fe_5O_{12}$, referred to as R:YIG) layer and a (111)-oriented Gadolinium Gallium Garnet ($Gd_3Ga_5O_{12}$, referred to as GGG) substrate or a (111)-oriented Substituted Gadolinium Gallium Garnet ($Gd_{2.675}Ca_{0.325}Ga_{4.025}Mg_{0.325}Zr_{0.65}O_{12}$, referred to as SGGG) substrate. When a temperature difference AT and a magnetic field H are applied along the z and x direction, respectively, one can detect the thermopower S_{STE} along the y direction. (b) Data of the thermopower S_{STE} for different rare-earth substituted YIG (R:YIG). The magnitude of S_{STE} varies depending on the choice of rare-earth element. Error bars are standard deviation. (c) Pearson correlation coefficient (PCC) matrix. The values with respect to S_{STE} are less than 0.5.*

Substitution in R:YIG with different rare earth elements changes the physical properties of the material and allows us to study the impact this has on STE phenomena. Figure 1b shows the thermal energy measured for Pt/R:YIG samples, fabricated on Gd3Ga5O12 (GGG) and Gd2.675Ca0.325Ga4.025Mg0.325Zr0.65O12 (SGGG) substrates and with different rare earth elements R - La, Ce, Pr , Nd , Sm, Eu, Gd, Tb, Dy, Ho, Er, Tm, Yb and Lu (Pm, which is radioactive, was excluded from the study). It is clear that the SSTE strongly depends on the choice of the element R. The differences in the measured SSTE can be dramatic; for example, the response of Pt/Yb:YIG to GGG is about three times that of Pt/YIG to GGG.

The striking dependence of the SSTE on the choice of R suggests that the physical parameters of R strongly influence the STE. We used machine learning to uncover and quantify this connection. As a first step, we

considered different descriptors that can encode the properties of different rare earth elements, such as atomic mass nR, spin and orbital angular momentum SR and LR, lattice mismatch Äa between R:YIG and substrate, number of unfilled orbitals, melting temperatures of elements, magnetic moments and ground state volumes, etc. However, it is difficult to experimentally isolate and extract the dependence of SSTE on a given physical parameter R. To delineate the relationship between atomic mass nR and SSTE, for example, it would be necessary to measure SSTE for different nR while keeping all other predictors fixed, which is not experimentally feasible. To reveal the subtle correlations and physical origins of the STE hidden in the initial experimental results, we first calculated the Pearson correlation coefficient (PCC) [shown in Fig. 1(c)]. There appears to be a roughly linear relationship between Äa, nR, SR, LR, and SSTE. However, for SSTE, the absolute PCC values are less than 0.5, making the results inconclusive. In order to get more reliable information, we conducted another investigation using supervised machine learning.

Modeling Using Machine Learning

We used four types of supervised machine learning models: decision tree regression (DTR), elastic network (EN), quadratic polynomial LASSO (QP-LASSO), and neural network (NN). DTR and EN models are limited to simple dependencies only, but they are easy to use and can be used to extract dominant descriptors. In contrast, the NN model is very flexible and can reproduce highly nonlinear dependence, but is much more difficult to interpret and prone to overfitting. QP-LASSO is somewhere between NN and EN in terms of complexity and interpretability. To reduce the risk of overfitting the available experimental data, we fix the number of descriptors at four, namely Äa, nR, SR and LR. In the Methods section, we discuss how these parameters were selected from a large set (#) of possible descriptors.

We begin by constructing a DTR model that predicts the target variable—in this case, SSTE—by learning a series of simple decision rules based on descriptors (Äa, nR, SR, and LR). Figure 2a shows a visualization of the DTR model. Simple decision rules based on inequalities sort the data points quite accurately. Note that the white numbers and percentages in the figure indicate the mean SSTE values and proportion of data points for each group. By observing the DTR model, we can directly derive the relationship between SSTE and descriptors. Smaller SR, smaller Äa, and larger nR lead to large SSTE in the DTR model. However, we were unable to obtain a relationship between SSTE and LR through this model.

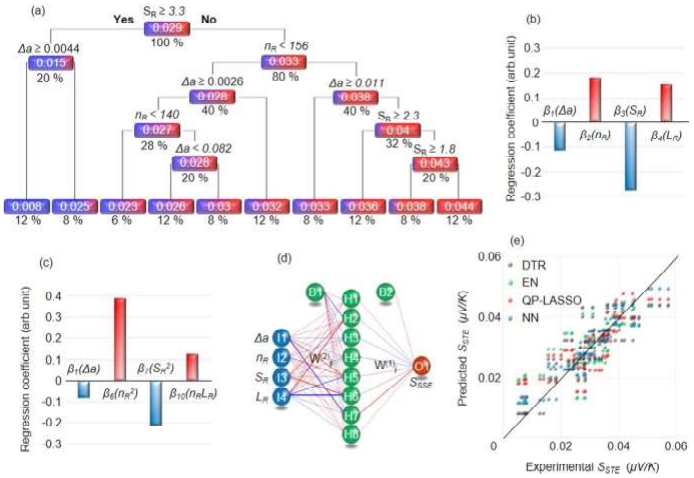

***Figure 2**: Informatics approach. (a) Visualization of the decision tree regression (DTR). Äa and S_R are negatively correlated with S_{STE}, while the n_R have positive correlation with S_{STE}. (b) Regression coefficients for the elastic net (EN) model. The value of constant term $\hat{a}_0$ is 0.3310662. Äa and S_R are negatively correlated with S_{STE}, while the n_R and L_R have positive correlation with S_{STE}, (c) Regression coefficient in the quadratic polynomial LASSO (QP-LASSO). The value of $\hat{a}_0$ is 0.3039554. Äa and S2R are negatively correlated with S_{STE}, while the n2R and n_RL_R have positive correlation with S_{STE}, (d) Visual representation of the neural network (NN) model. The line width represents the connection strength between units. Red/blue color demonstrate positive/negative correlation. (e) Predicted vs. measured values of S_{STE} for the DTR, EN, QP-LASSO and NN models. The cross validation error of the DTR, EN, QP-LASSO and NN are 8.56×10^{-2}, 8.80×10^{-2}, 8.55×10^{-2} and 5.52×10^{-2}, respectively.*

As a next step, we constructed a generalized linear model, EN, which is a combination of Ridge and LASSO regressions. This method assumes linear relationship between S_{STE} and the descriptors:

$$S_{STE}(\Delta a,\, n_R,\, S_R,\, L_R) = \beta_0 + \beta_1 \Delta a + \beta_2 n_R + \beta_3 S_R + \beta_4 L_R \quad (1)$$

Although linearity can be an unnecessarily strong assumption, it helps minimize over-fitting. Figure 2b shows the values of β_1, β_2, $\beta_3$andβ_4 obtained as a result of the regression fit. We can directly interpret the relationship between descriptors and S_{STE}. The n_R and L_R have positive correlation with respect to $S_{STE,}$ while the Δa and S_R have negative correlation with S_{STE}. However, DTR and especially EN models are very constrained and preclude proper modeling of more complicated dependencies. Therefore, to verify the patterns found by the EN, non-linear regression analysis using quadratic polynomial LASSO (QP-LASSO)

model is applied next. We expand the linear model in equation 1 into a quadratic one:

$$\begin{aligned} S_{STE}(\Delta a,\, n_R,\, S_R,\, L_R) \;=\; & \beta_0 + \beta_1 \Delta a + \beta_2 n_R + \beta_3 S_R + \beta_4 L_R \\ & + \beta_5 \Delta a^2 + \beta_6 n_R^2 + \beta_7 S_n^2 + \beta_8 L_n^2 \\ & + \beta_9 n_R S_R + \beta_{10} n_R L_R + \beta_{11} S_R L_R \end{aligned} \qquad (2)$$

(Note that interaction terms between the extrinsic (Δa) and the intrinsic (n_R, S_R, L_R) factors with respect to the R element were deliberately not included.) QP-LASSO performs descriptor selection by adding L_1 regularization term. This term tends to suppress the coefficients $(\beta_0,\ \ldots.,\beta_{11})$, and as a result only the ones in front of the most significant descriptors remain finite. Here, the QP-LASSO automatically selected four important descriptors: Δa, n_R^2, S_R^2 *and* $n_R L_R$. The values of these coefficients $-\beta_1, \beta_6, \beta_7 \text{and} \beta_{10} -$ are shown in Fig. 2c. The n_R and $n_R L_R$ terms are positively correlated with S_{STE}, while the coefficients in front of Δa and S_R^2 are negative. This agrees with the conclusions of the EN models.

The fourth algorithm we use is the NN - by far the most flexible of the four machine learning models we have employed. The flexibility comes at the price of significant risk of over-fitting, as well as difficulties interpreting the results. Figure 2d shows a visualization of the NN modeling result. By investigating the complex connections between the nodes (balls) carefully, we can find that the S_{STE} increases with increasing of n_R and L_R, while the S_{STE} increases with decreasing of Δa and S_R.

Figure 2e shows the accuracy of DTR, EN, QP-LASSO, and NN models. The horizontal and vertical axes are the values of S_{STE} measured in the experiments and those predicted by the machine learning models, respectively. We see that the NN model has better accuracy than the DTR, EN and QP-LASSO models, due to its much higher complexity. On the other hand, although the accuracy of the DTR, EN and the QP-LASSO models is not as high, interpreting their implications is much more straightforward. Despite these differences, all four machine learning algorithms converge on a similar picture in which S_{STE} is positively correlated with n_R and $L_{R,}$ while negatively correlated with Δa and S_R.

The correlations between S_{STE} and Ä*a*, n_R, and S_R can be explained based on the conventional understanding of the STE phenomena. However, the positive correlation between L_R and S_{STE} uncovered by the machine learning models appears to be beyond our current knowledge of STE. (The details of the physical interpretation underlying these relations are discussed in Supplementary Information 3). The surprising connection between S_{STE}

and L_R, discovered by the machine learning models here, can lead to a more comprehensive understanding of the mechanism of STE.

Development of a Superior STE Material

We now demonstrate that the unanticipated results of the machine learning modelling can indeed help us develop improved STE materials. We use the positive correlation between L_R and S_{STE} to search for other STE materials relying on anomalous Nernst effect (ANE). The SSE and the ANE are distinct but similar spin-driven thermoelectric (STE) phenomena, both originating in the spin-orbit interaction. Thus, it is reasonable to conjecture that tuning the orbital angular momentum L_R can enhance not only the SSE but also the ANE. In conventional STE materials utilizing ANE, FePt alloy has exhibited the largest thermopower so far. Therefore, we expect that adding rare-earth elements R with L_R into Fe-Pt alloy will increase the thermopower. As an initial example, we investigate the thermopower of Fe-Pt-Sm ternary alloy, where we have selected Sm as one of the R elements with large L_R.

Figure 3a shows the general configuration of the STE device using ANE. When a temperature difference ÄT and a magnetic field H are applied along the z and the x direction, respectively, one can detect the thermopower S_{STE} along the y direction, just like the case of SSE shown in Fig. 1a. In order to optimize the composition within the ternary alloy, various Fe-Pt-Sm alloy with different composition were investigated. The details of this device are provided in the Supplementary Information 4.

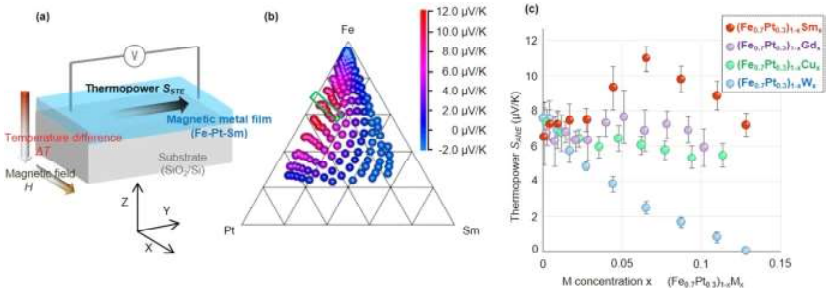

Figure 3: *Development of better STE material using ANE. (a) Schematic of the spin-driven thermoelectric (STE) devise using anomalous Nernst effect (ANE) consisting of a Fe-Pt-Sm layer and SiO_2/Si substrate. (b) Thermopower S_{ANE} of Fe-Pt-Sm on SiO_2/Si as a function of composition data. (c) Thermopower S_{STE} of $(Fe_{0.7}Pt_{0.3})_{1-x}M_x$ on SiO_2/Si as a function of composition data. Error bars show standard deviations.*

Figure 3b shows the measured S_{STE} values for the Fe-Pt-Sm as a function of composition. The largest S_{STE} was detected near composition $Fe_{0.7}Pt_{0.3}Sm_{0.05}$. To further investigate the region outlined by the green

rectangle in greater detail and to confirm the contribution of L_R (Sm), we investigated the thermopower of $(Fe_{0.7}Pt_{0.3})_{1-x}M_x$ alloy with small amount of different M atoms (M=Sm, Gd, Cu and W). Of these elements only Sm has finite orbital angular moment while the other have L_R=0. Figure 3c shows the S_{STE} of the $(Fe_{0.7}Pt_{0.3})_{1-x}M'_x$. It is clear that a small amount of Sm is necessary to maximize S_{STE}. With Gd, Cu and W, there is no S_{STE} enhancement, thus confirming the crucial role of large L_R.

Discussion

To compare the SSTE of the Fe-Pt-Sm material, we compared it with other STE materials with ANE. According to Ikhlas et al. are the SSTE of most ferromagnetic materials on the order of 0.1 $\mu V / K$. In comparison, the largest SSTE obtained here (11.12 $\mu V / K$ Fe0.665Pt0.27Sm0.065 in Fig. 3c) is at least one order of magnitude larger than that of other known ANE materials. It is interesting to note that while some of the highest SSTE values of previously known materials consist of Fe and Pt in a 50/50 concentration (Pt/Fe and L10 FePt multilayers with SSTE$\leq$ 1 $\mu V / K$),

our investigation shows that the optimal Fe-Pt occurs around Fe0.7Pt0.3 (with SANE H $\approx$ 7 $\mu V / K$), which is then further enhanced by Sm substitution as discussed above.

The STE device has two possible large-scale applications – thermoelectric generation4 and heat flow sensing. Thermoelectric generators enable the reuse of ubiquitous and wasted thermal energy and become an indispensable part of energy harvesting systems. Heat flow sensors, on the other hand, can be used in intelligent thermal management systems to map the flow of thermal energy. For STE devices to be practical for both of these applications, significant improvements in their thermal performance are required. The identification here of a new material with dramatically increased thermal energy shows that such improvements are possible and STE technologies represent a viable path to a more energy efficient future.

In summary, we have demonstrated the utility of machine learning both in investigating the fundamental physics of STE phenomena and in optimizing materials exploiting these effects. Using a data-driven approach allowed us to develop unbiased statistical models for STE, leading us to a material design rule that is not rooted in conventional STE theory. Combined with experimentation, we discovered STE material with SSTEs an order of magnitude larger than any previously known ANE material. Thus, machine learning was the key to an important step in turning STE into a practical and affordable technology.

Methods

Fabrication of STE Devices Using SSE (Pt/R:YIG/GGG or SGGG)

The manufacturing method of STE devices using SSE was carried out in two steps. First, a layer of R:YIG (GGG or SGGG, thickness 500 ìm) was formed on the substrate by the metal-organic-decomposition (MOD) method. The MOD solution contains R, Y and Fe carboxylate dissolved in organic solvents. Its chemical composition is R:Y:Fe=1:2:5. The MOD solution was spin coated onto the substrate at 1000 rpm. for 30 seconds and then dried at 150°C for 5 minutes. After pre-annealing at 450 °C for 5 min, it was annealed at 700 °C for 14 h in air to form a crystallized R:YIG layer. Its thickness was estimated to be 60 nm from an interference thickness gauge. After the completion of the R:YIG layer, a 10 nm thick layer of Pt was sputtered onto the R:YIG layer. For the measurements, the devices were cut into small chips whose length and width were 8.0 mm and 2.0mm, respectively.

Fabrication of STE Devices Using ANE (Fe-Pt-Sm/SiO2/Si)

STE devices using ANE were fabricated as follows. A composition gradient Fe-Pt-Sm film was deposited on a 3 inch SiO 2 /Si wafer by combinatorial sputtering at room temperature. The thickness of the Fe-Pt-Sm, SiO2, and Si layer is 150 nm, 0.5 μm, and 381 ìm, respectively. For measurement, it was cut into small chips with the same length and width as those cut from the Pt/R:YIG film.

Measurement for STE Thermopower S STE

A temperature difference ÄT directed in the z direction, as shown in Fig. 1a and 3a, was applied between the top and bottom of the device by sandwiching them between a copper heat bath at 300 K and 300+ ÄT K. A magnetic field H was applied in the x direction. Under these conditions, the thermal performance of the STE can be detected in the y direction. The distance between the voltage detection terminals was set to 6 mm.

Selecting descriptors and hyperparameters for machine learning models

One of the main challenges in developing machine learning models is to avoid overfitting. In general, if the amount of available data is small, the number of descriptors should be limited. For example, Seko et al. used machine learning to predict the melting point, with a number of data points (compounds) and descriptors (predictors) of 248 and 10, respectively. In our case, there are only 112 data points, so it is appropriate to use an even smaller number of descriptors. We considered a number of descriptors covering different properties of rare earth elements. These include atomic

mass, spin and orbital angular momentum, number of unfilled orbitals, melting points, magnetic moments, volumes, and space groups (the last four are calculated for the elemental ground state). Magpie software was used to create some of them. For data preprocessing, we calculated PCC to detect multicollinearity. Almost all descriptors calculated by Magpie software have a high PCC value with respect to either Äa, nR, SR or LR. They can be easily interpreted and connected to STE phenomenology, and at the same time, models built with only them have an accuracy comparable to models using the full list of descriptors. In the future, we hope to increase the size of the experimental data to include more descriptors in the model.

The hyper-parameters of the models are determined using Leave-Out-One Cross-Validation (LOOCV) - a widely used model validation technique. In this scheme, one data point is kept as validation data for model testing, while the rest of the dataset is used as training data. The hyper parameters of the model are determined by minimizing an error indicator such as root mean square error (RMSE) or root mean square error (MSE) at the test point. In this paper, we used RMSE as an error indicator. LOOCV was performed by the "caret" package in the R programming language.

Decision Tree Regression (DTR)

The Decision Tree Regression is a non-parametric machine learning model based on a series of simple decision rules, which combine flexibility with interpretability. The only model hyperparameter – complex parameter (cp) – was set to 3.90625×10^{-3} by LOOCV, with cross validation error of 8.560104×10^{-2}. The DTR was carried out by "rpart" package in R programming language.

Elastic Net (EN)

The Elastic Net is a generalized linear model, combination of Ridge and Lasso regressions. The mixing ratio of the Ridge and the Lasso (Ridge: Lasso) was set to 1: 0 based on the LOOCV. Therefore, in our case the EN model was equivalent to a Ridge regression. The LOOCV also decided the magnitude of generalization $\left(\lambda: 3.90625 \times 10^{-3}\right)$, and the cross validation RMSE was 8.798218×10^{-2}. The EN was carried out by "glmnet" package in R programming language.

Quadratic Polynomial Least Absolute Shrinkage and Selection Operator (QP-LASSO)

The LASSO is a regression analysis method that performs both variable selection and regularization. The QP-LASSO selects among quadratic,

linear and constant terms. In this case QP-LASSO selected four valuables, including Δa, n_R^2, S_R^2 *and* $n_R L_R$, from equation (2). The LOOCV-determined magnitude of generalization is $\left(\lambda: 7.55559\times10^{-3}\right)$, and the cross validation RMSE is 8.547411× 10^{-2}. The QP-LASSO was carried out by "glmnet" package in R programming language.

Neural Network (NN)

The NN method models the data by means of a statistical learning algorithm mimicking the brain. Here we have utilized simple 3-layer perceptron NN, with the number of input units, hidden units and output units being 4, 8 and 1, respectively. The hidden units and the output unit simulate the activation of a neuron by applying the hyperbolic tangent and the sigmoid functions, respectively. Mathematically, the NN models the non-linear function $S_{STE}\left(\Delta a,\ n_R,\ S_R,\ L_R\right)$ by performing the following calculation.

$$S_{STE}(\Delta a,\, n_R,\, S_R,\, L_R) = S_{STE}(x,\, w) = \sigma\left(\sum_{j=0}^{8} w_j^{(2)} h\left(\sum_{i=0}^{4} w_{ij}^{(1)} x_i\right)\right)$$

The x_1, x_2, x_3, x_4, h and σ are Δa, n_R, S_R, L_R, hyperbolic tangent function and sigmoid function, respectively. The weights and the bias parameters W^2j and W^2ji are determined by minimizing the cost function with the backpropagation algorithm. A decay value was set to 1.220703×10^{-4}. The hyper parameters, such as the number of hidden units and the value of the decay were decided by LOOCV, and cross validation RMSE of 5.516461×10^{-2} was achieved. For NN analysis, we used "nnet" package in R programming language.

References

1. Rowe, D. M. *CRC Handbook of Thermoelectrics: Macro to Nano* (CRC Press, 2005).
2. Goldsmid, H. J. *Introduction to Thermoelectricity* (Springer, 2010).
3. Bell, L. E. Cooling, heating, generating power, and recovering waste heat with thermoelectric systems. *Science* **321**, 1457–1461 (2008).
4. Kirihara, A. *et al*. Spin-current-driven thermoelectric coating. *Nature mater.* **11**, 686–689 (2012).
5. Kirihara, A. *et al*. Flexible heat-flow sensing sheets based on the longitudinal spin Seebeck effect using one-dimensional spin-current conducting films. *Sci. Rep.* **6**, 23114 (2016).
6. Bauer, G. E. W., Saitoh, E. & van Wees, B. J. Spin caloritronics. *Nature mater.* **11**, 391 (2012).
7. Uchida, K. *et al*. Observation of the spin-Seebeck effect. *Nature* **455**, 778–781 (2008).
8. Uchida, K. *et al*. Spin Seebeck insulator. *Nature Mater.* **9**, 894–897 (2010).

9. Uchida, K. *et al*. Longitudinal spin Seebeck effect: from fundamentals to applications. *J. Phys.: Condens. Matter* **26**, 343202 (2014).
10. Uchida, K., Nonaka, T., Ota, T. & Saitoh, E. Longitudinal spin-Seebeck effect in sintered polycrystalline (Mn, Zn)Fe_2O4. *Appl. Phys. Lett.* **97**, 262504 (2010).
11. Huang, S. Y., Wang, W. G., Lee, S. F., Kwo, J. & Chien, C. L. Intrinsic Spin-Dependent Thermal Transport. *Phys. Rev. Lett.* **107**, 216604 (2011).
12. Sakuraba, Y. Potential of thermoelectric power generation using anomalous Nernst effect in magnetic materials. *Scr. Mater.* **111**, 29 (2016).
13. Taniguchi, T. Phenomenological spin transport theory driven by anomalous Nernst effect. *J. Phys. Soc. Jpn.* **85**, 074705 (2016).
14. Azevedo, A., Vilela Leao, L. H., Rodriguez-Suarez, R. L., Oliveira, A. B. & Rezande, S. M. Dc effect in ferromagnetic resonance: Evidence of the spin-pumping effect. *J. Appl. Phys.* **97**, 10C715 (2005).
15. Saitoh, E., Ueda, M., Miyajima, H. & Tatara, G. Conversion of spin current into charge current at room temperature: Inverse spin-Hall effect. *Appl. Phys. Lett.* **88**, 182509 (2006).
16. Costache, M. V., Sladkov, M., Watts, S. M., van der Wal & van Wees, B. J. Electrical Detection of Spin Pumping due to the Precessing Magnetization of a Single Ferromagnet. *Phys. Rev. Lett.* **97**, 216603 (2006).
17. Valenzuela, M. V. & Tinkham, M. Direct electronic measurement of the spin Hall effect. *Nature* **442**, 176–179 (2006).
18. Tikhonov, K. S., Sinova, J. & Finkel'stein, A. M. Spectral non-uniform temperature and non-local heat transfer in the spin Seebeck effect. *Nature Commun.* **4**, 1945 (2013).
19. Adachi, H. *et al*. Gigantic enhancement of spin seebeck effect by phonon drag. *Appl. Phys. Lett.* **97**, 252506 (2010).
20. Butler, K. T., Davies, D. W., Cartwright, H., Isayev, O. & Walsh, A. Machine learning for molecular and materials science. *Nature* **559**, 547–555 (2018).

Frequency and Phase Characteristics of Candle Flame Oscillations

Kumari Archana

Research Scholar, Dept. of Physics, J.P. University, Chapra

Abstract

Candle burning shows different dynamic behavior. Connecting several candles together will result in flickering of the candle flames, which is generally described as a non-linear oscillator. The influence on the flame frequency of several factors such as the arrangement, number and asymmetry of the oscillators is discussed. Experimental results show that the frequency gradually decreases with the increasing number of candles in the case of the isolated oscillator, while the alternation between in-phase and out-of-phase synchronization appears in the coupled system of two oscillators. In addition, the envelopes of the oscillating brightness amplitude are displayed when the candles are connected asymmetrically. Since the coupling between the oscillators is dominated by thermal radiation, a "overlapping peak model" is proposed to phenomenologically explain the relationship between temperature distribution, coupling strength, and collective behavior in a coupled system of candlestick oscillators in both symmetric and asymmetric cases.

Introduction

The ability to use fire allowed homo-sapiens to get rid of darkness and cold, move out of caves and become the most advanced species in the world. Derived from the ancient torch, candles have a long history of use for lighting purposes dating back to early civilization. Great availability, low cost and stability make candles ideal for people to explore the properties of diffusion flames. Nowadays, the complex dynamics of candle flames can be recorded and measured with the help of a high-speed camera. In previous works, it was found that candle flames are capable of spontaneously clustering and exhibit limit cycle oscillation. Similar systems of limit-cycle oscillators have been observed and comprehensively discussed in the natural and technical sciences, such as synchronization in the flickering of fireflies, rhythms in crowd applause, trends in stock markets, pendulum swings, oscillations of inverted bottle oscillators, and so on. Abundant collective behavior has been observed in systems of coupled oscillators, including various synchronizations, amplitude death,

and the formation of spatiotemporal patterns. The study of coupled oscillatory systems will be useful for understanding nonlinear dynamical behavior such as synchronization and emergence. In addition, fire control should be explored to prevent ignition and combustion and flame instability.

Nonlinear oscillation of candle flames was introduced and analyzed by imaging technique by Chamberlin et al. in 1948 for the first time. Decades later, two groups of burning candles were examined using video clips by Kitahata et al. where the oscillation consists mainly of two modes depending on the distance between these oscillators. Phase synchronization was observed when the two groups were closely spaced, while a sufficiently large distance led the system to antiphase synchronization. According to previous research, thermal radiation was considered to be the main cause of coupling between flames, and a theoretical model was proposed that emphasizes the importance of distance and typical modes of flame oscillation. Since then, various experiments with coupled burning candles have been proposed. In 2015, Forrester observed a number of oscillatory modes with different spatial separations and arrangement topologies. Following the initial work of Forrester where three candles in an equilateral triangle arrangement were examined among others. Okamoto et al. examined in detail three groups of candles with an equilateral triangular arrangement and discovered four distinct oscillatory modes: in-phase synchronization, partial in-phase synchronization, rotation, and death. The frequencies of occurrence of these modes with different side lengths were calculated and explained by vortex and bifurcation theories.

Three key properties of flame oscillation were investigated in this work. First, a negative linear correlation is discovered between the number of candles bound in a single oscillator and its frequency. Furthermore, the influence of different arrangements of candles on amplitude and frequency is studied. Second, we analyzed a coupled system of two identical oscillators with an infrared camera to measure the temperature distribution in the flame and particularly focused on in-phase and anti-phase oscillations. A concise and illustrative "overlapping peak model" is proposed to explain the bonding interactions between flames from a phenomenological perspective. As will be seen, the width of the temperature distribution curve of a single oscillator reflects its effective radiative range, while the overlap region of two coupled oscillators reflects the coupling strength. A phase mode only appears when the oscillators are close enough to maintain coupling to each other at all times. Other

modes appear when the coupling strength remains stable for a minimum time, leading to phase-locked synchronization. Flames oscillate asynchronously when they are far enough apart as the coupling strength decreases. Finally, the model is extended to a system with two non-identical oscillators, where asymmetric structures are found to cause imperfect in-phase and anti-phase oscillations. A weaker oscillator will be subordinated to a stronger one and will supply less radiation range, leading to a deviation from pure in-phase or anti-phase synchronization. When the distance is large enough, the phase difference will constantly drift due to the lack of coupling. The proposed model aims to explain how the distance between candlestick oscillators leads to their diverse collective behavior.

Methods

All candles in our experiments are made of paraffin with a diameter of 6mm and a height of 60mm. The initial size of each candle is considered the same. Unless otherwise noted, the candles in the group are tightly banded into a compact structure, and the flame oscillator contains three candles. Our experiments are conducted in the open air at indoor temperature and without ambient light or external air flow.

The image sequences of our experiments were recorded with a high-speed camera (Cube4, Mikrotron, Germany). A 10-second grayscale movie was recorded at 480 frames per second and was therefore converted to a 4800 frame sequence using MATLAB to investigate the flame brightness oscillation. Amplitude is calculated by integrating the brightness (grayscale values) in the corresponding region for each frame. The brightness (at each instant) in these images is indicated by the mean gray scale value of each image with fixed camera parameters. Brightness is therefore dimensionless.

Temperature curves are obtained with an infrared camera (FLIR ONE, FLIR, U.S.A.) on a black background with diffuse reflection. The acquired infrared images are converted into temperature matrices using FLIR TOOLS, which are plotted as curves after calculating the mean value of each column of the matrix. Schlieren images are acquired with a single-mirror Schlieren system in which a concave spherical mirror has a focal length of 1000mm and a diameter of 203mm.

Result

The Effect of the Number of Candles on One Oscillator

Kitahata et al. pointed out that the flame of a single candle oscillator will flicker periodically if it consists of at least 3 candles. Otherwise, it maintains stable combustion. The origin of the oscillation and the influence

of the number of candles in the oscillator therefore deserve a detailed investigation. Flame oscillators containing 1 to 10 candles were experimentally tested.

The arrangement of the candles is indicated by the yellow dots in Fig. 1. The high-speed camera is aligned with the center of the candle flames with a fixed distance between them. All frames are recorded when the flame reaches a stable oscillatory state, and as shown in Fig. 1 , the grayscale images show the peak moment of each group of flames. The flame profile varies in amplitude, which generally tends to increase monotonically with the number of candles. In one candle, the flame shows no visible oscillations and remains stable; for group 2 candles, the flame brightness increases slightly and the flame occasionally shows slight fluctuations, but neither regularly nor obviously. For a group consisting of more than 3 candles, the flame exhibits a regular oscillation that has a more or less stable amplitude and frequency. As the number of contained candles increases, the brightness increases monotonically. Time series are obtained (see Methods section) and shown in Fig. 2(a). The frequency spectrum of each oscillator is obtained by Fast Fourier Transform (FFT) and its dependence on the number of candles is shown in Fig. 2(b). When the number is less than 3, the flames remain stable but non-periodic. When the number is equal to or greater than 3, oscillation occurs and the frequency decreases monotonically as the number increases. Moreover, the frequency remains in the range of 10–12Hz, which is expectedly consistent with the results of T. Maxworthy and Hamins et al., in which diffusion flames were involved and the frequency was determined by the diameter of the nozzles and the strength of the nozzles. flow. The data fit the empirical formula between frequency and burner diameter: $f \propto D^{-0.49}$.

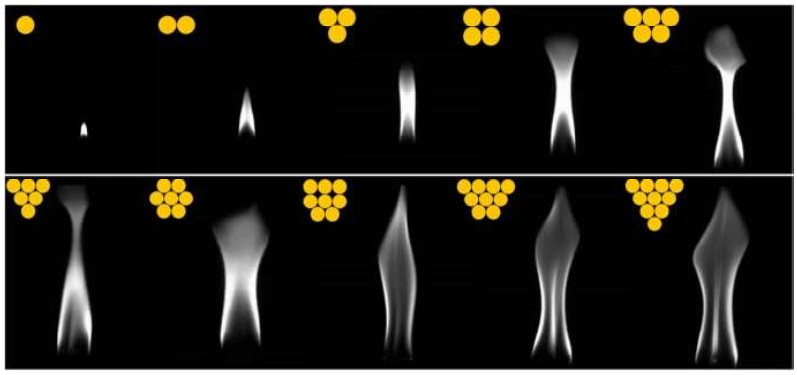

Figure 1: *Gray-scale images of 1 to 10 candles. As the number increases, the flame becomes larger in width and height. The dots on the upper left represent the arrangement of bound candles in each group.*

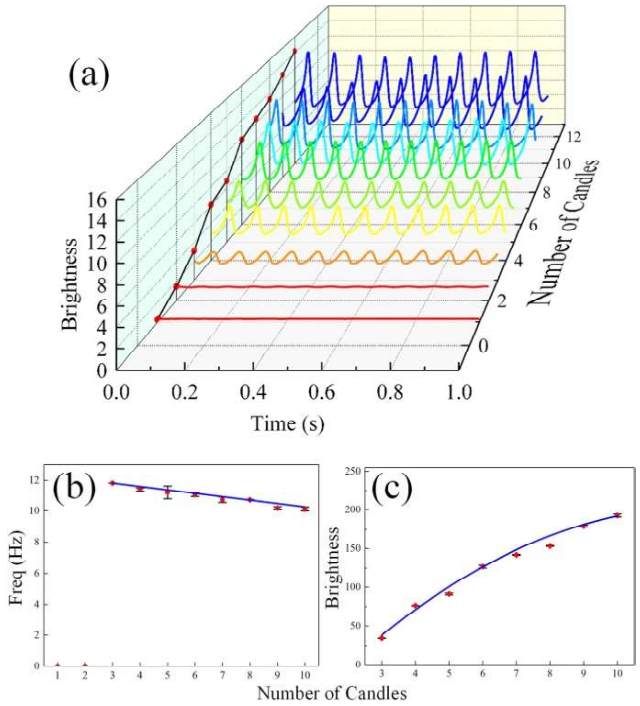

Figure 2: *(a) Time series of the flame brightness with different number of candles in a group. As the number increases, the amplitude and average value of brightness increases dramatically. (b) Number — Frequency diagram. When the number is less than 3, frequencies are null; when the number is 3 or more, frequencies decrease monotonically. The blue line was a linear fit. (c) Number — Brightness diagram. The brightness is the average value in a single period for each group. The brightness increases as the number increases. Both of the error bars stand for standard deviation of six repetitive experiments.*

When the number of candles contained increases, the fuel flow rate accordingly increases and thus leads to the growing demand for oxygen. The open air around the burning candles has a rather low flow rate, which can be viewed as quasi-static. It takes more time to replenish the needed air to the burning region when the reaction is more drastic. Meanwhile, the puff generated by the candles becomes larger as the number increases, requiring a longer time to float upward into the open air. In consequence, the frequency of oscillator decreases with the increasing number.

It is noteworthy that arrangement affects the oscillation behavior as well, even with the same number of candles in an oscillator. In the case of 6 candles, for instance, three types of arrangement are checked in our experiment, and it is found that the brightness and the frequencies are all different. The first type, as shown in the left of Fig. 3(a), has the largest

amplitude and smallest frequency due to its greatest width. On the other hand, the most closely arranged group has the highest frequency but smallest amplitude, since a smaller reaction surface will result in both less consumption of oxygen and smaller puff as mentioned above. However, the difference in these three cases are not significant in reality, which indicates that the impact of arrangement is much weaker than the number of candles.

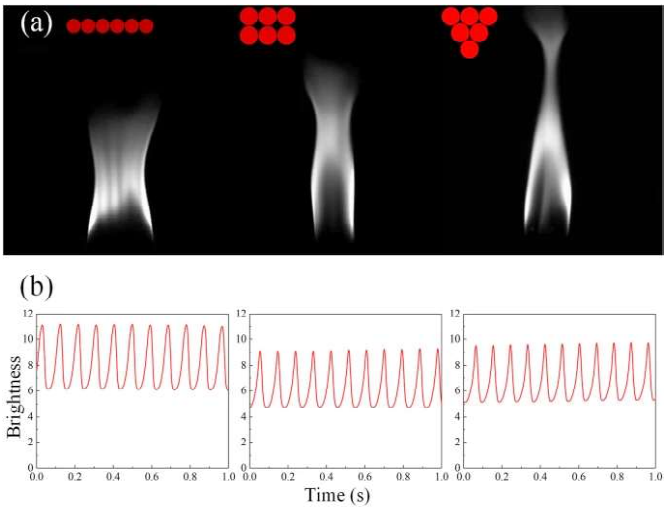

Figure 3: Different arrangement of 6 candles in a group. (a) Gray-scale images and (b) time series of each type. Corresponding frequencies are 10.7227 Hz/ 10.7802 Hz/10.9570Hz (left to right).

Synchronization Between two Identical Symmetric Oscillators

The impact of the number of the candles and the arrangement on oscillation amplitude and frequency for a single oscillator is discussed in the previous section. In this section, we investigate a coupled system of two identical oscillators. Kitahata *et al*. found that two flame oscillators exhibited the in-phase synchronization when the distance between them is between 20mm and 30mm and the anti-phase synchronization for the distance between 30mm and 48mm. In our experiments, the distance between the candles is set to 20mm initially but ends at 60mm, with a step size of 5mm. Figure 4 shows the gray-scale images of the in-phase and anti-phase oscillation. As the distance increases, the synchronization state of the system changes from the in-phase to the anti-phase at about 35 mm and from the anti-phase to the incoherent at 60mm. The relationship between the distance and the frequency of the oscillators is recorded and analyzed, and comply well with former result[1]. The frequency increases slightly when the system is in-phase synchronized, but decreases from a

high frequency in the anti-phase. Furthermore, Schlieren images were presented in order to investigate the synchronization states between candle groups. Comparing the flow patterns of in-phase and anti-phase synchronization, we can make a distinction between them. As for the in-phase mode, the outline of the flow pattern shows spatial symmetry and the inner profile is close to a straight line. Asymmetrical curves are observed for the outline and the inner line when it comes to anti-phase mode. The observation of flow patterns can provide another perspective of distinguishing the synchronization modes.

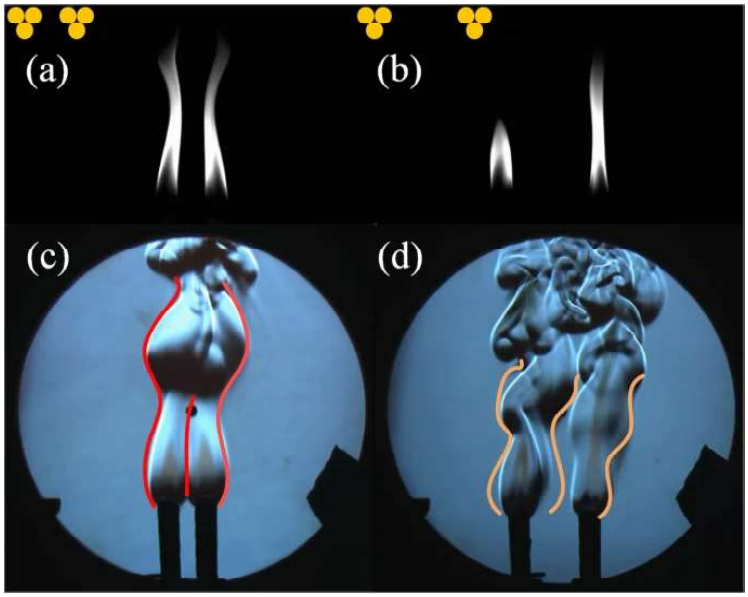

Figure 4: *(a) The gray-scale image of the in-phase (20 mm between two oscillators, left) and (b) anti-phase synchronization (35 mm, right).(see Supplementary Vids S1 and S2) (c) Schlieren images of the in-phase mode (see Supplementary Vid. S3), and (d) anti-phase mode.*

After the study of the symmetrically coupled system of two oscillators, we proceed to the system of three candles positioned in isosceles triangle. When the distances between them are small enough, each single candle in the triangle which burned stably starts to oscillate and shows in-phase synchronization with each other. As shown in Fig. 5, a smaller amplitude of the flame oscillation is observed on the candle sitting at the apex when this angle is smaller than 60 degrees, and a larger amplitude is seen for an apex angle greater than 60 degrees. According to our analysis, the difference is associated with different coupling strengths. The coupling strength consists of heat radiation and heat flux[1], as well as vortex driven airflow[3,29]. Closer distance leads to higher temperature between flames

and higher velocity of the vortex, which lead to greater impact on coupling strength. In the former case, the triangle has two long sides and a short base. Therefore, the candle at the apex is weakly coupled to the other two and has lower amplitude, while in the latter case the coupling becomes relatively stronger which leads to higher amplitude.

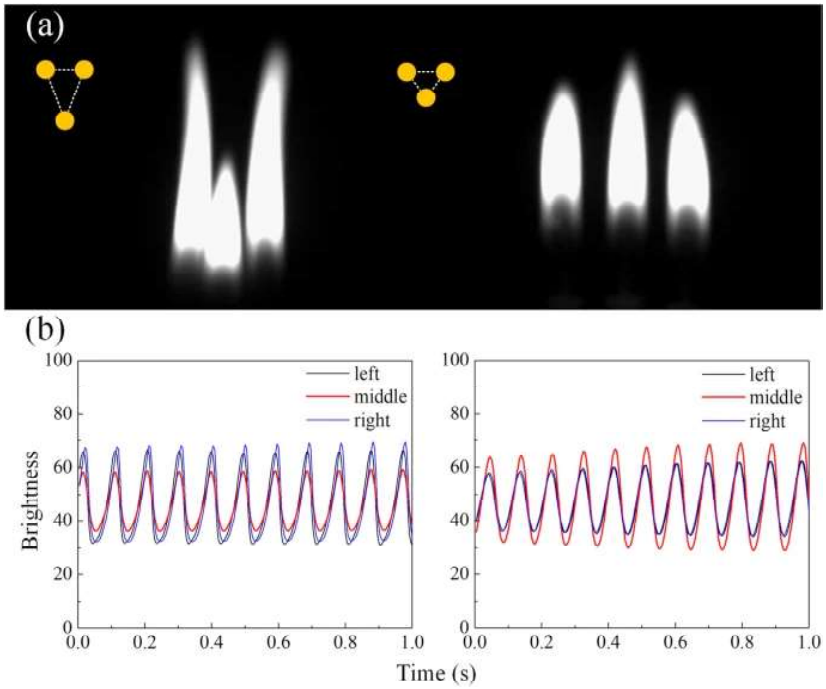

Figure 5: *(a) Gray-scale images of three candles arranged in isosceles triangle with bases of 2 cm. The dots on the upper left represent the arrangements. The apex angle of the left is 39 degrees (<60 degrees), and the right one is 120 degrees (>60 degrees). (b) Time series of the brightness. That of the apex candle (sitting in the middle in the gray-scale images) is plotted with red curves which have lowest or highest amplitudes respectively, and the others are black and blue.*

In our experiments, we focus on the impact generated by heat radiation, which is positively correlated with temperature. Hence the measurement of the temperature between flames can indicate the coupling strength between oscillators. Since the radiation flux decays with an inverse square law in distance, we suppose that for a single oscillator, there is an effective radiation range in which another flame is considerably influenced while the effect of radiation can be ignored outside. The higher temperature, the greater coupling strength and vice versa. When it drops down to near ambient temperature, the oscillators cannot maintain their coupling. Therefore, the coupling strength decreases monotonically with

the increasing distance between candles, which will be used to forge a phenomenological explanation of the results later.

Many researches have shown that when the coupling strength gradually changes between coupled oscillators, there exists a threshold value for the transition of synchronization states, or the basin stability of coherent states changes along with the change of coupling strength. Considering the experiments of two identical oscillators, we might intuitively arrive at a conclusion that the coupling strength should decay along with the augmentation of distance between them. When decayed to a certain point, the synchronization state should switch from coherent to incoherent. However, this intuition does not comply with the result shown in Fig. 6. When the distance increases, the state turns from in-phase to anti-phase synchronization. This means that the transition of states is not caused by the change of basin. Therefore, the cause of the state transition deserves further research.

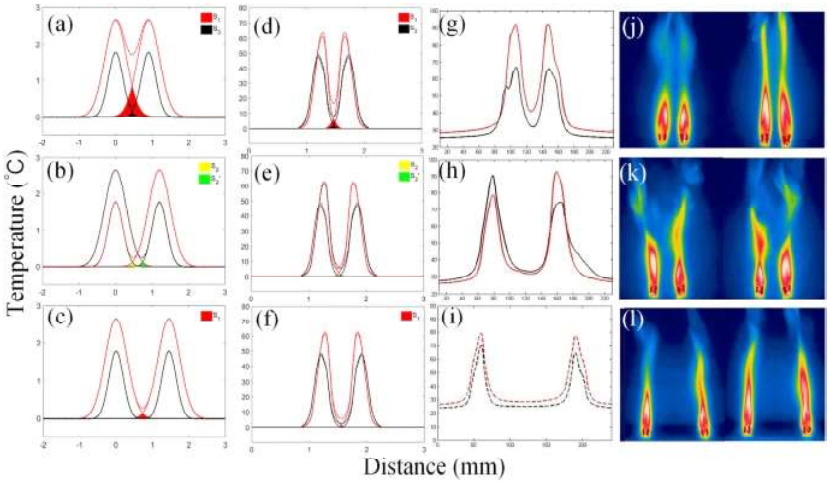

Figure 6: *Phenomenological explanation of the mechanism of synchronization in the symmetric system. Each column is arranged in the order of in-phase, anti-phase and incoherent solution, as the distance increases. (a–c) Phenomenological model curves. (d–f) Simulation curves using the data of temperature distribution of single group containing 3 candles. (g–i) Real temperature distribution curves. (j–l) Infrared images.*

Considering the thermal radiation-driven coupling between the flame oscillators, the temperature distribution between the two oscillators was probed using an infrared camera. Figure 6(j–l) shows the case of in-phase (20 mm between two oscillators), anti-phase (40mm) and incoherent (70mm) oscillations. Based on all these experimental observations, the "overlapping peaks model" was proposed to explain the phenomena.

Using the mode l, we could link the change in distance with the transition of synchronization states. The model was shown in Fig. 6 and described as follows. As shown in Fig. 6(a–c) , the red solid line represents the range at maximum radiation and the black represents the range at minimum. Both straight lines are Gaussian curves.

The horizontal axis indicates negligible radiation intensity. For coupled oscillators, the coupling strength is represented by the overlapping area under the two effective emission curves. The key point of the model is the maximum and minimum radiation curves. Obviously, in the case of two coupled flames, there will be four overlapping domains formed by these two pairs of curves. The overlapping domain of the two minimum profiles is filled in black and marked as S3 and the maximum overlapping is marked in red and S1, as shown in Fig. 6(a) ; the yellow (green) domain, labeled as S2(S22), indicated the overlaps formed by one flame reaching its maximum (minimum) curve and the other reaching its minimum (maximum) curve, as shown in Fig. 6(b) . for example. It should be noted that these domains may overlap each other. To ensure the definition of each domain, not all of them are shown in each subfigure. For example, in Fig. 6(a) domain S1 is partially covered by S3, and S2 and S2' are not expressed while they actually exist. When the oscillators are close enough, the relation S1 > S2 > S3 > 0 is satisfied, as shown in Fig. 6(a). This means that even if the two flames drop to their minima, the system still has adequate coupling to maintain phase synchronization. As the distance increases, the S3 domain disappears, therefore S1 > S2 > 0 = S3 as shown in Fig. 6(b) . In this case the flames cannot maintain a strong enough coupling to maintain coherence if they both reach a minimum, whereas in anti-synchronization both flames alternatively reach a minimum and are able to maintain coupling and coherence. When the distance is small enough, S1 > 0 = S2 = S3 as shown in Fig. 6(c). In this situation, the flames cannot maintain either in-phase or anti-phase synchronization because the coupling strength is not strong enough most of the time and the oscillation becomes incoherent, i.e. the phase difference between the two oscillators cannot be locked.

If the proposed model is correct, then the temperature curve and phenomena should match the model prediction. To validate our model, we took infrared images of one group of candle flames as they reach their maximum and minimum independently. Then the temperature distribution curve is calculated and considered as the effective radiation range of one oscillator. The ambient temperature is considered to be the lower asymptotic line for the curves because the bond strength on both

sides is zero when the curves drop to ambient temperature. We apply two sets of identical curves to simulate the temperature distribution in a coupled system of two identical oscillators. By comparing these simulated curves (d–f) with the curves given by the model on the left (a–c) and the actual temperature distributions on the right (g–i), we obtained consistent results using the same plotting methods. These results indicate that our model provides a valid and meaningful prediction of the phenomena observed in the experiments. So far, based on this model, it has been possible to explain the state of synchronization phenomenologically: when the oscillators are close enough to each other, the positive feedback of thermal radiation leads to an in-phase mode; as the distance increases, the system must maintain a ð-phase difference to remain stable; when the distance is large enough, the coupling strength is so weak that the oscillators cannot cohere with each other no matter what the phase difference is.

Synchronization Between Mismatched asymmetric Oscillators and Their Phase Difference

Several interesting phenomena are observed in a symmetric coupled system, and in this section we study a coupled system of two non-identical oscillators. Two asymmetric systems are discussed. (1) The "3 + 6" pattern, which consists of an oscillator containing 3 candles and one containing 6 candles, as shown in Fig. 7(a) , while the corresponding analysis is shown in Fig. 8. (2) The pattern " 1 + 6", which consists of a single candle oscillator and another with 6 candles as shown in Fig. 9(a).

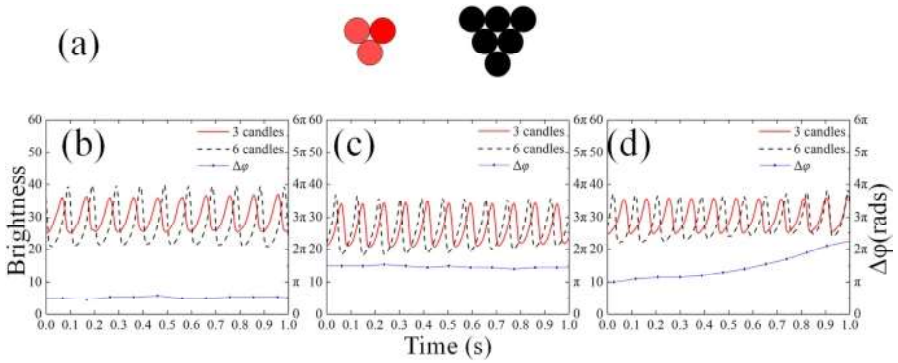

Figure 7: *(a) Asymmetric arrangement of the "3 + 6" system. (b–d) Time series and phase differences. Black dashed lines for the 6-candle group, red solid lines for the 3-candle group and Blue dotted lines for the phase difference. (b) the near-in-phase synchronization (15 mm–35 mm), (c) the near-anti-phase synchronization(35 mm–55 mm), (d) the incoherent oscillation (>55mm).*

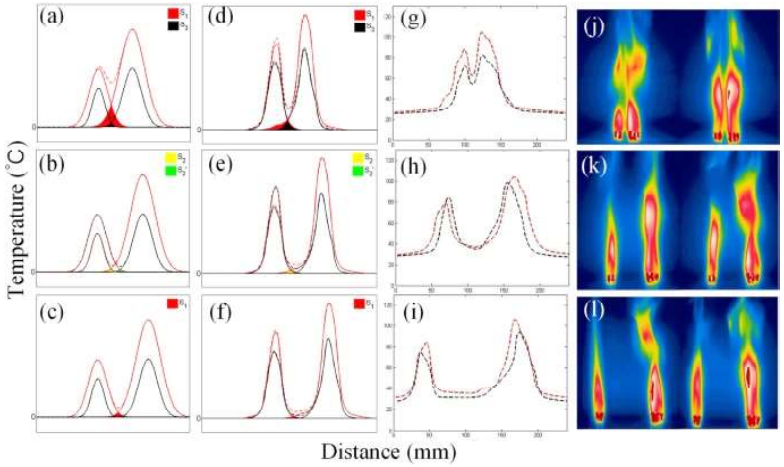

Figure 8: *Phenomenological explanation on the mechanism of synchronization in the asymmetric system. Each column is arranged as the distance increases. (a–c) Phenomenological model curves. (d–f) Simulation curves using the data of temperature distribution of a single group containing 3 candles. (g–i) Real temperature distribution curves. (j–l) Infrared images.*

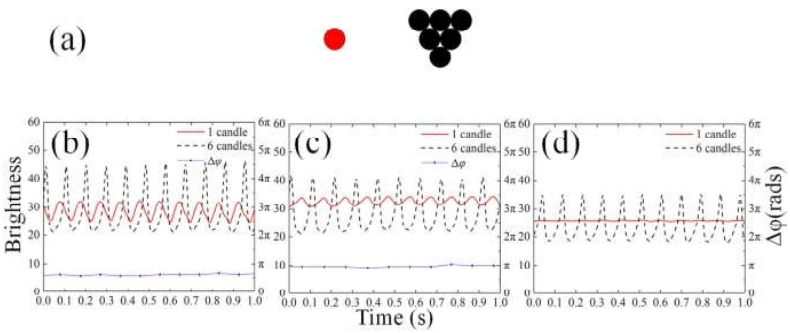

Figure 9: *(a) Asymmetric arrangement of the "1 + 6" system. (b–d) The time series and phase differences. Black dashed lines for the 6 candles, red solid lines for the single candle and Blue dotted-lines for the phase difference. (b) Synchronization close to the in-phase (15 mm–35 mm), (c) synchronization close to the anti-phase (35 mm–55 mm), (d) the incoherent oscillation (>55 mm).*

Let's start with the "3 + 6" pattern. Similar to the symmetrical system, the flames were synchronized and phase locked. When the flames are very close (15 mm–35 mm in our experiments), the phase difference is no longer zero due to its asymmetry. As the distance increases (35 mm–55 mm), the system switches to phase-lock synchronization close to anti-phase. When the distance is larger than 55 mm, the flames become incoherent and the phase difference changes smoothly. Figure 7(b–d) shows the time series for these cases. The same results are obtained as far as the frequency domain is concerned. The synchronization state near

antiphase has a higher frequency that decreases as the distance between the oscillators increases, while the state near inphase has a lower but increasing frequency.

The "overlapping peaks model" can also be used to explain synchronization in an asymmetric system. Similar methods are implemented, although some details have been changed. According to our model, the synchronization state should resemble an in-phase mode when the distance is smaller and an anti-phase mode when it is larger. Also, the oscillation should be dominated by the larger "6" group, which is stronger in bond strength. In Fig. 8, the left oscillators represent a lean oscillator containing 3 candles, while the right curves represent a robust 6 candle oscillator. In contrast to the symmetric cases, the effective radiation ranges of "3" and "6" are not identical, and therefore the overlapping domains are also not symmetric, especially for the S2 and S22 regions, which determine the strength of the bond to the other. and they are no longer equal. In case S1 > S2 (>S22) > S3 > 0, oscillator "6" will obviously show a stronger coupling to "3" (which means "6" has higher temperature or stronger radiation), thus "3" will reach its maximum peak earlier because its peak is lower than "6" and a certain phase difference appears. For S1 > S2 (>S22) > 0 = S3, this mode shifts from the predicted antiphase with some difference due to the asymmetry in S2 and S22 . When the distance is large enough, the coupling strength becomes negligible and leads to phase incoherence, which has a monotonically changing phase difference due to the different natural frequency for "3" and "6", rather than the barely changing phase difference in a symmetrical system. .

Simulation curves and real temperature distribution profiles are plotted in a similar way and show agreement with our model. Our model could also be applied to this case: sufficiently closed oscillators more affected by radiation lead to an in-phase regime; greater distance requires the system to maintain the same anti-phase mode to remain stable; the oscillators lose their coherence when the distance is large enough.

At the end of this section, the "1+6" pattern is discussed, the asymmetry of which is much more pronounced than the "3 +6" case. As observed earlier, a single candle flame does not oscillate and remains stable in an isolated situation. However, when oscillator "6" is placed nearby (<15mm), "1" starts to oscillate, which is due to the coupling from "6", and exhibits near-in-phase synchronization, similar to the case from "3 + 6". As the distance increases, somewhere between 15 mm and 45 mm, the amplitude of the "1" oscillation decreases to a small value, showing antiphase synchronization. When the distance is greater than 45 mm, the coupling weakens enough that the flame of one candle stops

oscillating and regains its stability. Meanwhile, the "6" group is still oscillating. The related time series are shown in Fig. 9(b–d) and the temperature distribution in Fig. 10. As the distance increases, the temperature midway between the two flames drops to ambient temperature, indicating that the effective radiative coupling becomes negligible.

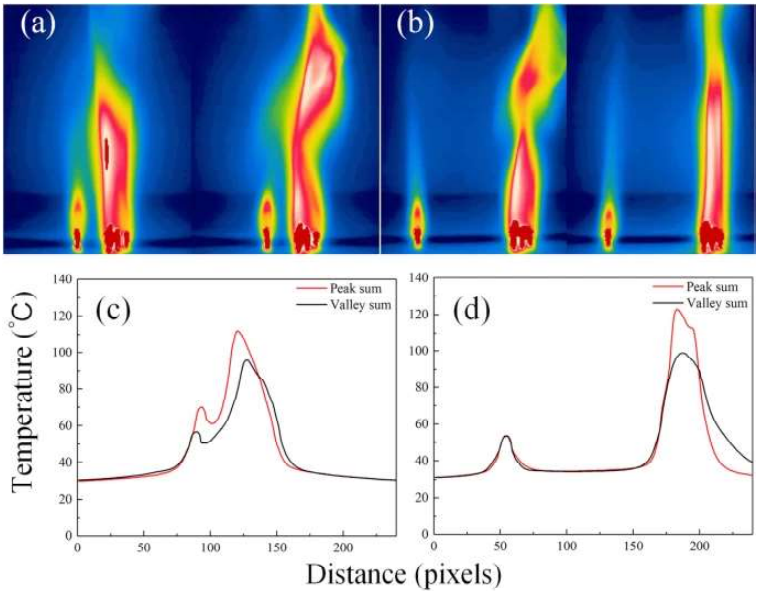

Figure 10: *(a,b) The infrared images and (c,d) the temperature distribution in horizontal direction. (c) When the distance is near (20 mm), the single candle flame is affected by the radiation of "6" and starts to oscillate. The temperature in the middle space between two flames is distinctly higher than the ambient temperature. (d) When the distance is large (60 mm), the coupling strength is negligible and the single candle flame remains stable with no oscillation. The temperature between them is close to the ambient temperature.*

Discussion on the Changes of Phase Difference in Coupled Systems

A discrete phase that envelopes the time series and displays the steps in the phase difference. Their distinction and origin will be discussed in the following section.

The first case of phase change is due to the large distance between the flames, which leads to a coupling too weak to maintain coherence. For an ideal symmetrical system, the phase difference should remain constant even if the distance between the oscillators is large, because the natural frequency of the oscillators is the same. However, in our experiment, a certain small deviation in the phase difference is observed, which changes

slowly in half of the period (maintains in the range of π). Based on observation and analysis, this kind of change is attributed to the unstable burning of the candle. When the flame lasts for more than 10 seconds, the wicks of the candles involved in the burning lengthen and tilt outward, thus the flame loses symmetry and tightness and causes irregular oscillation. A subtle change in amplitude will also cause changes in frequency and phase difference. For an asymmetric system, it is clear that the phase difference should vary monotonically because the natural frequencies of non-identical oscillators are different, as observed in our experiments.

In the second case, more interesting changes in the phase difference are observed in our experiments. Another asymmetric "3 + 6" system is considered, as shown in Fig. 11(c) . The amplitudes of both oscillators show periodic envelopes. The rate of phase change in this case is much higher than in the first case, almost twice as much. This kind of continuous change in phase difference is probably due to periodic amplitude envelopes, indicating a periodically varying frequency.

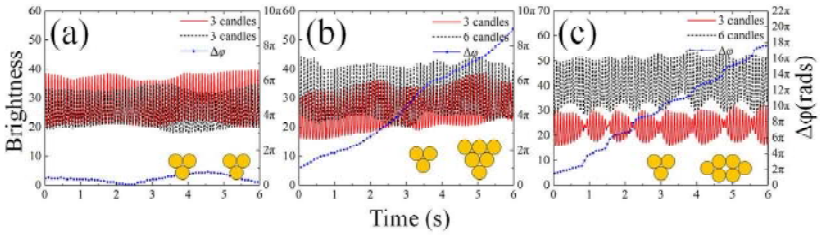

Figure 11: *Comparison of multiple types of changing of phase difference. Red solid and black dashed lines for the time series of two oscillators and blue dotted-lines for the phase difference. (a) Symmetric system of "3 +3" at a distance of 80mm. The amplitude of each group fluctuates slightly and the phase difference changes subtly. (b) Asymmetric system of "3 + 6" at a distance of 55 mm. Though amplitudes change barely, the phase difference increases monotonically since the inherent frequencies are different. (c) Another arrangement of the asymmetric "3 + 6" system at a distance of 30 mm, which is illustrated by the yellow dots at lower right corner. In this case, amplitudes of both groups exhibit periodic envelopes and phase difference increases with "steps".*

Numerical Modeling Method

The Fire Dynamics Simulator (FDS), developed by NIST, was used to model fire behavior. The simulated results were compared and evaluated based on a visual representation of the flame shape as well as the temperature distribution around the flame tip.

The heat-related parameters used in the simulation model are fixed at certain values and may not be completely consistent with actual situations

due to the lack of heat flow measurement equipment. First, we simulated the situation corresponding to Section 3.2. In order to obtain appropriate initial values for simulating one group of candles, we used a method similar to that in Section 3.1, which determines the heat release rate per unit area (HRRPUA) of the burning part in the model was continuously adjusted to find the minimum usable parameters for the group . We also performed simulations of other circumstances to observe the outcome.

For the simulation, a 140 × 60 × 200 mm3 domain containing 210,000 cells was created around the virtual candle. The boundary condition was set as opening vents for the 4 side walls and the candle ceiling and as a cold inert wall for the floor. The candle model has been simplified to reduce the consumption of computational resources, consisting of an inert candle base of 11 × 11 × 20 mm3 and a wick of 5.5 × 5.5 × 10 mm3. The base and wick are coaxially aligned and the wick surfaces have a uniform HRRPUA of 1340.0 kW/mm2 as standard. The properties of burning wax were also taken from earlier measurement results. The initial parameters of both candles are set to be identical at the beginning of the simulations.

The same process for two identical oscillators was then repeated in the simulation. The results are shown in Fig. 12. As the distance between them increases, we find in-phase and anti-phase oscillations at 30 mm and 45 mm. Also, when the distance is larger than 70 mm, the oscillators become incoherent, which is similar to the experimental results. The simulation verified that the synchronization modes can change with increasing distance. The similarity between the experimental and simulation results also serves as a verification for the proposed phenomenological model.

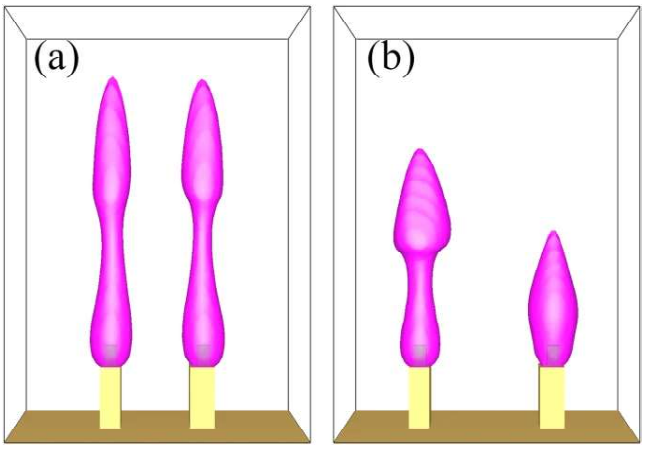

Figure 12: *A snapshot of FDS simulation results for in-phase and anti-phase synchronizations. (a) In-phase mode at 30 mm and (b) anti-phase mode at 45 mm. Both figures share the parameters mentioned above and the flame regions are represented with 3D temperature contour surface (pink) approximately.*

Conclusion

Single group candle flame oscillators and coupled oscillators were discussed experimentally and theoretically in this article. When three or more candles are closely connected in a group, the flame begins to oscillate. As the number of candles increases, the oscillation decreases linearly and the temperature rises. For a coupled system of two identical oscillators, whether this will lead to in-phase, anti-phase and incoherent oscillations depends on the distances between the flames. The numerical simulation is consistent with the experiments. Experiments are performed for arrangements of isosceles but inequilateral triangles, and radiation-based explanations for the change in peak candle flame amplitude are proposed. The same explanation applies to non-identically bound groups, while asymmetry induces phase shifts to perfect in-phase or anti-phase synchronization. A phenomenological model based on the infrared temperature distribution, the "overlapping peaks model", is proposed that successfully explains all experimentally observed states in both symmetric and asymmetric cases, including several interesting cases of phase difference evolution found in our experiments. The model reveals the relationship between the synchronization states and the distances between the oscillators and successfully explains the basic mechanism of the synchronization state transition. In addition, a fire dynamics simulator (FDS) was successfully used to model candle flame behavior and produced valuable results in simulation that agree reasonably well with experimental results.

References

1. Kitahata, H. *et al*. Oscillation and synchronization in the combustion of candles. *The Journal of Physical Chemistry A* **113**, 8164–8168 (2009).
2. Forrester, D. M. Arrays of coupled chemical oscillators. *Scientific reports* **5** (2015).
3. Okamoto, K., Kijima, A., Umeno, Y. & Shima, H. Synchronization in flickering of three-coupled candle flames. *Scientific reports* **6**, 36145 (2016).
4. Strogatz, S. *Sync: The emerging science of spontaneous order*. (Penguin UK, 2004).
5. Smith, H. M. Synchronous flashing of fireflies. *Science* **82**, 151–152 (1935).
6. Kurths, J., Pikovsky, A. & Rosenblum, M. *Synchronization: a universal concept in nonlinear sciences*. (Cambridge University Press New York, 2001).
7. Day, R. H. & Chen, P. *Nonlinear dynamics and evolutionary economics*. (Oxford University Press Oxford, 1993).
8. Bennett, M., Schatz, M. F., Rockwood, H. & Wiesenfeld, K. Huygens's clocks. *Proceedings: Mathematics, Physical and Engineering Sciences* 563–579 (2002).
9. Jia, J. *et al*. Experimental and modeling analysis of asymmetrical on-off oscillation in coupled non-identical inverted bottle oscillators. *Chaos: An Interdisciplinary Journal of Nonlinear Science* **26**, 116301 (2016).

10. Arenas, A., Daz-Guilera, A., Kurths, J., Moreno, Y. & Zhou, C. Synchronization in complex networks. *Physics reports* **469**, 93–153 (2008).
11. Pecora, L. M. Synchronization conditions and desynchronizing patterns in coupled limit-cycle and chaotic systems. *Physical review E* **58**, 347 (1998).
12. Aihara, I. Modeling synchronized calling behavior of japanese tree frogs. *Physical Review E* **80**, 011918 (2009).
13. Hinkel, D. *et al*. Creation of hot radiation environments in laser-driven targets. *Physical review letters* **96**, 195001 (2006).
14. Rodrigues, F. A., Peron, T. K. D., Ji, P. & Kurths, J. The kuramoto model in complex networks. *Physics Reports* **610**, 1–98 (2016).
15. Reddy, D. R., Sen, A. & Johnston, G. L. Time delay induced death in coupled limit cycle oscillators. *Physical Review Letters* **80**, 5109 (1998).
16. Reddy, D. R., Sen, A. & Johnston, G. L. Experimental evidence of time-delay-induced death in coupled limit-cycle oscillators. *Physical Review Letters* **85**, 3381 (2000).
17. Karnatak, R., Ramaswamy, R. & Prasad, A. Amplitude death in the absence of time delays in identical coupled oscillators. *Physical Review E* **76**, 035201 (2007).
18. Prasad, A. Amplitude death in coupled chaotic oscillators. *Physical Review E* **72**, 056204 (2005).
19. Koseska, A., Volkov, E. & Kurths, J. Oscillation quenching mechanisms: Amplitude vs. oscillation death. *Physics Reports* **531**, 173–199 (2013).
20. Wu, Y., Liu, W., Xiao, J., Zou, W. & Kurths, J. Effects of spatial frequency distributions on amplitude death in an array of coupled landau-stuart oscillators. *Physical Review E* **85**, 056211 (2012).

Homotopy and Homeomorphism in Mathematics

Rakesh Kumar Bharti

Reseach Scholar Dept. of Mathematics, Jai Prakash University Chapra

Apstract

In topology, two continuous functions from one topological space to another are called homotopic (Greek (*hom*σ*s*) = same, similar, and (*t*σ*pos*) = place) if one can be "continuously deformed" into the other, such a deformation being called a homotopy between the two functions. An outstanding use of homotopy is the definition of homotopy groups and cohomotopy groups, important invariants in algebraic topology.

In practice, there are technical difficulties in using homotopies with certain spaces. Algebraic topologists work with compactly generated spaces, CW complexes, or spectra. In the mathematical field of topology, a homeomorphism or topological isomorphism or bicontinuous function is a continuous function between topological spaces that has a continuous inverse function.

Keywords: Continuous Functions, Topological Space, Algebraic Topology, Homotopy

Introduction

Formally, a homotopy between two continuous functions f and g from a topological space X to a topological space Y is defined to be a continuous function $H : X \times [0,1] \to Y$ from the product of the space X with the unit interval $[0,1]$ to Y such that, if $x \in X$ then $H(x,0) = f(x)$ and $H(x,1) = g(x)$.

If we think of the second parameter of H as time then H describes a *continuous deformation* of f into g: at time 0 we have the function f and at time 1 we have the function g.

An alternative notation is to say that a homotopy between two continuous functions $f, g : X \to Y$ is a family of continuous functions $h_t : X \to Y$ for $t \in [0,1]$ such that $h_0 = f$ and $h_1 = g$, and the map $t \mapsto h_t$ is continuous from $[0,1]$ to the space of all continuous functions $X \to Y$. The two versions coincide by setting $h_t(x) = H(x,t)$.

Homeomorphisms are the isomorphisms in the category of topological spaces—that is, they are the mappings that preserve all the topological properties of a given space. Two spaces with a homeomorphism between them are called homeomorphic, and from a topological viewpoint they

are the same. Roughly speaking, a topological space is a geometric object, and the homeomorphism is a continuous stretching and bending of the object into a new shape. Thus, a square and a circle are homeomorphic to each other, but a sphere and a donut are not.

An often-repeated mathematical joke is that topologists can't tell their coffee cup from their donut, since a sufficiently pliable donut could be reshaped to the form of a coffee cup by creating a dimple and progressively enlarging it, while shrinking the hole into a handle.

Topology is the study of those properties of objects that do not change when homeomorphisms are applied. As Henri Poincaré famously said, mathematics is not the study of objects, but instead, the relations (isomorphisms for instance) between them.

Properties

Continuous functions f and g are said to be homotopic if and only if there is a homotopy H taking f to g as described above. Being homotopic is an equivalence relation on the set of all continuous functions from X to Y. This homotopy relation is compatible with function composition in the following sense: if f_1, $g_1 : X \to Y$ are homotopic, and f_2, $g_2 : Y \to Z$ are homotopic, then their compositions $f_2 \neq f_1$ and $g_2 \neq g_1 : X \to Z$ are also homotopic.

Homotopy Equivalence

Given two spaces X and Y, we say they are homotopy equivalent or of the same homotopy type if there exist continuous maps $f : X \to Y$ and $g : Y \to X$ such that $g \neq f$ is homotopic to the identity map id_X and $f \neq g$ is homotopic to id_Y.

The maps f and g are called homotopy equivalences in this case. Every homeomorphism is a homotopy equivalence, but the converse is not true: for example, a solid disk is not homeomorphic to a single point, although the disk and the point are homotopy equivalent.

Two spaces X and Y are homotopy equivalent if they can be transformed into one another by bending, shrinking and expanding operations. For example, a solid disk or solid ball is homotopy equivalent to a point, and R^2 - {(0,0)} is homotopy equivalent to the unit circle S^1. Spaces that are homotopy equivalent to a point are called contractible.

Null-homotopy

A function f is said to be null-homotopic if it is homotopic to a constant function. (The homotopy from f to a constant function is then sometimes called a null-homotopy.) For example, a map from the circle S^1 is null-homotopic precisely when it can be extended to a map of the disc D^2.

It follows from these definitions that a space X is contractible if and only if the identity map from X to itself—which is always a homotopy equivalence—is null-homotopic.

Homotopy Invariance

Homotopy equivalence is important because in algebraic topology many concepts are homotopy invariant, that is, they respect the relation of homotopy equivalence. For example, if X and Y are homotopy equivalent spaces, then:

- If X is path-connected then so is Y.
- If X is simply connected then so is Y.
- The (singular) homology and cohomology groups of X and Y are isomorphic.
- If X and Y are path-connected, then the fundamental groups of X and Y are isomorphic, and so are the higher homotopy groups. (Without the path-connectedness assumption, one has $\pi_1(X,x_0)$ isomorphic to $\pi_1(Y,f(x_0))$ where $f : X \to Y$ is a homotopy equivalence and $x_0 \in X$.)

An example of an algebraic invariant of topological spaces which is not homotopy-invariant is compactly supported homology (which is, roughly speaking, the homology of the compactification, and compactification is not homotopy-invariant).

Relative Homotopy

In order to define the fundamental group, one needs the notion of homotopy relative to a subspace. These are homotopies which keep the elements of the subspace fixed. Formally: if f and g are continuous maps from X to Y and K is a subset of X, then we say that f and g are homotopic relative to K if there exists a homotopy $H : X \times [0,1] \to Y$ between f and g such that $H(k,t) = f(k) = g(k)$ for all $k \in K$ and $t \in [0,1]$. Also, if g is a retract from X to K and f is the identity map, this is known as a strong deformation retract of X to K. When K is a point, the term pointed homotopy is used.

Homotopy Groups

Since the relation of two functions $f, g : X \to Y$ being homotopic relative to a subspace is an equivalence relation, we can look at the equivalence classes of maps between a fixed X and Y. If we fix $X = [0,1]^n$, the unit interval $[0,1]$ crossed with itself n times, and we take our subspace to be its boundary $\partial([0,1]^n)$ then the equivalence classes form a group, denoted $\pi_n(Y,y_0)$, where y_0 is in the image of the subspace $\partial([0,1]^n)$.

We can define the action of one equivalence class on another, and so we get a group. These groups are called the homotopy groups. In the case $n = 1$, it is also called the fundamental group.

Homotopy Category

The idea of homotopy can be turned into a formal category of category theory. The homotopy category is the category whose objects are topological spaces, and whose morphisms are homotopy equivalence classes of continuous maps. Two topological spaces X and Y are isomorphic in this category if and only if they are homotopy-equivalent. Then a functor on the category of topological spaces is homotopy invariant if it can be expressed as a functor on the homotopy category.

For example, homology groups are a *functorial* homotopy invariant: this means that if f and g from X to Y are homotopic, then the group homomorphisms induced by f and g on the level of homology groups are the same: $H_n(f) = H_n(g) : H_n(X) \to H_n(Y)$ for all n.

Likewise, if X and Y are in addition path connected, and the homotopy between f and g is pointed, then the group homomorphisms induced by f and g on the level of homotopy groups are also the same: $\pi_n(f) = \pi_n(g) : \pi_n(X) \to \pi_n(Y)$.

Timelike Homotopy

On a Lorentzian manifold, certain curves are distinguished as timelike. A timelike homotopy between two timelike curves is a homotopy such that each intermediate curve is timelike.

No closed timelike curve (CTC) on a Lorentzian manifold is timelike homotopic to a point (that is, null timelike homotopic); such a manifold is therefore said to be multiply connected by timelike curves. A manifold such as the 3-sphere can be simply connected (by any type of curve), and yet be timelike multiply connected.

Homeomorphism

A function $f: X \to Y$ between two topological spaces (X, T_X) and (Y, T_Y) is called a homeomorphism if it has the following properties:

- f is a bijection (one-to-one and onto),
- f is continuous,
- The inverse function f^{-1} is continuous (f is an open mapping).

A function with these three properties is sometimes called bicontinuous.

If such a function exists, we say X and Y are homeomorphic. A self-homeomorphism is a homeomorphism of a topological space and itself. The homeomorphisms form an equivalence relation on the class of all

topological spaces. The resulting equivalence classes are called homeomorphism classes.

Notes

The third requirement, that f^{-1} be continuous, is essential. Consider for instance the function f: $[0, 2\pi) \to S^1$ defined by $f(\varphi) = (\cos(\varphi), \sin(\varphi))$. This function is bijective and continuous, but not a homeomorphism (S^1 is compact but $[0, 2\pi)$ is not). Homeomorphisms are the isomorphisms in the category of topological spaces. As such, the composition of two homeomorphisms is again a homeomorphism, and the set of all self-homeomorphisms $X \to X$ forms a group, called the homeomorphism group of X, often denoted Homeo(X); this group can be given a topology, such as the compact-open topology, making it a topological group.

For some purposes, the homeomorphism group happens to be too big, but by means of the isotopy relation, one can reduce this group to the mapping class group. Similarly, as usual in category theory, given two spaces that are homeomorphic, the space of homeomorphisms between them, Homeo(X, Y), is a torsor for the homeomorphism groups Homeo(X) and Homeo(Y), and given a specific homeomorphism between X and Y, all three sets are identified.

Properties

- Two homeomorphic spaces share the same topological properties. For example, if one of them is compact, then the other is as well; if one of them is connected, then the other is as well; if one of them is Hausdorff, then the other is as well; their homotopy & homology groups will coincide. Note however that this does not extend to properties defined via a metric; there are metric spaces that are homeomorphic even though one of them is complete and the other is not.
- A homeomorphism is simultaneously an open mapping and a closed mapping; that is, it maps open sets to open sets and closed sets to closed sets.
- Every self-homeomorphism in S^1 can be extended to a self-homeomorphism of the whole disk D^2 (Alexander's trick).

Informal Discussion

The intuitive criterion of stretching, bending, cutting and gluing back together takes a certain amount of practice to apply correctly—it may not be obvious from the description above that deforming a line segment to a point is impermissible, for instance. It is thus important to realize that it is the formal definition given above that counts.

This characterization of a homeomorphism often leads to confusion with the concept of homotopy, which is actually *defined* as a continuous deformation, but from one *function* to another, rather than one space to another. In the case of a homeomorphism, envisioning a continuous deformation is a mental tool for keeping track of which points on space X correspond to which points on Y—one just follows them as X deforms. In the case of homotopy, the continuous deformation from one map to the other is of the essence, and it is also less restrictive, since none of the maps involved need to be one-to-one or onto. Homotopy does lead to a relation on spaces: homotopy equivalence. There is a name for the kind of deformation involved in visualizing a homeomorphism. It is (except when cutting and regluing are required) an isotopy between the identity map on X and the homeomorphism from X to Y.

Conclusion

Topology emerged through the development of concepts from geometry and set theory, such as space, dimension, and transformation. Ideas that are now classified as topological were expressed as early as 1736. Toward the end of the 19th century, a distinct discipline developed, which was referred to in Latin as the *geometria situs* ("geometry of place") or *analysis situs* (Greek-Latin for "picking apart of place"). This later acquired the modern name of topology. By the middle of the 20th century, topology had become an important area of study within mathematics. A new approach uses a functor from filtered spaces to crossed complexes defined directly and homotopically using relative homotopy groups; a higher homotopy van Kampen theorem proved for this functor enables basic results in algebraic topology, especially on the border between homology and homotopy, to be obtained without using singular homology or simplicial approximation. This approach is also called nonabelian algebraic topology, and generalises to higher dimensions ideas coming from the fundamental group.

References

Joseph, Pedlosky, *Geophysical fluid dynamics*, Springer, 1987.

Lass, Harry, *Vector and Tensor Analysis*, McGraw-Hill Book Company, 1950.

Lipschutz, Seymour, *Schaum's Outline of General Topology*, McGraw-Hill, 1968.

Maunder, C. R. F.: *Algebraic Topology*, Van Nostrand Reinhold, London, 1970.

Mendelson, Bert: *Introduction to Topology*, Dover Publications, 1990.

Nahin, Paul J., *Oliver Heaviside: the life, work, and times of an electrical genius of the Victorian age*, JHU Press, 2000.

Peter Hilton; Stammbach, U. *A.: Course in homological algebra*, Springer-Verlag, New York, 1997.

Ronald Brown: *Topology and groupoids,* Booksurge, U.K., 2006.

Rudin, Walter: *Principles of Mathematical Analysis*, McGraw-Hill, 1976.

Schey , H. M., *Div Grad Curl and all that: An informal text on vector calculus*, W. W. Norton & Company, 2005.

Sepanski, Mark R.: *Compact Lie Groups*, Springer-Verlag, 2007.

Strang, Gilbert, *Linear Algebra and Its Applications,* Brooks Cole, 2006.

Victor Bryant, *Metric Spaces: Iteration and Application*, Cambridge University Press, 1985.

Effects of Sublethal Concentrations of the Herbicide, Glyphosate, on Embryonic Development of the Indian Major Carp, Labeo rohita

Ranbir Kumar Singh

Research Scholar, Dept. Of Zoology, JP University Chapra

Abstract

Aquaculture is one of the fastest growing sectors worldwide. Currently, 50% of global fish consumption is provided by aquaculture. In India, the major cultivated fishes are *Labeo catla, Labeo rohita, Cirrhinus mrigala, Hypophthalmichthys molitrix, Ctenopharyngodon idella*, and *Cyprinus carpio*. Among these, *L. rohita* is a widely consumed fish. We aimed to study the effect of one of the most widely used herbicides, glyphosate, on the embryonic development of *L. rohita.* The 96 h LC_{50} of glyphosate for *L. rohita* embryos was found to be 20.89 mgL^{-1}. The embryos were exposed to $1/10^{th}$, $1/5^{th}$, and $1/3^{rd}$ concentrations of LC_{50} for 96 h. The observed deformities included abdominal curvature, kink formation in the tail, yolk sac edema, pericardial edema, and improperly flattened swim bladder. Besides, we could observe a reduction in pigmentation at 96 h and a decrease in heart rate at 24, 48, 72, and 96 h. All these deformities led to the mortality of embryos. This study indicated that the herbicide (glyphosate) can adversely affect the natural population of the Indian major carp, *L. rohita*.

Introduction

Glyphosate [N-(phosphonomethyl)glycine], CAS number: 1071-83-6, is a chemical used to control weeds. The half-life of the molecule ranges from 2 to 215 days in soil and 2 to 91 days in water. Weeds compete with cultivated crops for nutrients and sunlight. They adversely affect plant growth [2]. Glyphosate has inhibitory effects on EPSPS (5-enolpyruvyl shikimate 3-phosphate synthase). Inhibition of EPSP leads to depletion of the aromatic amino acids tryptophan, tyrosine and phenylalanine, which are required for protein synthesis. This organophosphate group of pesticides was first synthesized and marketed in 1950 by a Swiss pharmaceutical company, but its herbicidal properties were unknown. E. Franz of the Monsanto Company studied the herbicidal properties of glyphosate under the trade name Roundup. Since then, it has been used in agriculture, horticulture and forestry. Its use expanded after the

discovery of glyphosate-resistant crops in the 1980s, and its use increased 100-fold; it is still the most widely used herbicide worldwide. This polyprotic molecule has phosphonate, carboxyl and amino groups as three polar functional groups. Glyphosate has been used as a herbicide for many years. However, it has been banned in some countries around the world over the past few years because it affects soil, water and soil microflora. In India, it was banned in Kerala and Punjab. In other states it is only allowed for limited use. In Odisha, glyphosate is commonly used for weed control in rice, maize, cotton and vegetables. Glyphosate (GLY) has been classified as a group 2B and group 2A human carcinogen and is often found in aquatic ecosystems. So far, GLY has been detected in natural waters in many countries at concentrations generally between 3 and 700 μg/L.

Aquaculture is the controlled process of raising, raising and harvesting pinnipeds, molluscs and aquatic plants for human consumption. Fish offer hope in the fight against malnutrition, as they are foods rich in protein, calcium, omega-3 fatty acids and vitamins such as A and B12. Currently, 50% of global fish consumption is covered by aquaculture. In addition, it creates space for employment and contributes to economic growth. Fish and aquaculture support the livelihoods of 12% of the world's population. It is one of the fastest growing sectors in the world.

According to the State of World Fisheries and Aquaculture study, the growth of aquaculture, especially in Asia, has increased total fisheries and aquaculture production to 214 million tons in 2020, which includes 178 million tons of aquatic animals and 36 million tons of algae. Globally, India is the second largest producer of fish after China. About 95% of total aquaculture production is freshwater aquaculture. The application of advanced technologies has resulted in an increase in aquaculture production in India by 7% with an annual production of 5.77 million tonnes. This upward shift of the growth curve was achieved by induced breeding of fish such as the three major Indian carps (Labeo catla, Labeo rohita and Cirrhinus mrigala) and mixed culture of large carps as well as exotic carps (Hypophthalmichthys molitrix, Ctenopharyngodon idella, and Cyprinus carpio). Of these, L. rohita is a highly consumed farmed fish. The presence of pollutants in water bodies affects the growth and development of fish and ultimately adversely affects aquaculture production in terms of quality and quantity. The development of fish depends on the factors present in the surrounding environment. So any change in the environment can induce developmental changes, and these changes can persist into adulthood, even if exposure to pollutants is stopped. This study aims to determine the developmental toxicity of one of the widely used herbicides, glyphosate, on the commercially important fish L. rohita.

Materials and Methods

Test Chemicals

The commercial grade of glyphosate-based herbicide, "Clear off," was obtained from Safex Chemicals Ltd., Delhi, India. The effective concentration was 41%. The three different concentrations taken were 1/3rd, 1/5th, and 1/10th of LC_{50} (6.96 mgL^{-1}, 4.18 mgL^{-1}, and 2.08 mgL^{-1}, respectively). To prepare these concentrations in 500 ml of water, 8.7, 5.22, and 2.6 ¼l were mixed into water, respectively.

Collection of Eggs

Fertilized eggs of *L. rohita* were collected from ICAR-Central Institute of Freshwater Aquaculture, Bhubaneswar, Carp Hatchery Unit. A pair of 3-year-old male and female fish was bred. The female fish weighed 2.2 kg with 38.5 cm length. The male fish was of 1.8 kg weight with 33 cm length.

Screening of Fertilized Eggs

The fertilized eggs were screened in the laboratory depending on their transparent appearance which was visible by naked eyes. The unfertilized dead embryos were opaque in appearance. The embryos were observed under microscope and those showing cleavage were selected for the toxicity test.

Median Lethal Concentration

The median lethal concentration (LC_{50}) was determined by Finney's method. To prepare 1, 10, 20, 30, 40, and 50 mgL^{-1} concentrations of glyphosate, 0.25, 2.5, 5.0, 7.5, 10, and 12.5 μl volumes were added in 80 ml of water, respectively. Ten fertilized eggs were released to each concentration 4 h after fertilization. The number of dead embryos was counted and noted down at an interval of 24 h, and the rate of mortality was calculated. Then, the probit value was noted down from Finney's table. The logarithm values of respective concentrations were calculated. A graph was plotted taking logarithm values of concentrations along the *X*-axis and probit values of mortality in respective concentrations along the *Y*-axis. Then, probit of 5 was located on *Y*-axis. Then, by moving down the *X*-axis, we could find the logarithm of $LC_{50.}$ By calculating the anti-logarithm, we could determine the LC_{50}.

Exposure of Embryos to Glyphosate

The 4 hpf (hours post fertilization) embryos were exposed to 1/3rd, 1/5th, and 1/10th of the median lethal concentration of glyphosate. The three treatments were designated as treatment-I, II, and III depending upon the concentration of glyphosate. The dosages were 2.08, 4.17, and 6.96 mgL^{-1} for treatment-I, treatment-II, and treatment- III, respectively. The

concentrations were loaded 30 min before the release of embryos. Fifty embryos were released to each Petri plate containing 500 ml of water. The experiment was conducted in a set of 3 replicates. The embryos were observed under a microscope and photographed. The observations include duration of hatching, heart, and optic cup formation, eye development, formation of the branchial artery, edema, and kink formation. The percentage of deformed embryos was calculated for 24, 48, 72, and 96 h as a function of time. The percentage of deformed embryos was calculated as the ratio of deformed embryos/larvae to the number of alive embryos/ larvae at 24 h. For 48, 72, and 96 h, it was calculated as a cumulative percentage.

Results

The median lethal concentrations for 72 and 96 h were 26.3 and 20.89 mgL^{-1}, respectively. The differentiation of the head, yolk sac, and tail was observed in all treatments and control at 13 hpf. The twitching movement was also observed after the 13th hour of development. In control and treatment-I, hatching occurred between the 16th and 27th hpf, whereas in treatment-II and treatment-III, it occurred between the 16th and 22nd hpf. The optic cup formation was delayed in all three treatments. In control, it occurred at 24 hpf, but in all three treatments, it was found at 27 hpf. At the 16th hour of development, the red blood cells (RBCs) were formed in all treatments and control except two embryos in treatment-II. Branch arteries were formed at 37 hpf in control and all treatments. Other deformities observed were yolk sac edema, pericardial edema, abdominal curvature, and tail kink formation. At 24 hours, 2 deformed embryos were observed in treatment-I with yolk sac edema, pericardial edema, and elongated yolk sac. In the rest of the treatment and control, all embryos were normal. After 48 h, more abnormalities were observed at higher concentrations compared to lower concentrations. At 2.08 mgL−1, 4 deformed embryos were found, 3 of which contained yolk sac edema and 2 pericardial edema. In treatment II, 7 deformed embryos were observed, of which 4 had deformed yolk sacs and pericardium, and 6 embryos contained deformed spinal cords. Eight deformed embryos were observed in treatment III, of which 4 had yolk sac and pericardial edema and 2 had tail kink formation. At 72 h, 6 embryos were detected with yolk sac edema, 4 with pericardial, 1 with abdominal curvature, and 2 with kinking of the tail. In treatment II, 6 embryos had yolk sac edema, 4 pericardial edema, and 3 tail kink formation. At the highest glyphosate concentration, yolk sac edema, pericardial edema, and abdominal curvature were noted in 6, 5, and 1 embryos, respectively. After 96 hours, more changes were observed at the high concentration compared to the lower concentrations.

Tail kink formation was observed in 1 embryo in both treatment-I and treatment-II. Abdominal curvature was observed in one embryo in treatment III. Embryos treated with glyphosate showed less pigmentation. In addition, the air bladder was not properly flattened in embryos treated with III. The percentage of deformed embryos at different concentrations of glyphosate at different time intervals is shown in Table 1. The heart rate was calculated for the embryos of all treatments and the control at an interval of 24 h. It was found that in all four observations, the heart rate of the control embryos was higher than that of the treatment and decreased in a concentration-dependent manner.

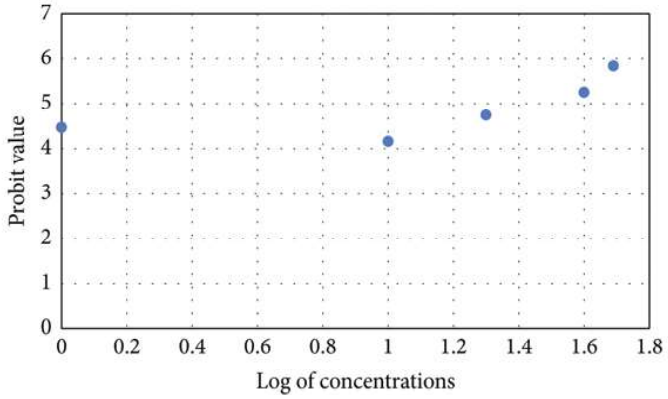

Figure 1: *The graph showing the 96 h* LC_{50} *value of glyphosate for embryos of Labeo rohita.*

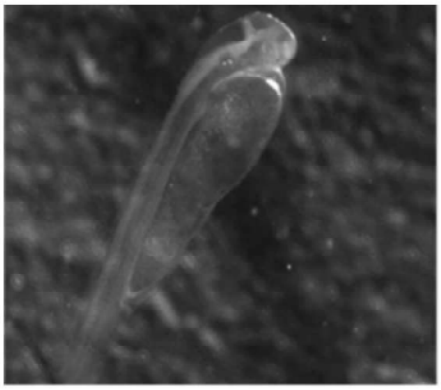

Figure 2: *Development of embryos of* Labeo rohita *at 24 hpf.*

Table 1: The percentage of deformed embryos of **Labeo rohita** *at various concentrations of glyphosate at different time intervals.*

Treatments/time interval	Percentage of deformed embryos			
	24 h	48 h	72 h	96 h
Control	0	0	0	0
Treatment-I	2	11	33	46
Treatment-II	0	14	36	53
Treatment-III	0	17	42	62

Treatment-I: 2.08 mgL^{-1}, treatment-II: 4.17 mgL^{-1}, and treatment-III: 6.96 mgL^{-1}.

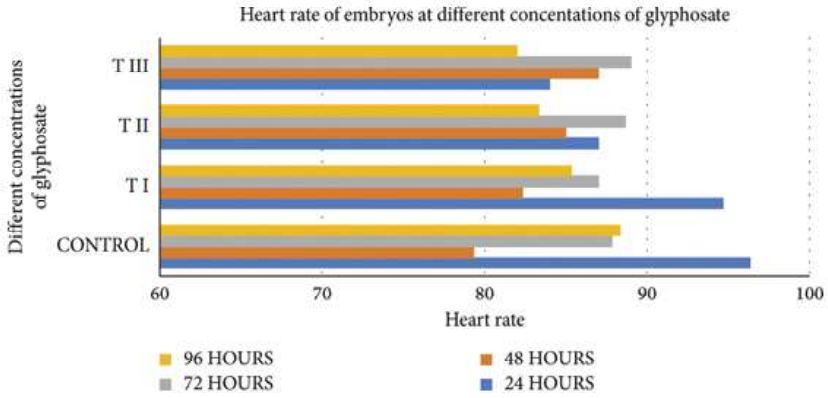

Figure 3: *Heart rate of* Labeo rohita *embryos in different treatments (2.08, 4.1, and 6.96 mgL^{-1}) of glyphosate.*

Discussion

In this experiment, we studied the sublethal effects of glyphosate on the development of embryos of *L. rohita.* The 96 hpf is a crucial period for embryos. In zebrafish, more developmental abnormalities were observed when the embryos were exposed to glyphosate for 96 h after 4 h of fertilization as compared to the exposure for 96 h at 3 days post fertilization. Hence, in this experiment, we exposed the 4 hpf embryos to different

concentrations of glyphosate for a period of 96 h. It could be observed that the deformities in embryos increased with an increase in glyphosate concentration and duration of exposure. The same observations were reported in zebrafish exposed to 1, 5, 10, and 100 mg/L concentrations of glyphosate for 24, 48, 72, and 96 h. Before hatching, no deformities were observed in any treatment or control due to the presence of chorion membrane. The chorion is a secondary membrane secreted by the developing oocyte. It is a cellular layer present immediately above the plasma membrane of an ovum. This membrane protects the embryo from pollutants present in the external environment. According to the study by Villalobos et al., the chorion membrane protects the medaka embryos from the toxic effects of Thiobencarb. This information supports our findings.

The heart rate was found to be decreased in all the treatments compared to the control. It slowed down with an increased concentration of glyphosate. In the case of medaka embryos, the heart rate increased at first and then it decreased. The increased heart rate was described as an adaptation to stress environment, and the decreased heart rate might have resulted due to destruction of cells in the heart wall. Our findings differed from it. The heart rate was decreased in glyphosate-treated fish in a dose-dependent manner. The same results were observed in the case of zebrafish exposed to 50 ¼g/ml of glyphosate. They described it as a result of cell death in the heart and the concentrations taken were higher, so the embryos could not acclimate to the stress condition.

The first deformities were observed in 2.08 mgL^{-1} concentration at 23rd h. We could observe 2 deformed embryos in the 23rd h of development at 2.08 mgL^{-1} only, but no deformities were observed at higher concentrations. The embryos are more susceptible to lower concentrations of glyphosate during early stages within 24 h. During later stages of development, they were more susceptible to higher concentrations (Table 1). Such changes were observed in zebrafish exposed to methyl mercury. More number of deformed embryos were observed at 20 ¼g/l compared to 30 ¼g/l after 16 hpf. The spinal curvature and kink formation in the tail were observed in all the treatments, but not in the control. Hence, it is clear that these changes resulted due to exposure to glyphosate. These could be due to decreased collagen synthesis. In the case of medaka embryos, several developmental deformities were reported, such as bent tail and abdominal enlargement after exposure to glyphosate. The concentrations used in this experiment (100, 200, 300, 400, and 500 mgL^{-1}) were much higher than the concentrations used in our experiment. This indicates that the embryos of *L. rohita* are more sensitive to glyphosate as compared to medaka.

Spinal curvature was reported in zebrafish exposed to 0.620 (0.436–0.963), 0.475 (0.302–0.801), and 0.341(0.177–0.617) mg·L^{-1} concentration of organophosphate insecticide, Sumithion. Glyphosate was identified as a potent teratogen to the Japanese medaka fish (*Oryzias latipes*) embryos and can induce developmental abnormalities at a concentration of 0.5 mg/L. The abnormalities include spinal curvature, enlarged yolk sac, and greying of the yolk sac. The yolk sac edema was noticed in the African catfish (*Clarias gariepinus*) exposed to a group of metallic chemical elements, such as chromium, cadmium, copper, and agrochemicals like sodium pentachlorphenol (NaPCP) and malathion. The yolk sac is the site for early blood flow. Remodeling of blood vessels occurs at this site. Glyphosate caused rupture of early blood vessels near yolk sac. The yolk sac edema was observed in zebrafish (*Danio rerio*) after 96 h of exposure to 2,3,7,8-tetrachlorodibenzo-*p*-di- Polychlorinateddibenzo-*p*-dioxins (PCDDs) and dibenzo-oxin (TCDD). In this experiment, the first yolk sac edema was observed at 24 h at a 2.08 mgL^{-1} concentration of glyphosate.

The well-developed swim bladder was observed at 96 hpf. This organ serves as a bouncy device. In teleost, it consists of two chambers, anterior and posterior. The posterior chamber is vascularised and gas release occurs in this chamber. In the case of carp, the one-chambered swim bladder develops at 96 hpf and the two-chambered swim bladder develops at 192 hpf. In our experiment, the swim bladder was improperly flattened only at a 6.96 mgL^{-1} concentration of glyphosate. A similar observation was made in zebrafish exposed to glyphosate-based herbicides. The different concentrations were 11.7, 35, and 58.3 mgL^{-1}. The abnormality was observed in a dose-dependent manner. A reduced pigmentation was observed in glyphosate-treated embryos. Such a reduction in pigmentation has been observed in algae treated with various pesticides. However, no such study has been conducted on animals. The effects of glyphosate on chromatophore cells can be explored further.

Conclusion

This research presents an enormous effect of glyphosate in *L. rohita* embryos. The teratogenic effects of glyphosate led to deformed embryos, decreased heart rate, and high mortality in a dose-dependent manner. This chemical would also adversely affect the natural population of the carps and pond culture system which receives runoff from agricultural land. To sustain the production of food fish from aquaculture, an amelioration mechanism (feed supplementation) can be developed further for combating the impact of the herbicide.

References

1. I. W. Selderslaghs, A. R. Van Rompay, W. De Coen, and H. E. Witters, "Development of a screening assay to identify teratogenic and embryotoxic chemicals using the zebrafish embryo," *Reproductive Toxicology*, vol. 28, no. 3, pp. 308–320, 2009.
2. G. M. Dill, R. D. Sammons, P. C. Feng et al., "Glyphosate: discovery, development, applications, and properties," *Glyphosate resistance in crops and weeds: History, Development, and Management*, pp. 1–33, 2010.
3. T. S. Hamazaki, Y. Nagahama, I. Iuchi, and K. Yamagami, "A glycoprotein from the liver constitutes the inner layer of the egg envelope (zona pellucida interna) of the fish, *Oryzias latipes*," *Developmental Biology*, vol. 133, no. 1, pp. 101–110, 1989.
4. T. M. Uren Webster, L. V. Laing, H. Florance, and E. M. Santos, "Effects of glyphosate and its formulation, roundup, on reproduction in zebrafish (*Danio rerio*)," *Environmental Science and Technology*, vol. 48, no. 2, pp. 1271–1279, 2014.
5. L. de Brito Rodrigues, R. de Oliveira, F. R. Abe et al., "Ecotoxicological assessment of glyphosate based herbicides: effects on different organisms," *Environmental Toxicology and Chemistry*, vol. 36, no. 7, pp. 1755–1763, 2017.
6. W. A. Battagli, M. T. Meyer, K. M. Kuivila, and J. E. Dietze, "Glyphosate and its degradation product AMPA occur frequently and widely in US soils, surface water, groundwater, and precipitation," *Journal of the American Water Resources Association*, vol. 50, no. 2, pp. 275–290, 2014.
7. S. Singh, V. Kumar, S. Datta et al., "Glyphosate uptake, translocation, resistance emergence in crops, analytical monitoring, toxicity and degradation: a review," *Environmental Chemistry Letters*, vol. 18, no. 3, pp. 663–702, 2020.
8. P. Jayasankar, "Present status of freshwater aquaculture in India-A review," *Indian Journal of Fisheries*, vol. 65, no. 4, pp. 157–165, 2018.
9. D. Pal and S. K. Maiti, "Seasonal variation of heavy metals in water, sediment, and highly consumed cultured fish (*Labeo rohita* and *Labeo bata*) and potential health risk assessment in aquaculture pond of the coal city, Dhanbad (India)," *Environmental Science and Pollution Research*, vol. 25, no. 13, pp. 12464–12480, 2018.
10. O. S. Panetto, H. F. Gomes, D. S. F. Gomes et al., "The effects of Roundup® in embryo development and energy metabolism of the zebrafish (*Danio rerio*)," *Comparative Biochemistry and Physiology, Part C: Toxicology and; Pharmacology*, vol. 222, pp. 74–81, 2019.
11. J. S. de Araujo, I. F. Delgado, and F. J. Paumgartten, "Glyphosate and adverse pregnancy outcomes, a systematic review of observational studies," *BMC Public Health*, vol. 16, no. 1, pp. 1–13, 2016.
12. J. P. K. Gill, N. Sethi, A. Mohan, S. Datta, and M. Girdhar, "Glyphosate toxicity for animals," *Environmental Chemistry Letters*, vol. 16, no. 2, pp. 401–426, 2018.
13. W. Ding, Y. Shangguan, Y. Zhu et al., "Negative impacts of microcystin-LR and glyphosate on zebrafish intestine: linked with gut microbiota and microRNAs?" *Environmental Pollution*, vol. 286, 2021.
14. G. Haylor, "Poverty reduction and aquatic resources," 2004, https://core.ac.uk/download/pdf/11018196.pdf.
15. R. Subasinghe, D. Soto, and J. Jia, "Global aquaculture and its role in sustainable development," *Reviews in Aquaculture*, vol. 1, no. 1, pp. 2–9, 2009.
16. Fao, "The state of World fisheries and aquaculture 2022," *Towards Blue*

Transformation, FAO, Rome, Italy, 2022.

17. D. J. Finney, *Probit Analysis*, Cambridge University Press, London, UK, 1971.
18. D. Bridi, S. Altenhofen, J. B. Gonzalez, G. K. Reolon, and C. D. Bonan, "Glyphosate and Roundup® alter morphology and behavior in zebrafish," *Toxicology*, vol. 392, pp. 32–39, 2017.
19. E. Sulukan, M. Köktürk, H. Ceylan et al., "An approach to clarify the effect mechanism of glyphosate on body malformations during embryonic development of zebrafish (Daino rerio)," *Chemosphere*, vol. 180, pp. 77–85, 2017.
20. F. Cotelli, F. Andronico, M. Brivio, and C. L. Lamia, "Structure and composition of the fish egg chorion (*Carassius auratus*)," *Journal of Ultrastructure and Molecular Structure Research*, vol. 99, pp. 70–78, 1988.

Study and Evaluation of *Rungia Pectinata* (L.) Nees. Root as Female Herbal Contraceptive

Amrendra Kumar Anand

Department of Botany, B.S.S. College, Supaul, B.N. Mandal University, Madhepura Bihar (INDIA)

Vinod Prasad

Department of Botany, Patna University, Patna Bihar (INDIA)

ABSTRACT: The concept of small and healthy family is priority for all citizen in modern era. It is beneficial for family itself, society and the nation. For sustainable development, human population must be under control especially in over populated country like India. To avoid population explosion, human beings uses different devices, drugs, pills and behavioral and ritual practices either to avoid or terminate the unwanted pregnancy. In ancient period different types of methods were in practice. Modern methods of contraception rely on use of drugs, hormones, chemicals which may interfere with maturation and release of ova, implantation of fertilized ova or may cause fetal abortion. Although, modern methods are simple, easy to use and are easily available but many health risks are also associated with them. The young generation must be aware how to enjoy conjugal life and handle the unintended pregnancy. Active constituents of many plants have potential to control birth. These phytochemicals are present in roots, stem, leaves, fruits, seeds, bark, flowers, bulbs, and in whole plants. *R. pectinata* (L.) Nees. is one of the potent plants which are widely used by tribal people for birth control as daily female contraceptive pill. The present work is tried to correlate the Indian Traditional Knowledge System (TKS) to the well-being of human society to contribute in the sustainable development goals (SDGs).

Key words: Birth control, Contraception, *R. pectinata*, SDGs.

Introduction:

Contraception is intentional prevention of pregnancy by the means of drugs, barriers, devices, surgery or any practices. Simply, it is the act of preventing unwanted birth. Any drugs, devices or acts which is used to prevent a woman from becoming pregnant can be considered as contraceptive.[1] Birth control is essential parameter for the overall development of family, society and nation particularly for developing countries like India which is now the most populated country. Population

growth is proportionally related with resource utilization which affects the health and wealth of people. Also, it has direct impact on environment. For sustainability of environment and resources, population growth rate of a country must be under control. For this, all person should be personally aware and conscious about health and birth control measures. Family members will be healthy only if the family is small.

Sexual relationship is a basic physical and psychological demand for both male and female. It is important to aware of the possible consequences of unprotected sex and safe options of contraception. Curiosity about opposite sex and sexual relationship is natural in teenagers, so it is very important to have proper information about pregnancy and contraception. Use of suitable contraceptive allows couples to enjoy sexual life without the fear of unwanted pregnancy. It gives freedom for planned pregnancy and for spacing births. In addition, physical barriers like male and female condoms provide protection from STDs such as HIV/AIDS, syphilis, gonorrhea etc. It is interesting to note that India is first among the countries which officially adopted family planning program as early as 1950.[2] Unfortunately, the goal is still far away primarily due to unawareness which is the main hurdle in achieving SDGs.

History of Contraception:

The history of contraception is as old as human civilization. Human beings practices different forms of contraceptive methods to reduce the size of family and spacing the child birth. From the early of civilization, people know the importance of small family. In ancient era, small sized family was preferred over longer one. People used mantras, talisman, mechanical barrier, oral drugs and other artificial devices to prevent conception after conjugation.[3] Rigveda which is written around 2000 B.C. warns against large family as *'A man with many children succumbs to miseries'*. In ancient religious, medical and sexological classical literature, much emphasize on the preservation of seminal fluid (semen) or shukra in body and strongly prohibited masturbation. Semen preservation promotes body strength, complexion, immunity to fight with disease and longevity.[4] Indian classical texts, rituals and believes directly or indirectly portrayed message of small and healthy family. The whole human life is divided into four periods (*ashrams) Brahmacharya* (student), *Grihastha* (householder), *Vanprastha* (retired) and *Sanyas* (renunciation) and marriage is prescribed in second one I.e. grihastha aashram. The ashram system emphasized four proper goals of human life i.e. *purushartha* which are artha, dharma, kama and moksha for fulfillment, happiness, and spiritual liberation.[5] Manusmriti prohibited sexual act on certain *tithi* (dates) like in amavashya (new moon days), astami (8th day of lunar month). Besides these occasions, days like *shraddha* (last rites), and when guest or superior

family member is present in house, sexual act should be avoided.[6] Also, one should get married only after completing the study or after 25 years and married life continue only up to 50 years of age, and not thereafter.[6] All such believes, suggestions and practices helps in spacing and limiting child birth.

Methods of Contraception:

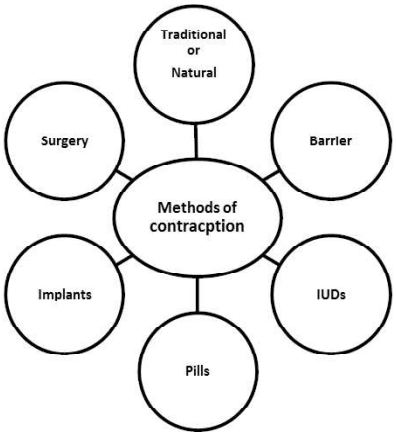

Fig. Methods of Contraception

There are various methods and practices are available for birth control which can be classified as traditional or natural and modern methods of contraception. As the name implies, traditional methods don't use any drugs, synthetic products or barriers and is based on partner's mutual control and co-ordination. It can be make effective by monitoring the physiological, behavioral or bodily changes of female partner. This method includes – *coitus interruptus* or withdrawal (withdrawal of penis from vagina before ejaculation), *lactational amenorrhea* (delay in menstruation because of active breast feeding), *rhythm method* (avoidance of sexual intercourse by predicting the ovulation period through recording menstrual pattern, body temperature and cervical mucus inspection).

The modern quick and ready-to-use contraceptive methods are based on the use of drugs, hormones and chemicals which may interfere with maturation and release of ova and implantation of fertilized ova. The physical barriers prevent deposition of sperms in female genital tract and their meeting with the ova. The modern birth control methods includes- (a) Barriers in the form of male and female condoms, cervical caps, diaphragm and vaults (b) IUDs which may be non-medicated (Lipps loop), Cu-releasing (Cu-T, Cu-7, Multiload-375) or hormone releasing (Progestasert, LNG-20) (c) Pills or Oral contraceptive pills (Progestine-only Pills-POPs or Combined oral Contraceptive Pills-COCs) (d) Implants (Progestogen alone or Combined- releasing both progesterone and

estrogen) and (e) Surgery (Vasectomy for male and Tubectomy for female). Although, modern methods are simple, easy to use and are easily available but many health risks are associated with them. For example, combined oral contraceptives increases the risks of cerebral thrombosis[7], increases level of triglyceride, HDL, and cholesterol and increases mortality due to cardiovascular diseases as well as malignant tumors in any organs, poor glucose tolerance or diabetes, nausea abdominal pain, headache, obesity and menstrual changes.[8,9,10] The risk of cardiovascular disease is higher in COCs- user then non-user especially after 35 year of age.[11] This risk again increases when women have smoking habit and continuously using pills.[12] Pills cause depression. High levels of estrogen and progestin increase the concentration of a brain enzyme that reduces the level of serotonin and cause depression.[13] The condition becomes worst when an already depressed women use only progestin pill.[14] Use of pill also increase the risk of hypertension.[15]

An Intrauterine device (IUD) is an effective measure of contraception, but users may face some side effects. There are several side effects of both types of IUDs. Since the IUD punctures the uterine wall, its insertion can cause severe bleeding and infection. The copper based IUD increases the menstrual bleeding spotting between periods and also in some cases it is expelled out from the uterus to increase the risk of pregnancy.[16] The hormonal IUD can cause inflammation of vagina, pelvic pain, headache, painful menstruation, sore breasts, ectopic pregnancy ovarian cyst formation etc. In some cases, its symptoms appear in the form of mood swings, and acne and if someone has got pregnancy then it promotes miscarriage or preterm birth. And, many more direct or indirect side-effect are associated with these modern options of birth control.[17]

Plants used in various forms of Contraception:

Since time immemorial, mankind uses plants and their products for health benefits, to cure diseases and as nutritional supplements for physical fitness. Today, herbal preparation in different forms are recognized and recommended world-wide mainly because of very less or no side effects in long term, easy availability and their better suitability. Herbal medicine has acceptability in every culture and tradition, especially among tribal population. According to WHO about 80% of world population relay on plant based medicines. More than 35000 plant species are being used in various human cultures around the world for medicinal purposes.[18] In India, the sacred vedas dating back between 35000 BC and 8000BC mentioned medicinal values of plants. The old *Virikshayurveda* compiled even before the beginning of Christian era and formed the basis of medicinal studies in ancient India. Rigveda mentioned the use of cinnamon (*Cinnamonum verum* Prel.), ginger (*Zingiber officinalis* Rose.), sandalwood (*Santalum album* L.) etc. not only in religious ceremonies but also for

medicinal use.[19] At one time nearly all medicines were derived from natural products.[20] In India, almost 95% of the medical prescriptions are plant based in traditional system of AYUSH pharmacology.[21]

Plants synthesize a wide variety of chemical compounds of medicinal importance. Many of these active phytochemicals have beneficial effects on human health and hence can be effectively used to treat diseases and physical ailments. Chemical compounds in plants mediate their effects on the human body through processes identical to those already well understood for the chemical compounds in conventional drugs; thus herbal medicines do not differ greatly from conventional drugs in terms of how they work. The control of birth by the use of herbal preparation may be more effective when physiological and psychological condition of female properly monitored.

Active constituents of many plants have potential to control birth. These phytochemicals are present in roots, stem, leaves, fruits, seeds, bark, flowers, bulbs, and in whole plants.[22] They may affect the functioning of ovary, fallopian tube, uterus and testes by change in their histological and anatomical features and by modulating the secretion of sex hormones. As potential contraceptive, phyto-constituents are effective for both male and female. On female side, many herbs show effects on before-fertilization processes whereas others impose their effects after successful fertilization. Herbs can impair fertility by rapid expulsion of fertilized ova from the fallopian tube, inhibition of implantation of fertilized ova due to disturbance in estrogen – progesterone balance, fetal abortion perhaps due to lack of supply of nutrients to the uterus and the embryo. On male side, plant constituent affect fertility through affecting sperm count, their motility and viability.[23]

Based on potential impact on reproductive physiology, plants with contraceptive properties can be categorized as:

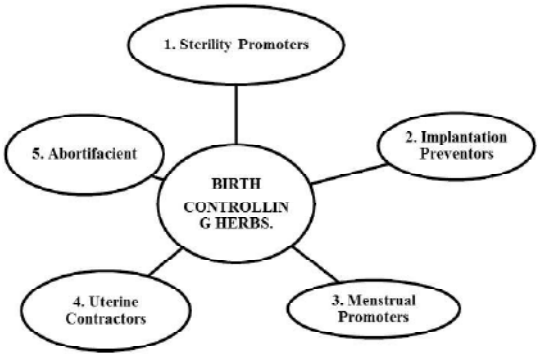

Diagram2: Classification of Birth controlling herbs.

Example: 1. *Lithospermum rudarale* Douglas ex Lehm and *Cardus benedictus Linn.*

2. *Daucus carota* Linn. and *Polygonum hydropiper* Linn.

3. *Agave Americana* Linn. and *Cannabis sativa* Linn.

4. *Aristolochia* sp. Linn. and *Gossypium herbaceum* Linn.

5. *Carica papaya* Linn. and *Mentha pulengium* Linn.

Materials and Methods:

Rungia pectinata (L) Nees.- The Experimental Plant Material

Rungia pectinata(L) Nees. is a herbaceous plant of dicot family acanthaceae or the *Barleria* family. It is commonly found in Bangladesh, Bhutan, India, Laos, Myanmar, Nepal, Sri Lanka, Thailand, and Vietnam. It is known to various Indian cultures by different vernacular names such as *Sut, mashi* (Marathi), *Parwati, Gumathi Hada*(Jharkhand), *Pindi* (Bengali/ Sanskrit) etc. R. pectinata (L) Nees. is a forest dwelling, shade loving plant generally found under canopy of large trees like *Butea monosperma* (H. Palas). For the present work, root of the plant was taken as preferred part for the experimental work and for authenticating its efficacy in contraception. The tribal female of Jharkhand state use roots of this plant as such on daily basis for preventing pregnancy. They stop consumption when wish to become pregnant. The mentioned plant was scientifically identified by Botanical Survey of India, Howrah, West Bengal, India (Reference No: CNH/28/2013/Tech-II).

The experimental plant was selected after survey with tribal people of Jharkhand mainly in the forest areas of Banari and Netarhat of Gumla district. Plants were collected in its flowering stage with the help of local medicine man (LMM) and local tribal people. Tribal peoples are well acquainted with the traditional knowledge regarding medicinal properties of plants. They are mostly dependent upon the plant products for their livelihood and disease treatment.

These nature-friendly peoples know many plants as birth controlling herbs. They mostly rely on R. pectinata (L) Nees. for contraception. Hence the same plant was considered as experimental plant of interest. After collection of plants, roots were separated and stored in cool dry place and taken all measures to avoid microbial infection.

Fig.: a. Young plant b. Flowering twig c. Tape root

Swiss Albino Mice: The Animal Model:

The Swiss albino mice (*Mus musculus*) were taken as model organism for experimental observation. They were reared at mice house of Mahavir Cancer Sansthan and Research Centre (MCSRC), Patna under prescribed guideline. Mice were housed in polypropylene cages at 22±1p C, with a 12:12hour day and night cycle. All the mice were randomly divided in four groups. For easy identification, they were marked with colour on body. Prescribed diet was given to all. A total of 36 female Swiss albino mice were taken, of which 12 were separated as controlled group. Rest of the 24 mice was divided into four groups, 06 in each. All the groups of mice were considered for histological observations of reproductive organs (Fallopian tube, uterus and ovary) and for the study of hormonal changes after treatment.

Preparation of Root Extract and its Administration:

For the preparation of drug, plant specimen was collected in morning near about 10: AM. Roots were removed from the plant and properly washed in tap water to remove soil. The roots were left for shade dry and then powdered by grinding and fine non-powdered fraction was removed by filtration through muslin cloth. Gum Arabica was also added to the powder as it acts as binder for the active constituents of the material. Drug was prepared by dissolving 800.00 mg root powder with 2% gum Arabica in 10.00 ml distilled water.[24] Drug was administered as per the body weight of the mice. It is administered as 800.00 mg per kg body weight of the mice. Drug was given orally on each day around 12.00 Noon, approx. 30 minutes after meal. The volume of prepared drug given was variable as 0.10 ml drug given for 10.00 g body weight. The drug was given for 30 days.

After 30 days of drug administration, sexually mature male mice were provided in each cage for copulation and fertilization in the ratio of one male for three females. Male partner was left together for 10 days. Thereafter, male mice were removed from the cage and carefully observed

for histological changes in female mouse. The same procedure was followed for the controlled group of mice.

Obsevations and Discussion:

The ovary, fallopian tube and uterus are the principal female reproductive organs. These organs were considered for histological observation. In treated groups of mice these organs showed no any structural differences and were externally same as of the controlled groups. In controlled groups histological sections of ovary reveals mature Graafian follicles with ovum and nucleus. In some of the sections nucleolus was not prominent. The corona radiata was seen normal in all sections. The zone of granulosa was also clear and surrounded by theca externa and theca interna layers. The follicular cells that surround the ovum and the membrane granulosa were also well defined. Ovary of treated mice revealed some abnormalities in layer of corona radiata. In some of them its thickness was much reduced and in others totally absent. Improperly distributed and distorted cells were also observed in corona radiata. Similar abnormalities observed in the layer of theca externa and theca interna. In layers of cumulus oophoricus dead cells were observed.

L.S. of fallopian tube of both controlled and treated mice showed distinct layers of outer longitudinal and circular muscles. In inner lining of fallopian tube wall of controlled mice had developed epithelial cells and ciliated cells. But in the treated mice, poorly developed ciliated cells were observed which may be due to low secretion of estrogen.[25]

Histology of uterus of controlled mice showed well developed perimetrium, myometrium and endometrium. Endometrium is associated with estrogen secretion. Hence its healthy development in controlled mice was due to normal secretion of the same enzyme. In treated mice, perimetrial and myometrial layers were well developed but endometrium was much reduced which may be due low secretion of estrogen.

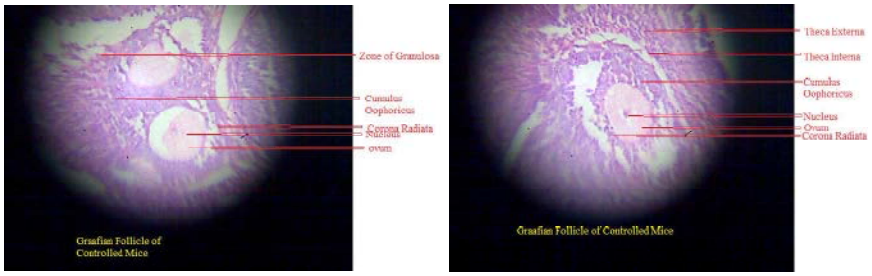

a. b.

Fig: a. & b.: Ovaries of Controlled Mice

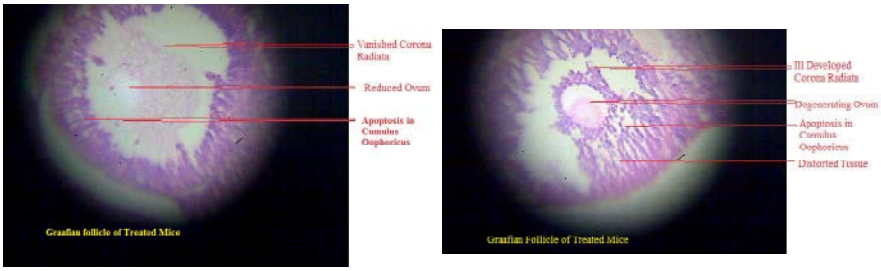

a. b.

Fig: a. & b.: Ovaries of Treated Mice

As shown in the histological slides of ovaries (especially Graafian follicles) of controlled mice, all important components such as ovum, nucleus of ovum, corona radiata, thica interna and thica externa etc. are well defined, whereas in that of the treated mice there is very much reduced or absent corona radiata , distorted thica externa, thica interna and the growth of ovum is also very reduced. Development of abnormalities in such structures favour contraception.

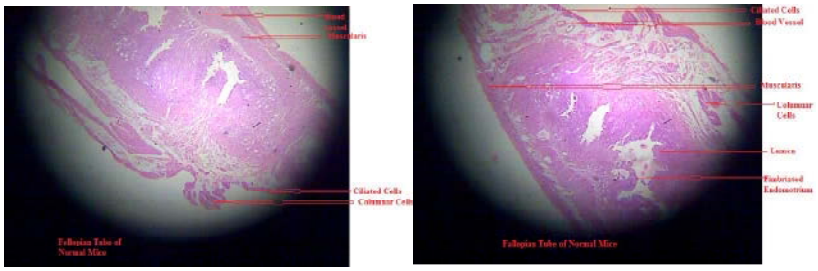

a. b.

Fig.: a. & b. Fallopian Tube of Controlled Mice

In these slides of fallopian tubes there is well defined muscular layers, columnar cells and ciliated cells around the central lumen that promotes movement of spermatozoa.

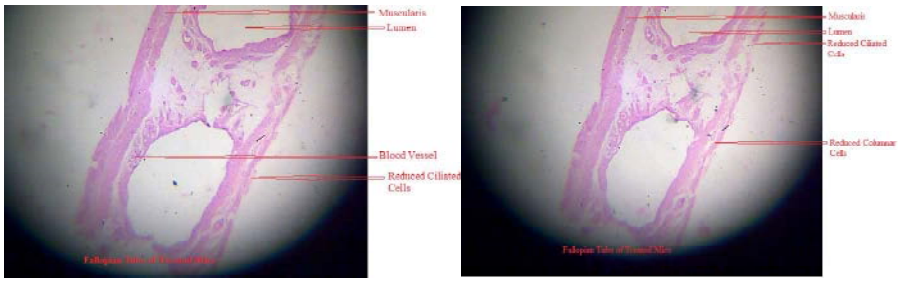

a. b.

Fig.: a. & b. Fallopian Tube of Treated Mice

In the histological slides of uterus of treated mice there are ill developed endometrial layer that don't favour implantation and proper growth of foetus.

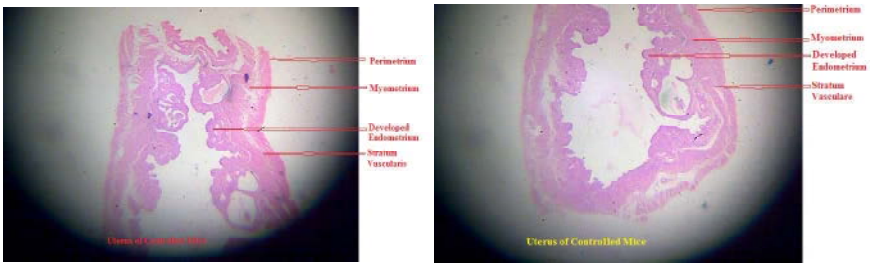

a. b.

Fig.: a. & b. Uterus (Controlled Mice)

In the slides of uterus of controlled mice there are well defined endometrial layer which is a sign of healthy uterus for proper implantation and growth of foetus.

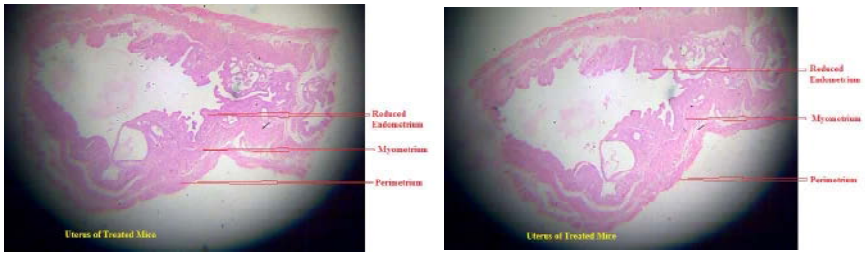

a. b.

Fig.: a. & b. Uterus of Treated Mice

In the histological slides of uterus of treated mice there are ill developed endometrial layer that don't favour implantation and proper growth of foetus.

Conclusion:

The present study reveals that the roots of *Rungia pectinata* (L.) Nees. may contain active phyto-constituents of birth control potential that causes histological abnormalities in the reproductive organs- uterus, fallopian tube and ovary. Such abnormalities make them unsuitable for their proper functioning. The active constituents exhibit multiple impacts. The ovaries after treatment are unable to form the normal and functional egg. Poorly developed ciliated cells of fallopian tube unable to assist the movement of fertilized egg and much reduced endometrium layer of uterus will unsuitable for attachment of the zygote. So we can conclude that roots of *R. pectinata* (L) Nees. have some active phytochemicals which prevents pregnancy in female. The findings also support the traditional knowledge

of tribal communities which requires much more scientific exploration in future for sustainable future.

References:

1. J Rakhi and M Sumathi. Contraceptive methods: Needs, Options and utilization. *The Journal of obstetrics and gynecology of India.* 2011; 61(6):626–634.
2. G Shweta, R Chetna, Soni Jinkal, Shah Nancy, Jain Hitesh. (2011), Herbal plants used as contraceptives. *International Journal of Current Pharmaceutical Review and Research.* 2011; 2(1); 47-53.
3. Das, Bhagwan & Basu R.N. Methods for sterlization and contraception in ancient and mediaeval India"; *Planning Commission of India.* 1968; 3(1).
4. Susruta, *Susrutasamhita.* Nirnayasagara Press, Bombay;1954; 15:5.
5. Widgery, Alban. The Principles of Hindu Ethics. *International Journal of Ethics*. 1930; 40(2): 232-245.
6. Manusmriti, 4:1 & 5:169
7. Lideguard O, Kreiner S. *Contraception.* 2002; 65: 197-205.
8. VS Kasture, CT Chopde; VK Deshmukh. *Journal of Ethnopharmacology*. 2000; 71: 65-75.
9. G Lacobellis. *Cardiaovascular Drug therapy*. 2004. 18: 239-40.
10. Sanersak S, Korsakul C. *J. Med. Assoc. Thai*. 2006; 89:741-47.
11. Gierisch JM, Coeytaus RR, Urrutia RP. Oral contraceptive use and risk of breast, cervical, colorectal, and endometrial cancers: a systematic review. *Cancer Epidemiol Biomarkers Prev.* 2013; 22(11): 1931 – 43.
12. Rang HP, Dale MM, Ritter JM, Flower RJ, Henderson G. The reproductive system, Rang and Dale's pharmacology, 7th ed., Edinburgh: Elsevier/Churchill Livingstone; 2012; 426.
13. Kulkarni J. Contraceptive Pill Linked to Depression. Monash Newsline. (Retrieved 2007-10-29).
14. FFPRCH. The UK Medical Eligibility Criteria for Contraceptive Use (2005/2006) (PDF). Archived from the original on 2007-06-19. Retrieved 2007-03-31.
15. La Corte ALC, Carter AM, Turner AJ, Grant PJ, Hooper NM. The bradykinin-degrading aminopeptidase P is increased in women taking the oral contraceptive pill. *Journal of Renin-Angiotensin-Aldosterone System.* 2008; 94(4):221.
16. Grimes DA. Intrauterine devices (IUDs). *Contraceptive Technology*. New York: Ardent, 19th ed.: 117 –143.
17. Nall R. What are the side effects of an IUD? *Medical News Today*. 2023
18. Lewington A. Medicinal plants and plant extracts: A review of their importation into Europe. Cambridge, UK; Traffic International. 1993.
19. Bentley R and Trimen H. Medicinal Plants, J. and A. Churchill, London. 1980; I-IV.
20. State of Environment Report. Ministry of Environment and Forest, Government of India, New Delhi. 2001; 77-79.
21. Satyavati GV, Gupta AK, Tondon N (editors) (1987); Medicinal Plants of India, New Delhi, ICMR.1987; Vol.:2,
22. K Rajandeep, Sharma Anil, Kumar Ravinder and Kharb Rajeev. Rising trends towards herbal contraceptives; *J. Nat. Prod. Plant Resource*. 2011; 1 (4): 5-12.

23. Ciganda C, Laborde, A. Herbal infusions used for induced abortion. *Journal of toxicology and Clinical toxicology.* 2003; 41(3): 235—239.

24. Swain S R, Sinha B N & Murthy P N (2008). Antiinflamatory, Diuretic and Antimicrobial activities of *Rungia pectinata* Linn. and *Rungia repens* Nees.; *Indian journal of Pharmaceutical Sciences.* 2008; 70 (5): 679-683.

25. Daftary S, Chakravarty S (2011); *Manual of obstetrics*, Elsevier. 2011; 3rd Ed.: 1-16.

ACKNOWLEDGEMENT: Authors are very thankful to MCSRC for providing experimental facilities on Swiss Albino Mice. They are also thankful to BSI, Howrah for the identification of experimental plant material.

ETHICAL APPROVAL: Authors have written permission of Ethical Committee to conduct the experiments on Animal model.

Solar Energy As An Alternative Energy Source: Analysis in Applied Role in Sustainable Development

Dr. Seema Singh

Department of Physics, Hawabagh College, Jabalpur, MP

Abstract

Solar energy is any type of energy generated by the sun. Solar energy is produced by nuclear fusion, which takes place in the sun. Solar energy is a powerful energy source that can be used to heat, cool and light homes and businesses.

More energy from the sun hits Earth in one hour than everyone in the world uses in one year. Various technologies convert sunlight into usable energy for buildings. The most commonly used solar technologies for homes and businesses are solar photovoltaics for electricity, passive solar design for heating and cooling, and solar water heating.

Solar energy is an environmentally friendly technology, a large energy reserve and one of the most important renewable and green energy sources. It plays an essential role in achieving energy solutions for sustainable development. Therefore, the huge amount of solar energy available daily makes it a very attractive source for electricity production. Technologies, concentrated solar power applications and solar photovoltaics, are constantly evolving to meet our energy needs. Thus, in the same context, the large installed capacity of solar energy applications around the world supports the energy sector and corresponds to the labor market to obtain sufficient development. This paper highlights the applications of solar energy and their role in sustainable development and considers the overall employment potential of renewable energy. It thus provides an overview and analysis of the sustainability of solar energy, including environmental and economic development.

Keywords: Solar energy, sustainable development, application of solar energy, perspective of solar energy

Introduction

Energy is an essential need for the existence and growth of human communities. Consequently, the need for energy gradually increased as human civilization progressed. Moreover, in the last few decades, the rapid growth of the world's population and its dependence on technological developments have increased energy demands. In addition, green

technology resources play an important role in sustainable energy supply, especially in mitigating climate change. At present, fossil fuels remain dominant and will continue to be the primary source of large-scale energy for the foreseeable future; however, renewable energy should play a vital role in the future of global energy. The global energy system is undergoing a shift towards more sustainable energy sources.

Energy production from fossil fuel sources has peaked, with solar energy expected to lead energy production in the near future. Additionally, by 2050, solar power generation is projected to increase to 48% due to economic and industrial growth.

In recent years, it has become increasingly clear that the world must reduce greenhouse gas emissions by 2050, ideally to net zero, if we are to meet the Paris Agreement's goal of reducing the rise in global temperatures.

Role and Importance of Solar Energy

Solar energy is the radiant light and heat from the Sun that is harnessed through a range of technologies such as solar power to generate electricity, solar thermal (including solar water heating) and solar architecture. It is a fundamental source of renewable energy and its technologies are generally characterized as passive solar or active solar depending on how they capture and distribute solar energy or convert it into solar energy. Active solar techniques include the use of photovoltaic systems, concentrated solar power and solar water heating to harness energy. Passive solar techniques include orienting the building to the Sun, choosing materials with favorable thermal mass or light-scattering properties, and designing spaces that naturally circulate air.

Demand for cleaner energy sources has increased in recent decades. Based on this, decision-makers in all countries have developed plans that depend on renewable resources through a long-term strategy. Thus, such plans reduce dependence on traditional energy sources and replace traditional energy sources with alternative energy technologies. As a result, the global community is beginning to move towards using sustainable energy sources and reducing reliance on traditional fossil fuels as a source of energy.

Businesses and industry use solar technology to diversify energy sources, increase efficiency and save money. Energy developers and utilities are using solar photovoltaic and concentrating solar technologies to generate electricity on a massive scale to power cities and small towns.

Installed Capacity and Use of Solar Energy Worldwide

The history of solar energy can be traced back to the seventh century when solar powered mirrors were used. In 1893, the photovoltaic (PV)

effect was discovered; after many decades scientists have developed this technology to produce electricity. Based on this, after many years of research and development by scientists around the world, solar energy technology is divided into two key applications: solar thermal and solar PV.

PV systems convert the sun's energy into electricity using solar panels. Due to their ubiquitous deployment, these photovoltaic devices have quickly become the cheapest option for new electricity generation in many locations around the world. For example, during the period 2010 to 2018, the cost of electricity production by solar PV plants decreased by 77%. However, progress in the installed capacity of solar PV power plants increased a hundredfold between 2005 and 2018. As a result, solar PV plants have become a key component in the low-carbon sustainable energy system needed to provide access to affordable and reliable electricity that helps fuel the climate of Paris agreement and in achieving the goals of sustainable development by 2030.

Installed solar power capacity around the world has increased rapidly to meet energy demands. The installed capacity of PV technology increased from 40,334 to 709,674 MW from 2010 to 2020, while the installed capacity of concentrated solar power (CSP) applications, which was 1,266 MW in 2010, increased to 6,479 MW after 10 years. Therefore, solar PV technology has more installations than CSP applications. Thus, stand-alone solar PV plants and large-scale grid-connected PV plants are widely used worldwide and are used in space applications.

Methods of Energy Storage

Thermal mass systems can store solar energy in the form of heat at domestic useful temperatures over a daily or inter-seasonal period. Thermal storage systems generally use readily available materials with high specific heat capacity, such as water, soil and rock. Well-designed systems can reduce peak consumption, shift usage to off-peak hours and reduce overall heating and cooling requirements.

Another heat storage medium is phase change materials such as paraffin and Glauber's salt. These materials are inexpensive, readily available, and can provide useful domestic temperatures (around 64 °C or 147 °F). The "Dover House" (in Dover, Massachusetts) was the first to use Glauber's salt heating system in 1948. Solar energy can also be stored at high temperatures using liquefied salts. Salts are an effective storage medium because they are cheap, have a high specific heat capacity, and can deliver heat at temperatures compatible with conventional energy systems. The Solar Two project used this method of energy storage, which

allowed it to store 1.44 tera joules (400,000 kWh) in its 68 m3 reservoir, with an annual storage efficiency of about 99%.

Off-grid PV systems traditionally use rechargeable batteries to store excess electricity. In grid-tied systems, excess electricity can be sent to the transmission grid, while standard grid electricity can be used to cover shortfalls. Net metering programs give home systems credit for all the electricity they feed into the grid. This is addressed by "rolling back" the meter whenever the house produces more electricity than it uses. If the net electricity consumption is below zero, the company will then carry over the kilowatt-hour credit to the next month. Other approaches include using two meters to measure electricity consumed vs. electricity produced. This is less common due to the increased cost of installing a second meter. Most standard meters measure accurately in both directions, so a second meter is not needed.

Pumped hydroelectricity stores energy in the form of water pumped when power is available from a lower elevation reservoir to a higher elevation reservoir. Energy is recovered when demand is high by releasing water, with the pump becoming a hydropower generator.

Application of solar energy

Energy can be obtained directly from the Sun - so-called solar energy. Globally, there has been an increase in solar energy applications as it can be used to generate electricity, water desalination and heat generation, etc. The taxonomy of solar energy applications is as follows: (i) PVs and (ii) CSPs.

Solar cells are devices that convert sunlight directly into electricity; typical semiconductor materials are used to create PV solar cell devices. The characteristics of these materials are based on atoms with four electrons in their outer orbit or shell. Semiconductor materials are from group "IV" of the periodic table or from a mixture of groups "IV" and "II", the latter named as "II–VI" semiconductors. In addition, a mixture of group "III" and "V" elements in the periodic table can form "III–V" materials.

PV devices, sometimes called solar cells, are electronic devices that convert sunlight into electrical energy. PV is also one of the fastest growing renewable energy technologies today. It is therefore expected to play a significant role in the long-term evolution of the world's electricity generation mix.

Solar PV systems can be integrated to supply electricity at a commercial level or installed in smaller clusters for mini-grids or individual use. Using PV modules to power mini-grids is a great way to offer electricity to those

who don't live near power lines, especially in developing countries with abundant solar energy resources. In the last decade, the cost of producing photovoltaic modules has fallen drastically, making them not only available, but sometimes the cheapest form of energy. PV arrays have a lifespan of 30 years and come in different shades depending on the type of material used in their production.

The most typical method for solar PV desalination technology used for desalination of sea or salt water is electrodialysis (ED). Therefore, solar PV modules are directly connected to the desalination process. This technique uses direct current to remove salt from sea or salt water.

PV–thermal (PV–T) technology involves conventional solar PV modules coupled with a thermal collector mounted on the back of the PV module to preheat domestic hot water. This allows more of the solar energy hitting the collector to be converted into useful electrical and thermal energy.

A zero-energy building is a building that is designed for zero net energy emissions and emits no carbon dioxide. Building integrated PV technology (BIPV) is associated with solar energy sources and devices in buildings that are used to supply energy needs. Thus, Building Integrated Thermal Photovoltaics (BIPV/T) include creative technologies such as solar cooling.

A PV water pumping system is usually used to pump water in rural, isolated and desert areas. The system consists of photovoltaic modules for powering the water pump to the point where water is needed. The speed of water pumping depends on many factors, such as pumping height, intensity of sunlight, etc.

A PV-powered cathodic protection (CP) system is designed to power a CP system for metal surface corrosion control. This technique is based on the impressive current obtained from photovoltaic solar energy systems and is used to bury pipes, tanks, concrete structures, etc.

Concentrated PV (CPV) technology uses either refractive or reflective concentrators to increase solar radiation to PV cells. Typically, highly efficient solar cells consisting of many layers of semiconductor materials stacked on top of each other are used. This technology has an efficiency of >47%. In addition, the devices generate electricity and the heat can be used for other purposes.

For CSP systems, the sun's rays are concentrated using mirrors in this application. These rays heat the fluid, resulting in steam used to drive a turbine and generate electricity. Large power plants use CSP to generate electricity. An array of mirrors usually redirects the beams to a tall thin tower in a CSP plant. Thus, many large flat heliostats (mirrors) are used

to track the Sun and focus its light onto a receiver in power tower systems, sometimes known as central receivers. The hot liquid can be used immediately to produce steam or stored for later use. Another big advantage of a CSP plant is that it can be built from molten salts to store heat and generate electricity outside of daytime.

Mirrored dishes are used in dish engine systems to focus and concentrate sunlight onto a receiver. The dish assembly tracks the Sun's movement to capture as much solar energy as possible. The engine includes thin tubes that work outside the four-piston cylinders and it opens into the cylinders containing hydrogen or helium gas. The pistons are driven by the expanding gas. Finally, the pistons drive an electric generator by turning a crankshaft.

A further water-treatment technique, using reverse osmosis, depends on the solar-thermal and using solar concentrated power through the parabolic trough technique. The desalination employs CSP technology that utilizes hybrid integration and thermal storage allows continuous operation and is a cost-effective solution. Solar thermal can be used for domestic purposes such as a dryer. In some countries or societies, the so-called food dehydration is traditionally used to preserve some food materials such as meats, fruits and vegetables.

The Role of Solar Energy in Sustainable Development

Sustainable energy development is defined as the development of the energy sector in terms of production, distribution and use of energy, which is based on the rules of sustainability. Energy systems will significantly affect the environment in both developed and developing countries. Consequently, a global sustainable energy system must optimize efficiency and reduce emissions.

The sustainable development scenario is based on an economic perspective. It also examines what actions will be needed to deliver long-term co-benefits on climate, clean air and energy access. The short-term details are based on the IEA's Sustainable Recovery Strategy, which aims to support economies and jobs through the development of cleaner and more reliable energy infrastructure. In addition, sustainable development includes the use of renewable energy applications, smart grid technologies, energy security and energy pricing, and sound energy policy.

Demand-side response can help meet flexibility requirements in electrical systems by shifting demand over time. As a result, the integration of renewable technologies to help ease peak demand is reduced, maintaining system stability and reducing overall costs and CO2

emissions. Demand response is currently used mainly in Europe and North America, where it is primarily aimed at large commercial and industrial customers of electricity.

International standards are an essential part of a high-quality infrastructure. The introduction of legislative convergence, increased competition and the promotion of innovation will allow participants to participate in the global world photovoltaic market. Many other countries could benefit from more active involvement in the development of global standards for solar PV. Leading countries in the production and deployment of solar PV have adopted global standards for PV systems and made a significant contribution to the development of clean energy. Additional aid and capacity building to improve quality infrastructure in developing economies can also help support wider implementation and compliance with international standards for solar PV. Support can thus align legal requirements and frameworks and provide further impetus for trade in safe and high-quality solar PV products.

The continued trade-led deployment of solar PV and other renewable technologies will strengthen the nation's infrastructure. For example, off-grid solar energy alternatives such as stand-alone systems and mini-grids could be easily deployed to help healthcare facilities improve service levels and power portable testing sites and vaccine coolers. In addition to helping with the immediate medical crisis, trade-led adoption of solar PV could help improve the economy after the COVID-19 outbreak, not least by creating jobs in the renewable energy sector, which are estimated to reach more than 40 million by 2050.

A framework for developing energy sustainability using solar energy is one way to achieve this goal. With the large availability of solar energy sources for PV and CSP energy applications, we can move towards energy sustainability.

The environmental aspects of such applications have been assessed, including the aspect of environmental conditions, operating conditions, etc. It is clean, environmentally friendly and also energy efficient. In addition, this technology has no removable parts, low maintenance and long life.

Economic and social development is considered by offering employment opportunities to the community and providing cheaper energy options. It can also improve people's income; in return, the standard of living will increase. Energy is therefore paramount and is considered the most important element of human life, social progress and economic development.

With efforts to increase the energy transition to sustainable energy systems, the next decade is expected to see a continued boom in solar energy and all clean energy technologies. Scientists from all over the world see research and innovation as essential driving forces for increasing the efficiency of such solar application technology.

Solar Energy Perspective

Investment in solar energy can meet energy goals and environmental protection by reducing carbon emissions without having a detrimental effect on the country's development. There is a huge potential for solar energy in countries located in the "Sun Belt", where there is an abundance of global horizontal solar radiation throughout the year. As a result, these countries, including the Middle East, Australia, North Africa, China, the US and South Africa to name a few, have great potential for solar energy technology. The average annual solar radiation intensity is >2800 kWh/m2 and the average daily solar radiation intensity is >7.5 kWh/m2.

Conclusion

This document emphasizes the importance of sustainable energy development. Solar energy would help stabilize energy prices and provide a range of social, environmental and economic benefits. It indicates the contribution of solar energy to achieving sustainable development through meeting energy requirements, creating jobs and protecting the environment.

Earth receives 174 petawatts (PW) of incoming solar radiation (insolation) in the upper atmosphere. About 30% is reflected back into space, while the rest, 122 PW, is absorbed by clouds, oceans, and land masses. The spectrum of sunlight on the Earth's surface is mostly scattered in the visible and near-infrared bands with a small portion in the near-ultraviolet. Most of the world's population lives in areas with solar radiation levels of 150-300 watts/m2, or 3.5-7.0 kWh/m2 per day.

Globally, the market share of thin-film technologies in photo-voltaics remains around 5% by 2023. However, thin-film technology has become significantly more popular in the United States, where CdTe cells alone account for nearly 30% of new utility-scale deployments in 2022.

In 2021, Lazard estimates the break-even cost of new construction for unsubsidized utility-scale solar at less than $37 per MWh, and existing coal above that amount. The 2021 report also said that new solar power was also cheaper than new gas power, but generally not existing gas power.

Installed capacity increased from 3 GW in 2020 to 13 GW in 2022, surpassing the forecast of 10 GW by 2025. The World Bank estimates that

there are 6,600 large bodies of water suitable for floating solar energy, with a technical capacity of over 4,000 GW if 10% of their surfaces were covered with solar panels.

References

1. *"Solar Energy Technologies and Applications". Canadian Renewable Energy Network. Archived from the original on 25 June 2002.*
2. *Frank Kryza (2003). The Power of Light. McGraw Hill Professional. pp. 64, 135. ISBN 978-0-07-140021-3.*
3. *Smith, Zachary Alden; Taylor, Katrina D. (2008). Renewable And Alternative Energy Resources: A Reference Handbook. ABC-CLIO. p. 174. ISBN 978-1-59884-089-6.*
4. *Marques Lameirinhas, Ricardo A.; N Torres, João Paulo; de Melo Cunha, João P. (2022). "A photovoltaic technology review: History, fundamentals*
5. *Karuppu, Karthik; Sitaraman, Venk; NVICO (2019). Solar Assessment Guidance: A Guide for Solar Trainee, Trainer & Assessor Examination. Notion Press. ISBN 978-1646505227.*
6. *Frank Kryza (2003). The Power of Light. McGraw Hill Professional. pp. 64, 135. ISBN 978-0-07-140021-3.*
7. *"IEA Says Solar May Provide a Third of Global Energy by 2060". Bloomberg Businessweek. 1 December 2011. Archived from the original on July 21, 2012.*
8. *"Renewables' power ahead to become the world's cheapest source of energy in 2020". World Economic Forum. 5 July 2021.*
9. *"Levelized Cost Of Energy, Levelized Cost Of Storage, and Levelized Cost Of Hydrogen". Lazard.com.*
10. Sorensen B. *Renewable Energy: Physics, Engineering, Environmental Impacts, Economics and Planning*. 4th edn. London: Academic Press, 2010.
11. IEA, IRENA, WMO, WBG, WHO. *Tracking SDG7: The Energy Progress Report 2021.* Washington, DC: The World Bank, 2021